# Journal of Mechanics of Materials and Structures

Volume 7, No. 1 January 2012

mathematical sciences publishers

# JOURNAL OF MECHANICS OF MATERIALS AND STRUCTURES

jomms.net

Founded by Charles R. Steele and Marie-Louise Steele




See http://jomms.net for submission guidelines.


JoMMS (ISSN 1559-3959) is published in 10 issues a year. The subscription price for 2012 is US $555/year for the electronic version, and $735/year (+$60 shipping outside the US) for print and electronic. Subscriptions, requests for back issues, and changes of address should be sent to Mathematical Sciences Publishers, Department of Mathematics, University of California, Berkeley, CA 94720–3840.

JoMMS peer-review and production is managed by EditFLOW® from Mathematical Sciences Publishers.

PUBLISHED BY
mathematical sciences publishers
http://msp.org/

A NON-PROFIT CORPORATION

Typeset in LaTeX

JOURNAL OF MECHANICS OF MATERIALS AND STRUCTURES
Vol. 7, No. 1, 2012

msp

# DYNAMICS OF FRP STRENGTHENED UNIDIRECTIONAL MASONRY WALLS I: A MULTILAYERED FINITE ELEMENT

ODED RABINOVITCH AND HAZEM MADAH

The dynamic response of unidirectional FRP strengthened masonry walls is investigated. The examined walls are strengthened using externally bonded composite materials. In this part of the paper, a nonlinear multilayered finite element for the nonlinear dynamic analysis of the unidirectional strengthened wall is developed. The formulation reduces the general 2D problem to a 1D form using high order kinematic assumptions that are based on the static deformation fields in the various components. The model aims to face the challenges associated with the combination of length scales, differences in elastic properties, irregular points, cracking, crushing, and inelastic behavior of the masonry substrate. The geometrical nonlinearity, the layered configuration, and the variation of the stresses through the depth the adhesive layers are also addressed. A numerical study that examines the capabilities of the model and its convergence with refinement of the spatial and temporal meshes is presented. Emphasis is placed on the global nonlinear dynamic response, the local effects near the joints, the interfacial stresses, and their temporal variation under dynamic loads.

## 1. Introduction

The strengthening of existing masonry structures by means of externally bonded layers of composite materials is recognized as an advantageous solution for structural upgrade [Albert et al. 2001; Hamilton and Dolan 2001; Griffith et al. 2004; Gilstrap and Dolan 1998]. The demands for upgrade and strengthening mainly stem from the limited (if any) ability of the masonry construction to carry tensile stresses and the resulting vulnerability to dynamic out-of-plane loads. The externally bonded composite layer overcomes this obstacle and provides the existing wall with a strong, stiff, lightweight, and durable tensile resisting layer and thus with a supplemental load resisting mechanism.

The effective design, analysis, and use of masonry walls strengthened with composite material require adequate analytical and computational tools. While finite element analysis (FEA) is the leading computational tool of modern structural engineering, its application to the dynamic analysis of the FRP strengthened masonry wall is involved with significant difficulties. In fact, the entire family of FRP strengthened structural members is a class of structures that their classical 2D or 3D elasticity based FEA is very complicated, computational effort demanding, and, in some cases, subjected to divergence. The problematic nature stems from five major features of the unique structure:

(1) The layered configuration and the assembly of layers of significantly different thickness scale. As a

This research was supported by The Israel Science Foundation, Grant No. 772/06.

*Keywords:* masonry wall, composite material, nonlinear analysis, dynamic analysis, finite element, nonlinear dynamics, strengthening.

rule, the thickness of the adhesive and the composite layers ranges between parts of a millimeter to few millimeters whereas the thickness of the masonry wall is in the range of hundreds of millimeters.

(2) The different length scales in the masonry construction itself. The masonry construction is an assembly of blocks and mortar joints. The length scale of the blocks (hundreds of millimeters) is much larger than the one of the joints (few millimeters).

(3) The assembly of materials with significantly different elastic properties. In most cases, the elastic modulus of the composite material is two to three orders of magnitude larger than the one of the adhesive layer and about ten times larger than the elastic moduli of the masonry wall.

(4) The presence of structural irregularities in the form of edges of the bonded reinforcement, debonded regions, masonry joints, cracks, etc.

(5) The nonlinearities involved with the structural response. The brittleness of masonry construction, the contact effects at the joints, the nonlinear response of the mortar material under compression, and its inelastic response under cyclic loading introduces material nonlinearities [Hamed and Rabinovitch 2007b; 2008]. Wrinkling and local buckling when the thin FRP strips are subjected to compressive stresses (a scenario that may be inevitable under dynamic loads) and global instability or snap-through of the entire wall [Rabinovitch 2004; Hamed and Rabinovitch 2007a] stem from geometrical nonlinearity. The potential evolution of debonding and interlaminar cracking is involved with interfacial nonlinearities [Rabinovitch 2010].

The combination above yields structural phenomena with length scales that range from the global dimensions of the wall to the thickness of the thinnest layer. The global response can usually be detected using standard techniques. The localized effects associated with stress concentrations near edges and joints, cracking or crushing of the mortar joints, and the transfer of stresses between the masonry wall and the strengthening system are the ones that make the analysis complicated and challenging. The interaction with the dynamic response of the wall and the various nonlinearities make the quantification of the structural response of the dynamically loaded masonry wall even more challenging.

The shortcomings of standard finite element analysis (FEA) of FRP strengthened elements in general, and FRP strengthened masonry walls as a particular case, are reflected by many works that applied FE to the analysis of the strengthened wall. For example, Pan and Leung [2008] studied the effect of tapering of the FRP strip on the debonding process and assessed the edge stresses using two types of FEA. For the elastic case, 8-node quadratic elements with characteristic size of about 1/5 the thickness of the adhesive layer were used. For the nonlinear case, additional nonlinear link elements that account for the degradation of the interfacial shear resistance were added. In both cases, the number of elements required for the analysis of a realistic scale structure is huge. A similar problem was encountered in the 3D FEA presented in [Huang and Lyons 2007]. In this case, the problem of mesh refinement to elements smaller than $1 \cdot 10^{-6}$ of the span was tackled using a submodeling technique. In the substructure, the average element size equals the thickness of the FRP strip and the smaller elements are about two orders of magnitude smaller than that. The finite element model presented in [Li et al. 2009] focused on the interfacial stresses and used elements that are of the same order as the thickness of the adhesive layer. The results of the FEA reveal that in certain cases, the numerical analysis fails to satisfy the zero shear condition at the plate end; see also [Gao et al. 2006; Teng et al. 2002; Rabinovitch and Frostig 2000].

Another aspect, discussed in the last two of these references and in [Hamed and Rabinovitch 2007a], is the divergence of the peak stresses at the critical point; its impact is observed in the FEA results outlined in [Yang et al. 2004]. Due to singularities near irregular points, the critical peak stresses tend to diverge with the refinement of the mesh. This trend shades on the reliability of such analyses and on their applicability to practical design.

The above studies mainly focused on FRP strengthened concrete beams. In general, the dynamic FEA of FRP strengthened walls is even more complicated. The additional levels of complexity are attributed to the effect of cracking, crashing, and geometrical irregularity at the mortar joints and to the unique boundary conditions. Under dynamic loads, the combination of the two phenomena yield a time dependent arching effect, rocking, and coupling between in-plane and out-of-plane responses.

A state of the art FE treatment of the dynamic response of unidirectional externally strengthened masonry members is reported in [Davidson et al. 2005]. This study focuses on masonry walls made of hollow concrete masonry units under blast loads. The walls are strengthened with polymeric layers. The nonlinear FEA focuses on a one-way response and uses a highly refined mesh with as much as 100,000 elements. The analysis accounts for the development of arching effects [Dafnis et al. 2002], the masonry-polymer interfacial response, the high strain rate, and the separation at mortar joints. On the other hand, the large number of elements required for the nonlinear dynamic analysis highlights one of the drawbacks of the conventional FE approach. The same drawbacks also dictate the refined mesh required for the hygrothermal analysis of FRP patched masonry walls described in [Khoshbakht et al. 2009].

The above survey highlights some of the inherent drawbacks of conventional FEA of FRP strengthened elements in general and FRP strengthened masonry walls in particular. In light of these obstacles, Lam et al. [2003] raised concerns about the viability of this type of modeling and pointed in favor of macromodels that simulate the global load-deflection response obtained from experiments. On the other hand, in the case of the strengthened masonry wall, such geometrical homogenization may overlook critical aspects like of the stress concentrations near irregular points.

Analytical models for the static and dynamic nonlinear analysis of FRP masonry walls (see, e.g., [Hamed and Rabinovitch 2007a; 2007b; 2008]) can overcome some of the above critical obstacles. The analytical approach can also handle the combination of global and localized physical effects under a unified analytical platform. The localized stress concentrations near the edges of the FRP system, near the cracked mortar joints, near debonded regions that develop in the vicinity of the cracked joints, and in regions that are wrinkled due to geometrical nonlinearity are taken into account through consideration of the high order stress and deformation fields in the compliant adhesive layers. On the other hand, these models are still limited in terms of the ability of expansion to more demanding problems like bidirectional nonlinear dynamic response and in terms of implementation in more general computational environments for structural analysis.

Specially tailored finite elements for the analysis of layered structures such as sandwich beams or masonry arches strengthened with FRP strips were developed by Buller [Buller 2005] and Elmalich and Rabinovitch [Elmalich and Rabinovitch 2009; Elmalich and Rabinovitch 2010], respectively. However, these models are limited to the linear elastic and static case [Buller 2005], the quasinonlinear, elastic, and static case [Elmalich and Rabinovitch 2009], or the physically nonlinear but static case [Elmalich and

Rabinovitch 2010]. As such, these models cannot address the unique features of the nonlinear, inelastic, and dynamic response of the strengthened masonry wall studied here.

The objective of this part of the paper is to develop a special finite element approach for the nonlinear dynamic analysis of unidirectional FRP strengthened masonry walls. The paper aims to combine the advantages of the analytical models presented in [Hamed and Rabinovitch 2007a; 2007b; 2008] with those of the finite element method and to derive a special finite element for the nonlinear dynamic analysis of the wall. The unique nonlinear dynamic finite element formulation developed here aims to face the challenges stemming from the combined length scales, the different elastic scales, the existence of irregular points, the material nonlinearity of the mortar joints, the layered configuration of the strengthened wall, and some aspects of the geometrical nonlinearity.

***Article organization.*** The modeling assumptions, which follow the analytical models described in the three articles just cited, and the mathematical formulation are presented next. They are followed by a convergence study that examines the capabilities of the finite element model. An experimental study on full scale FRP strengthened wall and comparison of the numerical results with results of the experiments are presented and discussed in the second part of this paper [Rabinovitch and Madah 2012].

## 2. Finite element model

**2.1.** ***Modeling and assumptions.*** The strengthened wall, the notation, and the sign conventions appear in Figure 1. The modeling assumptions follow the main analytical concepts described in [Hamed and

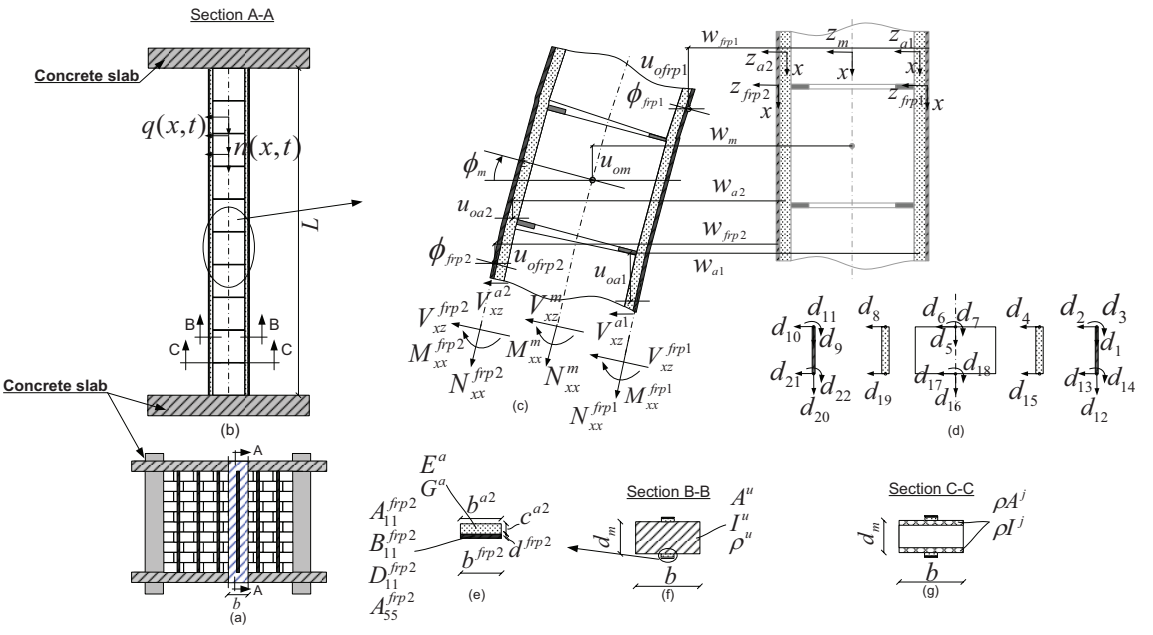


**Figure 1.** Notation and sign convention: (a) A unidirectional strengthened wall and a characteristic strip. (b) cross section and distributed loads; (c) deformations and stress resultants; (d) degrees of freedom; (e)–(g) cross sections.

Rabinovitch 2007a; 2007b; 2008] and the phenomenological aspects of the wall's response. For simplicity, the formulation focuses on a masonry wall strengthened with vertical FRP strips or with FRP sheets that are extended to the beams or slabs at the top and bottom (Figure 1a). This configuration, and the pattern of bed joints yield vertical flexural "strips" that are stiffer and stronger than the lateral ones and therefore transfer loads more effectively towards the upper and lower supporting element. Under these conditions, as well as in cases where the boundary conditions allow transfer of loads to the upper and the lower supporting elements but not to the lateral ones (if any), it is assumed that the out-of-plane dynamic loads yield a unidirectional flexural action in the height direction. Therefore, it is assumed that the stress and displacement fields are uniform through the width of each component. With these assumptions in mind, the analysis focuses on a characteristic structural strip. In the case of FRP strips, the width of the characteristic strip equals the spacing between two adjacent FRP strips. In the case of FRP sheets, a unit wide characteristic strip is examined.

The characteristics of the strengthened masonry wall require the use of a refined modeling approach that can capture the global behavior but also the localized behavior of each component. In particular, the layered configuration, the differences in material properties, the presence of structural irregularities such as edges, debonded regions, masonry joints, and cracks, the physical nonlinearities of the brittle masonry construction, and the geometrical nonlinearities due to wrinkling, local buckling or global instability motivate a refined and detailed modeling approach. In light of that, the modeling approach adopted in this paper aims to be able to capture the above phenomenological aspects of the FRP strengthened wall. To achieve this, it considers the strengthened wall as a structural element that is composed of five layers. The formulation of each layer is presented using its own coordinate system (Figure 1) and the layers are joined together through the conditions of compatibility of deformations.

Out of the five, the two outer layers are the FRP strips or sheets. These layers, indicated by subscript or superscript "$frp1$" and "$frp2$", are modeled using first-order shear deformation theory (Timoshenko beam; see [Timoshenko and Gere 1961; Reddy 1999]) with an intermediate class of deformations (large deflections, moderate rotations, small strain). The FRP strips are assumed linear elastic and their constitutive behavior is governed by classical lamination theory (see [Vinson and Sierakowski 1986]).

The middle layer is the masonry wall. This layer is comprised of an assembly of masonry units (designated with "$mu$") and masonry joints (designated with "$mj$"). Both components are modeled using first order Timoshenko beam theory with large deflections but moderate rotations and small strains. The distinction between the masonry units and the mortar joints comes into effect through their constitutive model. The masonry units are assumed linear and elastic. The mortar material is subjected to cracking, nonlinear behavior under compression, and inelastic behavior under loading-unloading cycles. In that sense, it is assumed that the material nonlinearity that governs the behavior of the masonry construction is concentrated in the mortar joints and introduced through the constitutive model for the mortar material. Since the masonry units and the mortar joints are modeled using the same kinematic assumptions (but with different constitutive relations), both components are designated with the subscript / superscript "$m$". In cases where the formulation makes a distinction between the two, the notation "$mu$" and "$mj$" is used.

The FRP layers are attached to the masonry walls using adhesive layers. These layers, which are designated with the subscripts/superscripts "$a1$" and "$a2$", are modeled as 2D elastic media. The adhesive layers resist shear and out-of-plane normal stresses. Their in-plane rigidities, which are significantly

lower than those of the adjacent components, are neglected (also [Hamed and Rabinovitch 2007a; 2007b; 2008; Rabinovitch and Frostig 2000]). The modeling of the adhesive layers assumes material linearity and, akin to assumption of small strain applied to the masonry wall and the FRP strip, the strains are assumed small.

The entire structural element is mathematically assembled together by imposing continuity and compatibility conditions. The continuity conditions between the masonry units and the mortar joints require continuity of the in-plane displacement, out-of-plane displacement, and cross-sectional rotation. The conditions at the interfaces of the adhesive layers with the FRP layers and the masonry wall require compatibility of the in-plane and out-of-plane displacements. In that sense, it is assumed that the interfaces can transfer the shear and out-of-plane normal stresses stemming from the compatibility conditions. The effect of interfacial debonding, in which the compatibility conditions are relaxed and the interfacial stresses vanish, is not directly addressed here. Alternatively, the physical debonding conditions can be simulated by locally controlling the properties of the materials involved.

The formulation introduces the dissipative effects due to damping through a combination of external (mass proportional) and internal (stiffness proportional) viscous components and the Rayleigh damping model (see, for example, in [Clough and Penzien 1993]). Therefore, the model for the undamped strengthened wall is derived first and then the proportional damping is introduced. Finally, it is assumed that the loads are exerted at the masonry wall only and that the kinematic relations and deformation fields developed for the static case can be applied to the dynamic case as well.

**2.2.** ***Principle of virtual work.*** The finite element formulation is based on the principle of virtual work. For the undamped structure, the principle of virtual work reads

$$\delta K + \delta' U + \delta W = 0 \tag{1}$$

where $\delta K$, $\delta' U$, and $\delta W$ are the incremental (virtual) works of the inertial forces, stresses, and external loads, respectively. The prime is used to emphasize that $U$ is not necessarily a potential function. The virtual work of the inertial forces is

$$\begin{aligned}
\delta K = -\Bigg[ & \int_{V^m} \rho^m \big(\ddot{w}_m(x, z_m, t)\delta w_m(x, z_m, t) + \ddot{u}_m(x, z_m, t)\delta u_m(x, z_m, t)\big)\, dV^m \\
& + \int_{V^{frp1}} \rho^{frp1} \big(\ddot{w}_{frp1}(x, z_{frp1}, t)\delta w_{frp1}(x, z_{frp1}, t) + \ddot{u}_{frp1}(x, z_{frp1}, t)\delta u_{frp1}(x, z_{frp1}, t)\big)\, dV^{frp1} \\
& + \int_{V^{frp2}} \rho^{frp2} \big(\ddot{w}_{frp2}(x, z_{frp2}, t)\delta w_{frp2}(x, z_{frp2}, t) + \ddot{u}_{frp2}(x, z_{frp2}, t)\delta u_{frp2}(x, z_{frp2}, t)\big)\, dV^{frp2} \\
& + \int_{V_{a1}} \rho^{a1} \big(\ddot{w}_{a1}(x, z_{a1}, t)\delta w_{a1}(x, z_{a1}, t) + \ddot{u}_{a1}(x, z_{a1}, t)\delta u_{a1}(x, z_{a1}, t)\big)\, dV^{a1} \\
& + \int_{V^{a2}} \rho^{a2} \big(\ddot{w}_{a2}(x, z_{a2}, t)\delta w_{a2}(x, z_{a2}, t) + \ddot{u}_{a2}(x, z_{a2}, t)\delta u_{a2}(x, z_{a2}, t)\big)\, dV^{a2} \Bigg]
\end{aligned} \tag{2}$$

where $\rho^i$ $(i = m, frp1, frp2, a1, a2)$ is the mass density of the masonry $(i = m)$, the FRP $(i = frp1, frp2)$ and the adhesive $(i = a1, a2)$; $w_i(x, z_i, t)$ and $u_i(x, z_i, t)$ $(i = m, frp1, frp2, a1, a2)$ are the out-of-plane and the in-plane displacements, respectively; $V^i$ is the volume of each component; and $\ddot{}$ represents the second derivative with respect to time, $t$.

The virtual work of the stresses is

$$\begin{aligned}\delta' U = -\Bigg[ & \int_{V^m} \left(\sigma^m_{xx}(x,z_m,t)\delta\epsilon^m_{xx}(x,z_m,t) + \tau^m_{xz}(x,z_m,t)\delta\gamma^m_{xz}(x,z_m,t)\right) dV^m \\ & + \int_{V^{frp1}} \left(\sigma^{frp1}_{xx}(x,z_{frp1},t)\delta\epsilon^{frp1}_{xx}(x,z_{frp1},t) + \tau^{frp1}_{xz}(x,z_{frp1},t)\delta\gamma^{frp1}_{xz}(x,z_{frp1},t)\right) dV^{frp1} \\ & + \int_{V^{frp2}} \left(\sigma^{frp2}_{xx}(x,z_{frp2},t)\delta\epsilon^{frp2}_{xx}(x,z_{frp2},t) + \tau^{frp2}_{xz}(x,z_{frp2},t)\delta\gamma^{frp2}_{xz}(x,z_{frp2},t)\right) dV^{frp2} \\ & + \int_{V^{a1}} \left(\tau^{a1}_{xz}(x,z_{a1},t)\delta\gamma^{a1}_{xz}(x,z_{a1},t) + \sigma^{a1}_{zz}(x,z_{a1},t)\delta\epsilon^{a1}_{zz}(x,z_{a1},t)\right) dV^{a1} \\ & + \int_{V^{a2}} \left(\tau^{a2}_{xz}(x,z_{a2},t)\delta\gamma^{a2}_{xz}(x,z_{a2},t) + \sigma^{a2}_{zz}(x,z_{a2},t)\delta\epsilon^{a2}_{zz}(x,z_{a2},t)\right) dV^{a2}\Bigg] \end{aligned} \tag{3}$$

where $\sigma^i_{xx}(x,z_i,t)$ and $\epsilon^i_{xx}(x,z_i,t)$ are the in-plane normal stresses and strains in the masonry wall ($i=m$) and the FRP ($i=frp1,frp2$); $\tau^i_{xz}(x,z_i,t)$ and $\gamma^i_{xz}(x,z_i,t)$ ($i=m,frp1,frp2,a1,a2$) are the shear stresses and shear angles, respectively; and $\sigma^j_{zz}(x,z_j,t)$ and $\epsilon^j_{zz}(x,z_j,t)$ ($j=a1,a2$) are the out-of-plane normal stresses and strains in the adhesive, respectively. The virtual work of the external loads equals

$$\begin{aligned}\delta W = & \int_{x=0}^{x=H} \left(q_z(x,t)\delta w_m(x,t) + n_x(x,t)\delta u_{0m}(x,t)\right) dx \\ & + \sum_{k=1}^{NC} \int_{x=0}^{x=H} \left(P_k(t)\delta w_m(x_k,t) + N_k(t)\delta u_{0m}(x_k,t) + M_k(t)\delta\phi_m(x_k,t)\right)\delta_D(x-x_k)\,dx \end{aligned} \tag{4}$$

where $q_z(x,t)$ and $n_x(x,t)$ are distributed out-of-plane and in-plane loads, respectively, $P_k(t)$, $N_k(t)$, and $M_k(t)$ are concentrated loads and moments at $x=x_k$, $\delta_D$ is Dirac's function, and $NC$ is the number of concentrated loads/moments. (In the physical sense, the concentrated loads stem from knife-edge loads uniformly distributed through the width of the wall).

### 2.3. *Kinematic and constitutive relations.*

**2.3.1.** *The masonry wall.* The modeling of the masonry wall applies the same kinematic relations to the masonry units and the mortar joint. The distinction between the two is introduced through their constitutive relations. The kinematic assumptions for the masonry units and the mortar joints use first-order shear deformation theory with an intermediate class of deformations (large deflections, moderate rotations, small strain) as follows:

$$w_m(x,z_m,t) = w_m(x,t), \tag{5}$$

$$u_m(x,z_m,t) = u_{0m}(x,t) - z_m\phi_m(x,t), \tag{6}$$

$$\gamma^m_{xz}(x,z_m,t) = w_{m,x}(x,t) - \phi_m(x,t), \tag{7}$$

$$\epsilon^m_{xx}(x,z_m,t) = u_{0m,x}(x,t) + \tfrac{1}{2}\left(w_{m,x}(x,t)\right)^2 - z_m\phi_{m,x}(x,t), \tag{8}$$

where $u_{0m}(x,t)$ and $\phi_m(x,t)$ are the in-plane displacement at the reference line and the cross-sectional rotation of the masonry unit or the mortar joint, respectively, and subscript , $x$ represents differentiation

with respect to $x$. The reference line of the masonry wall is located at its middle and $z_m$ is measured from the reference line. The term $\frac{1}{2}(w_{m,x}(x,t))^2$ stems from the general expression for Green's strain tensor in the 1D case and the assumption that the strains are small (and therefore the term $\frac{1}{2}\big(u_{0m,x}(x,t)\big)^2$ is negligible) but the rotations are moderate and therefore considered (see [Fung 1965]). In physical terms, this term reflects the effect of the rotation on the projection of a length segment of the deformed reference axis (see for example, [Brush and Almroth 1975]).

The constitutive model for the masonry wall follows [Rabinovitch and Madah 2011] and introduces the nonlinearity and the inelasticity associated with the masonry construction through the definition of the stress resultants:

$$N^m_{xx} = \int_{A^m} \sigma^m_{xx}\big(\epsilon^m_{xx}(x,z_m,t)\big)\,dA^m = N^m_{xx}(\epsilon^{m0}_{xx}(x,t),\phi_{m,x}(x,t)), \tag{9}$$

$$M^m_{xx} = \int_{A^m} \sigma^m_{xx}(\epsilon^m_{xx}(x,z_m,t))z_m\,dA^m = M^m_{xx}(\epsilon^{m0}_{xx}(x,t),\phi_{m,x}(x,t)), \tag{10}$$

$$V^m_{xz} = \int_{A^m} \tau^m_{xz}(\gamma^m_{xz}(x,z_m,t))\,dA^m = V^m_{xz}(w_{m,x}(x,t),\phi_m(x,t)), \tag{11}$$

where $N^m_{xx}$, $M^m_{xx}$, $V^m_{xz}$ are the in-plane, bending, and shear resultants, $\sigma^m_{xx}(\epsilon^m_{xx})$ is the axial stress-strain relation, $\tau^m_{xz}(\gamma^m_{xz})$ is the shear stress-shear strain relation and

$$\epsilon^{m0}_{xx}(x,t) = u_{0m,x}(x,t) + \tfrac{1}{2}\big(w_{m,x}(x,t)\big)^2, \tag{12}$$

where $\epsilon^{m0}_{xx}(x,t)$ is the strain at the reference axis. The stress resultants defined by (9)–(11) also depend on the straining history but opposed to the state variables $u_{0m,x}(x,t)$, $w_m(x,t)$, $\phi_m(x,t)$ and thus $\epsilon^{0m}_{xx}(x,t)$, the strain history is a known function of the spatial coordinates and time.

The model assumes that the material nonlinearity is limited to the mortar joints. The masonry units are therefore assumed linear elastic so that (9)–(11) particularize as follows:

$$N^m_{xx}(x,t) = E^{mu}A^{mu}\epsilon^{m0}_{xx}(x,t), \tag{13}$$

$$M^m_{xx}(x,t) = -E^{mu}I^{mu}\phi_{m,x}(x,t), \tag{14}$$

$$V^m_{xz}(x,t) = \kappa^{mu}G^{mu}A^{mu}\big(w_{m,x}(x,t) - \phi_m(x,t)\big), \tag{15}$$

where $E^{mu}$ and $G^{mu}$ are the elastic and shear moduli of the masonry unit, $E^{mu}A^{mu}$, $E^{mu}I^{mu}$, and $G^{mu}A^{mu}$ are the in-plane, bending, and shear rigidities of the masonry unit cross section, and $\kappa^{mu}$ is the shear correction factor of the masonry cross section.

In general, the mortar material is brittle and tends to crack under tensile strains. The nonlinear and inelastic compressive behavior for the mortar material depends on the current straining state as well as the loading history, which is designated by the tensor $\boldsymbol{\epsilon}^h$. The response of the mortar material can be approximated by the following expression (also see [Rabinovitch and Madah 2011]):

$$\sigma^m_{xx}(\epsilon^m_{xx},\epsilon^h_{xx}) = \begin{cases} f(\epsilon^m_{xx}) & \text{if } \epsilon^m_{xx} \le \epsilon^h_{xx} \\ f^*(\epsilon^m_{xx},\epsilon^h_{xx}) & \text{if } \epsilon^h_{xx} < \epsilon^m_{xx} \le 0, \\ 0 & \text{if } 0 < \epsilon^m_{xx}, \end{cases} \tag{16}$$

where $f(\epsilon^m_{xx})$ describes the virgin loading path, $f^*(\epsilon^m_{xx}, \epsilon^h_{xx})$ describes the unloading and reloading paths, and $\epsilon^h_{xx}$ is the peak negative (compressive) strain at the material point:

$$\epsilon^h_{xx}(x, z, t) = \min_{t^*=0}^{t^*=t}(\epsilon_{xx}(x, z, t^*)) \tag{17}$$

In the present case, the shear stress shear angle relation is approximated by a model that does not take into account the hysteretic or dilatational effects and the coupling with the axial effect excluding the assumption that the cracked mortar material cannot transfer shear (yet, models that are more sophisticated also apply). Under these assumptions, the constitutive law for shear of the mortar material reads:

$$\tau^m_{xz}(\gamma^m_{xz}, \epsilon^m_{xx}) = \begin{cases} s(\gamma^m_{xz}) & \text{if } \epsilon^m_{xx} \le 0, \\ 0 & \text{if } 0 < \epsilon^m_{xx}, \end{cases} \tag{18}$$

where $s(\gamma^m_{xz})$ describes the shear behavior of the compressed mortar.

Introducing (16)–(18) into (9)–(11) defines the cross sectional constitutive relations for the mortar joint. Due to the nonlinearity of the mortar material, they take the form of nonlinear implicit functions of the unknowns and their derivatives.

**2.3.2.** *The FRP layers.* The FRP layers are also modeled as extensional/flexural members by using first-order shear deformation theory with an intermediate class of deformations. Although the thickness of the FRP layers is generally small (compared with the wall itself) and although their main structural action is in the axial direction, the localized response near irregular points such as edges or mortar joints is involved with localized bending of the layer. In addition, the evolution of compressive forces in the external layer (due to global bending of the strengthened wall or due to the arching effect) may yield localized buckling or wrinkling, which are also involved with flexure of the external layer. Therefore, the flexural action of the FRP layers is also taken into account. Shear deformation theory is adopted for three reasons. First, the shear stiffness of the FRP cross section is usually attributed to the resin matrix whereas the flexural and longitudinal stiffnesses are generally attributed to the fibers. Therefore, the FRP composite may involve shear deformations that are not negligible. Second, the localized region in which flexure and shearing of the FRP laminate take place is usually confined to the close vicinity of the irregular point. In this confined region, the length of the region over the thickness of the FRP strip ratio may be such that shear deformations have an effect. Finally, it is adopted for consistency with the formulation adopted for the masonry wall itself. Since the wall and the FRP layers interact through an adhesive layer, the consistency in the formulation is essential for the soundness of the FE formulation of the adhesive layer. It should also be noted that the modeling of the FRP layers and the modeling of the wall use similar kinematics, however, each layer is modeled independently. The different components are later coupled by means of the conditions of compatible deformations at the interfaces of the adhesive layers. Based on the above, the kinematic relations for the FRP layers read

$$w_{frpi}(x, z_{frpi}, t) = w_{frpi}(x, t), \tag{19}$$

$$u_{frpi}(x, z_{frpi}, t) = u_{0frpi}(x, t) - z_{frpi}\phi_{frpi}(x, t), \tag{20}$$

$$\gamma^{frpi}_{xz}(x, z_{frpi}, t) = w_{frpi,x}(x, t) - \phi_{frpi}(x, t), \tag{21}$$

$$\epsilon^{frpi}_{xx}(x, z_{frpi}, t) = u_{0frpi,x}(x, t) + \tfrac{1}{2}\big(w_{frpi,x}(x, t)\big)^2 - z_{frpi}\phi_{frpi,x}(x, t), \tag{22}$$

where $u_{0frp1}(x,t)$, $u_{0frp2}(x,t)$, $\phi_{frp1}(x,t)$ and $\phi_{frp2}(x,t)$ are the in-plane displacement at the reference line and the cross-sectional rotation of each FRP layer. The reference lines are independently located at the middle of each layer and $z_{frpi}$ are measured from the reference line.

Assuming a linear elastic behavior for the FRP layers, the stress resultants, defined analogously to (9)–(11), can be expressed as follows:

$$N_{xx}^{frpi}(x,t) = A_{11}^{frpi} \cdot \left(u_{0frpi,x}(x,t) + \tfrac{1}{2}\left(w_{frpi,x}(x,t)\right)^2\right) - B_{11}^{frpi} \cdot \phi_{frpi,x}(x,t), \tag{23}$$

$$M_{xx}^{frpi}(x,t) = B_{11}^{frpi} \cdot \left(u_{0frpi,x}(x,t) + \tfrac{1}{2}\left(w_{frpi,x}(x,t)\right)^2\right) - D_{11}^{frpi}(x,t)\phi_{frpi,x}(x,t), \tag{24}$$

$$V_{xz}^{frpi}(x,t) = \kappa^{frpi} A_{55}^{frpi} \cdot \left(w_{frpi,x}(x,t) - \phi_{frpi}(x,t)\right) \tag{25}$$

where $A_{11}^{frpi}$ $B_{11}^{frpi}$, $D_{11}^{frpi}$ and $A_{55}^{frpi}$ are the extensional, coupling, flexural, and shear rigidities of the inner FRP layer ($i = 1$) or the outer layer ($i = 2$) [Vinson and Sierakowski 1986] multiplied by its width, and $\kappa^{frpi}$ is the shear correction factor [Reddy 1999]. In the general case where the FRP layer is a composite laminate comprised of orthotropic layers, the rigidities are defined by

$$A_{11}^{frpi} = b \sum_{k=1}^{N_{\text{ply}}} \left(\bar{Q}_{11}^{frpi}\right)_k [h_k - h_{k-1}], \tag{26}$$

$$A_{55}^{frpi} = b \sum_{k=1}^{N_{\text{ply}}} \left(\bar{Q}_{55}^{frpi}\right)_k [h_k - h_{k-1}], \tag{27}$$

$$B_{11}^{frpi} = \frac{b}{2} \sum_{k=1}^{N_{\text{ply}}} \left(\bar{Q}_{11}^{frpi}\right)_k [h_k^2 - h_{k-1}^2], \tag{28}$$

$$D_{11}^{frpi} = \frac{b}{3} \sum_{k=1}^{N_{\text{ply}}} \left(\bar{Q}_{11}^{frpi}\right)_k [h_k^3 - h_{k-1}^3] \tag{29}$$

where $(\bar{Q}_{11}^{frpi})_k$ and $(\bar{Q}_{55}^{frpi})_k$ are the transformed longitudinal and shear stiffnesses of the $k$-th layer (lamina) within the laminate, $N_{\text{ply}}$ is the number of layers, and $h_k$ is the vector distance from the mid-plane of the FRP strip to the lower surface of the $k$-th layer [Vinson and Sierakowski 1986]. In the general case, $B_{11}^{frpi}$ represents the bending-stretching coupling effect that relates bending moments to mid-surface strains and axial forces to curvatures. When the FRP laminate is symmetric about the mid-surface, this term vanishes [Vinson and Sierakowski 1986].

Note that the above constitutive relations do not take viscoelastic damping into account. Alternatively, the model incorporates them in a global sense based on Rayleigh's model (see, for example, in [Clough and Penzien 1993]). Also, they assume that the rigidities of the FRP layers do not vary in time or along the wall. This assumption well complies with the nature of the type of FRP reinforcement commonly used for strengthening applications.

**2.3.3.** *The adhesive layers.* The kinematic strain-displacement relations and the constitutive laws for the adhesive layer are based on geometrically linear 2D elasticity and read as follows:

$$\epsilon_{zz}^{ai}(x, z_{ai}, t) = w_{ai,z}(x, z_{ai}, t), \tag{30}$$

$$\gamma_{xz}^{ai}(x, z_{ai}, t) = u_{ai,z}(x, z_{ai}, t) + w_{ai,x}(x, z_{ai}, t), \tag{31}$$

$$\sigma_{zz}^{ai}(x, z_{ai}, t) = E^{ai}\epsilon_{zz}^{ai}(x, z_{ai}, t), \tag{32}$$

$$\tau_{xz}^{ai}(x, z_{ai}, t) = G^{ai}\gamma_{xz}^{ai}(x, z_{ai}, t), \tag{33}$$

where $E^{ai}$ and $G^{ai}$ $(i = 1, 2)$ are the elastic and shear moduli of the adhesive, respectively.

In most classical theories for the dynamics of beams and plates, the static kinematic assumption (i.e., the functional form of the displacement field and the strain-displacement relations) are also applied to the dynamic case. Following this concept, the dynamic displacement field for the adhesive layer is based on the static one (also see [Schwarts-Givli et al. 2007]). The static displacement field of the adhesive layer is derived in [Hamed and Rabinovitch 2007a; 2007b; 2008] by following the concepts outlined in [Rabinovitch and Frostig 2000]. In this field, the out-of-plane displacement takes the form of a parabolic function of the out-of-plane coordinate and the axial displacement takes the form of a cubic function of the out-of-plane coordinate. Under the hypothesis that the longitudinal (axial) stiffness of the adhesive layer is negligible (with respect to the stiffness of the adjacent components) and by means of the kinematic and constitutive relations of (30)–(33), the parabolic and cubic displacement field derived in the references just cited strictly satisfies the static 2D elasticity governing equations of the adhesive medium. However, this solution is expressed in terms of the displacements of the adherents and the shear stress in the adhesive layer. As such, it cannot be implemented in a classical, displacement based, finite element formulation. Alternatively, the functional form of the displacement field derived in the same references; i.e.,the parabolic and cubic out-of-plane and longitudinal displacements, respectively, is adopted here for a displacement based formulation (also see [Buller 2005; Elmalich and Rabinovitch 2009; 2010]). This aims to take advantage of the close form solution of the 2D elasticity equations but yet to handle it through a displacement based form. Following the above approach, the out-of-plane and the in-plane displacements are assumed to take a parabolic and cubic polynomial forms that generally read

$$w_{ai}(x, z_{ai}) = w_{0i}(x) + w_{1i}(x) \cdot \left(\frac{z_{ai}}{c^{ai}}\right) + w_{2i}(x) \cdot \left(\frac{z_{ai}}{c^{ai}}\right)^2, \tag{34}$$

$$u_{ai}(x, z_{ai}) = u_{0i}(x) + u_{1i}(x) \cdot \left(\frac{z_{ai}}{c^{ai}}\right) + u_{2i}(x) \cdot \left(\frac{z_{ai}}{c^{ai}}\right)^2 + u_{3i}(x) \cdot \left(\frac{z_{ai}}{c^{ai}}\right)^3, \tag{35}$$

where $i = 1$ for the inner adhesive layer and $i = 2$ for the outer one; $w_{ji}(x)$ $(j = 0, 1, 2;\ i = 1, 2)$ and $u_{ki}(x)$ $(k = 0, 1, 2, 3;\ i = 1, 2)$ are unknown functions of $x$ only, $z_{ai}$ $(i = 1, 2)$ are the out-of-plane coordinates of the adhesive layer that are measured from the middle of each layer outwards, and $c^{a1}$ and $c^{a2}$ are the thicknesses of the inner and outer adhesive layers, respectively.

The deformation fields of the adhesive layer must satisfy the conditions of compatibility of deformations with the adjacent layers. These conditions read

$$w_{a1}\left(x, z_{a1} = \tfrac{1}{2}c^{a1}\right) = w_m(x), \qquad u_{a1}\left(x, z_{a1} = \tfrac{1}{2}c^{a1}\right) = u_{0m}(x) + \tfrac{1}{2}d^m\phi_m(x), \tag{36}$$

$$w_{a1}\left(x, z_{a1} = -\tfrac{1}{2}c^{a1}\right) = w_{frp1}(x), \qquad u_{a1}\left(x, z_{a1} = -\tfrac{1}{2}c^{a1}\right) = u_{0frp1}(x) - \tfrac{1}{2}d^{frp1})\phi_{frp1}(x), \tag{37}$$

$$w_{a2}\left(x, z_{a2} = \tfrac{1}{2}c^{a2}\right) = w_{frp2}(x), \qquad u_{a2}\left(x, z_{a2} = \tfrac{1}{2}c^{a2}\right) = u_{0frp2}(x) + \tfrac{1}{2}d^{frp2}\phi_{frp2}(x), \tag{38}$$

$$w_{a2}\left(x, z_{a2} = -\tfrac{1}{2}c^{a2}\right) = w_m(x), \qquad u_{a2}\left(x, z_{a2} = -\tfrac{1}{2}c^{a2}\right) = u_{0m}(x) - \tfrac{1}{2}d^m\phi_m(x), \tag{39}$$

where $d^m$, $d^{frp1}$, and $d^{frp2}$ are the thicknesses of the masonry wall and the FRP layers, respectively.

Introducing the displacement fields from (34)–(35) into the compatibility conditions (36)–(39) and solving for $w_{11}(x)$, $w_{21}(x)$, $u_{21}(x)$, $u_{31}(x)$, $w_{12}(x)$, $w_{22}(x)$, $u_{22}(x)$, and $u_{32}(x)$ defines 8 out of the 14 unknown functions in terms of the other unknowns. Four of the remaining six unknown functions $[u_{01}(x), u_{11}(x), u_{02}(x), u_{12}(x)]$ are determined by introducing the displacement field back into the static form of the variational principle, i.e., the last two terms in (1), applying the basic lemma of the calculus of variations [Dym and Shames 1973], and solving the algebraic equations that correspond to $\delta u_{01}(x)$, $\delta u_{11}(x)$, $\delta u_{02}(x)$, and $\delta u_{12}(x)$. The last two functions $w_{01}(x)$, $w_{02}(x)$ remain unknown. Thus, the static displacement fields in the adhesive layers take the following form:

$$w_{a1}(x, z_{a1}) = w_{01}(x) + \big(w_m(x) - w_{frp1}(x)\big)\frac{z_{a1}}{c^{a1}} + \big(2w_m(x) - 4w_{01}(x) + 2w_{frp1}(x)\big)\Big(\frac{z_{a1}}{c^{a1}}\Big)^2, \tag{40}$$

$$\begin{aligned} u_{a1}(x, z_{a1}) &= \big(2w_{01,x}(x) - w_{frp1,x}(x) - w_{m,x}(x)\big)\frac{2}{3}\frac{z_{a1}^3}{(c^{a1})^2} + \big(w_{frp1,x}(x) - w_{m,x}(x)\big)\frac{1}{2}\frac{z_{a1}^2}{c^{a1}} \\ &\quad + \big(c^{a1}(w_{m,x}(x) + w_{frp1,x}(x) - 2w_{01,x}(x)) + 6u_{0m}(x) - 6u_{0frp1}(x) + 3d^{frp1}\phi_{frp1}(x) + 3d^m\phi_m(x)\big)\frac{z_{a1}}{6c^{a1}} \\ &\quad + \tfrac{1}{8}(c^{a1}(w_{m,x} - w_{frp1,x}) + 4(u_{0m}(x) + u_{0frp1}(x)) + 2(d^m\phi_m(x) - d^{frp1}\phi_{frp1}(x))) \end{aligned} \tag{41}$$

$$w_{a2}(x, z_{a2}) = w_{01}(x) + \big(w_{frp2}(x) - w_m(x)\big)\frac{z_{a2}}{c^{a2}} + \big(2w_{frp2}(x) - 4w_{01}(x) + 2w_m(x)\big)\Big(\frac{z_{a2}}{c^{a2}}\Big)^2 \tag{42}$$

$$\begin{aligned} u_{a2}(x, z_{a2}) &= \big(2w_{01,x}(x) - w_{0,x}(x) - w_{frp2,x}(x)\big)\frac{2}{3}\frac{z_{a2}^3}{(c^{a2})^2} + \big(w_{m,x}(x) - w_{frp2,x}(x)\big)\frac{1}{2}\frac{z_{a2}^2}{c^{a2}} \\ &\quad + \big(c^{a2}(w_{frp2,x}(x) + w_{m,x}(x) - 2w_{01,x}(x)) + 6u_{0frp2}(x) - 6u_{0m}(x) + 3d^m\phi_m(x) + 3d^{frp2}\phi_{frp2}(x)\big)\frac{z_{a2}}{6c^{a2}} \\ &\quad + \tfrac{1}{8}(c^{a2}(w_{frp2,x}(x) - w_{m,x}(x)) + 4(u_{0frp2}(x) + u_{0m}(x)) + 2(d^{frp2}\phi_{frp2}(x) - d^m\phi_m(x))) \end{aligned} \tag{43}$$

Analogously to the common case where the static displacement field is used for the dynamic analysis, (40)–(43) are applied to the dynamic case, yielding

$$\begin{aligned} &w_{a1}(x, z_{a1}, t) \\ &\quad = w_{01}(x, t) + \big(w_m(x, t) - w_{frp1}(x, t)\big)\frac{z_{a1}}{c^{a1}} + \big(2w_m(x, t) - 4w_{01}(x, t) + 2w_{frp1}(x, t)\big)\Big(\frac{z_{a1}}{c^{a1}}\Big)^2, \end{aligned} \tag{44}$$

$$\begin{aligned} &u_{a1}(x, z_{a1}, t) \\ &\quad = \big(2w_{01,x}(x, t) - w_{frp1,x}(x, t) - w_{m,x}(x, t)\big)\frac{2}{3}\frac{z_{a1}^3}{(c^{a1})^2} + \big(w_{frp1,x}(x, t) - w_{m,x}(x, t)\big)\frac{1}{2}\frac{z_{a1}^2}{c^{a1}} \\ &\qquad + \big(c^{a1}(w_{m,x}(x, t) + w_{frp1,x}(x, t) - 2w_{01,x}(x, t)) \\ &\qquad\quad + 6u_{0m}(x, t) - 6u_{0frp1}(x, t) + 3d^{frp1}\phi_{frp1}(x, t) + 3d^m\phi_m(x, t)\big)\frac{z_{a1}}{6c^{a1}} \\ &\qquad + \tfrac{1}{8}\big(c^{a1}(w_{m,x}(x, t) - w_{frp1,x}(x, t)) + 4(u_{0m}(x, t) + u_{0frp1}(x, t)) + 2(d^m\phi_m(x, t) - d^{frp1}\phi_{frp1}(x, t))\big), \end{aligned} \tag{45}$$

$$\begin{aligned} &w_{a2}(x, z_{a2}, t) \\ &\quad = w_{01}(x, t) + \big(w_{frp2}(x, t) - w_m(x, t)\big)\frac{z_{a2}}{c^{a2}} + \big(2w_{frp2}(x, t) - 4w_{01}(x, t) + 2w_m(x, t)\big)\Big(\frac{z_{a2}}{c^{a2}}\Big)^2 \end{aligned} \tag{46}$$

$$u_{a2}(x, z_{a2}) = \big(2w_{01,x}(x) - w_{01,x}(x) - w_{frp2,x}(x)\big)\frac{2}{3}\frac{z_{a2}^3}{(c^{a2})^2} + \big(w_{m,x}(x) - w_{frp2,x}(x)\big)\frac{1}{2}\frac{z_{a2}^2}{c^{a2}} \tag{47}$$
$$+\big(c^{a2}(w_{frp2,x}(x) + w_{m,x}(x) - 2w_{01,x}(x)) + 6u_{0frp2}(x) - 6u_{0m}(x) + 3d^m\phi_m(x) + 3d^{frp2}\phi_{frp2}(x)\big)\frac{z_{a2}}{6c^{a2}}$$
$$+\tfrac{1}{8}\big(c^{a2}(w_{frp2,x}(x) - w_{m,x}(x)) + 4(u_{0frp2}(x) + u_{0m}(x)) + 2(d^{frp2}\phi_{frp2}(x) - d^m\phi_m(x))\big).$$

The formulation presented in [Hamed and Rabinovitch 2008] uses the displacements and shear stress as unknowns. This leads to the introduction of additional assumptions and neglects of the high order terms in the distributions of velocities and accelerations. Opposed to that, the formulation presented here is based on displacement unknowns only and, therefore, the velocity and acceleration fields are directly determined by the temporal derivatives of (44)–(47). In addition, the use of a displacement formulation allows for a direct implementation in the finite element formulation, which is discussed next.

**2.4.** ***Finite element approximation.*** The FE approximation of the displacements reads:

$$v_i \approx v_i^h = \sum_{A \in S_{vi}} N_A(x) d_A(t), \tag{48}$$

$$\delta v_i \approx \delta v_i^h = \sum_{A \in S_{vi}} N_A(x) \delta d_A(t), \tag{49}$$

where $d_A(t)$ are generalized unknown displacements, $\delta d_A(t)$ are virtual displacements; $N_A(x)$ are shape function, $v_i$ is the i-th entry of the unknown displacements vector

$$\boldsymbol{v} = [u_{0frp1}, u_{0m}, u_{0frp2}, w_{frp1}, w_m, w_{frp2}, \phi_{frp1}, \phi_m, \phi_{frp2}, w_{01}, w_{02}]^T,$$

and $s_{v_i}$ is the group of shape functions that correspond to the unknown function $v_i$. Introducing the FE approximation — see (48) and (49) — into the principle of virtual work, Equation (1), and applying the basic lemma of the calculus of variations [Dym and Shames 1973] yields the standard form of equations of motion:

$$\boldsymbol{M}\ddot{\boldsymbol{d}}(t) + \boldsymbol{g}(\boldsymbol{d}(t)) - \boldsymbol{P}(t) = \boldsymbol{0}, \tag{50}$$

where $\boldsymbol{d}(t) = [d_A(t)]$ is the vector of unknown displacements, $\boldsymbol{M} = [M_{AB}]$ is the mass matrix, $\boldsymbol{g}(\boldsymbol{d}(t)) = [g_A(\boldsymbol{d}(t))]$ is a set of nonlinear functions of the unknown functions $\boldsymbol{d}(t)$, and $\boldsymbol{P}(t)$ is a vector of external loads. If $d_A(t)$ is prescribed, the $A$-th equation in (50) is replaced with

$$d_A(t) - \bar{d}_A(t) = 0, \tag{51}$$

where $\bar{d}_A$ is the prescribed displacement.

The FE form of the initial conditions read

$$\left.\begin{aligned} d_A(0) &= \bar{d}_A(0) \\ \dot{d}_A(0) &= \bar{\dot{d}}_A(0) \end{aligned}\right\} \quad \text{for all } A, \tag{52, 53}$$

where $\bar{d}_A(0)$ and $\bar{\dot{d}}_A(0)$ are prescribed displacements and velocities at $t = 0$.

The present formulation uses the simplest linear ("tent") shape functions for all 11 unknowns:

$$\left.\begin{aligned} N_i &= 1-(x-x_e)/l_e \\ N_j &= (x-x_e)/l_e \end{aligned}\right\} \quad \text{for } x \in [x_e, x_e+l_e], \tag{54}$$

(55)

where $x_e$ is the upper coordinate of the element, $l_e$ is the length of the element; $N_i$ corresponds to the upper ($i$-th) node,and $N_j$ corresponds to the lower ($j$-th) node. The element includes 11 degrees of freedom at each node. The elemental DOFs are illustrated in Figure 1d.

The global mass matrix, the tangent matrix, the nonlinear vector, and the load vector are evaluated at the element level and then assembled into the global scale:

$$\boldsymbol{M} = \boldsymbol{A}_e(\boldsymbol{M}_e), \tag{56}$$

$$\boldsymbol{K} = \frac{\partial \boldsymbol{g}(\boldsymbol{d}(t))}{\partial \boldsymbol{d}(t)} = \boldsymbol{A}_e\Big(\frac{\partial \boldsymbol{g}_e(\boldsymbol{d}_e(t))}{\partial \boldsymbol{d}_e(t)}\Big), \tag{57}$$

$$\boldsymbol{g}(\boldsymbol{d}(t)) = A_e\big(\boldsymbol{g}_e(\boldsymbol{d}_e(t))\big), \tag{58}$$

$$\boldsymbol{P}(t) = A_e\big(\boldsymbol{P}_e(t)\big) + \boldsymbol{P}_{\text{node}}(t), \tag{59}$$

where the subscript $e$ designates the element level, $\boldsymbol{A}_e$ is the assembly operator for matrices, $A_e$ is the assembly operator for vectors, and $\boldsymbol{P}_{\text{node}}(t)$ is a vector of concentrated loads at the joints.

The effect of damping is introduced using the simplest Rayleigh model. By means of this approximation, the equation of motion (46) changes to

$$\boldsymbol{M}\cdot\ddot{\boldsymbol{d}}(t) + \boldsymbol{C}\cdot\dot{\boldsymbol{d}}(t) + \boldsymbol{g}(\boldsymbol{d}(t)) - \boldsymbol{P}(t) = \boldsymbol{0}, \tag{60}$$

where $\boldsymbol{C}$ is the proportional damping matrix given by:

$$\boldsymbol{C} = \alpha_0\boldsymbol{M} + \alpha_1 \frac{\partial \boldsymbol{g}}{\partial \boldsymbol{d}}\Big|_{d(t)=\boldsymbol{0}^-}. \tag{61}$$

The proportionality factors $\alpha_0$ and $\alpha_1$ of Rayleigh's damping model are assessed by prescribing the damping ratio at two selected modes [Clough and Penzien 1993].

The formulation above yields two types of elements. The first one uses the constitutive relations in the form of (13)–(15) and corresponds to the masonry units. The second element uses the constitutive relations of (9)–(11) and corresponds to the mortar joints. Both types of elements are assembled into the global model.

The nonlinear initial value problem given by (60) and (51) with the initial conditions in (52) and (53) is transformed into a set of successive nonlinear algebraic problems using Newmark's method [1959]. These equations are solved at every time step for $\boldsymbol{d}(t_i)$ using the Newton method. Unlike the formulation presented in [Hamed and Rabinovitch 2008], which used direct iterations with updated secant moduli, the present iterative scheme takes advantage of the quadratic convergence of the Newton method. This advantage simplifies the analysis and improves its convergence characteristics. Furthermore, it simplifies its implementation in a more general finite element based computational environment.

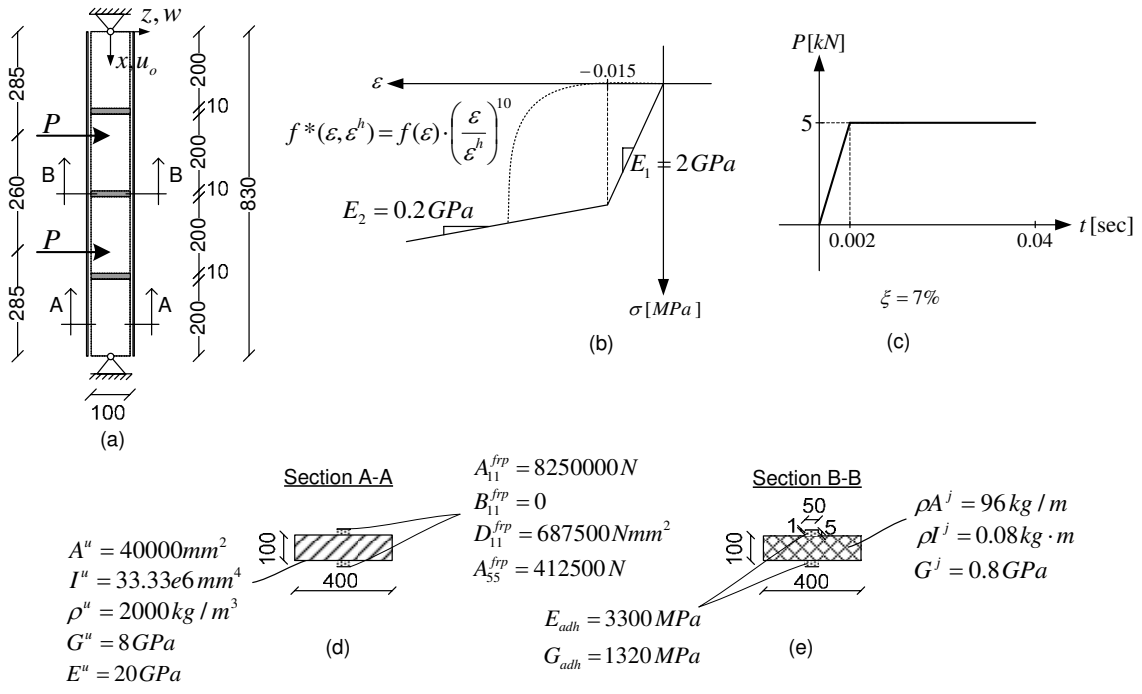


**Figure 2.** Geometry, loading, and mechanical properties for the convergence study (a) geometry and loading (dimensions are in mm); (b) stress-strain curve for the mortar material (c) dynamic loading scheme (d) cross section and elastic properties of the masonry units and the FRP strips; (e) cross section and elastic properties of the mortar joints and the adhesive layers.

## 3. Numerical convergence study

In this section, the behavior of a small-scale strengthened wall specimen is examined numerically. The study includes two cases. First, the effect of refinement of the mesh on the numerical analysis of the response to a static load is examined. Then, the effect of the mesh characteristics and the size of the time step on the dynamic response to a step load is examined.

The geometry, loading, supporting, and material properties of the specimen appear in Figure 2. The width of the examined strip equals 400 mm and it is strengthened using two 50 mm wide CFRP strips, one strip on each face. In order to allow several steps of mesh refinement, the study focuses on a relatively small specimen that is comprised of four masonry units and three joints. As in many practical cases, it is assumed that the construction technique does not provide the upper and the lower units with a sufficient rotational constraint yielding simply supported conditions. In the first case, the wall is subjected to two static concentrated loads. The magnitude of each load equals 5 kN. In the second case, the wall is subjected to the same loading scheme but the out-of-plane load is applied dynamically as shown in Figure 2c. In practice, masonry walls are usually subjected to compressive loads, either due to their self weight or due to load transferred by adjacent structural elements such slabs or beams. In order to

take at least some aspects of this effect into account, the examined wall specimens are also subjected to axial precompression load. In both analyses, this load equals 6 kN and it is applied by prescribing the displacement at the top support. It should be noted that the magnitude of the precompression load is relatively high (compared with the dynamic out-of-plane load) yet, the precompressive stains it yields in the mortar joints are relatively small and well within the initial stiffer range of the loading stress-strain curve.

**3.1.** ***Response to a static load.*** Four finite element meshes are examined. The meshes are titled M1–M4 and their properties appear in Table 1. In meshes M1–M3, the nodes are equally spaced along the specimen. Mesh M4 uses smaller elements for the joint region. The element size ranges form about the thickness of the externally bonded layers to about one tenth of this measure (see Table 1). Since the problem at hand does not have an analytical closed form solution, the convergence of the numerical analysis and the measure of accuracy are defined with respect to the most refined mesh (M4). The run time of the analysis is selected as a measure of the computational efficiency. These measures, normalized with respect to the run time with mesh M1 appear in Table 1 and quantify the increase in computational effort associated with the refinement of the mesh. It appears that mesh M4, which is not involved with a significant increase in number of DOFs, is involved with a significant increase in run. This is attributed to the increased number of nonlinear joint elements.

The out-of-plane deflections and the in plane deflections in the masonry specimen and the FRP strips appear in Figure 3. In that figure, as in the ones that follow, the circular markers designate the nodes of the finite element mesh. The nodes are connected by straight lines. The global scale distribution of the out-of-plane deflections (Figure 3, top) clearly reveals the sharp rotation at the joint. Zoom plots on the compressed FRP strip, the masonry wall, and the tensioned FRP strip appear in the second row of graphs in Figure 3, and reveal the effect of the rotation of the joint on the localized deformations. It is also observed that the peak out-of-plane deformations of the FRP strips are slightly smaller than that of the masonry wall. This effect, which is attributed to the out-of-plane deformability of the adhesive layer, is more pronounced in the tensioned layer where the strip is compressed against the adhesive layer and the masonry wall.

The comparison between the different meshes reveals only minor differences that consistently vanish with refinement. It seems that the results obtained with mesh M1 are slightly too coarse, but the ones obtained with mesh M2 and M3 are satisfactorily close to the results obtained with mesh M4. This implies that in the present case, the extensive computation effort required for mesh M4 is not required.

| Mesh | No. of elements through joint | No. of elements through the unit | Total no. of DOFs | Size of smallest element [mm] | Run time (normalized w.r.t. M1) | Line style in Figures 3–7 |
|---|---|---|---|---|---|---|
| M1 | 2 | 40 | 1837 | 5.000 | 1 | – · – · – |
| M2 | 4 | 80 | 3663 | 2.500 | 2.12 | – – – |
| M3 | 8 | 160 | 7315 | 1.250 | 5.12 | · · · · · · |
| M4 | 24 | 160 | 7843 | 0.416 | 7.07 | —— |

**Table 1.** Mesh properties for static analyses.

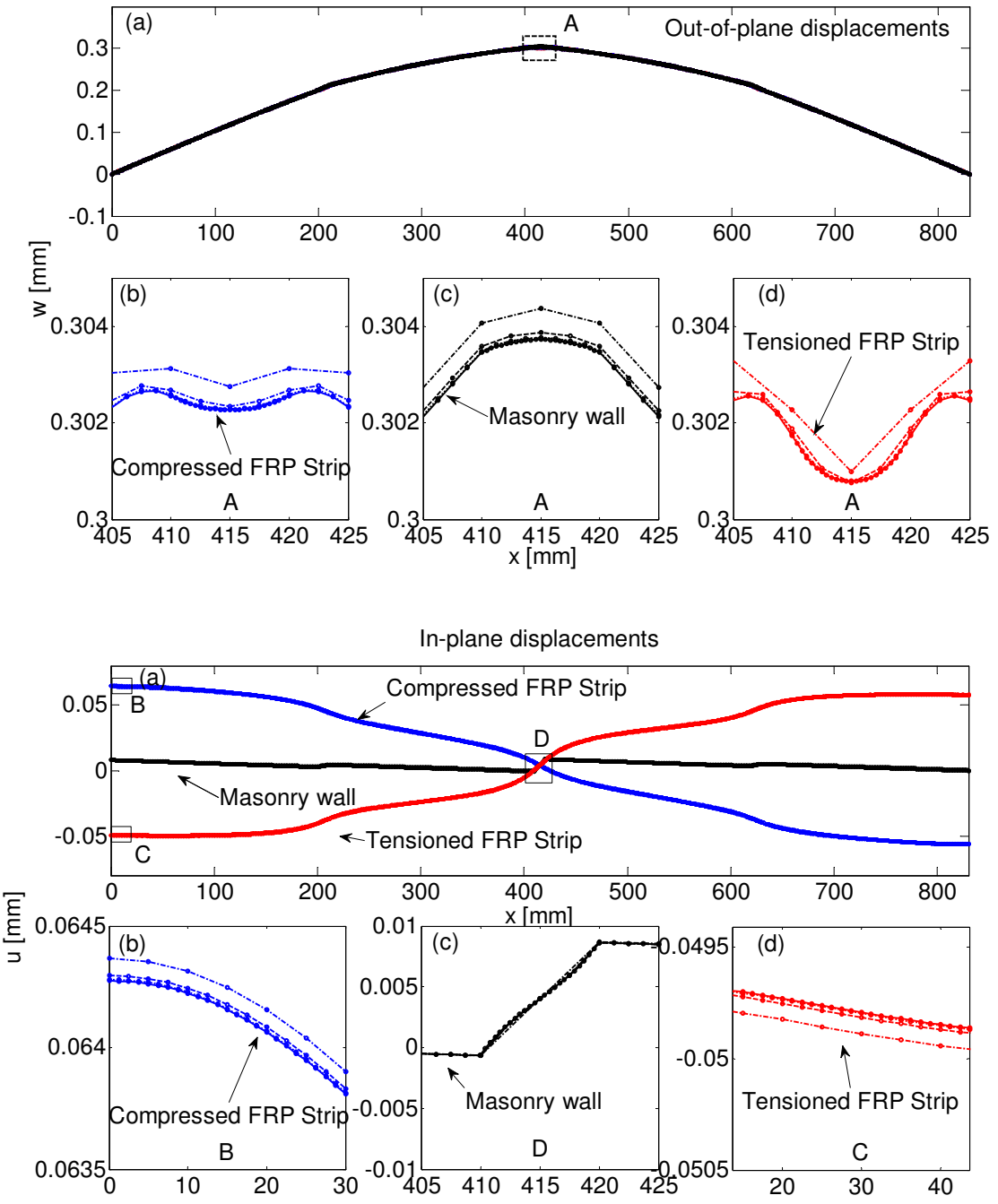


**Figure 3.** Distributions of out-of-plane (top half) and in-plane (bottom half) deflections along the wall, for different meshes. In each case, part (a) shows the global distributions, and parts (b)–(d) zoom in on a specific zone of (a), showing the deflections of the compressed FRP strip (b), the wall (c), and the tensioned FRP strip (d). Legend: — · — · — Mesh M1; — — — Mesh M2; · · · · · · Mesh M3; —— Mesh M4, ∘ FE nodes.

The axial deformations are studied in the bottom half of Figure 3. Also here, the global scale results as well as the zoom plots reveal the effect of the cracking at the joint and the asymmetry due to the precompression. In terms of convergence, the differences between the various meshes are even smaller than the ones observed in the top half of the figure. Even near the joint — part (c) in bottom row — or near the edges of the strips — parts (b) and (d) on bottom row — the division of the joint to 2 elements (M1) yields a reasonable assessment and the differences between the meshes M2, M3, and M4 are negligible.

The bending moment, axial forces, and shear forces in the FRP strips and in the masonry wall are studied in Figure 4, respectively. The distributions of the bending moments (top half of figure) and the axial forces (bottom half) reveal the transition of the global bending moment resistance mechanism near the joint. Due to cracking of the joint, the flexural stiffness of the wall drops down and a larger portion of the global bending moment is carried in the form a force couple with tension in the outer FRP strip and compression in the wall. As a result, the axial force in the tensioned strip is amplified and the bending moment in the masonry wall is reduced. Note that the axial forces (bottom half of Figure 4) sum up to a level of compression higher than the applied precompression. This is attributed to the arching effect. The cracking of the joints shifts the axis of rotation of the cracked joint form the level of the mid-surface to the level of the crack tip. On the other hand, the axis of rotation at the supports (in the case studied here) remains at the mid-surface level. As a result, the out-of-plane displacement of the wall and the rotation of the relatively stiff masonry blocks push the outer blocks against the supports. Since both supports are longitudinally fixed, this process results in a build-up of a compressive force and an "arch" type of action. In the present case, this effect is much more significant than the influence of the precompression.

The comparison between the different analyses reveals minor differences between meshes M2-M4. The coarse mesh (M1) does not provide sufficiently smooth and accurate results, but the more refined meshes do. Even mesh M2, in which the joint is divided to four elements, provides a reasonable assessment of the distributions of the axial forces and the bending moments. The zoom plots on the middle joint, displayed in parts (b)–(d) of Figure 4, top and bottom, show that the results with the intermediate meshes M2 and M3 almost coincide with the analysis with mesh M4. Figure 5, on the other hand, indicates that the distributions of the shear forces are more sensitive to the size of the element. The zoom plot on the upper joint reveals differences that are not very prominent. On the other hand, the distributions of the shear forces in the FRP strips near the edges are slightly different. In this region, the analysis with mesh M1 yields a "zig-zag" pattern around the results obtained with the refined meshes. This "zig-zag" effect becomes less significant with mesh M2 and it vanishes with mesh M3.

Figure 5 also reveals that the distributions of the shear forces exhibit rapid and significant variations near the cracked joints. This is an outcome of the development of shear stress concentrations in the adhesive layers, which can be observed in Figure 6. The total (or "global") shear force, which is the sum of the shear forces in all structural components, takes into account the sum of the shear forces carried by the wall and the FRP strips as well as the shear forces that develop in the adhesive layers. In the present formulation, which is derived in the framework of the variational calculus, all shear forces are defined as the variational counterparts of the corresponding out-of-plane displacements. Near the joints, the shear forces that develop in the adhesive layer are significantly amplified (as a result of the change in the bending resistance mechanism form the block region to the joint region). Consequently, the shear resultants in the adhesive layer (defined as the variational counterparts of $w_{01}$ and $w_{02}$) become nonnegligible. This component provides the "missing" contribution to the global shear equilibrium.

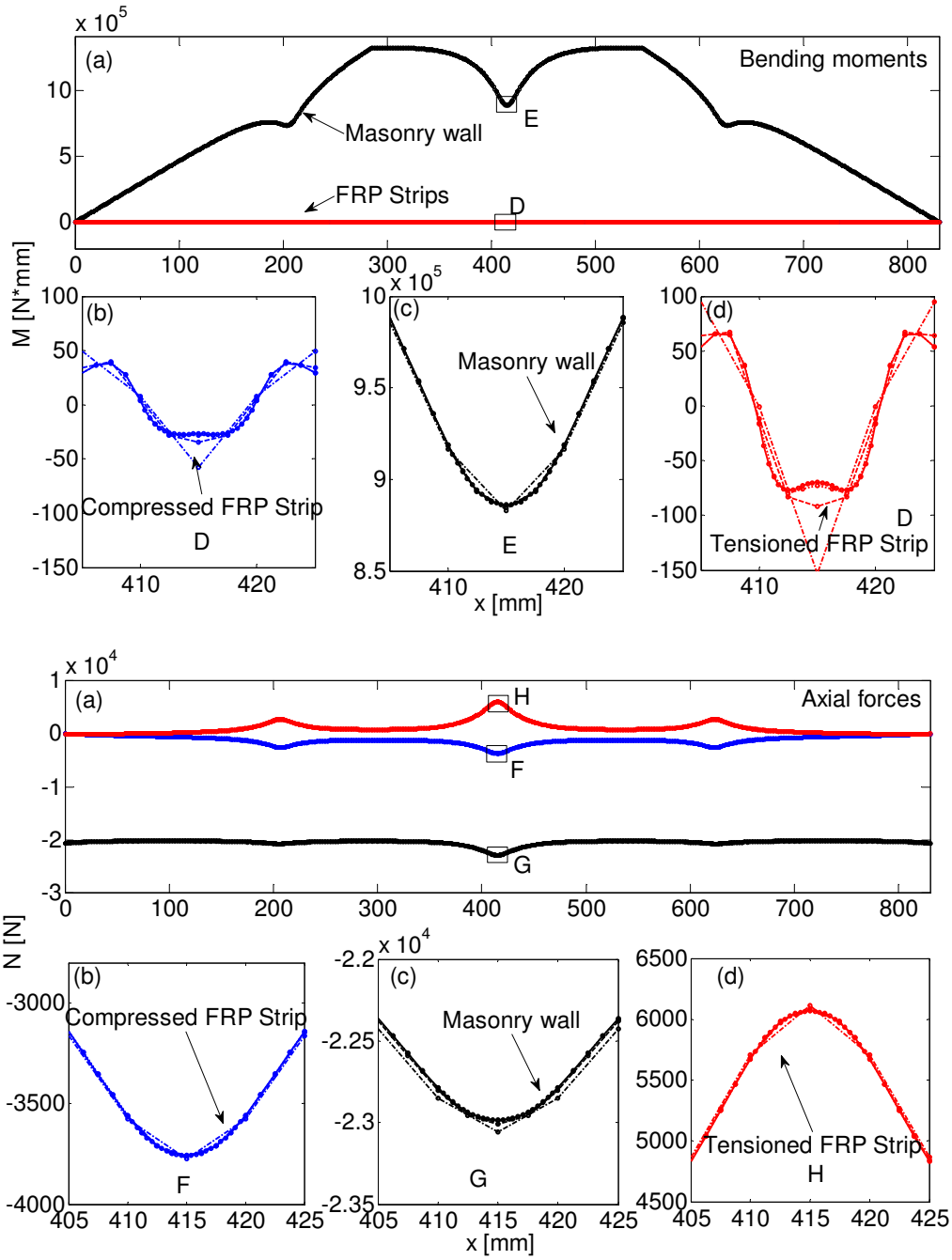


**Figure 4.** Distributions of bending moments (top) and axial forces (bottom) along the wall. In each case, part (a) shows the global distributions, and parts (b)–(d) zoom in on a specific zone of (a), showing the bending moments or axial forces in the compressed FRP strip (b), the wall (c), and the tensioned FRP strip (d). Legend: – · – · – Mesh M1; – – – Mesh M2; · · · · · · Mesh M3; —— Mesh M4, ∘ FE nodes.

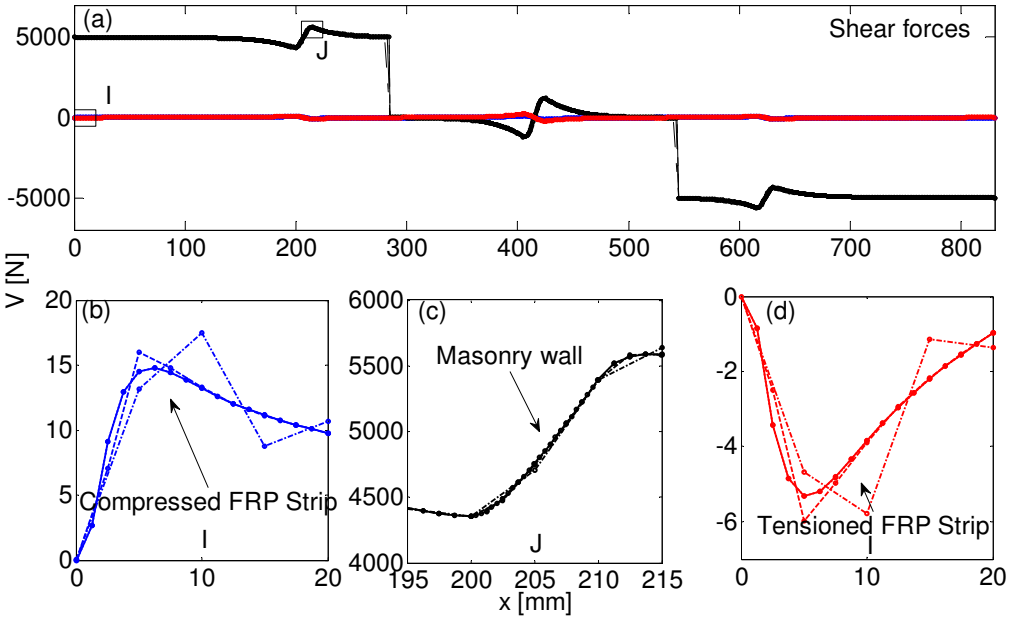


**Figure 5.** Distributions of shear forces along the wall: (a) global distributions; (b) shear forces in the compressed FRP strip at zone "I"; (c) shear forces in the wall at zone "J"; (d) shear forces in the tensioned FRP strip at zone "I". Legend: $-\cdot-\cdot-$ Mesh M1; $---$ Mesh M2; $\cdots\cdots$ Mesh M3; —— Mesh M4, $\circ$ FE nodes.

Thus, the sum of the shear forces in the two FRP layer, the two adhesive layers, and the wall itself strictly corresponds to the value deduced by global equilibrium. Nevertheless, the localized evolution of shear concentrations in the adhesive interfaces near the joint is a critical aspect of the response of the strengthened wall specimen. This aspect, as well as the evolution of out-of-plane normal stresses and their anticipated impact in terms of the numerical sensitivity of the FE model, are studied next.

The distributions of the shear stresses that appear in Figure 6 reveal the significant stress concentrations near the joints. The global scale distributions indicate that the stresses observed in the adhesive layer that bonds the tensioned FRP strip are higher than those observed in the adhesive layer that bonds the compressed strip. This pattern is in agreement with the distribution of the axial forces that develop in the FRP strips (Figure 4, bottom). The zoom plots on the stresses near the edge (Figures 6b and 6c) and near the middle joint (Figures 6d and 6e) reveal that also here the analysis with the coarse mesh (M1) yields a "zig-zag" pattern. The refined meshes M2 and M3 reveal a more smooth behavior and converge towards the finer mesh M4.

Figures 6b and 6c also show that with all meshes, the zero shear boundary condition at $x = 0$ is satisfied. In that sense, the present FE model overcomes one of the drawbacks observed in standard (2D elasticity based) FE analysis of FRP strengthened elements. The distributions of the out-of-plane normal stresses at the interfaces of the adhesive layers are studied in Figure 7. The global scale results shown in the graphs (a), top and bottom, quantify the stress concentrations that develop near the cracked joints and near the edges of the FRP strip. They also reveal that the FE model captures the variation of the

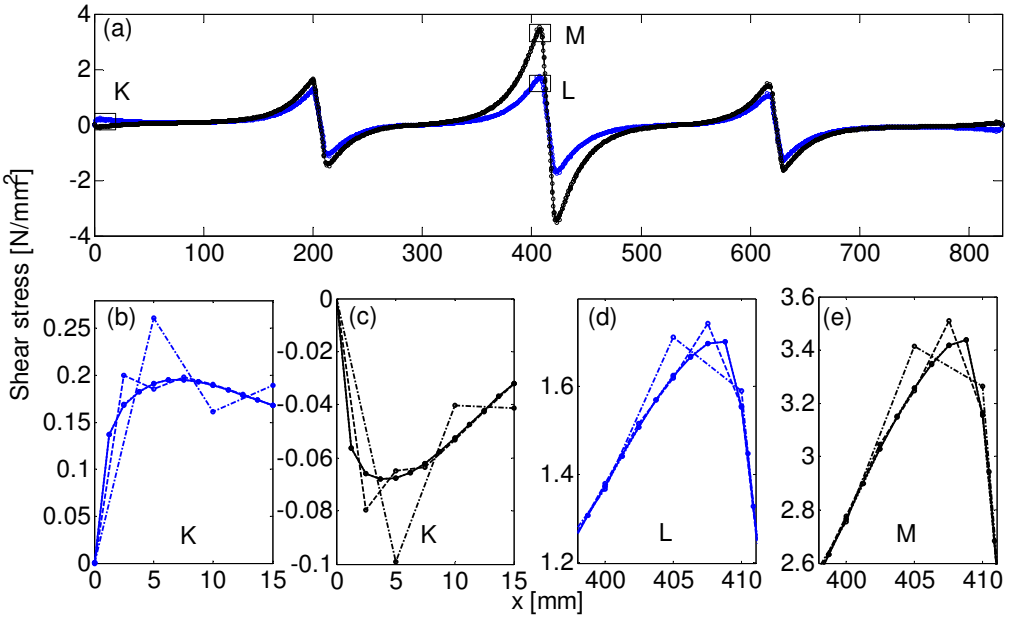


**Figure 6.** Distributions of shear stresses in the adhesive layers: (a) global distributions; (b) near the edge of the compressed FRP strip (zone "K"); (c) near the edge of the tensioned FRP strip (zone "K"); (d) near the middle of the compressed FRP strip (zone "L"); (e) near the middle of the tensioned FRP strip (zone "M"). Legend: $-\cdot-\cdot-$ Mesh M1; $---$ Mesh M2; $\cdots\cdots$ Mesh M3; —— Mesh M4, $\circ$ FE nodes.

stresses though the depth of the adhesive layer. The comparison between the graphs (a) in the top and bottom parts of Figure 7 implies that in this case, the stress concentrations near the tensioned strip (top) are significantly higher than the ones near the compressed strip (bottom).

The zoom plots that appear in Figure 7 reveal that the analysis with the coarse mesh M1 is strongly affected by the "zig-zag" behavior. This analysis does not provide a satisfactory description of the response. Near the middle joint, for example, the analysis with mesh M1 overestimates the compressive stresses at the adhesive-FRP interface and does not capture the transition from tension to compression at the adhesive-masonry interface; see graphs (d) and (e), respectively, in the top part of Figure 7. The analyses with the refined meshes yield a better description of the interfacial stresses. The differences between meshes M3 and M4 are rather negligible and even mesh M2 provides a reasonable description of the interfacial stresses.

The above results demonstrate that the FE model can effectively handle the localized effects, in spite of the order of magnitude deviation of characteristic length scales. It is also observed that the peak values observed at the edges of the adhesive layer are not sensitive to the mesh characteristics and the values obtained by the four analyses are very close. This demonstrates that the present formulation is not subjected to divergence near the irregular point. In that sense, it overcomes another drawback of the standard FE analysis of FRP strengthened flexural members.

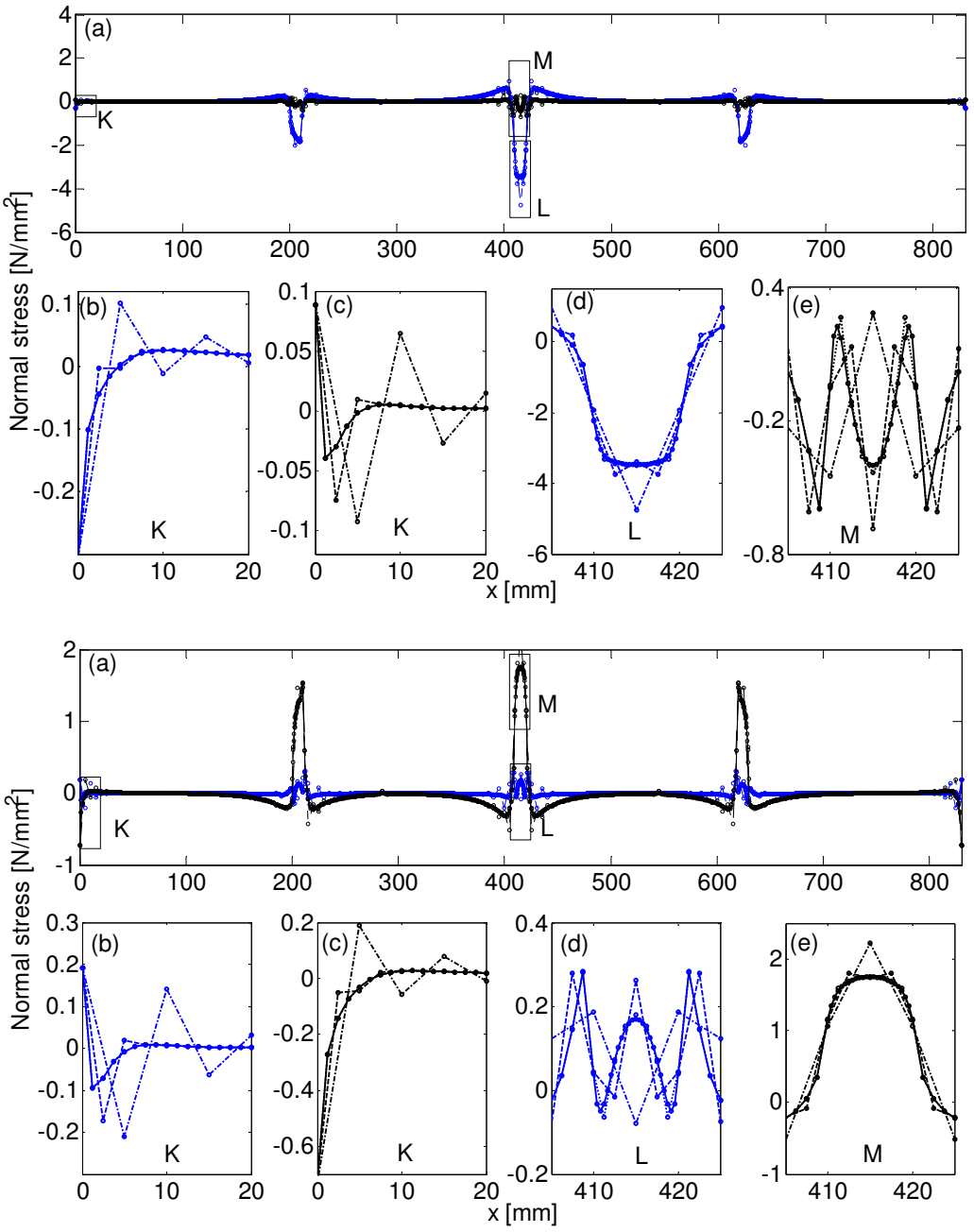


**Figure 7.** Distributions of normal out-of-plane stresses in the adhesive layers bonding the tensioned (top) and compressed (bottom) FRP strip. (a) global distributions; (b) adhesive-FRP interface near the edge (zone "K"); (c) adhesive-masonry interface near the edge (zone "K"); (d) adhesive-FRP interface near the middle joint (zone "L"); (e) adhesive-masonry interface near the middle joint (zone "N"). Legend: $-\cdot-\cdot-$ Mesh M1; $---$ Mesh M2; $\cdots\cdots$ Mesh M3; —— Mesh M4, $\circ$ FE nodes.

| Mesh | No. of elements through joint | No. of elements through the unit | Total No. of DOFs | Time step [mili-sec] | Run-time (normalized w.r.t. M2T1) | Line style in Figures 8–11 |
|---|---|---|---|---|---|---|
| M2T1 | 4 | 80 | 3663 | 0.25 | 1.00 | – · – · – |
| M3T1 | 8 | 160 | 7315 | 0.25 | 2.64 | – – – |
| M2T2 | 4 | 80 | 3663 | 0.125 | 1.84 | · · · · · · |
| M3T2 | 8 | 160 | 7315 | 0.125 | 4.51 | —— |

**Table 2.** Mesh properties for dynamic analyses.

**3.2.** ***Response to dynamic load.*** This section examines the dynamic response of the strengthened specimen to the loading described in Figure 2c. The two intermediate meshes, M2 and M3, and two time steps, 0.25 ms and 0.125 ms, are examined. The larger time step is about 1/25 the period of the first vibration mode of the specimen. The analyses with the larger time step are designated with T1 and the analyses with the smaller time step are designated with T2. Therefore, the four examined combination are designated M2T1, M2T2, M3T1, and M3T2. The properties of the various meshes are summarized in Table 2. The damping coefficients are selected to yield 7% damping ratio in the first two elastic modes. In the figures discussed in the following paragraphs, the circular marks designate the time steps.

The temporal variation of the out-of-plane deflections at mid-height is studied in Figure 8. The results reveal the typical response to a step load and mainly the transient response that is damped towards a

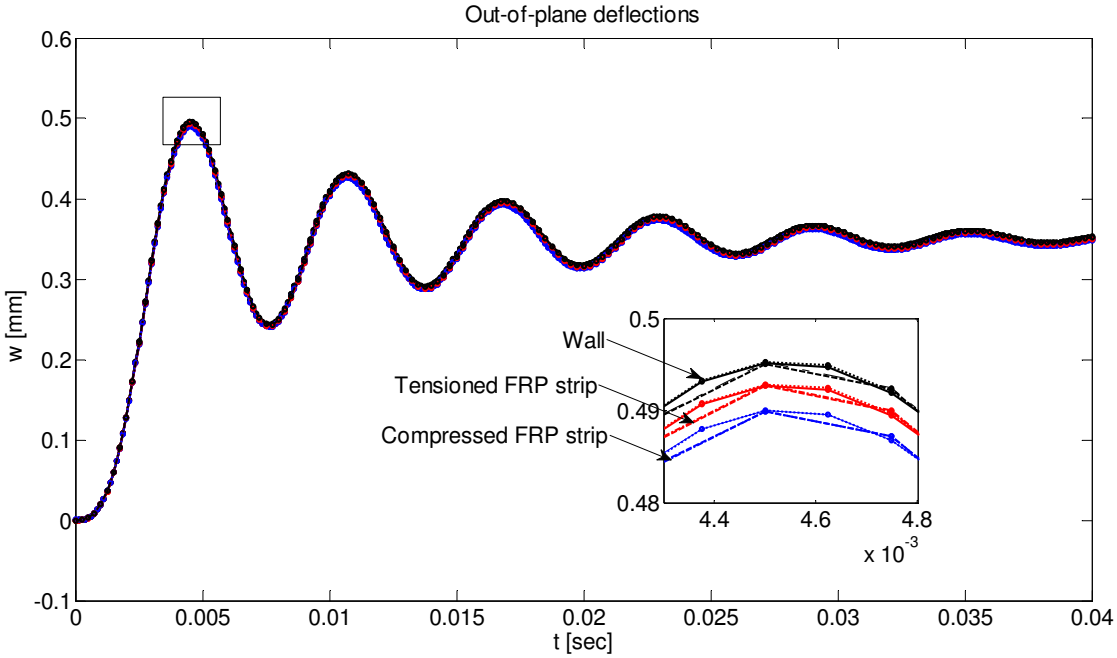


**Figure 8.** Out-of-plane deflections at mid-height versus time. Legend: – · – · – Mesh M2T1; – – – Mesh M3T1; · · · · · · Mesh M2T2; —— Mesh M3T2, ∘ time steps.

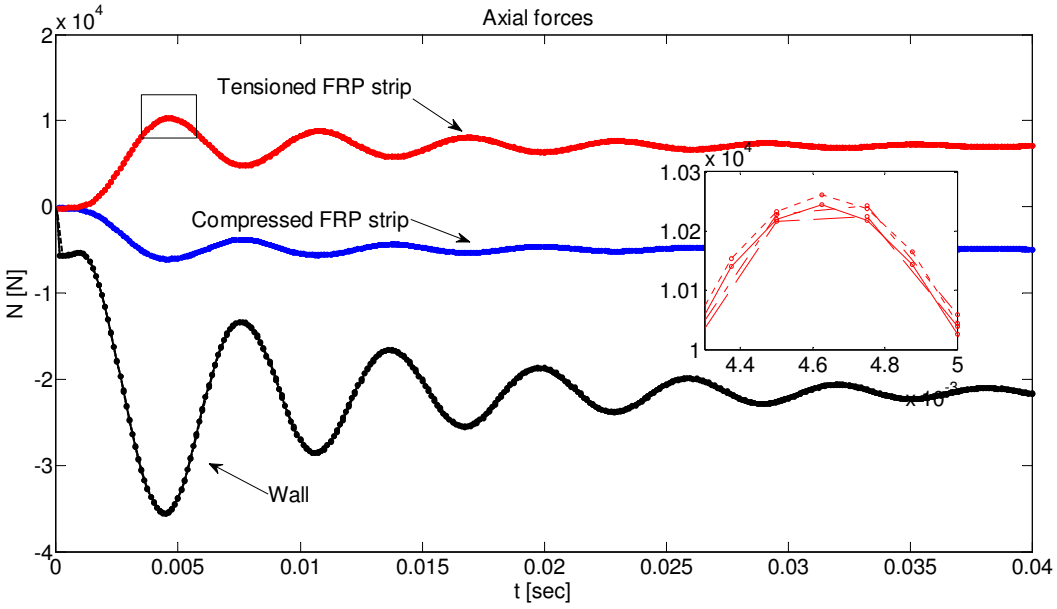


**Figure 9.** Axial forces at mid-height versus time. Legend: $-\cdot-\cdot-$ Mesh M2T1; $-\,-\,-$ Mesh M3T1; $\cdots\cdots$ Mesh M2T2; —— Mesh M3T2, $\circ$ time steps.

steady state solution. Due to the nonlinear-inelastic behavior and damage accumulation in the joints, the peak deflections at this case are slightly higher than in the case of static loading (Figure 3). A zoom plot on the first peak reveals the differences between the peak displacement of the masonry wall and those of the FRP strips. It also reveals that the differences between the various meshes are not significant and that a reasonable level of description can be achieved with a coarse mesh M2T1.

The time history of the axial forces in the wall and in the FRP strips at mid-height is studied in Figure 9. These results quantify the transient amplification of the forces due to the dynamic response and its rapid decay due to damping. It also reveals the evolution of a dynamic arching effect in which the global compressive force (the sum of axial forces in the wall and the FRP strips) is amplified due to cracking of the joint and the out-of-plane deflections, and varies in time. Also here, the effect of the arching force is more significant than the precompression. The zoom plot on the first peak in the response of the tensioned FRP strip reveals that the differences between the various meshes are not significant. In that sense, the relatively coarse mesh M2T1 provides an acceptable assessment of these aspects of the dynamic response.

The variation of the shear stresses in the adhesive layers is studied in Figure 10. The shear stresses are sampled near the middle joint at $x = 407.5$ mm (see Figure 6). In this location, both spatial meshes have nodes. The comparison between the results reveals some differences between the two spatial meshes. This is a result of the movement of the peak stresses with the refinement of the mesh. In the analysis with mesh M3, the peak stress travels from $x = 407.5$ mm to 408.75 mm, a node that does not exist in mesh M2. The zoom plot of the first temporary peak reveals that the differences between the analyses with the different time steps are rather minor and both of them provide an acceptable assessment of the nonlinear solution.

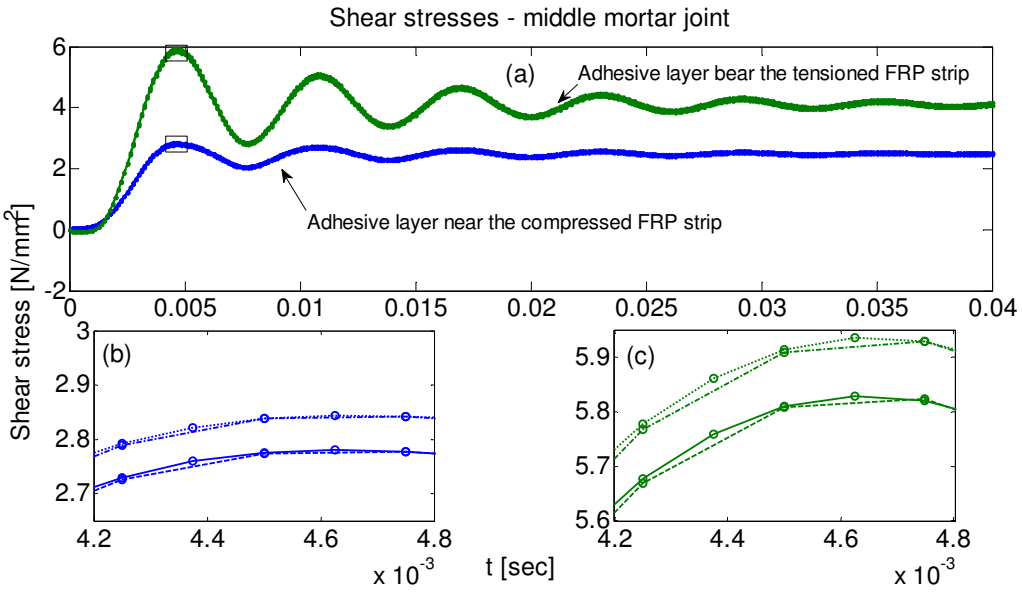


**Figure 10.** Peak shear stresses near the middle joint versus time. Legend: – · – · – Mesh M2T1; – – – Mesh M3T1; · · · · · · Mesh M2T2; —— Mesh M3T2, ∘ time steps.

The distributions of the dynamic axial forces (Figure 9) and the shear stresses (Figure 10) also clarify why in the static case the peak out-of-plane deflection of the compressed FRP strip is larger than that of tensioned strip (Figure 3, top half) whereas in the dynamic case it is the other way around (Figure 8). This shift is mainly attributed to the effect of the shear stresses near the joint and to the differences between the relative levels of axial tension/compression in the FRP strips. The interfacial shear stresses near the joints tend to increase the tensile force in the tensioned strip and to increase the compressive force in the compressed strip near the joint (see Figure 4, bottom half). The stresses are however, eccentric (with respect to the mid-surface of the FRP strips), evolve at the adhesive-FRP interface, and therefore yield localized bending in the FRP layer. This localized bending yields the slight "backwards deflection" (i.e., in the direction opposite to the global out-of-plane displacement), which can be observed in graphs (b) and (d) on the second row of Figure 3. Both in the static and in the dynamic cases studied here, the absolute value of the axial force in the tensioned FRP strip is larger than the one in the compressed strip and the magnitude of the shear stresses in the interface between adhesive and tensioned FRP interface are higher than in the interface between adhesive and compressed FRP strip (see Figure 6). Consequently, the effect of the backwards deflection in the tensioned FRP strip is larger than in the compressed one.

In the dynamic case, the ratio of the peak force in the tensioned strip over the peak one in the compressed strip (both in absolute values) and the ratio of the peak shear stress at the adhesive-tensioned strip interface over the peak one at the adhesive - compressed strip interface are slightly smaller than in the static case. As a result, in the dynamic case, the impact of the "backwards deflection" on the tensioned strip is slightly less prominent than in the static case and its effect on the compressed strip is slightly more prominent than in the static case. As the overall out-of-plane displacements combine the global ones with the localized bending effect near the joint, this yields the differences observed in the orders of the displacements in the static and the dynamic cases.

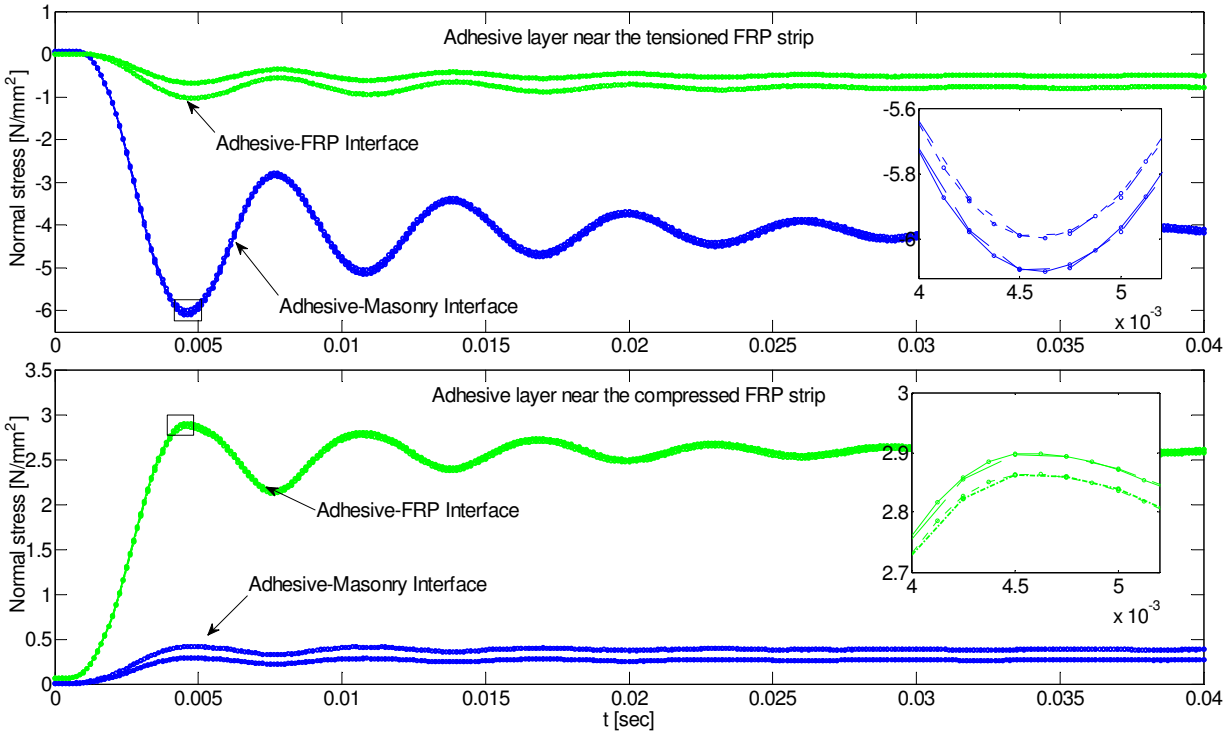


**Figure 11.** Out-of-plane normal stresses at $x = 415$ mm versus time. Legend: $-\cdot-\cdot-$ Mesh M2T1; $-\,-\,-$ Mesh M3T1; $\cdots\cdots$ Mesh M2T2; —— Mesh M3T2, ∘ time steps.

The evolution of the out-of-plane normal stresses at the interfaces of the inner and outer adhesive layers is studied in Figure 11. (The outer layer is the one that bonds the tensioned FRP strip.) The results are presented in terms of the stress at the middle of the specimen. The results capture and quantify the temporary amplification of the interfacial normal stresses, which are the main cause to premature debonding failures. In terms of numerical analysis, the curves reveal some differences between one spatial mesh and another. Yet, both analyses quantify a very similar pattern and the differences in terms of the peak values are not too significant. It is also observed that the differences between the temporal meshes are rather minor and they do not point at a prominent advantage of the refined mesh.

Finally, the analyses are compared in terms of run-time. The analysis with the coarse mesh M2T1 is considered as reference. The run-times of the analyses with meshes M2T2, M3T1, and M3T3 are 1.84, 2.64, and 4.51 times the reference run-time. This observation and the convergence characteristics discussed above indicate that mesh M2T1 may be sufficient for the dynamic analysis. Mesh M3T1 provides a good combination of accuracy and computation time.

## 4. Summary and conclusions

The dynamics of unidirectional FRP strengthened masonry walls has been investigated. In this part of the paper, a finite element for the nonlinear dynamic analysis of unidirectional strengthened masonry

walls has been developed. The finite element formulation has adopted a high-order theory approach in attempt to face the challenges associated with the combination of length scales, the significant differences in elastic properties, the presence of irregular points, the cracking and inelastic behavior of the mortar joints, and the layered structure of the strengthened wall. The finite element formulation has adopted a set of kinematic assumptions that stem form a high order representation of the static stress and displacement fields in the adhesive layer. This has allowed for the consideration of the variation of the stresses through the thickness of the adhesive layer and the evolution of interfacial stress concentrations while avoiding the divergence near irregular points and the increase in computational effort due to the 2D effects. The model has also taken into account the geometrical nonlinearity and has assumed that material nonlinearity due to cracking and crushing is concentrated in the mortar joints.

The performance of the analytical-numerical model has been examined through a static and dynamic convergence study. This study has pointed at the convergence characteristics of the model and has provided a measure of the level of refinement required in attempt to capture the localized effects. The numerical convergence study has indicated that the finite element model can overcome some of the critical problems encountered in standard FE analysis of strengthened walls. In that sense, it provided a computational framework that uses a 1D representation but can still handle the main features of the nonlinear dynamic response. The conversion of the above abilities into a FE based model allows for the use of standard computational and numerical procedures as well as for coupling with other elements and future implementation in a wider analysis framework.

## References

[Albert et al. 2001] M. L. Albert, A. E. Elwi, and J. J. R. Cheng, "Strengthening of unreinforced masonry walls using FRPs", *J. Compos. Constr.* (*ASCE*) **5**:2 (2001), 76–84.

[Brush and Almroth 1975] D. O. Brush and B. O. Almroth, *Buckling of bars, plates, and shells*, McGraw-Hill, New York, 1975.

[Buller 2005] O. Buller, "Special finite element for the analysis of sandwich panels with a transversely flexible core", Master's thesis, Technion – Israel Institute of Technology, Haifa, 2005. In Hebrew.

[Clough and Penzien 1993] R. W. Clough and J. Penzien, *Dynamics of structures*, 2nd ed., McGraw-Hill, New York, 1993. Revised in 2010.

[Dafnis et al. 2002] A. Dafnis, H. Kolsch, and H.-G. Reimerdes, "Arching in masonry walls subjected to earthquake motions", *J. Struct. Eng.* (*ASCE*) **128**:2 (2002), 153–159.

[Davidson et al. 2005] J. S. Davidson, J. W. Fisher, M. I. Hammons, J. R. Porter, and R. J. Dinan, "Failure mechanisms of polymer-reinforced concrete masonry walls subjected to blast", *J. Struct. Eng.* (*ASCE*) **131**:8 (2005), 1194–1205.

[Dym and Shames 1973] C. L. Dym and I. H. Shames, *Solid mechanics: a variational approach*, McGraw-Hill, New York, 1973.

[Elmalich and Rabinovitch 2009] D. Elmalich and O. Rabinovitch, "Masonry and monolithic circular arches strengthened with composite materials: a finite element model", *Comput. Struct.* **87**:9–10 (2009), 521–533.

[Elmalich and Rabinovitch 2010] D. Elmalich and O. Rabinovitch, "Nonlinear analysis of masonry arches strengthened with composite materials", *J. Eng. Mech.* (*ASCE*) **136**:8 (2010), 996–1005.

[Fung 1965] Y. C. Fung, *Foundations of solid mechanics*, Prentice-Hall, Englewood Cliffs, NJ, 1965.

[Gao et al. 2006] B. Gao, J.-K. Kim, and C. K. Y. Leung, "Optimization of tapered end design for FRP strips bonded to RC beams", *Compos. Sci. Technol.* **66**:10 (2006), 1266–1273.

[Gilstrap and Dolan 1998] J. M. Gilstrap and C. W. Dolan, "Out-of-plane bending of FRP-reinforced masonry walls", *Compos. Sci. Technol.* **58**:8 (1998), 1277–1284.

[Griffith et al. 2004] M. C. Griffith, N. T. K. Lam, J. L. Wilson, and K. Doherty, "Experimental investigation of unreinforced brick masonry walls in flexure", *J. Struct. Eng.* (*ASCE*) **130**:3 (2004), 423–432.

[Hamed and Rabinovitch 2007a] E. Hamed and O. Rabinovitch, "Geometrically nonlinear effects in the flexural response of masonry walls strengthened with composite materials", *J. Mech. Mater. Struct.* **2**:5 (2007), 829–855.

[Hamed and Rabinovitch 2007b] E. Hamed and O. Rabinovitch, "Out-of-plane behavior of unreinforced masonry walls strengthened with FRP strips", *Compos. Sci. Technol.* **67**:3–4 (2007), 489–500.

[Hamed and Rabinovitch 2008] E. Hamed and O. Rabinovitch, "Masonry walls strengthened with composite materials: dynamic out-of-plane behavior", *Eur. J. Mech. A Solids* **27**:6 (2008), 1037–1059.

[Hamilton and Dolan 2001] H. R. Hamilton, III and C. W. Dolan, "Flexural capacity of glass FRP strengthened concrete masonry walls", *J. Compos. Constr.* (*ASCE*) **5**:3 (2001), 170–178.

[Huang and Lyons 2007] D. Huang and J. Lyons, "Numerical stress analysis of the bond between a reinforced concrete T-beam and FRP sheets", *J. Reinf. Plast. Compos.* **26**:12 (2007), 1225–1237.

[Khoshbakht et al. 2009] M. Khoshbakht, M. W. Lin, and C. A. Feickert, "A finite element model for hygrothermal analysis of masonry walls with FRP reinforcement", *Finite Elem. Anal. Des.* **45**:8–9 (2009), 511–518.

[Lam et al. 2003] N. T. K. Lam, M. Griffith, J. Wilson, and K. Doherty, "Time-history analysis of URM walls in out-of-plane flexure", *Eng. Struct.* **25**:6 (2003), 743–754.

[Li et al. 2009] L.-J. Li, Y.-C. Guo, P.-Y. Huang, F. Liu, J. Deng, and J. Zhu, "Interfacial stress analysis of RC beams strengthened with hybrid CFS and GFS", *Constr. Build. Mater.* **23**:6 (2009), 2394–2401.

[Newmark 1959] N. M. Newmark, "A method of computation of structural dynamics", *J. Eng. Mech. Div.* (*ASCE*) **85**:EM3 (1959), 67–94.

[Pan and Leung 2008] J. Pan and C. K. Y. Leung, "Effect of end tapering on crack-induced FRP debonding from the concrete substrate", *J. Compos. Constr.* (*ASCE*) **12**:1 (2008), 15–24.

[Rabinovitch 2004] O. Rabinovitch, "Nonlinear (buckling) effects in RC beams strengthened with composite materials subjected to compression", *Int. J. Solids Struct.* **41**:20 (2004), 5677–5695.

[Rabinovitch 2010] O. Rabinovitch, "Buckling-driven debonding in stiff block: compliant joint structural assemblies patched with composite materials", *Int. J. Fract.* **165**:1 (2010), 21–38.

[Rabinovitch and Frostig 2000] O. Rabinovitch and Y. Frostig, "Closed-form high-order analysis of RC beams strengthened with FRP strips", *J. Compos. Constr.* (*ASCE*) **4**:2 (2000), 65–74.

[Rabinovitch and Madah 2011] O. Rabinovitch and H. Madah, "Finite element modeling and shake-table testing of unidirectional infill masonry walls under out-of-plane dynamic loads", *Eng. Struct.* **33** (2011), 2683–2696.

[Rabinovitch and Madah 2012] O. Rabinovitch and H. Madah, "Dynamics of FRP strengthened unidirectional masonry walls, II: Experiments and comparison", *J. Mech. Mater. Struct.* **7** (2012), 29–44.

[Reddy 1999] J. N. Reddy, *Elastic plates*, Taylor & Francis, Philadelphia, 1999.

[Schwarts-Givli et al. 2007] H. Schwarts-Givli, O. Rabinovitch, and Y. Frostig, "High-order nonlinear contact effects in the dynamic behavior of delaminated sandwich panels with a flexible core", *Int. J. Solids Struct.* **44**:1 (2007), 77–99.

[Teng et al. 2002] J. G. Teng, J. W. Zhang, and S. T. Smith, "Interfacial stresses in reinforced concrete beams bonded with a soffit plate: a finite element study", *Constr. Build. Mater.* **16**:1 (2002), 1–14.

[Timoshenko and Gere 1961] S. P. Timoshenko and J. M. Gere, *Theory of elastic stability*, 2nd ed., McGraw-Hill, New York, 1961.

[Vinson and Sierakowski 1986] J. R. Vinson and R. L. Sierakowski, *The behavior of structures composed of composite materials*, Martinus-Nijhoff, Dordrecht, 1986. 2nd ed. published in 2002.

[Yang et al. 2004] Q. S. Yang, X. R. Peng, and A. K. H. Kwan, "Finite element analysis of interfacial stresses in FRP–RC hybrid beams", *Mech. Res. Commun.* **31**:3 (2004), 331–340.

Received 29 Aug 2010. Revised 9 Feb 2011. Accepted 10 Feb 2011.

ODED RABINOVITCH: cvoded@tx.technion.ac.il
*Faculty of Civil and Environmental Engineering, Technion – Israel Institute of Technology, Haifa, 32000, Israel*

HAZEM MADAH: hazem@tx.technion.ac.il
*Faculty of Civil and Environmental Engineering, Technion – Israel Institute of Technology, Haifa, 32000, Israel*

JOURNAL OF MECHANICS OF MATERIALS AND STRUCTURES
Vol. 7, No. 1, 2012

msp

# DYNAMICS OF FRP STRENGTHENED UNIDIRECTIONAL MASONRY WALLS II: EXPERIMENTS AND COMPARISON

ODED RABINOVITCH AND HAZEM MADAH

In this part of the paper, the dynamic out-of-plane behavior of a unidirectional strengthened masonry wall is studied experimentally. The experimental phase focuses on shake-table testing of a full-scale masonry wall strengthened with carbon fiber reinforced composite strips. The tested wall is subjected to different combinations of in-plane compression and out-of-plane excitation. The dynamic behavior of the wall is monitored with emphasis on the global out-of-plane displacements and accelerations as well as on the localized displacements and strains near the mortar joints. The experimental results are also used for the assessment of the finite element model developed in part I of the paper. The experimental results, the numerical analysis, and the comparison between the two throw light on the global and local aspects of the dynamic response. The numerical model allows for further study of local-scale results, which cannot be monitored experimentally. In particular, the dynamics of the shear and peeling stresses at the adhesive layers are examined. The comparison of the experimental results with ones obtained for the same wall before strengthening demonstrate the potential of the method and its impact on the dynamics of the masonry wall.

## 1. Introduction

Masonry walls are a structural form that can be found in almost every building around the world. Masonry construction characterizes many historic buildings but it still serves as a building technique widely used as infill walls in modern structural systems. Along with its many advantages, the unique characteristics of the masonry construction make the masonry wall vulnerable to out-of-plane static and mainly dynamic loads. For example, in [Rabinovitch and Madah 2011] we experimentally and analytically examined the behavior of unreinforced masonry walls under out-of-plane dynamic loads. The experimental observations reflected the limited ability of the wall to resist such loads and the impact of the boundary conditions and the level of in-plane compression on this limited ability. The tendency of the boundary conditions and the in-plane loading conditions to unfavorably change during a dynamic loading may lead to a severe degradation in the structural performance and to a potential collapse of the wall. In case of a seismic event, this type of behavior may endanger the occupants, even if the main structural skeleton is intact [Flanagan and Bennett 1999; Wu et al. 2005; Meisl et al. 2007].

The above observations highlight the need to strengthen the masonry wall, not only to resist in-plane loads but also to resist out-of-plane ones. The use of externally bonded composites is an excellent solution for this need [Albert et al. 2001; Hamilton and Dolan 2001; Griffith et al. 2004; Gilstrap and Dolan 1998]. The addition of a strong, stiff, lightweight, and durable externally bonded tensile resisting layer provides

This research was supported by The Israel Science Foundation, Grant No. 772/06.
*Keywords:* masonry wall, composite material, dynamic behavior, shake table experiments, strengthening.

the wall with a supplemental load resisting mechanism and with the ability to resist out-of-plane loads through flexure. This ability was demonstrated in various experimental programs that examined the static out-of-plane response of the strengthened wall [Albert et al. 2001; Hamilton and Dolan 2001; Griffith et al. 2004; Gilstrap and Dolan 1998; Hamed and Rabinovitch 2010a; Hamed and Rabinovitch 2010b]. The more important challenge is, however, to examine, characterize, and demonstrate the response of the strengthened wall to dynamic loads.

The dynamic behavior of masonry walls strengthened with externally bonded composite materials has been the subject of various experimental studies reported in the past decade, such as [ElGawady et al. 2002; 2003; Turek et al. 2007; El-Dakhakhni et al. 2004; Almusallam and Al-Salloum 2007; Altin et al. 2008]. These studies mainly focused on the in-plane response of the wall. The number of works that experimentally studied the dynamic out-of-plane response is much smaller. Among them, [Davidson et al. 2005] and [Myers et al. 2004] examined the out-of-plane dynamic response of masonry wall sprayed with polymeric layers to blast loads. The dynamic characteristics of these loads and, correspondingly, the strengthening technique, are different from the ones associated with the response to seismic or wind loads studied here.

Al-Chaar and Hasan [2002] studied the coupled and the out-of-plane response of masonry walls rehabilitated with composite overlays and subjected to uniaxial and triaxial dynamic excitation. The results showed that the composite overlay enhances the seismic resistance of the masonry wall by increasing its ultimate strength and modifying its dynamic properties by about 25–40%. On the other hand, it was observed that cracking and the nonlinear behavior of the wall couples the dominant frequencies and the level of damage (also see [Carpinteri and Pugno 2005; Thompson and Stewart 1986]). These important observations are mainly focused on the global-scale response of the wall. Further attention should be drawn to localized effects, which are critical for the understanding of the behavior of the structure and for the assessment of analytical or numerical models.

The objectives of this paper are to experimentally study the out-of-plane dynamic behavior of unidirectional strengthened masonry wall panels and to comparatively assess the FE model developed in part I [Rabinovitch and Madah 2012]. To achieve these goals, a full-scale unidirectional masonry wall that is strengthened with externally bonded strips made of carbon fiber reinforced polymer (CFRP) is tested under out-of-plane dynamic excitation. The shake table test setup follows the one used in [Rabinovitch and Madah 2011] for unreinforced unidirectional masonry walls. The results of the shake-table experiments and the comparison with the response of the same wall tested before strengthening (*loc. cit.*) are used in order to gain insight into the characteristics of the dynamic response. In addition, they are used for a critical evaluation and possible support of the numerical model developed in part I. With that in mind, additional results that cannot be directly detected experimentally but can be obtained through the numerical model, are presented and discussed. Emphasis is placed on the interfacial effects, on the stress concentrations near irregular points, and on their variation in time during the dynamic loading event.

The paper is organized as follows. The experimental setup, the material properties and characterization, and the finite element model are presented first. Then the experimental results of two tests that differ in the level of axial loading applied during the dynamic excitation are presented and discussed. The first set of results obtained under the higher level of axial loading is compared with the results of the FE analysis. The second set is compared with the response of the wall before strengthening [Rabinovitch and Madah

2011] with emphasis on the impact of the strengthening system on the dynamic response of the wall. The paper closes with a summary and conclusions.

## 2. Shake-table experiments and FE analysis

**2.1.** ***Test setup.*** The shake-table test setup follows the one reported in [Rabinovitch and Madah 2011] for testing the unstrengthened wall. For completeness, it is presented here. The shake table apparatus is illustrated in Figure 1. The wall is excited in its out-of-plane direction and therefore is it built inside a steel frame that is mounted on the shake table facing the direction of the motion (see Figure 1c). The steel frame is mounted on the table and rigidly supported at its top. The upper supporting point is connected to the shake table using the triangular steel construction shown in Figure 1c. This configuration yields a coordinated and controlled movement of the top and bottom of the wall. These conditions are designed to avoid interstorey drift and relative movement of the top of the wall with respect to its bottom. The wall is sandwiched between two concrete elements (beams) that simulate the lower and upper slabs. On

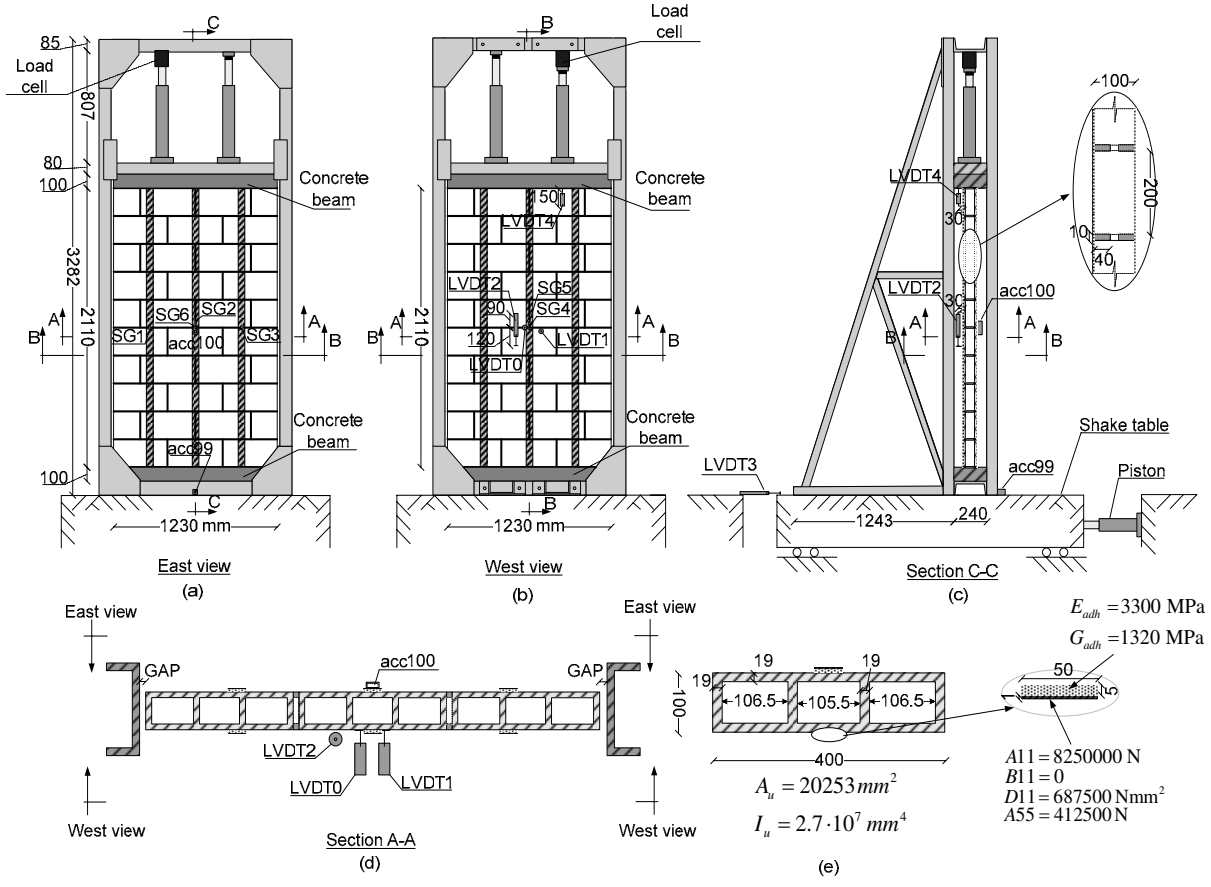


**Figure 1.** Dynamic test setup (dimensions in mm). (a) east view; (b) west view; (c) section C-C; (d) section A-A; (e) geometry and properties of the masonry unit, FRP strips, and adhesive layers.

the other hand, the wall is disconnected from the columns of the steel frame yielding a unidirectional out-of-plane flexural scheme and transfer of loads in the height direction only.

The simulation of the gravity load transferred to the wall from the upper slab is achieved using two hydraulic jacks (Figure 1a-c). The axial compression applied by the jacks also controls the level of cracking in the wall. The detail at the top of the wall restricts the lateral (out-of-plane) displacement and the rotation of the upper concrete beam but allows the beam to move in the vertical direction. This allows transferring the in-plane compressive load to the tested wall. It should, however, be noted that the preliminary testing has shown that the hydraulic system at the top of the wall (the two jacks and the hydraulic fluid lines) has a certain level of vertical compliance, which has to be taken into account. Along with the vertical load, the entire apparatus, which includes the shake table, the supporting steel frame, the wall, and the axial loading system at its top, are excited dynamically. The control system is based on closed loop dynamic controller.

The tested wall is built of 400/200/100 hollow concrete units. The cross section of the wall and the general layout of the masonry assembly are shown in Figure 1d,e. The masonry units are connected through mortar head and bed joints. Following conventional masonry building techniques, the mortar in the bed joints is applied in two strips on top of the masonry unit's outer shells. The width of each strip is about 400 mm and the thickness of the bed joints is about 10 mm. The thickness of the head joints is also about 10 mm. The overall dimensions of the tested wall are about 1230 by 2110 mm.

The wall was dynamically tested prior to strengthening. The results of this initial testing phase are reported in [Rabinovitch and Madah 2011]. At the initial phase of testing, the wall was subjected to different combinations of axial loading and out of plane dynamic excitation. Testing under 2800 N and a cyclic excitation with frequency of 8.3 Hz and amplitude of about $\pm 1$ mm yielded extensive cracking at the middle joint and brought the wall close to collapse (see [Rabinovitch and Madah 2011] for more details).

After the initial dynamic loading, the wall was strengthened using six externally bonded CFRP strips, three on each face. The configuration of the CFRP strips is shown in Figure 1. Before strengthening, the wall's surface was cleaned and a preliminary layer of epoxy was applied on the wall's surface. After the primer layer was cured, the CFRP strips were installed in place. The strips were not mechanically fastened or anchored at the edges, at the supporting frame, or at any other point. The final thickness of the adhesive equals about 5 mm.

The monitoring devices include five LVDTs, two accelerometers, one load cell, and six stain gauges. The various devices and their locations are illustrated in Figure 1. The out of plane displacements (relative to the surrounding frame) are monitored by LVDT0 and LVDT1. The crack opening across the middle bed joint and the crack opening between the upper masonry unit and the upper concrete element are detected by LVDT2 and LVDT4, respectively. The absolute displacement of the shake-table is monitored by LVDT3. The out-of-plane acceleration at the shake-table level and the out-of-plane acceleration at the middle of the wall are monitored by the two accelerometers (acc 99, and acc 100, respectively). The compressive load applied by the hydraulic system at the top of the wall and its temporal variation are dynamically monitored by the load cell.

The six strain gauges are bonded on the outer faces of the FRP strips in two groups. SG1, SG3, and SG6 are bonded on the three FRP strips mounted on the east face of the wall. These strain gauges are bonded across the middle-joint. SG2, on the other hand, is bonded on the middle strip on that

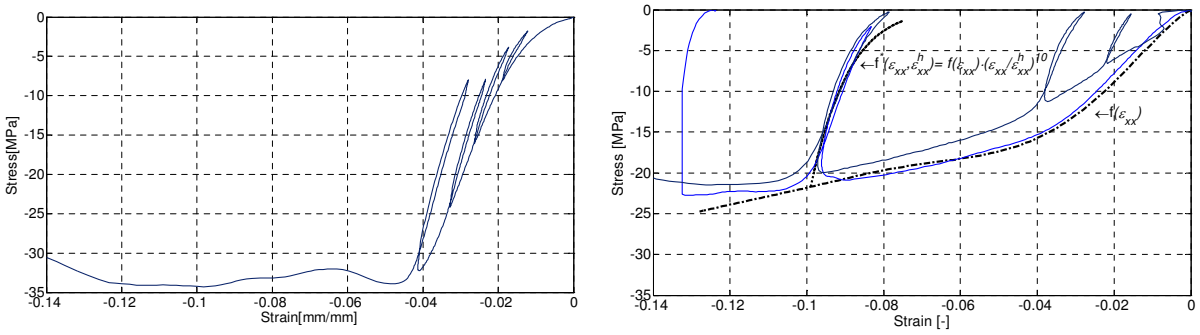


**Figure 2.** Constitutive relations for the masonry materials. (a) masonry shells; (b) mortar. Legend: —— experimental; − − − loading; · · · · · · · · · unloading/reloading.

face but about 30 millimeters above the joint. Similarly, SG4 and SG5 are bonded on the middle strip mounted on the west face of the wall across and above the joint, respectively. All sensors are sampled at 300 samples/sec.

**2.2.** ***Material properties.*** The equivalent elastic modulus of the FRP strips $E^{\mathrm{FRP}} = 165\,\mathrm{GPa}$ and its specific mass $\rho^{\mathrm{FRP}} = 1400\,\mathrm{kg/m^3}$ are based on the data provided by the manufacturer. The shear modulus of the FRP strip is estimated as 8.25 GPa and the shear correction factor is taken as 5/6. The elastic and shear moduli of the adhesive layer follow [Hamed and Rabinovitch 2010a; Hamed and Rabinovitch 2010b] and equal $E = 3.3\,\mathrm{GPa}$ and $G = 1.32\,\mathrm{GPa}$. Its specific mass is taken as $1070\,\mathrm{kg/m^3}$.

The elastic / mechanical properties of the masonry units are estimated based on monotonic and cyclic compressive tests of square 80 by 80 mm specimens cut out from the masonry shell. Some of the results appear in Figure 2a and reveal an approximately linear range running from about 20% up to about 85% of the ultimate load with minor inelastic effects due to unloading / reloading in this range. The crushing strength of the masonry shells is larger than 30 MPa. The average elastic modulus in the quasilinear range equals about 1100 MPa. These observations support the assumption of linear elastic behavior of the masonry unit used in [Rabinovitch and Madah 2012]. The shear modulus of the masonry unit is taken as 440 MPa and its mass density equals $1930\,\mathrm{kg/m^3}$. The shear correction factor for the masonry unit cross section is estimated using a 2D finite element analysis and taken as 0.675.

The mortar is made with cement-sand-lime ratio = 1:3:1 and its mass density is about $2400\,\mathrm{kg/m^3}$. The constitutive behavior of the mortar under cyclic uniaxial compression is determined experimentally. A characteristic result appears in Figure 2b (also see [Rabinovitch and Madah 2011]). The loading ($f(\epsilon_{xx})$) and the unloading/reloading ($f^*(\epsilon_{xx}, \epsilon^h_{xx})$) branches are approximated as follows (*loc. cit.*):

$$f(\epsilon_{xx}) = 314\epsilon_{xx} - 0.198\cdot 10^5\epsilon^2_{xx} - 0.706\cdot 10^6\epsilon^3_{xx} - 0.9\cdot 10^7\epsilon^4_{xx} - 0.5\cdot 10^8\epsilon^5_{xx} - 0.1\cdot 10^9\epsilon^6_{xx}\ [\mathrm{MPa}], \quad (1)$$

$$f^*(\epsilon_{xx}, \epsilon^h_{xx}) = f(\epsilon^h_{xx})\cdot(\epsilon_{xx}/\epsilon^h_{xx})^{10}\ [\mathrm{MPa}]. \quad (2)$$

The shear response of the compressed mortar, $s(\gamma_{xz})$, is assumed linear elastic with a shear modulus $G_j = 166\,\mathrm{MPa}$ ([Hamed and Rabinovitch 2010a; Hamed and Rabinovitch 2010b]. The initial tangent moduli of the mortar material are taken as $E_j = f_{,\epsilon}(\epsilon_{xx} = 0^-) = 314\,\mathrm{MPa}$ and $G_j = s_{,\gamma}(\gamma_{xz} = 0) = 166\,\mathrm{MPa}$.

**2.3.** ***Testing protocol.*** Following the observations and the data gained from testing of the unstrengthened wall [Rabinovitch and Madah 2011], the wall reported here is tested under a cyclic out-of-plane excitation with frequency of about 8.3 Hz and amplitudes of about $\pm 1$ mm. The application of this dynamic load and vertical loading of about 5000 N (2500 N in each jack) did not bring the unstrengthened wall to failure [Rabinovitch and Madah 2011]. On the other hand, the same dynamic protocol applied to the unstrengthened wall under vertical loading of 2800 N triggered extensive cracking at mid-height. Based on these observations, and in order to compare the results with the behavior of the wall before strengthening, the same two test protocols (i.e., [8.3 Hz, $\pm 1$ mm, 5000 N], [8.3 Hz, $\pm 1$ mm, 2800 N]) are examined here as well.

**2.4.** ***Finite element modeling.*** Two finite element models are examined. Following part I of the paper [Rabinovitch and Madah 2012], both model refer to a characteristic 400 mm wide unidirectional strip. The first model refers to the entire height of the wall. In order to allow analysis with a refined mesh and yet to keep the computational burden reasonable, the second model takes advantage of the out-of-plane symmetry and refers to half of the wall with symmetry conditions. The entire wall is strengthened with 3 strips on each face, therefore the 400 mm wide characteristic strip includes one FRP strip on each face. The full-height model of the characteristic strip includes 10 masonry units, 11 bed joints, and the upper and lower beams, which are assumed linear elastic with $E = 30$ GPa, $G = 12$ GPa, $\rho = 2400\,\mathrm{kg/m^3}$, and a solid cross section. The boundary conditions are applied at the ends of the lower and the upper supporting beams. The lower beam is clamped. The upper beam is free to move in the vertical (axial) direction but its rotation and out-of-plane displacement are constrained. In the vertical direction, the top of the beam is connected to a precompressed spring that simulates the applied load, the weight of the devices at the top of the wall (distributing beam, hydraulic jacks, load cells, etc), and the compliance of the hydraulic loading system. The spring constant is roughly estimated as 1000 kN/m for the examined 400 mm wide strip.

In the symmetric model, the boundary conditions at the bottom of the wall are replaced with sliding clamps at the middle of the mid-height joint. The sliding clamp conditions (free out-of plane displacement, fixed rotation and in-plane displacement) are applied to the masonry wall and the FRP strips. The conditions at the adhesive layers allow free out-of-plane displacement. Note that these conditions violate the lack of symmetry due to the in-plane configuration and the self-weight of the wall. In addition, the symmetric model cannot capture the antisymmetric out-of-plane modes.

The full-height FE mesh includes 502 elements through the height of the wall. Each joint is divided into 2 elements and each masonry unit is divided into 40 elements. The total number of DOFs is 5533. In part I of this paper it has been shown that this type of mesh provides an adequate assessment of the global response but only a rough estimate of the stress concentrations near the joints. For that purpose, the symmetric model uses a refined mesh with 4 elements through the height of the joint and 80 elements through the height of each masonry unit. The dynamic load for both models uses the reading of the accelerometer mounted on the shake-table as a ground acceleration signal. Along with the dynamic excitation, the models are also subjected to the self-weight of the wall, the weight of the loading devices at the top of the wall, and the vertical precompression load. Based on the preliminary convergence study outlined in part I of this paper, the time step of the numerical analysis equals $0.833 \cdot 10^{-3}$ sec. To meet this time step, linear interpolation of the recorded ground acceleration input signal is used. The

proportionality constants for the damping model are calibrated for assumed damping ratios of about 7% in the two first linear modes.

## 3. Results, comparison, and discussion

The results for the wall vertically loaded to 5000 N (2150 N per the examined 400 mm wide strip, including the added weight at the top of the wall) are presented first. The experimental results and their numerical counterparts are followed by complementary results that cannot be detected experimentally but can be obtained by the numerical analysis. Finally, the results per the wall vertically loaded to 2800 N (1430 N per the examined strip, including added weight) are presented and compared with the ones obtained per the unstrengthened wall under similar dynamic loading conditions.

**3.1.** ***Test and analysis results: higher level of vertical loading.*** The out-of-plane displacements and accelerations detected at the middle of the wall in the experiment, the analysis with the full-height model, and the analysis with the symmetric model are studied in Figure 3. Part (a) of the figure and the zoom plot in (b) reveal displacements in the order of $\pm 0.4$ mm. For comparison, the testing of the wall under the same conditions but before strengthening revealed similar levels of accelerations but

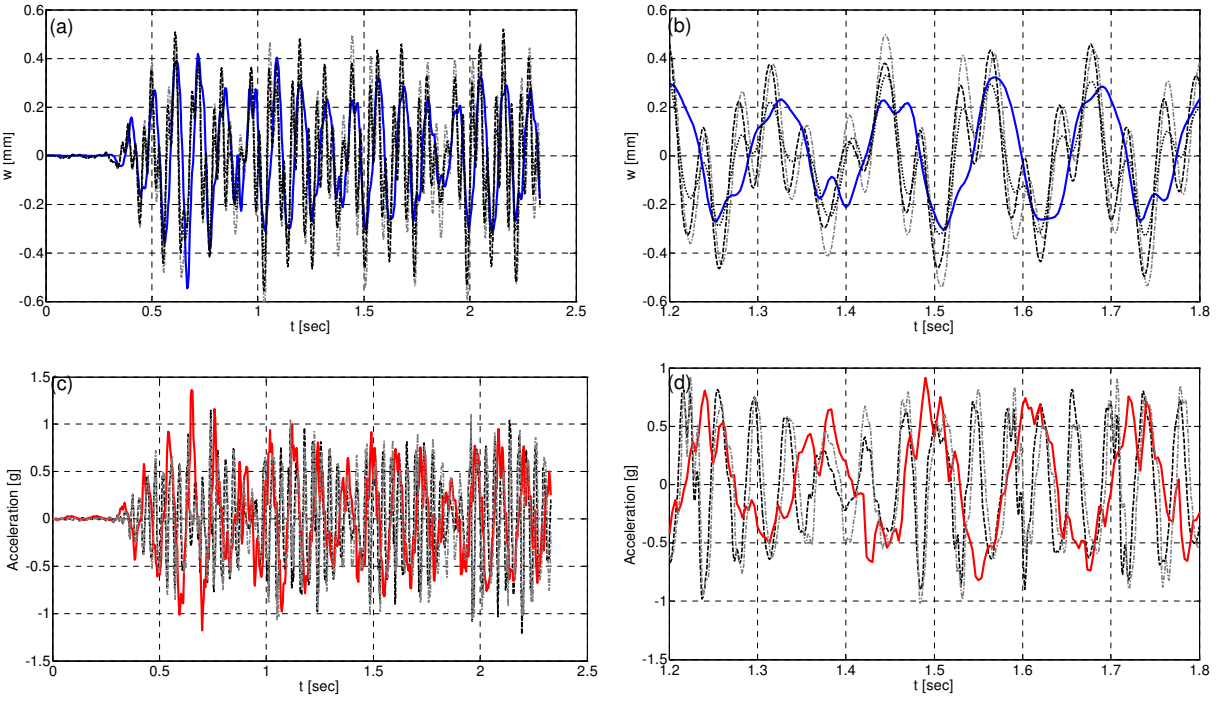


**Figure 3.** Dynamic response under higher level of vertical loading and out-of-plane excitation. (a) out-of-plane displacements at mid-height vs. time; (b) zoom on $t =$ 1.2–1.8 sec; (c) out-of-plane accelerations at mid-height vs. time; (d) zoom on $t =$ 1.2–1.8 sec. Legend: —— = experimental; − − − = analysis, full-height model; − · − · − = analysis, refined symmetric model; · · · · · · · · · = analysis, higher damping ratio (Figure 3b only).

displacements which are about 1.5–1.8 times larger [Rabinovitch and Madah 2011]. The comparison between the numerical and the experimental results and between the two numerical models reveals a reasonable agreement, both in terms of amplitudes and in terms of the leading frequency of the temporal variation. On the other hand, it is observed that both numerical models tend to overestimate the effect of higher frequencies. The higher frequencies are noticeable in the experimental response, but they are less dominant.

A fast-Fourier-transform (FFT) analysis of the results reveals that the higher frequencies are detected in the range of about 21–28 Hz. This range corresponds to the first elastic natural frequency of the strengthened wall. The overestimation of the effect of the natural frequencies, which, in the present case, are higher than the frequency of the dynamic load, implies that the level of damping assumed in the analysis is probably underestimated. In order to examine this hypothesis, the results of the analysis with an exaggerated global damping ratio (20% of the critical one in the first two modes) appear in a dotted line in Figure 3b (for clarity of the figure, this line is not presented in Figure 3a). The results of the model with the higher level of damping reveal a less prominent effect of the higher frequencies and a better agreement with the experimental observations. This implies that the actual level of damping is higher than the one assumed in the original analysis. It should, however, be noted that the higher level of damping is also strongly affected by contributions of the test apparatus and, particularly, the lateral and vertical hydraulic loading systems. Yet, the observations regarding the effect of dissipation indicates that improvement of the simplified proportional damping model adopted in the analysis, its replacement with a more sophisticated damping model, and its calibration using the detailed experimental results are necessary directions of future enhancement of the analysis.

The comparison between the results of the full-height model and the symmetric one reveal that the amplitudes described by the latter are slightly higher than the ones detected by the former. This is attributed to the different representations of the self-weight of the wall in the two models, the a-symmetry that the self-weight introduces, and the a-symmetry in the in-plane configuration. Another contributor to the differences between the two models is the different representation of damping, which depends on the dynamic characteristics of each model.

The comparison in terms of accelerations appears in Figure 3c-d and reveals that the two numerical simulations and the experimental results are in agreement in terms of magnitude. Figure 3c also shows that the numerical model captures the slight beat effect observed in the experimental result. On the other hand, as expected, the effect of the higher frequency observed in the displacement response is more pronounced here. This effect further stresses the need to investigate the dissipative mechanisms in the wall as well as their implementation in the numerical model.

Another important aspect of the dynamic response is the temporal variation of the axial reaction at the top of the wall. These numerical and experimental results appear in Figure 4a-b. In this case, the presentation of the numerical results is limited to the symmetric model. The results refer to the 400 mm wide strip and include the weight of the loading devices located at the top of the wall. The comparison between the numerical and the experimental results reveals a good agreement in terms of the magnitude of the dynamic component of the thrust force. On the other hand, the analysis predicts a more rapid variation of the thrust force with frequency that is close to the first natural frequency of the wall in its intact condition. The frequency of the dynamic component detected in the experiment is closer to the one governing the forced excitation (about 8.3 Hz). Also here, the higher frequency response observed

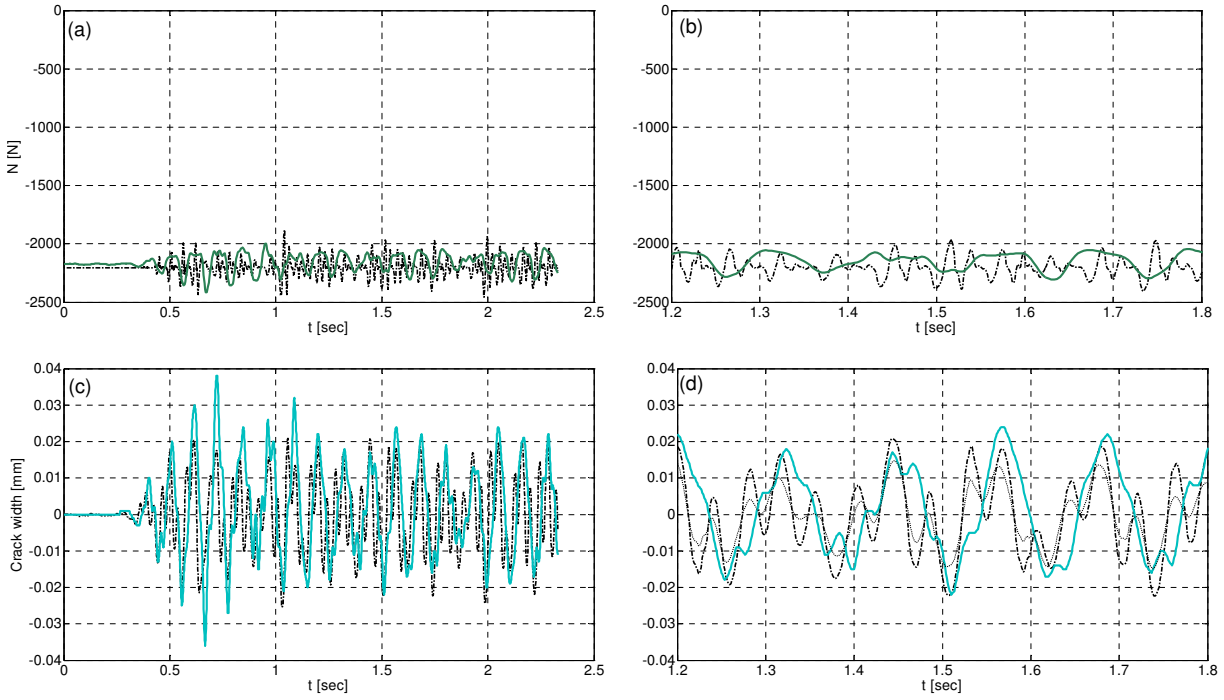


**Figure 4.** Dynamic response under higher level of vertical loading and out-of-plane excitation. (a) axial force at the top of the wall vs. time; (b) zoom on $t = 1.2$–$1.8$; (c) relative axial displacements across the middle joint (west face) versus time; (d) zoom on $t = 1.2$–$1.8$ sec. Legend: —— = experimental; $-\cdot-\cdot-$ = analysis, symmetric model; $\cdots\cdots$ = analysis, higher damping ratio (Figure 4d only).

in the analysis is attributed to underestimation of the damping and its effect on the out-of-plane response. On the other hand, the experimental observation reflects on coupling between the in-plane and the out-of-plane excitations. Such coupling, which may stem from imperfections in the test set-up, trigger auxiliary in-plane excitation of the wall with the same frequency as the out-of-plane one. This scenario, which can also explain the nonsymmetric or "nonsinusoidal" signal observed in the experimental results in Figure 4a-b, is not accounted for in the analysis.

The temporal variation of the axial deformations across the mid-height joint is studied in Figure 4c-d. In the experiment, the relative displacements are measured across two points located 90 and 120 mm above and below the center of the mid-height joint (LVDT2 in Figure 1). In the numerical analysis, the relative displacements are evaluated based on the reference axis displacements and rotations at these points. In both cases, the relative displacements due to the axial loading are not included and the presentation is limited to the results of the refined symmetric model, which provides a better description of the displacement field in the joint. The results appear in Figure 4c-d and indicate on a rather symmetric response with respect to the zero displacement line. This implies that under the examined conditions, the effect of shift of the axis of rotation ("neutral axis") and the effect of rocking are not significant. The comparison between the numerical and the experimental results indicates that the analysis well captures the variation of the axial displacements across the joints. At the first second of the response, the analysis

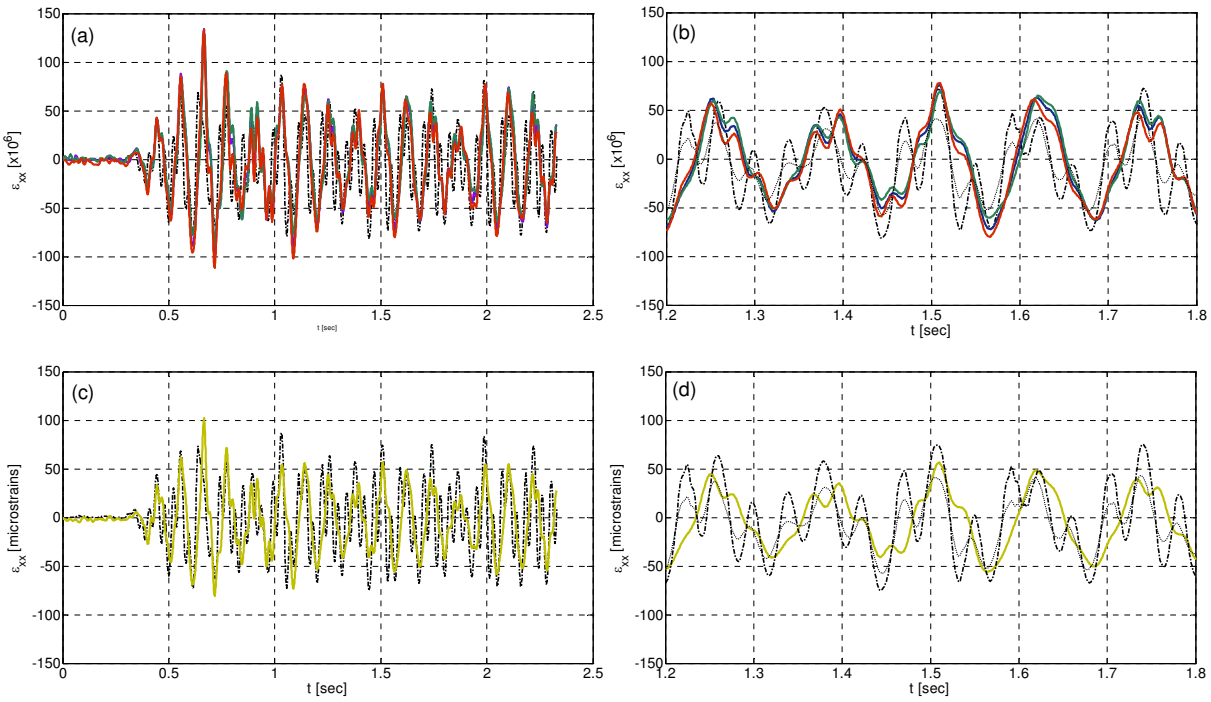


**Figure 5.** Strains at the outer face of the FRP strips versus time. (a) SG1,SG2, SG3 (middle of the joint) vs. time; (b) zoom plot $t = 1.2$–$1.8$ sec; (c) SG4 (30 mm above the middle joint-block interface, middle west strip; (d) zoom plot $t = 1.2$–$1.8$ sec. Legend: —— SG1; —— SG2 —— SG3, —— SG4 (experimental); $-\cdot-\cdot-$ analysis, symmetric model, damping ratio=7%; $\cdots\cdots$ analysis, symmetric model, damping ratio=20%.

slightly overestimates the level of displacements. Later on, the discrepancies decay, revealing a good agreement in terms of amplitudes. The slight overestimation of the effect of the higher frequency by the numerical model decays with the increase in damping ratio.

A more refined class of results that focus on a more "localized" aspect of the dynamic response of the wall examines the strains at the outer face of the FRP strips near the mid-height joint. These results are studied in Figure 5. Note that here the zero lines refer to the initiation of the dynamic test and do not take into account the strains due to the vertical loading. The numerical results are presented for the symmetric model and they refer to the strain at the middle of the 5 mm long strain gauge.

The comparison between the strains measured at the outer faces of the middle of the joint at the left, middle, and right FRP strips (Figure 5a and zoom plot in Figure 5b) reveal only minor differences between the measured values. This supports the assumption that in spite of the running bond texture and the inhomogeneous structure of the masonry wall, the structure is governed by a clear unidirectional action. It also supports the modeling assumption that the analysis can focus on a characteristic strip composed of one course of masonry units and one FRP strip bonded on each side. The results of the numerical model are in good agreement with the experimental ones. The FE model well captures the magnitude of the strains and their temporal variation. The increased weight given by the model to the excitation of the higher frequency decays with the increase of the damping ratio (see the dotted lines).

Another interesting aspect is the variation of the strain state from the masonry unit region to the joint region. This aspect is governed by the stress transfer through the adhesive layer. In order to examine this effect, the strains at the outer face of the FRP strip at a point located 30 mm above the upper mortar-block interface of the mid-height joint are plotted in Figure 5c. A zoom plot appears in Figure 5d. The comparison of these results with the ones obtained for the same FRP strip but at the middle of the joint (Figure 5a-b) reveals the amplification of the strains in the joint region. As the joints represent the weaker, more compliant, and more brittle component of the masonry construction, the amplification is an outcome of the transfer of loads from the masonry units to the FRP strips. This is achieved by means shear and out-of-plane normal stresses in the adhesive layers. The comparison between the numerical and the experimental results reveals a good agreement both at the joint region (Figure 5a-b), and at the block region (Figure 5c-d). Although to a slightly smaller extent, the model also captures the reduction in strain (negative ones, mainly) away from the joint.

**3.2.** ***Complementary numerical results: higher level of vertical loading.*** The spatial and temporal distributions of the shear stresses in the adhesive layers appear in Figure 6a and 6b, respectively. The results are presented based on the analysis of the refined symmetric model. The distributions along the upper half of the wall (Figure 6a) reveal the localized peaks near the mortar joints and near the edge of the FRP system. These peaks are affected by the dynamic out-of-plane response, the initial compressive loading, the evolution of the compressive force in the wall, and the nonlinear behavior of the mortar material. Figure 6a indicates that in the present case, the stresses near the edges of the strip attain the largest values.

The variation in time of the peak shear stresses near the edge ($x = 205$ mm) and near the middle joint ($x = 1047.5$ mm) (points I–IV in Figure 6a) is studied in Figure 6b. The results reveal two different types of temporal behavior. The stresses near the edge are mostly affected by the global out-of-plane response as well as by the relatively high frequency response attributed by the numerical model to the axial compressive force (the thrust force). On the other hand, the temporal variation of the shear stresses near the inner joint (Figure 6b,III–IV) reveals that the base level of stresses due to the compressive loading is monotonically amplified at the initial stages of the dynamic response. The amplified level of

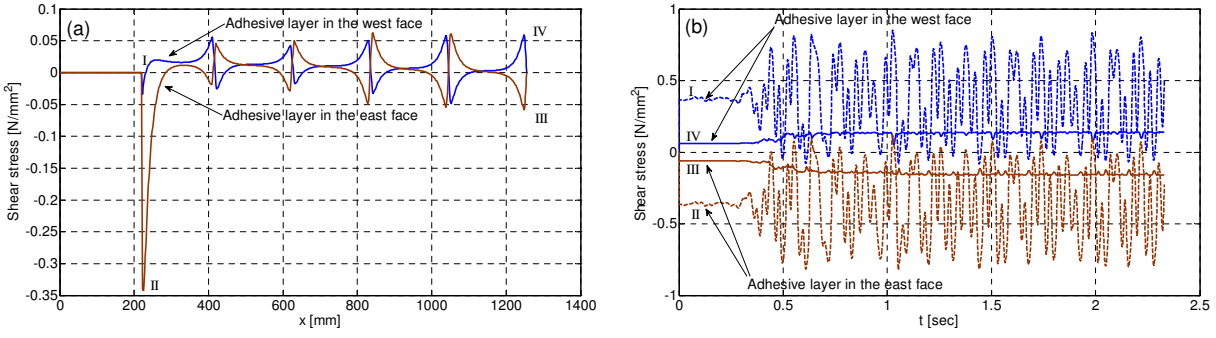


**Figure 6.** Spatial and temporal distributions of shear stresses in the adhesive layers. (a) distributions along the wall at $t = 1.56$ sec; (b) shear stresses at near the edge ($x = 205.0$ mm) and near the mid-height joint ($x = 1047.5$ mm) versus time. Legend: —— stresses at $x = 205$ mm; $- - -$ stresses at $x = 1047.5$ mm.

stress is less affected by the cyclic response revealing only a limited level of oscillations. This effect is attributed to the inelastic behavior of the mortar material and to the evolution of residual compressive strains in the mortar. Due to the inelastic behavior, the initiation of the dynamic load is associated with accumulation of compressive strains. As these compressive strains are inelastic by nature, they are not "released" during motion. Their evolution triggers the amplification of the shear stress at the first stages of the response. Later on, the steep unloading-reloading branch of the constitutive behavior of the mortar material dictates the high frequency oscillations and the pattern observed in Figure 6b.

The spatial and temporal variations of the out-of-plane normal stresses at the interfaces of the adhesive layer are studied in Figure 7. The spatial distributions reveal that in accordance with the shear stress concentration, the highest level of stresses is observed near the edge of the FRP strip. The temporal distributions reveal a notable oscillatory response that starts with the dynamic load. They also reveal that in both adhesive layers, the adhesive-masonry interface is mostly subjected to compressive normal stresses whereas the adhesive-FRP interface in mostly subjected to tension. The compressive stresses are amplified form a level of about 1.5 MPa under the vertical load to about 3.75 MPa under the dynamic excitation. The tensile stresses are also amplified by a similar ratio from about 0.5 MPa to about 1.35 MPa. These peeling stresses may trigger or accelerate a debonding failure. Furthermore, at certain points during the dynamic response, the compressive stresses that initially evolve at the critical adhesive-masonry

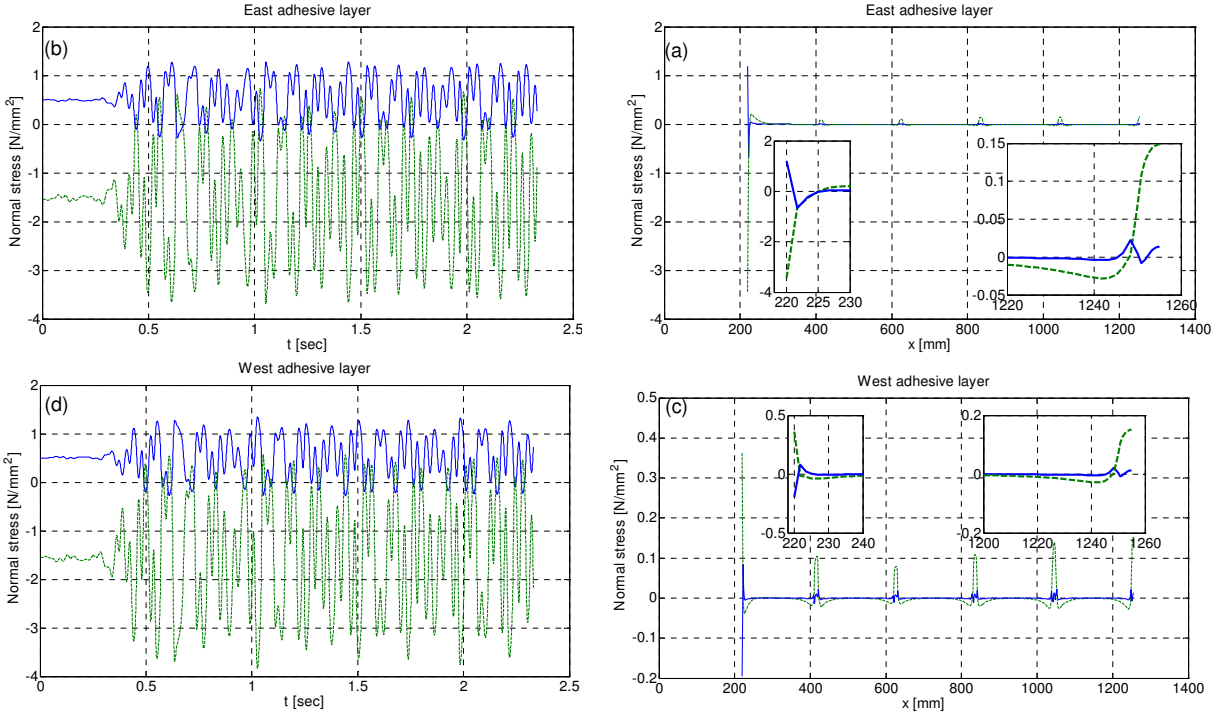


**Figure 7.** Spatial and temporal distributions of normal out-of-plane (peeling) stresses at the interface of the adhesive layers. (a) east layer, $t = 1.56$ sec; (b) east layer, $x = 1052.5$ mm; (c) west layer, $t = 1.56$ sec; (d) west layer, $x = 1052.5$ mm. Legend: —— adhesive FRP interface; − − − adhesive-masonry interface.

interface turn into tensile stresses (see for example Figure 7c). At other points, both adhesive-masonry interfaces may be subjected to tension. These interfaces are usually brittle and governed by the limited ability of the masonry substrate to resist tensile stresses. Therefore, this unique condition, which evolves under the dynamic loading, may accelerate the evolution of dynamic debonding failure and may endanger the resilience of the strengthening system.

**3.3.** ***Test and analysis results: lower level of vertical loading.*** In this section, the results of a similar test conducted with a reduced level of vertical loading are studied. For comparison, the results for the wall before strengthening, which are discussed in detail in [Rabinovitch and Madah 2011], are also presented. It should be noted that in order to prevent total collapse, testing of the unstrengthened was terminated by shutting down the high power component of the hydraulic system after about 1.6 seconds. The results of both experiments are therefore presented for this limited period only. The out-of-plane accelerations and displacements in the strengthened and the original walls appear in Figure 8a-b. The temporal variations of the axial reaction at the top of the wall and the crack opening at the middle joint appear in Figure 8c-d.

The comparison between the original and the strengthened wall reveal significant differences and clearly point at the impact of the strengthening system. The response of the original wall is governed by

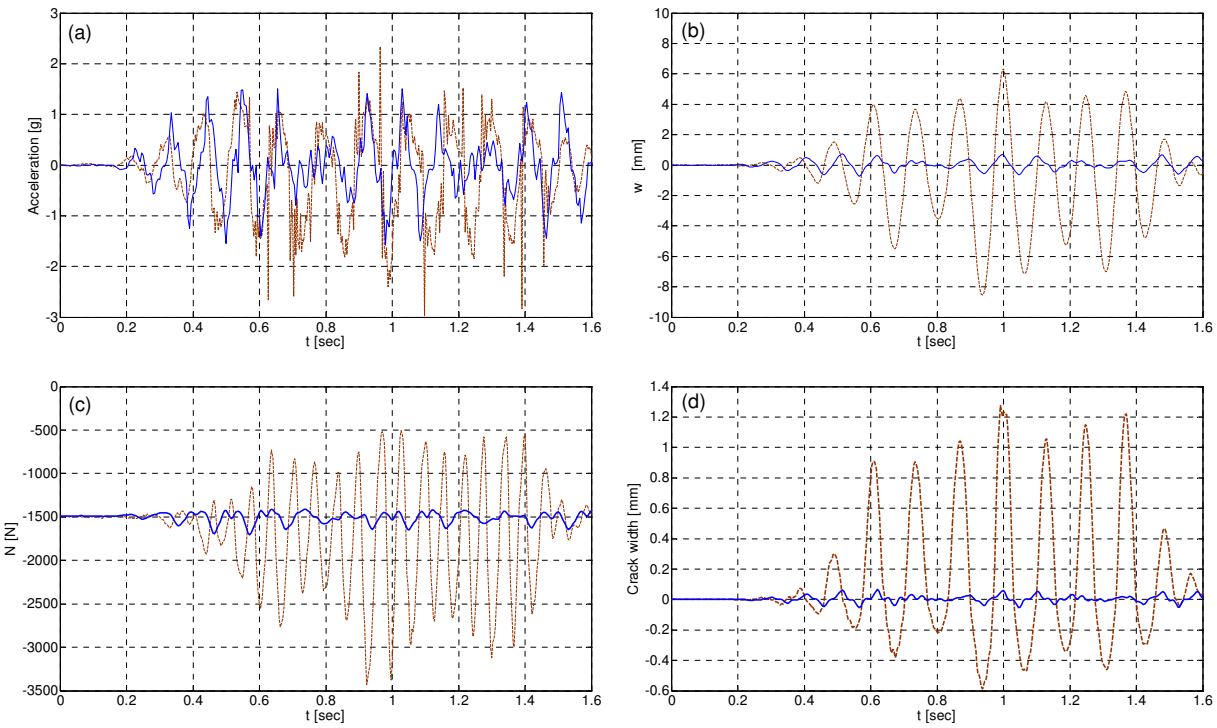


**Figure 8.** Dynamic response of strengthened and unstrengthened (original) walls under low level of vertical load and base excitation. (a) out-of-plane accelerations at mid-height; (b) out-of-plane displacements at mid-height; (c) axial reaction; (d) crack opening at mid-height. Legend: —— strengthened wall; – – – unstrengthened wall. The results for the unstrengthened wall are adapted from [Rabinovitch and Madah 2011].

much larger out-of-plane displacement, extensive cracking at midspan, extensive rocking and variation of the axial compressive force in time, and possible relaxation of the rotational constraint at the top of the wall (see [Rabinovitch and Madah 2011] for more details). None of the above effects is observed in the response of the strengthened wall. The levels of out-of-plane displacements and crack opening observed in the strengthened wall are significantly smaller. The temporal variation of the thrust force, which is a direct outcome of the crack opening, the rocking, and the arching effects, is also notably smaller in the strengthened wall. These observations indicate that the strengthening system effectively and meaningfully changes the nature of the dynamic response of the masonry wall and significantly improves its ability to resist out-of-plane dynamic loads.

## 4. Summary and conclusions

The dynamic behavior of unidirectional strengthened masonry walls has been experimentally and numerically studied. This part of the paper has focused on shake-table testing of full-scale unidirectional FRP strengthened masonry wall subjected to different levels of axial loading and out-of-plane dynamic excitation. The results have revealed various aspects of the dynamic response including the global out-of-plane displacements and accelerations, the variation of the thrust force, and the variation of strains in the externally bonded reinforcement. It has also clearly showed that the application of the FRP reinforcement effectively changes the dynamic behavior of the masonry wall and drastically improves its ability to withstand significant out-of-plane dynamic loads.

The experimental results have also been used as reference for the examination of numerical results obtained using the finite element model developed in part I of this paper [Rabinovitch and Madah 2012]. The comparison in terms of out-of-plane displacements, in-plane displacements across the mid-height joint, and the strains at the outer face of the FRP layer have revealed good agreement and have provided some support and validation to the numerical model. On the other hand, the comparison has revealed that the model tends to overestimate the role of the natural frequency of the wall and to underestimates the effect of damping. This designates the incorporation of a refined and less general model for damping as a needed direction of further enhancement of the model.

Along with the experimental results and the comparison with the numerical ones, additional results in term of the stresses in the adhesive layer, their variation along the wall and from one interface to another, and their variation in time have been presented. This class of results, which cannot be directly deduced from experimental dynamic measurements, has thrown some light on the stress transfer between the wall and the supplemental layer and on the effect of the dynamic response on this mechanism. In particular, it has revealed the effect of the dynamic loading and the inelastic response of the mortar material on the evolution of interfacial shear and peeling stresses near the joints. These aspects may play a critical role in the potential initiation of dynamic debonding failures.

The experimental and numerical results have revealed and demonstrated the potential of the FRP bonding as an effective method for the dynamic upgrade of masonry walls. The ability of the strengthening system to significantly modify the dynamic response of the wall, to provide it with a load resisting mechanism, and to prevent its collapse under out-of-plane loads are critical steps towards the structural upgrade of masonry elements to resist dynamic loads. The ability of the numerical model to assess these effects is also an important step towards achieving this goal.

## References


[Al-Chaar and Hasan 2002] G. K. Al-Chaar and H. A. Hasan, "Dynamic response and seismic testing of CMU walls rehabilitated with composite material applied to only one side", *Proc. Inst. Civ. Eng. Struct. Build.* **152**:2 (2002), 135–146.

[Albert et al. 2001] M. L. Albert, A. E. Elwi, and J. J. R. Cheng, "Strengthening of unreinforced masonry walls using FRPs", *J. Compos. Constr.* (*ASCE*) **5**:2 (2001), 76–84.

[Almusallam and Al-Salloum 2007] T. H. Almusallam and Y. A. Al-Salloum, "Behavior of FRP strengthened infill walls under in-plane seismic loading", *J. Compos. Constr.* (*ASCE*) **11**:3 (2007), 308–318.

[Altin et al. 2008] S. Altin, O. Anil, M. E. Kara, and M. Kaya, "An experimental study on strengthening of masonry infilled RC frames using diagonal CFRP strips", *Compos. B Eng.* **39**:4 (2008), 680–693.

[Carpinteri and Pugno 2005] A. Carpinteri and N. Pugno, "Towards chaos in vibrating damaged structures, I: Theory and period doubling cascade", *J. Appl. Mech.* (*ASME*) **72**:4 (2005), 511–518.

[Davidson et al. 2005] J. S. Davidson, J. W. Fisher, M. I. Hammons, J. R. Porter, and R. J. Dinan, "Failure mechanisms of polymer-reinforced concrete masonry walls subjected to blast", *J. Struct. Eng.* (*ASCE*) **131**:8 (2005), 1194–1205.

[El-Dakhakhni et al. 2004] W. W. El-Dakhakhni, A. A. Hamid, and M. Elgaaly, "Seismic retrofit of concrete-masonry-infilled steel frames with glass-reinforced fiber polymer laminates", *J. Struct. Eng.* (*ASCE*) **130**:9 (2004), 1343–1352.

[ElGawady et al. 2002] M. A. ElGawady, P. Lestuzzi, and M. Badoux, "Dynamic in-plane behavior of URM wall upgraded with composites", in *ICCI'02: Third International Conference on Composites in Infrastructure* (San Francisco, 2002), University of Arizona/Omnipress, Tucson, AZ, 2002.

[ElGawady et al. 2003] M. A. ElGawady, P. Lestuzzi, and M. Badoux, "In-plane lateral behavior of URM walls upgraded with composites", in *Response of structures to extreme loading: proceedings of XL-2003* (Toronto, 2003), Elsevier, Boston, 2003.

[Flanagan and Bennett 1999] R. D. Flanagan and R. M. Bennett, "Bidirectional behavior of structural clay tile infilled frames", *J. Struct. Eng.* (*ASCE*) **125**:3 (1999), 236–244.

[Gilstrap and Dolan 1998] J. M. Gilstrap and C. W. Dolan, "Out-of-plane bending of FRP-reinforced masonry walls", *Compos. Sci. Technol.* **58**:8 (1998), 1277–1284.

[Griffith et al. 2004] M. C. Griffith, N. T. K. Lam, J. L. Wilson, and K. Doherty, "Experimental investigation of unreinforced brick masonry walls in flexure", *J. Struct. Eng.* (*ASCE*) **130**:3 (2004), 423–432.

[Hamed and Rabinovitch 2010a] E. Hamed and O. Rabinovitch, "Failure characteristics of FRP-strengthened masonry walls under out-of-plane loads", *Eng. Struct.* **32**:8 (2010), 2134–2145.

[Hamed and Rabinovitch 2010b] E. Hamed and O. Rabinovitch, "Lateral out-of-plane strengthening of masonry walls with composite materials", *J. Compos. Constr.* (*ASCE*) **14**:4 (2010), 376–387.

[Hamilton and Dolan 2001] H. R. Hamilton, III and C. W. Dolan, "Flexural capacity of glass FRP strengthened concrete masonry walls", *J. Compos. Constr.* (*ASCE*) **5**:3 (2001), 170–178.

[Meisl et al. 2007] C. S. Meisl, K. J. Elwood, and C. E. Ventura, "Shake table tests on the out-of-plane response of unreinforced masonry walls", *Can. J. Civ. Eng.* **34**:11 (2007), 1381–1392.

[Myers et al. 2004] J. J. Myers, A. Belarbi, and K. A. El-Domiaty, "Blast resistance of FRP retrofitted un-reinforced masonry (URM) walls with and without arching action", *Masonry Soc. J.* **22**:1 (2004), 9–26.

[Rabinovitch and Madah 2011] O. Rabinovitch and H. Madah, "Finite element modeling and shake-table testing of unidirectional infill masonry walls under out-of-plane dynamic loads", *Eng. Struct.* **33**:9 (2011), 2683–2696.

[Rabinovitch and Madah 2012] O. Rabinovitch and H. Madah, "Dynamics of FRP strengthened unidirectional masonry walls, I: A multi-layered finite element", *J. Mech. Mater. Struct.* **7** (2012), 1–28.

[Thompson and Stewart 1986] J. M. T. Thompson and H. B. Stewart, *Nonlinear dynamics and chaos: geometrical methods for engineers and scientists*, Wiley, Chichester, 1986.

[Turek et al. 2007] M. Turek, C. E. Ventura, and S. Kuan, "In-plane shake-table testing of GFRP-strengthened concrete masonry walls", *Earthq. Spectra* **23**:1 (2007), 223–237.

[Wu et al. 2005] C. Wu, H. Hao, and Y. Lu, "Dynamic response and damage analysis of masonry structures and masonry infilled RC frames to blast ground motion", *Eng. Struct.* **27**:3 (2005), 323–333.

Received 29 Aug 2010. Revised 9 Feb 2011. Accepted 10 Feb 2011.

ODED RABINOVITCH: cvoded@tx.technion.ac.il
*Faculty of Civil and Environmental Engineering, Technion – Israel Institute of Technology, Haifa, 32000, Israel*

HAZEM MADAH: hazem@tx.technion.ac.il
*Faculty of Civil and Environmental Engineering, Technion – Israel Institute of Technology, Haifa, 32000, Israel*

JOURNAL OF MECHANICS OF MATERIALS AND STRUCTURES
Vol. 7, No. 1, 2012

msp

# PERIDYNAMIC ANALYSIS OF FIBER-REINFORCED COMPOSITE MATERIALS

ERKAN OTERKUS AND ERDOGAN MADENCI

Damage growth in composites involves complex and progressive failure modes. Current computational tools are incapable of predicting failure in composite materials mainly due to their mathematical structure. However, peridynamic theory removes these obstacles by taking into account nonlocal interactions between material points. This study presents an application of peridynamic theory to predict how damage propagates in fiber-reinforced composite materials subjected to mechanical and thermal loading conditions.

## 1. Introduction

Damage initiation and its subsequent propagation in fiber-reinforced composites are not understood as clearly as they are, for example, for metals because of the presence of stiff fibers embedded into the soft matrix material, causing inhomogeneity. Under the assumption of homogeneity, a lamina has orthotropic elastic properties. Even though this assumption is suitable for stress analysis, it becomes questionable when predicting failure. Most composite structures include notches and cutouts, not only reducing the strength of the composites but also serving as potential failure sites for damage initiation. They also promote common failure modes of delamination, matrix cracking, and fiber breakage. These failure modes are inherent to the inhomogeneous nature of the composite, thus the homogeneous material assumption taints failure analyses.

In order to better understand failure mechanisms, Hallett and Wisnom [2006] conducted experiments on double-edge-notched composite specimens made from E-glass. They reported the occurrence of matrix cracking before ultimate failure for all specimens, representing four different layups when loaded in tension. Furthermore, it was reported that fiber failure initiated at the notch tip. Later, Green et al. [2007] investigated the effect of scaling on the tensile strength of notched composites made from unidirectional carbon-fiber/epoxy pre-preg by considering the hole diameter and laminate thickness as independent variables. These experiments showed that failure mechanisms in composites are very complex due to matrix cracking, fiber breakage, and delamination.

In order to investigate the behavior of cracks, Wu [1968] considered unidirectional fiberglass-reinforced Scotch-plies with center cracks oriented in the direction of the fibers. The plies had fibers in the 0° and 45° directions and were loaded in tension, pure shear, and combined tension and shear. In all three types of loading, it was observed that the crack propagated in a direction colinear with the initial crack.

It is, therefore, evident that the inhomogeneous nature of the composites must be retained in the analysis to predict the correct failure modes. Each lamina with a different fiber orientation must be modeled with distinct matrix and fiber properties.

*Keywords:* peridynamics, damage, nonlocal, composite.

Numerical studies on the failure of notched composites have mostly utilized the finite element method (FEM) to investigate the damage path and the initial failure load; such recent studies include [Bogert et al. 2006; Satyanarayana et al. 2007]. They predicted fiber and matrix damage in center-notched laminates for different layups under tension. Both the experimental observations and numerical results suggest that damage initiation and crack propagation are dependent on ply orientation.

Despite the development of many important concepts for predicting material behavior and failure, the prediction of failure modes and residual strengths of composite materials is a challenge within the framework of FEM. The use of FEM to predict failure can be quite challenging because remeshing may be required to make an accurate prediction and damage can only propagate in certain directions. Remeshing can be avoided by employing special elements, such as cohesive elements. However, these elements require a priori knowledge of the damage path, which might not be available. Unless these elements are correctly placed during model generation, the damage predictions may be erroneous. In addition to the need to remesh, existing methods for fracture modeling also suffer from the requirement of an external crack-growth criterion. This criterion prescribes how damage evolves a priori based on local conditions, and guides the analysis as to when and how damage initiates and propagates. Considering the difficulty in obtaining and generalizing experimental fracture data, providing such a criterion for damage growth, especially in composite structures, clearly presents a major obstacle to fracture modeling using conventional methods. This prevents such methods from being applicable to problems in which multiple damage growth occurs and interacts in complex patterns.

The difficulty in predicting failure using concepts from fracture mechanics in conjunction with FEM comes from the mathematical form of the classical continuum mechanics equations. The equations of motion in classical continuum mechanics are in the form of partial differential equations that involve the spatial displacement derivatives; however, these derivatives are undefined when the displacements are discontinuous, such as across cracks or interfaces. Hence, failure prediction is posterior and requires special techniques.

Silling [2000], realizing the aforementioned limitation, reintroduced a nonlocal theory that does not require spatial derivatives — the bond-based peridynamic (PD) theory. This theory accounts for only pairwise interaction between material points, thus resulting in the reduction of independent material constants. In order to remove this reduction, Silling et al. [2007] generalized bond-based PD theory by including the interaction of many material points. Referred to as state-based PD theory, it accounts for deviatoric and volumetric deformations, thus enforcing plastic incompressibility. The main difference between PD theory and classical continuum mechanics is that the former is formulated using integral equations as opposed to derivatives of the displacement components. This feature allows damage initiation and propagation at multiple sites with arbitrary paths inside the material without resorting to special crack-growth criteria. In PD theory, internal forces are expressed through nonlocal interactions between pairs of material points within a continuous body, and damage is a part of the constitutive model. Interfaces between dissimilar materials have their own properties, and damage can propagate when and where it is energetically favorable for it to do so.

PD theory was applied successfully in [Colavito et al. 2007a; 2007b] to predict damage in laminated composites subjected to low-velocity impact and static indentation. Askari et al. [2006] and Xu et al. [2007; 2008] also used PD simulations to predict damage in laminates subjected to low-velocity impact and in notched laminated composites under biaxial loads. Recently, Kilic et al. [2009] predicted the

basic failure modes of fiber, matrix, and delamination in various laminates with a preexisting central crack under tension. Also, Oterkus et al. [2010] demonstrated that PD analysis is capable of capturing bearing and shear-out failure modes in bolted composite lap-joints.

This study presents an application of PD theory in the analysis of fiber-reinforced composite materials subjected to mechanical and thermal loading conditions. The PD approach to modeling a lamina is first verified against analytical solutions within the realm of classical continuum mechanics by considering uniaxial tension and uniform temperature change. Then, damage growth patterns from a preexisting crack in a lamina for different fiber orientations are computed and compared with experimental observations. This approach is further extended to analyze composite laminates and to predict damage growth patterns from a preexisting crack in two distinct laminate constructions under tension. In the absence of a crack, the PD displacement predictions are compared with those of the classical laminate theory. In the presence of a crack, damage patterns are qualitative compared with experimental observations.

## 2. Peridynamic theory

The deformation response of solid structures subjected to external forces can be obtained by assuming the structure as a continuous body or a continuum, without paying attention to its atomistic structure. Hence, it is possible to perform both static and dynamic analyses of large structures within a reasonable amount of time. The conventional approach that is used to analyze solid structures is known as "classical continuum mechanics" and has been successfully applied to numerous problems in the past. Within the classical continuum mechanics framework, it is assumed that the continuous body is composed of an infinite number of infinitesimal volumes, which are called material points. These material points interact with each other only if they are within the nearest neighborhood of each other; in other words, through a direct interaction (contact). These interactions are expressed in terms of contact forces or tractions, $\boldsymbol{T}$, as shown in Figure 1.

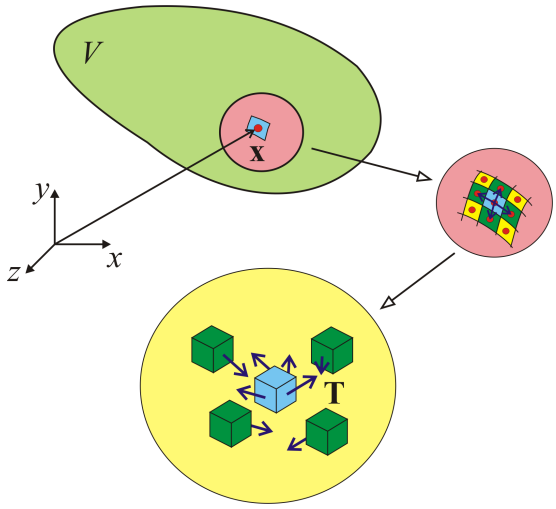


**Figure 1.** Interaction of material points in classical continuum mechanics.

Using the conservation of linear momentum and relating the traction vectors, $\boldsymbol{T}$, to the well-known stress tensor, $\boldsymbol{\sigma}$, results in the equation of motion of the material point, $\boldsymbol{x}$, in classical continuum mechanics:

$$\rho(\boldsymbol{x})\ddot{\boldsymbol{u}}(\boldsymbol{x},t) = \nabla\cdot\boldsymbol{\sigma} + \boldsymbol{b}(\boldsymbol{x},t), \tag{1}$$

where $\rho(\boldsymbol{x})$, $\boldsymbol{b}(\boldsymbol{x},t)$, and $\ddot{\boldsymbol{u}}(\boldsymbol{x},t)$ represent the mass density, body force density, and acceleration, respectively, of the material point located at $\boldsymbol{x}$. The spatial derivatives in the divergence operation associated with the stress tensor, $\boldsymbol{\sigma}$, do not exist on the discontinuity in the structure. Therefore, (1) is not valid for problems including discontinuities, such as cracks. Silling [2000] replaced the divergence term in (1) with an integral term, which makes the new form of the equation of motion applicable whether or not a discontinuity exists in the structure:

$$\rho(\boldsymbol{x})\ddot{\boldsymbol{u}}(\boldsymbol{x},t) = \int_H \boldsymbol{f}(\boldsymbol{x}'-\boldsymbol{x},\boldsymbol{u}'-\boldsymbol{u})\,dH + \boldsymbol{b}(\boldsymbol{x},t). \tag{2}$$

In (2), the domain of integration (neighborhood), $H$, includes all the material points that the material point $\boldsymbol{x}$ can interact with inside the body. The radius of the spherical neighborhood is referred to as the horizon, and it is denoted by $\delta$. The interaction force or PD force between material points $\boldsymbol{x}$ and $\boldsymbol{x}'$ can be expressed as $\boldsymbol{f}(\boldsymbol{x}'-\boldsymbol{x},\boldsymbol{u}'-\boldsymbol{u})$, and it is a function of the relative position vector, $\boldsymbol{x}'-\boldsymbol{x}$, and relative displacement vector, $\boldsymbol{u}'-\boldsymbol{u}$. The PD force is along the same direction of the relative position of these material points in the deformed configuration, that is, $\boldsymbol{y}'-\boldsymbol{y} = (\boldsymbol{x}'+\boldsymbol{u}')-(\boldsymbol{x}+\boldsymbol{u})$. For an elastic isotropic material, the PD force takes the form

$$\boldsymbol{f} = c(s-s^*)\frac{\boldsymbol{y}'-\boldsymbol{y}}{|\boldsymbol{y}'-\boldsymbol{y}|} = c\bar{s}\frac{\boldsymbol{y}'-\boldsymbol{y}}{|\boldsymbol{y}'-\boldsymbol{y}|}, \tag{3}$$

where $c$, $s$, $\bar{s}$ and $s^*$ represent the PD material parameter, total stretch, mechanical stretch, and thermal stretch between material points $\boldsymbol{x}$ and $\boldsymbol{x}'$, respectively. The total stretch, $s$, and the thermal stretch due to thermal loading, $s^*$, are defined as

$$s = \frac{|\boldsymbol{y}'-\boldsymbol{y}| - |\boldsymbol{x}'-\boldsymbol{x}|}{|\boldsymbol{x}'-\boldsymbol{x}|} \tag{4a}$$

and

$$s^* = \alpha\Delta T, \tag{4b}$$

where $\alpha$ and $\Delta T$ represent the coefficient of thermal expansion of the material and the temperature change, respectively. By using (4a) and (4b), the mechanical stretch, $\bar{s}$, can be computed as

$$\bar{s} = s - s^* = \frac{|\boldsymbol{y}'-\boldsymbol{y}| - |\boldsymbol{x}'-\boldsymbol{x}|}{|\boldsymbol{x}'-\boldsymbol{x}|} - \alpha\Delta T. \tag{5}$$

This form of the PD force representation, given in (3), accounts for pairwise interaction only between the material points. Therefore, it is limited to one independent material constant, $c$, with a Poisson's ratio of $\frac{1}{4}$ and $\frac{1}{3}$ in three- and two-dimensional analysis, respectively. This material parameter, $c$, can be related to the engineering material constants by equating the strain energy densities of the PD and

classical continuum theories at a material point inside a body due to simple loading, such as uniform expansion. Silling and Askari [2005] derived an explicit expression for parameter $c$ in the form

$$c = \frac{18\kappa}{\pi\delta^4}, \tag{6}$$

where $\kappa$ is the bulk modulus of the material and $\delta$ represents the radius of a spherical horizon.

Based on PD theory, the strain energy density of a material point at $\boldsymbol{x}$, $U_{\mathrm{PD}}$, can be expressed as

$$U_{\mathrm{PD}} = \frac{1}{2}\int_H w\, dH, \tag{7}$$

where the micropotential, $w$, is defined as

$$w = \tfrac{1}{2}c(s - s^*)^2\xi = \tfrac{1}{2}c\bar{s}^2\xi, \tag{8a}$$

with

$$\xi = |\boldsymbol{x}' - \boldsymbol{x}|. \tag{8b}$$

It can also be assumed that two material points, $\boldsymbol{x}$ and $\boldsymbol{x}'$, cease to interact with each other if the mechanical stretch between these material points exceeds a critical stretch value, $s_0$, as shown in Figure 2. This material model represents an elastic material behavior without allowing any permanent deformation.

Termination of the interaction between material points can be associated with the failure of the material by modifying the PD force relation given in (3) by introducing the failure parameter $\mu(\boldsymbol{x}' - \boldsymbol{x}, t)$

$$\boldsymbol{f} = \mu(\boldsymbol{x}' - \boldsymbol{x}, t)c(s - s^*)\frac{\boldsymbol{y}' - \boldsymbol{y}}{|\boldsymbol{y}' - \boldsymbol{y}|}, \tag{9}$$

where the failure parameter can be defined as

$$\mu(\boldsymbol{x}' - \boldsymbol{x}, t) = \begin{cases} 1 & \text{if } s(\boldsymbol{x}' - \boldsymbol{x}, t') - s^* < s_0 \text{ for all } 0 < t' < t, \\ 0 & \text{otherwise.} \end{cases} \tag{10}$$

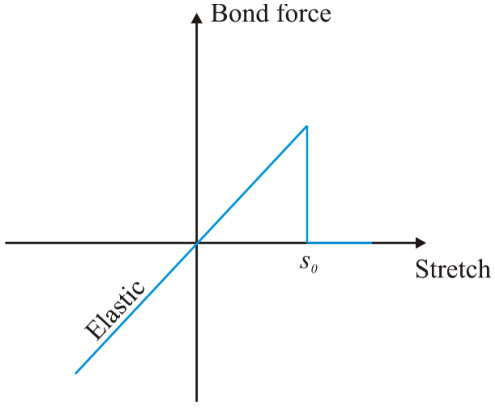


**Figure 2.** Constitutive relation between material points in an elastic material.

The inexplicit nature of local damage at a material point, $\boldsymbol{x}$, arising from the introduction of failure in the constitutive model, is removed by defining the local damage as

$$\varphi(\boldsymbol{x}, t) = 1 - \frac{\int_H \mu(\boldsymbol{x}' - \boldsymbol{x}, t)\, dH}{\int_H dH}. \tag{11}$$

Thus, local damage is the weighted ratio of the number of the broken interactions to the total number of interactions within the horizon, $H$. The extent of damage is defined by a value between 0 and 1, where 0 indicates that a material point has no damage and 1 indicates complete damage at the material point. Also, a damage value of 0.5 and above indicates possible cracking.

In the case of isotropic materials, value $s_0$ of the critical stretch can be related to the equivalent energy release rate as derived in [Silling and Askari 2005]:

$$s_0 = \sqrt{\frac{5G_0}{9\kappa\delta}}, \tag{12}$$

where $G_0$ is the critical energy release rate of the material and can be related to the fracture toughness of the material.

In order to solve (2), a collocation method is adopted and the numerical treatment involves the discretization of the domain of interest into subdomains. The domain can be discretized into cubic subdomains. With this discretization, the volume integration in (2) is approximated, leading to

$$\rho(\boldsymbol{x}_{(i)})\ddot{\boldsymbol{u}}(\boldsymbol{x}_{(i)}, t) = \sum_{j=1}^{M} \boldsymbol{f}\big(\boldsymbol{u}(\boldsymbol{x}_{(j)}, t) - \boldsymbol{u}(\boldsymbol{x}_{(i)}, t), \boldsymbol{x}_{(j)} - \boldsymbol{x}_{(i)}\big) V_{(j)} + b(\boldsymbol{x}_{(i)}, t), \tag{13}$$

where $\boldsymbol{x}_{(i)}$ is the position vector located at the $i$-th collocation (material) point and $M$ is the number of subdomains within the horizon of the $i$-th material point. The position vector $\boldsymbol{x}_{(j)}$ represents the location of the $j$-th collocation point. The volume of the $j$-th subdomain is $V_{(j)}$.

Since peridynamics is a nonlocal theory and its equations of motion utilize integrodifferential equations as opposed to partial differential equations in the case of the classical continuum theory, the application of boundary conditions is different from that of the classical continuum theory. The tractions or point forces cannot be applied as boundary conditions since their volume integrations result in a zero value [Oterkus and Madenci 2012]. Therefore, the boundary conditions are applied over the volumes as body forces, displacements, and velocities. As explained in [Macek and Silling 2007], the thickness of the region over which the boundary conditions are applied should be comparable to the size of the horizon.

## 3. Peridynamic analysis of a lamina

If a fiber-reinforced composite lamina is considered, the directional dependency must be included in the PD analysis. Therefore, two different PD material parameters are introduced as shown in Figure 3 to model a fiber-reinforced composite lamina with a fiber orientation of $\theta$. The material point $q$ represents material points that interact with material point $i$ only along the fiber direction. However, the material point $p$ represents material points that interact with material point $i$ in any direction, including the fiber

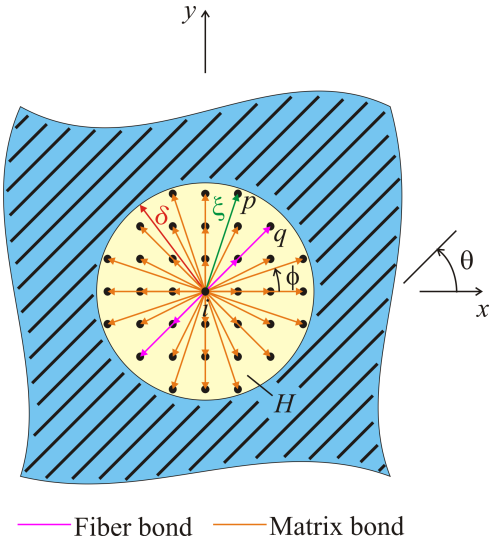


**Figure 3.** PD horizon for a lamina with a fiber orientation of $\theta$ and PD bonds between material point $i$ and other material points within its horizon.

direction. The orientation of a PD bond between the material point $i$ and the material point $p$ is defined by the angle $\phi$ with respect to the $x$-axis.

Associated with a lamina, the material parameter concerning the interaction of material points only in the fiber direction is denoted by $c_f$. The interaction of material points in all other directions within a lamina is governed by the material parameter, $c_m$. Extending the procedure introduced in [Gerstle et al. 2005] for isotropic materials, the PD material parameters, $c_f$ and $c_m$, can be expressed analytically in terms of the engineering material constants, $E_1$, $E_2$, $G_{12}$, and $\nu_{12}$, by equating strain energy densities of a material point based on the classical continuum mechanics and PD theory for simple loading conditions.

The constitutive or force-stretch relations for the in-plane interactions of two material points, referred to as fiber and matrix bonds, are shown in Figure 4. The critical parameters that define the failure of these

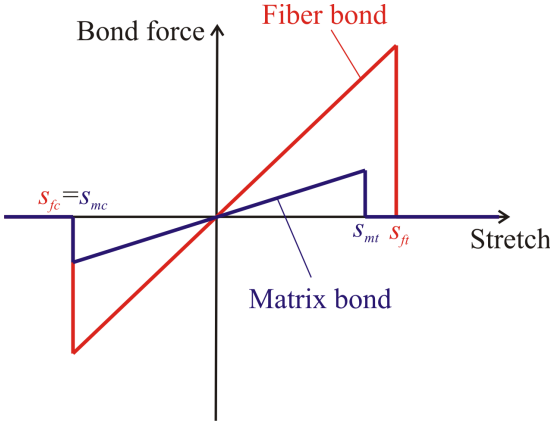


**Figure 4.** Force-stretch relation for fiber and matrix bonds.

bonds under tension and compressions are $(s_{\text{ft}}, s_{\text{mt}})$ and $(s_{\text{fc}}, s_{\text{mc}})$, respectively, and can be determined based on the experimental measurements. Determination of these critical stretch parameters are explained in Oterkus et al. [2012].

Based on the classical continuum mechanics, the strain energy density of a material point, $U_{\text{CCM}}$, for a two-dimensional composite lamina is expressed as

$$U_{\text{CCM}} = \tfrac{1}{2}\boldsymbol{\sigma}^T(\boldsymbol{\epsilon} - \boldsymbol{\epsilon}^*), \tag{14}$$

in which the stress, $\boldsymbol{\sigma}$, total strain, $\boldsymbol{\epsilon}$, and thermal strain vectors, $\boldsymbol{\epsilon}^*$, are defined as

$$\boldsymbol{\sigma}^T = \left\{\sigma_{xx} \;\; \sigma_{yy} \;\; \tau_{xy}\right\}, \qquad \boldsymbol{\epsilon}^T = \left\{\epsilon_{xx} \;\; \epsilon_{yy} \;\; \gamma_{xy}\right\}, \qquad \boldsymbol{\epsilon}^{*T} = \left\{\epsilon^*_{xx} \;\; \epsilon^*_{yy} \;\; \gamma_{xy}\right\}. \tag{15}$$

For a composite lamina with a fiber orientation of $\theta$, the stress and strain components are related through the constitutive relation as

$$\boldsymbol{\sigma} = \overline{\boldsymbol{Q}}(\boldsymbol{\epsilon} - \boldsymbol{\epsilon}^*), \tag{16}$$

where the transformed reduced stiffness matrix $\overline{\boldsymbol{Q}}$ is defined as

$$\overline{\boldsymbol{Q}} = \begin{bmatrix} \overline{Q}_{11} & \overline{Q}_{12} & \overline{Q}_{16} \\ \overline{Q}_{12} & \overline{Q}_{22} & \overline{Q}_{26} \\ \overline{Q}_{16} & \overline{Q}_{26} & \overline{Q}_{66} \end{bmatrix}. \tag{17}$$

The transformed reduced stiffness matrix, $\overline{\boldsymbol{Q}}$ is a function of four independent material constants of elastic modulus in the fiber direction, $E_1$, elastic modulus in the transverse direction, $E_2$, in-plane shear modulus, $G_{12}$, and in-plane Poisson's ratio, $\nu_{12}$. The explicit expressions for the components of $\overline{\boldsymbol{Q}}$ can be found in any textbook on mechanics of composite materials — for example, [Kaw 2006]. The thermal expansion coefficients in the fiber and transverse directions are specified as $\alpha_1$ and $\alpha_2$, respectively.

Alternatively, the strain energy density of the same material point in PD theory, $U_{\text{PD}}$, can be calculated using (7). However, the material parameter, $c$ has a directional dependency of the form

$$c = \begin{cases} c_f + c_m & \text{for } \phi = \theta, \\ c_m & \text{for } \phi \neq \theta. \end{cases} \tag{18}$$

Therefore, (8a) for the micropotential should be modified as

$$w = \tfrac{1}{2}c(\phi)\bar{s}^2(\phi)\xi(\phi), \tag{19}$$

in which $\phi$ represents the bond angle. With this representation, the integration in (7) for the strain energy density of material point $i$ shown in Figure 3 cannot be fully performed analytically. However, it can be approximated as

$$U_{\text{PD}} = \frac{1}{2}\sum_{q=1}^{Q}\frac{c_f s_{qi}^2 \xi_{qi}}{2}V_q + \frac{1}{2}\int_H \frac{c_m s^2 \xi}{2}\,dH, \tag{20}$$

in which $Q$ is the number of fiber bonds within its horizon, $\delta$. As apparent in this equation, the fiber bond constant, $c_f$ depends on the discretization, whereas the matrix bond constant, $c_m$, does not because it does not have a directional property unlike the fibers. The initial length of the bond in the fiber direction and its stretch after deformation between material points $q$ and $i$ are denoted by $\xi_{qi}$ and $s_{qi}$, respectively.

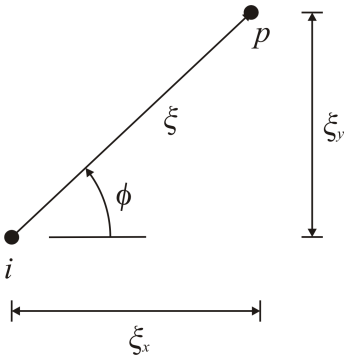


**Figure 5.** Components of the initial bond length between material points $i$ and $p$.

The volume of the material point $q$ that interacts with material point $i$ is denoted by $V_q$, which can be approximated as

$$V_q = \frac{\pi t \delta^2}{N}, \tag{21}$$

in which $N$ is the number of material points within its horizon, $\delta$, and $t$ is the thickness of the lamina.

The initial length and stretch of the bond between the material points $i$ and $p$ are referenced to a polar coordinate system $(\xi, \phi)$. As shown in Figure 5, the components of the initial bond length, $\xi$, in the $x$- and $y$-directions are denoted by $\xi_x$ and $\xi_y$, respectively, and are given by

$$\xi_x = \xi \cos\phi, \qquad \xi_y = \xi \sin\phi. \tag{22}$$

The PD strain energy density of a material point $i$, given in (20), can be expressed in terms of bond constants $c_f$ and $c_m$, representing the fiber and matrix, by identifying the direction of the bond

$$U_{\mathrm{PD}} = \beta_f c_f + \beta_m c_m. \tag{23}$$

The coefficients $\beta_f$ and $\beta_m$ in (23) can be determined by computing the stretch, $s_{pi}$, and the initial length, $\xi_{pi}$, of the bond between the material points $i$ and $p$, and the volume of material point $p$, $V_p$.

In order to determine the bond constants $c_f$ and $c_m$ in terms of the engineering constants $E_1$, $E_2$, $G_{12}$, and $\nu_{12}$, a uniaxial loading condition can be considered as explained in Appendix A. Equating the strain energy densities from PD theory and classical continuum mechanics for this loading condition results in explicit expressions for $c_f$ and $c_m$,

$$c_f = \frac{2E_1(E_1 - E_2)}{(E_1 - \frac{1}{9}E_2)\sum_{q=1}^{Q} \xi_{qi} V_q}, \qquad c_m = \frac{8E_1E_2}{(E_1 - \frac{1}{9}E_2)\pi t \delta^3}, \tag{24}$$

along with constraints on material constants $G_{12}$ and $\nu_{12}$,

$$G_{12} = \frac{\nu_{12}E_2}{1 - \nu_{21}\nu_{12}} = \frac{E_1E_2}{3(E_1 - \frac{1}{9}E_2)}, \qquad \nu_{12} = \frac{1}{3}. \tag{25}$$

As discussed in [Oterkus and Madenci 2012], because of the pairwise interaction of material points, four independent material constants of a lamina reduce to two independent constants. In the case of an isotropic material, the bond constant for fiber, $c_f$, given in $(24)_1$ becomes zero. This indicates that for

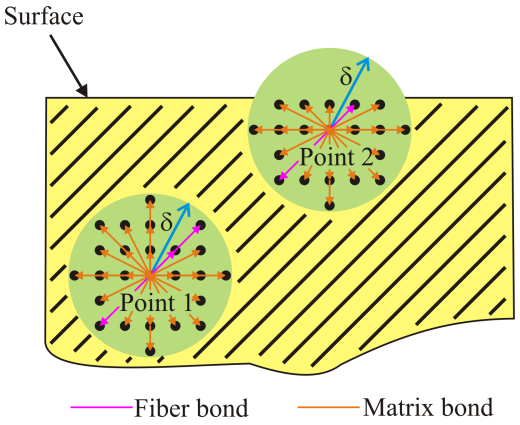


**Figure 6.** Surface effects in the domain of interest.

an isotropic material, the material should be described by using only one bond constant, $c_m$. In this case the expression for $c_m$ in $(24)_2$ recovers the expression for an isotropic material, that is, $c_m = 9E/\pi t\delta^3$, given in [Oterkus and Madenci 2012].

In the case of thermal loading, the stretch is obtained by (4b), and the coefficient of thermal expansion, $\alpha(\phi)$, for a lamina is also dependent on the bond orientation between material points $i$ and $p$. As derived in Appendix A, it can be expressed in terms of coefficients of thermal expansion for an angle lamina, $\alpha_x$, $\alpha_y$, and $\alpha_{xy}$, in the form

$$\alpha(\phi) = \alpha_x \cos^2\phi + \alpha_y \sin^2\phi + \alpha_{xy} \sin\phi \cos\phi. \tag{26}$$

**3.1.** ***Surface correction factors for a lamina.*** Surface correction is an important concept in PD theory. The response function given in (3) is derived under the assumption that the material point located at $\boldsymbol{x}$ is in a single material with its complete neighborhood entirely embedded within its horizon, $\delta$. However, this assumption becomes invalid when the material point is close to free surfaces (Figure 6). It results in a reduction in material stiffness near the free surfaces, and this stiffness reduction must be corrected. After determining the surface correction factor for each bond, the PD force in that bond is modified based on the associated surface correction factor. Determination of surface correction factors for isotropic materials is explained in detail by [Oterkus and Madenci 2012]. However, the determination of surface correction factors for a lamina is more complicated than that for an isotropic material because of two different PD bonds. Detailed derivations of the surface correction factors for fiber and matrix bonds are given in Appendix B.

## 4. Peridynamic analysis of a laminate

The PD formulation for a composite lamina can be extended to consider a composite laminate. In order to capture the deformation behavior of a laminate in the thickness direction and define the interaction between neighboring plies, two additional bond constants between neighboring plies are introduced, as shown in Figure 7.

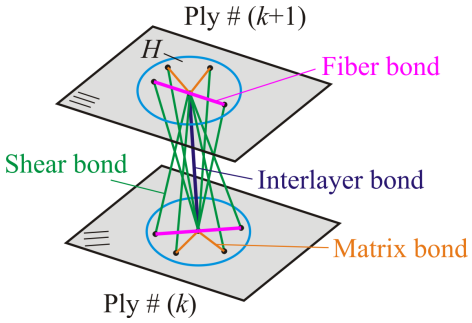


**Figure 7.** Four different bond constants for a fiber-reinforced composite material.

Similar to the approach implemented in the peridynamic code (Emu) developed in [Silling 2000], transverse normal and shear deformations between material points located on adjacent (neighboring) layers are related through the bond constants $c_{in}$ and $c_{is}$, respectively. As shown in Figure 7, interlayer bonds only exist in the normal direction, whereas shear bonds exist in all directions between the neighboring plies. Hence, a material point can interact with two other material points via interlayer bonds that have the same in-plane coordinates.

As in the case of in-plane deformation of a lamina, the interlayer and shear bond constants, $c_{in}$ and $c_{is}$, can be derived in the form

$$c_{in} = \frac{E_m}{t\overline{V}}, \qquad c_{is} = \frac{2G_m}{\pi t}\,\frac{1}{\delta^2 + t^2 \ln \dfrac{t^2}{\delta^2 + t^2}}, \tag{27}$$

where $E_m$ and $G_m$ are the elastic modulus and shear modulus of the matrix material, respectively, and $\overline{V}$ is the volume of a material point. Detailed derivations of these expressions are given in Appendix C.

Note that the shear bonds have a different characteristic than the fiber, matrix and interlayer bonds because the shear bond constant relates the body force density, $\boldsymbol{f}$, to the change in angle of the bond from its original orientation (shear angle), $\varphi$. Therefore, the force density and micropotential expressions for a shear bond can be written as

$$\boldsymbol{f} = c_s \varphi (\Delta x)^2 \frac{\boldsymbol{y}' - \boldsymbol{y}}{|\boldsymbol{y}' - \boldsymbol{y}|}, \qquad w = \tfrac{1}{2} c_s \varphi^2, \tag{28}$$

where $\Delta x$ is the spacing between material points on the in-plane of the lamina.

Failure of the interlayer and shear bonds corresponds to mode I and mode II, respectively. Interlayer damage represents the breakage of (interlayer) bonds between a layer and its adjacent layers above and below. Hence, it provides the extent of delamination between the adjacent layers. Therefore, the interlayer bonds are assumed to fail only in tension. The critical stretch value for the interlayer bonds, $s_{in}$, can be obtained analytically by equating the energy consumed by an advancing mode-I crack to the work required to break all interlayer bonds as

$$s_{in} = \sqrt{\frac{2G_{IC}}{tE_m}}, \tag{29}$$

where $G_{IC}$ is the mode-I critical energy release rate of the matrix material.

The shear bonds can fail if the shear angle of the bonds exceeds the critical shear angle value, $\varphi_c$. It can also be obtained analytically by equating the energy consumed by an advancing mode-II crack to the work required to break all shear bonds as

$$\varphi_c = \sqrt{\frac{G_{IIC}}{tG_m}}, \tag{30}$$

where $G_{IIC}$ is the mode-II critical energy release rate of the matrix material.

Derivations of the relationships between the critical stretch value for the interlayer bonds, $s_{in}$, and the mode-I critical energy release rate and between the critical shear angle value, $\varphi_c$, and the mode-II critical energy release rate are given in Appendix D.

## 5. Numerical results

**5.1.** ***A lamina under uniaxial tension and uniform temperature change.*** A unidirectional thin lamina with a fiber orientation of $\theta = 0°$ is considered, as shown in Figure 8. The length and width of the lamina are specified as $L = 15.24$ mm and $W = 7.62$ mm, respectively. It has a thickness of $t = 0.1651$ mm. Its elastic moduli in the fiber and transverse directions are $E_1 = 159.96$ GPa and $E_2 = 8.96$ GPa, respectively. The thermal expansion coefficients in the fiber and transverse directions are $\alpha_1 = -1.52$ ppm/°C and $\alpha_2 = 34.3$ ppm/°C, respectively. The PD model is generated by using a single layer of material points with a grid size of $\Delta x = 6.35 \times 10^{-4}$ m. The horizon radius is specified as $\delta = 3.015\Delta x$. Using (24), the fiber and matrix bond constants are computed as $c_f = 5.72 \times 10^{23}$ N/m$^6$ and $c_m = 1.86 \times 10^{22}$ N/m$^6$. The quasistatic solution is obtained by using the adaptive dynamic relaxation technique by using a time increment of 1 and stable mass density value of $7.005 \times 10^{18}$ kg/m$^3$ [Kilic 2008]. Failure is not allowed in order to verify the solution against analytical predictions based on classical continuum mechanics.

First, a uniaxial tension loading of $P = 159.96$ MPa is applied as a body load of $b_x = 5.95 \times 10^{10}$ N/m$^3$ along the edges of the lamina through a volumetric region with a depth of $b = 2.54 \times 10^{-3}$ m. The variation

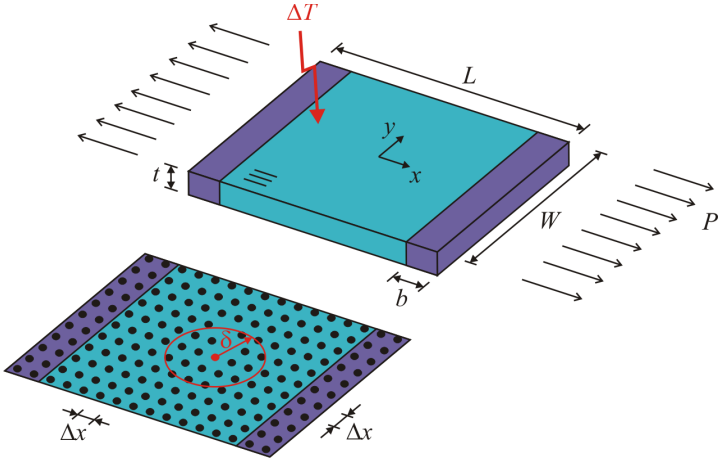


**Figure 8.** Loading and geometry of the unidirectional lamina under uniaxial tension and uniform temperature change.

of the horizontal and vertical displacement components along the central axes in the $x$- and $y$-directions, respectively, are computed at the end of 8000 time steps and compared with analytical results, as shown in Figures 9 and 10. Analytical results based on the classical continuum mechanics are computed by using the relations

$$u_x = \frac{P}{E_1}x, \qquad u_y = -\nu_{12}\frac{P}{E_1}y. \tag{31}$$

For both displacement components, there is remarkable agreement between the analytical and PD results.

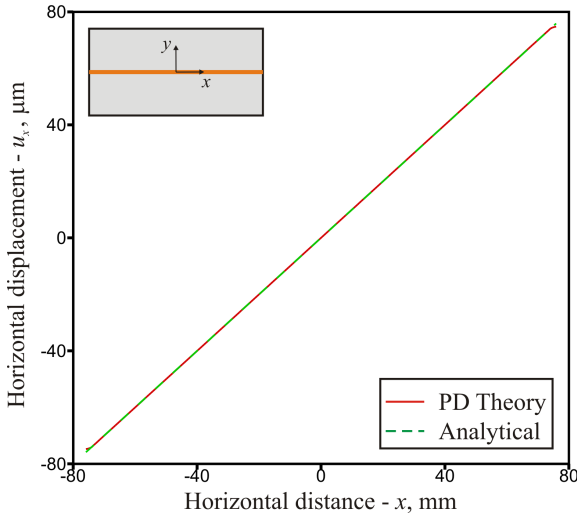


**Figure 9.** Horizontal displacement along the central axis at the end of 8000 time steps.

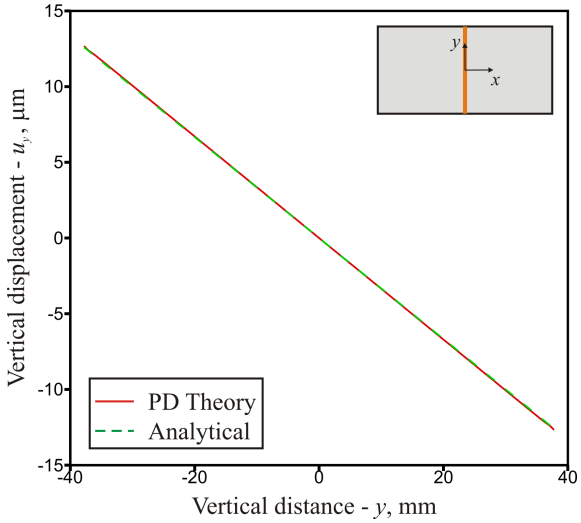


**Figure 10.** Vertical displacement along the central axis at the end of 8000 time steps.

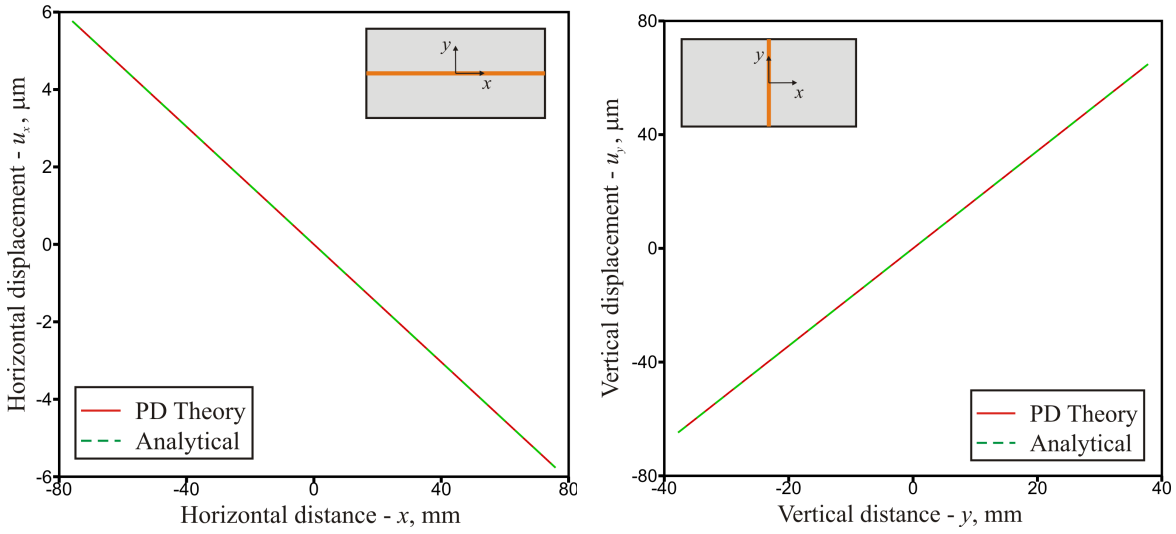


**Figure 11.** Variation of horizontal (left) and vertical (right) displacement along the central axis at the end of 8000 time steps when no failure is allowed.

Second, the lamina is only subjected to a uniform temperature change of $\Delta T = 50\,^{\circ}\text{C}$. For this loading condition, the analytical horizontal and vertical displacements along the central axes are computed by

$$u_x = \alpha_1 \Delta T x, \qquad u_y = \alpha_2 \Delta T y. \tag{32}$$

Comparisons of horizontal and vertical displacements obtained analytically and from PD analysis, shown in Figure 11, indicate remarkably close agreement.

**5.2.** ***Laminates under uniaxial tension.*** The validation is continued by considering two different 3-ply laminates with stacking sequences of [0°/90°/0°] and [0°/45°/0°] subjected to uniform tension loading, as

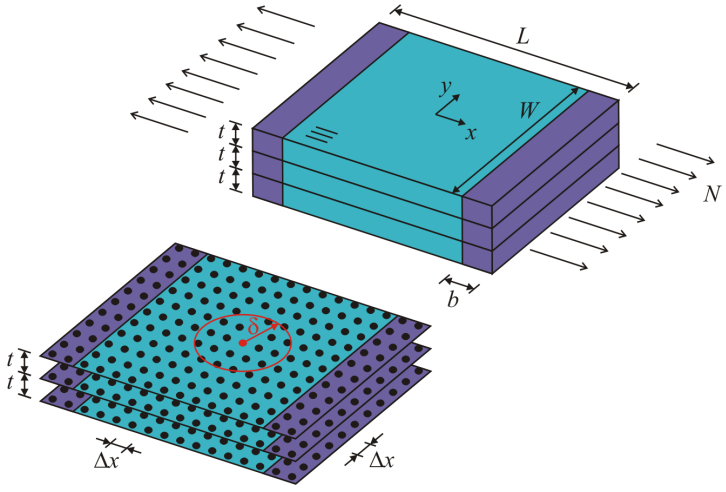


**Figure 12.** Loading and geometry of a composite laminate under uniaxial tension.

shown in Figure 12. The geometrical and material properties are the same as those of the lamina. Using (27), the interlayer and shear bond constants are computed as $c_{in} = 3.45 \times 10^{23}$ N/m$^6$ and $c_{is} = 1.55 \times 10^{18}$ N/m$^5$, respectively. The uniaxial tension loading is applied as a body load of $b_x = 5.95 \times 10^{10}$ N/m$^3$ through a volumetric region with a depth of $b = 2.54 \times 10^{-3}$ m. It corresponds to a stress resultant value of $N = 79228.2$ N/m along the edges of the laminate. During the solution, failure is not allowed in order to compare with the analytical solution based on the classical laminate theory.

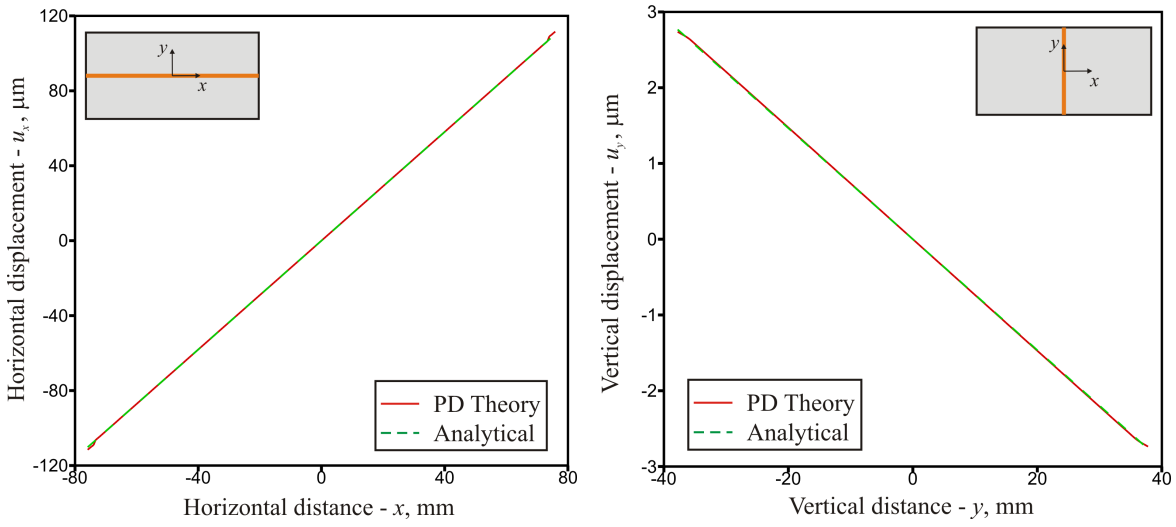


**Figure 13.** Horizontal (left) and vertical (right) displacement along the central axis in the 90° ply of the [0°/90°/0°] layup at the end of 8000 time steps.

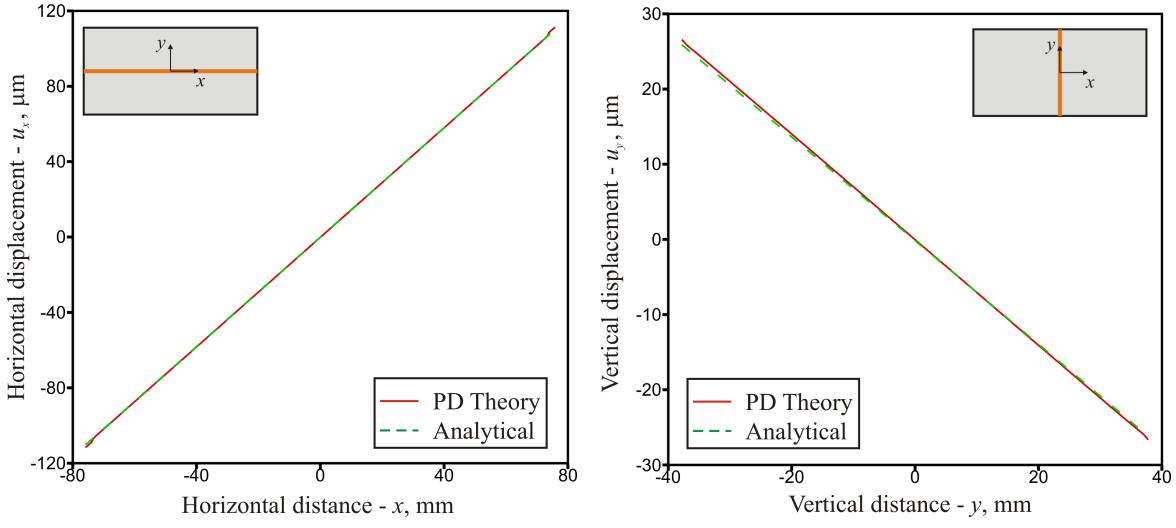


**Figure 14.** Horizontal (left) and vertical (right) displacement along the central axis in the 45° ply of the [0°/45°/0°] layup at the end of 8000 time steps.

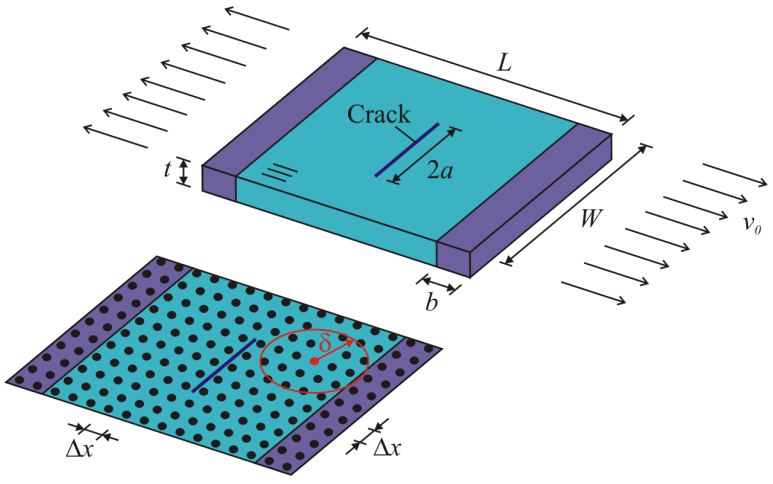


**Figure 15.** Loading and geometry of the unidirectional lamina with a crack under tension loading.

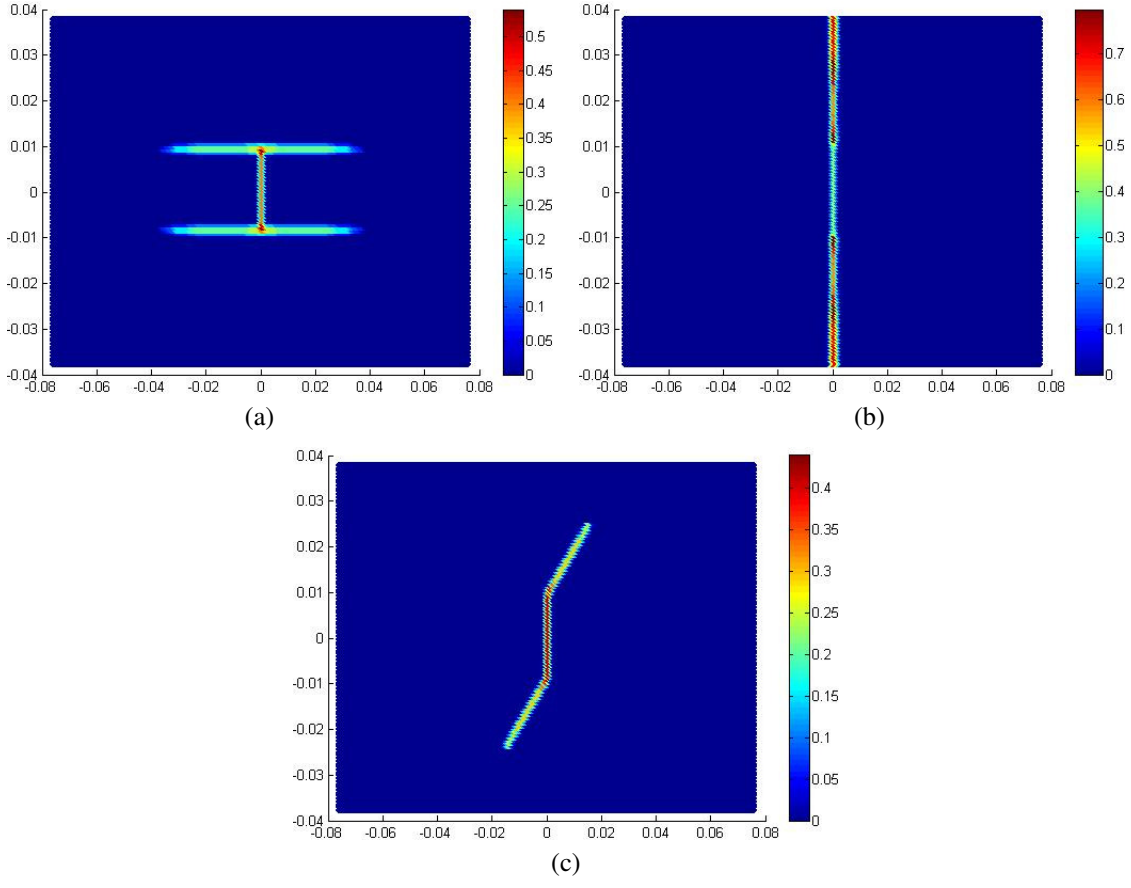


**Figure 16.** Damage plots for a lamina having a central crack with a fiber orientation of (a) $\theta = 0°$, (b) $\theta = 90°$, and (c) $\theta = 45°$.

The variation of the horizontal and vertical displacement components along the central axes in the $x$- and $y$-directions, respectively, for the 90° ply of the [0°/90°/0°] layup are computed at the end of 8000 time steps and compared with analytical results, as shown in Figure 13. The comparison of the displacement components in the 45° ply of the [0°/45°/0°] layup is shown in Figure 14. For both laminates, the agreement between the analytical and PD displacements is remarkably close.

**5.3.** ***A lamina with a preexisting central crack under tension.*** In order to demonstrate the failure prediction capability of the PD approach, the same lamina used previously, with a preexisting central crack, is considered for three different fiber orientations, $\theta = 0°$, 90°, and 45°. As shown in Figure 15, the crack is aligned with the $y$-axis and has a length of $2a = 0.01778$ m. The lamina is subjected to a velocity boundary condition of $v_0 = 2.02 \times 10^{-7}$ m/s along the edges of the lamina through a volumetric region with a depth of $b = 2.54 \times 10^{-3}$ m. Failure is only allowed in tension for the fiber and matrix bonds. The critical stretch for the matrix bond is specified as $s_{\text{mt}} = 0.0135$, which can be obtained by using the critical stretch expression given by (12) for an epoxy material. The procedure for computing this critical stretch value is demonstrated in Appendix D. For the fiber bond, it is assumed that its critical stretch value is twice the critical stretch for the matrix bond, that is, $s_{\text{ft}} = 0.027$.

As shown in Figure 16, in all cases the crack propagates in the fiber direction referred to as the splitting mode. Similar experimental observations confirm that current PD model accurately captures the failure modes.

**5.4.** ***Laminates with a preexisting central crack under tension.*** The failure prediction capability of the PD theory is further demonstrated by introducing a central crack in the two laminate layups of [0°/90°/0°] and [0°/45°/0°]. As shown in Figure 17, the crack is aligned with the $y$-axis and has a length of $2a = 0.01778$ m. The laminates are subjected to a velocity boundary condition of $v_0 = 2.02 \times 10^{-7}$ m/s. The critical stretch parameters specified for the fiber and matrix bonds are $s_{\text{ft}} = 0.027$ and $s_{\text{mt}} = 0.0135$, respectively. The critical stretch and angle parameters for the interlayer and shear bonds are computed

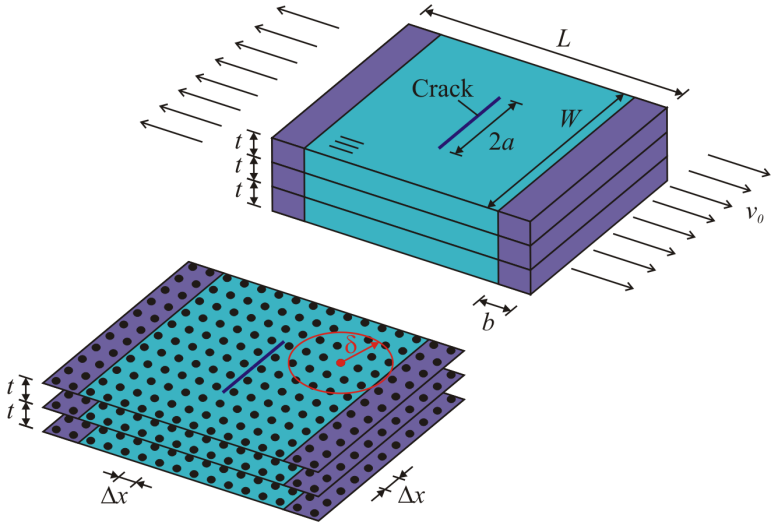


**Figure 17.** Loading and geometry of a composite laminate with a crack under tension loading.

analytically using (29) and (30) and are specified as $s_{in} = \varphi_c = 0.087$. The procedure for computing these critical stretch and angle values is explained in Appendix D.

For the [0°/90°/0°] laminate, an "H"-type splitting failure mode is observed for all plies, as shown in the left column of Figure 18. In this case, 0° plies are dominant in the loading direction; therefore, 0° plies determine the failure behavior of the laminate. However, in the [0°/45°/0°] laminate, a "Z"-type failure mode is obtained in all plies due to the presence of a 45° ply, as shown in Figure 18, right column. In both laminates, a delamination failure mode does not occur due to the high critical stretch values of interlayer and shear bonds with respect to fiber and matrix bonds.

If the bonding plies are weaker, smaller critical stretch and angle values can be specified for interlayer and shear bonds, respectively. If these parameters are specified as equal to the critical stretch of the matrix bond, that is, $s_{in} = \varphi_c = 0.0135$, the same intralayer failure modes are observed as in the previous case Figure 19. Also observed is the delamination failure mode between the plies due to the breakage of shear bonds around crack tip regions, shown in Figure 20. These damage patterns are consistent with those observed in [Bogert et al. 2006]. Consistent with their experimental observations, the effect of 45° ply has essentially a limited effect in the extent of the delamination except to influence the splitting mode of failure in the 0° layers.

## 6. Conclusions

Based on the numerical results, the peridynamic (PD) approach successfully predicts the damage growth patterns in fiber-reinforced laminates with preexisting cracks while considering the distinct properties of the fiber and matrix, as well as of the interlayer material between the plies. The predictions capture the correct failure mechanisms of matrix cracking, fiber breakage, and delamination without resorting to any special treatments, and agree with the experimental observations published in the literature. The simulations also capture failure modes among each ply, which are usually distinct; they heavily depend on fiber direction, which is realistically exhibited in the current results. It can be concluded that PD theory is a powerful method that can be employed for failure analysis of composite materials.

## Appendix A: PD material constants of a lamina

As shown in Figures A.1 and A.2, a lamina is discretized with a single layer of material points in the thickness direction. The domain of integral $H$ in (2) becomes a disk with radius $\delta$ and thickness $t$. The displacements of material points $i$ and $p$ are represented by $\boldsymbol{u}^{(i)}$ and $\boldsymbol{u}^{(p)}$, respectively. The initial relative position vector between these material points is denoted by

$$\boldsymbol{\xi} = \boldsymbol{x}^{(p)} - \boldsymbol{x}^{(i)}$$

and the relative displacement vector is

$$\boldsymbol{\eta} = \boldsymbol{u}^{(p)} - \boldsymbol{u}^{(i)}.$$

Similar to the determination of a PD material constant for an isotropic material [Oterkus et al. 2010], equating the strain energy density of a material point in a lamina computed using the PD theory and classical continuum mechanics results in the relationships between PD material constants, $c_f$ and $c_m$, and engineering constants, $E_1$, $E_2$, $G_{12}$, and $\nu_{12}$, as well as the coefficient of thermal expansion of a

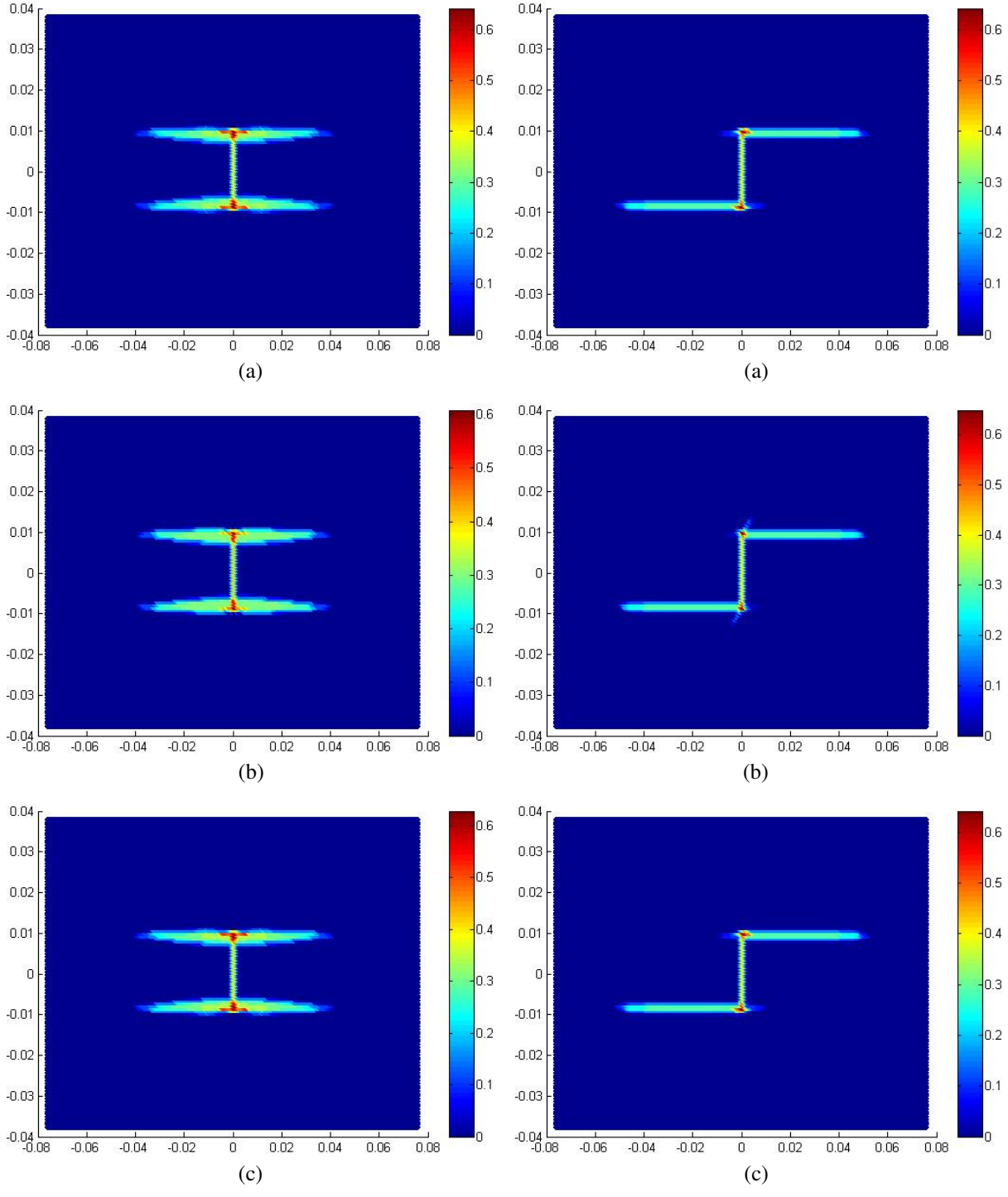


**Figure 18.** Matrix bond damage plots for a [0°/90°/0°] laminate (left column) and a [0°/45°/0°] laminate (right column) with a preexisting crack for $s_{\mathrm{mt}} \neq s_{i\mathrm{n}} = \varphi_c$: (a) bottom ply, 0°; (b) center ply, 90° or 45°, and (c) top ply, 0°.

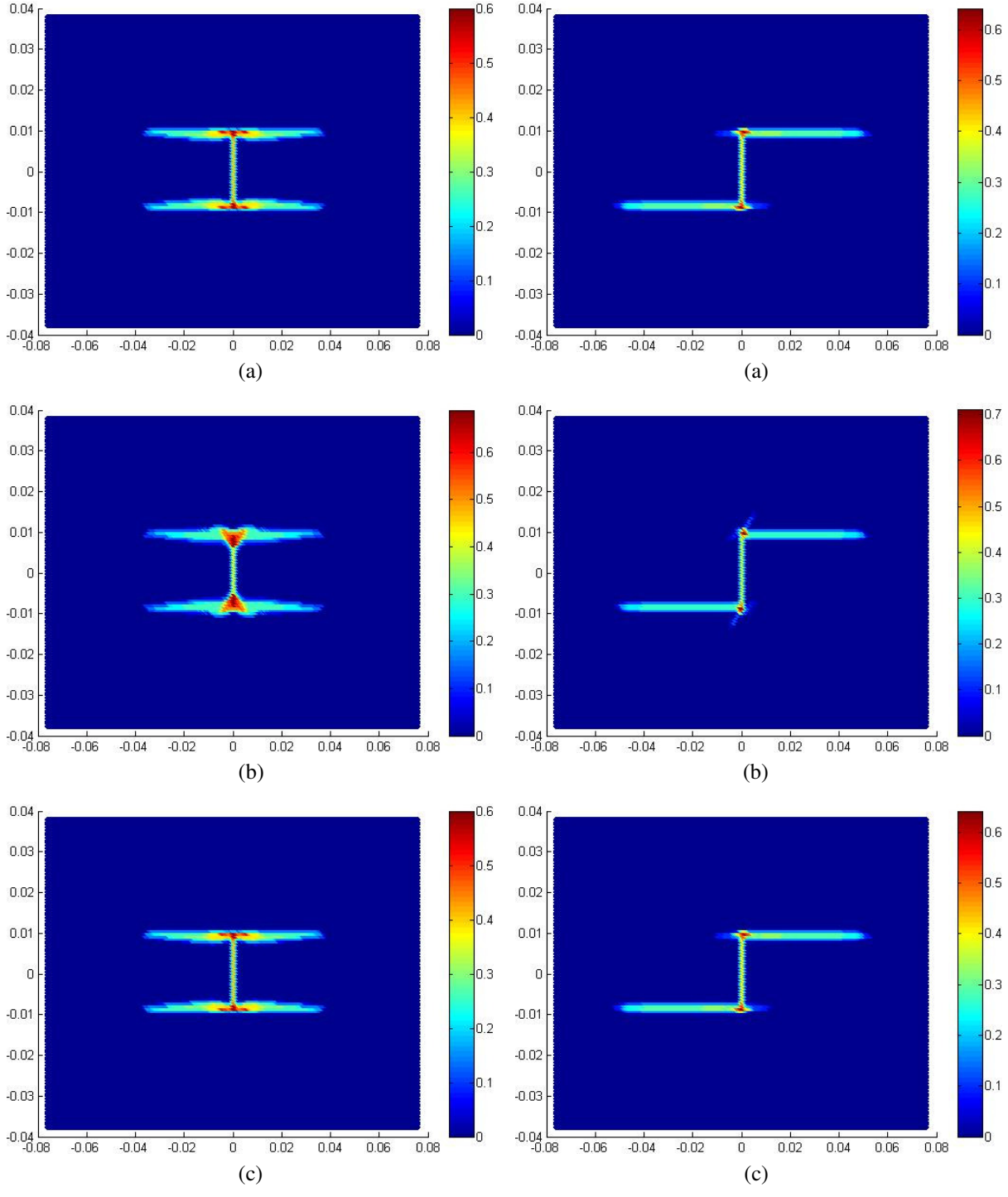


**Figure 19.** Matrix bond damage plots for a [0°/90°/0°] laminate (left column) and a [0°/45°/0°] laminate (right column) with a preexisting crack for $s_{\mathrm{mt}} = s_{i\mathrm{n}} = \varphi_c$: (a) bottom ply, 0°; (b) center ply, 90° or 45°, and (c) top ply, 0°.

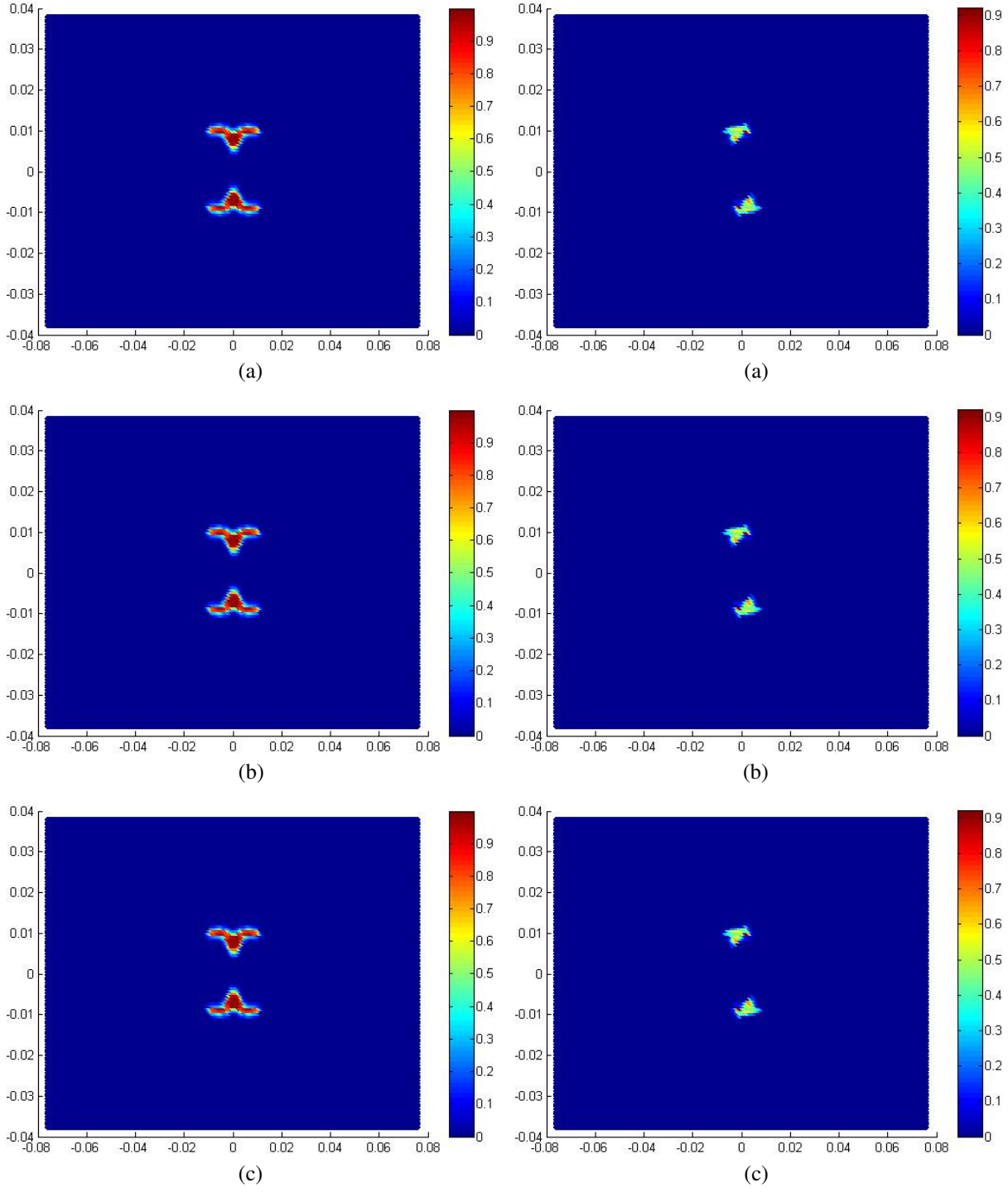


**Figure 20.** Shear bond damage plots for a [0°/90°/0°] laminate (left column) and a [0°/45°/0°] laminate (right column) with a preexisting crack for $s_{\text{mt}} = s_{i\text{n}} = \varphi_c$: (a) bottom ply, 0°; (b) center ply, 90° or 45°, and (c) top ply, 0°.

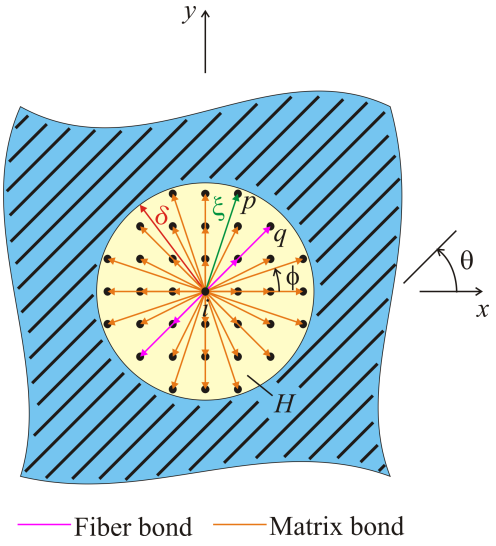


**Figure A.1.** PD horizon for a lamina with a fiber orientation of $\theta$ and PD bonds between material point $i$ and other material points within its horizon.

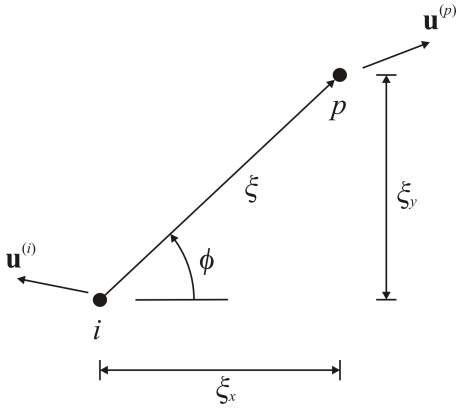


**Figure A.2.** PD bond between material points $i$ and $p$ with an orientation of $\phi$.

PD bond, $\alpha(\phi)$, in terms of thermal expansion coefficients, $\alpha_x$, $\alpha_y$, and $\alpha_{xy}$, for a lamina with a fiber orientation angle of $\theta$.

The strain energy densities are calculated by considering a combined mechanical and thermal loading condition that results in a deformation, as shown in Figure A.3.

The strain field arising from such deformation can be expressed as

$$\epsilon_{xx} = \zeta, \qquad \epsilon_{yy} = -\nu_{xy}\zeta, \qquad \gamma_{xy} = -\mu_{xy}\zeta, \tag{A.1a}$$

where $\mu_{xy}$ is a parameter defined as

$$\mu_{xy} = \frac{m_x E_x}{E_1}, \tag{A.1b}$$

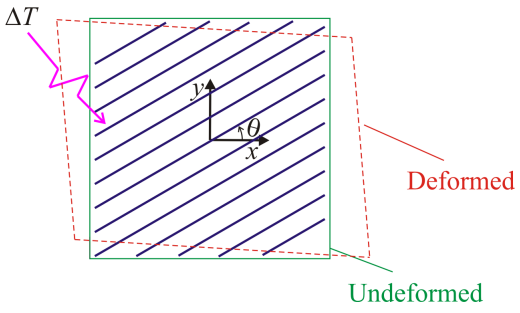


**Figure A.3.** Deformed configuration of an angle lamina subjected to a combined mechanical and thermal loading.

in which $m_x$ is a nondimensional shear coupling term that relates the normal stress in the $x$-direction to the shear strain in the $(x$-$y)$ plane. This strain field represents the uniaxial tension loading in the absence of uniform temperature change, that is, $\Delta T = 0$. The contribution to the strain field from the uniform temperature change can be expressed as

$$\epsilon^*_{xx} = \alpha_x \Delta T, \qquad \epsilon^*_{yy} = \alpha_y \Delta T, \qquad \gamma^*_{xy} = \alpha_{xy} \Delta T. \tag{A.2}$$

Therefore, the contribution to the strain field from the mechanical loading becomes

$$\bar{\epsilon}_{xx} = \zeta - \alpha_x \Delta T, \qquad \bar{\epsilon}_{yy} = -\nu_{xy}\zeta - \alpha_y \Delta T, \qquad \bar{\gamma}_{xy} = -\mu_{xy}\zeta - \alpha_{xy} \Delta T. \tag{A.3}$$

Similarly, the stretch of a PD bond due to mechanical loading between material points $i$ and $p$, $\bar{s}$, is the difference between the total stretch $s$ and thermal stretch $s^*$ as

$$\bar{s} = s - s^*. \tag{A.4}$$

The mechanical stretch, $\bar{s}$, can be expressed in terms of the relative displacement of the material points $i$ and $p$, arising from the mechanical loading, along the $X$-direction (the direction of their initial relative position vector, $\boldsymbol{\xi}$) as

$$\bar{s} = \frac{\bar{u}^{(p)}_X - \bar{u}^{(i)}_X}{\xi}. \tag{A.5}$$

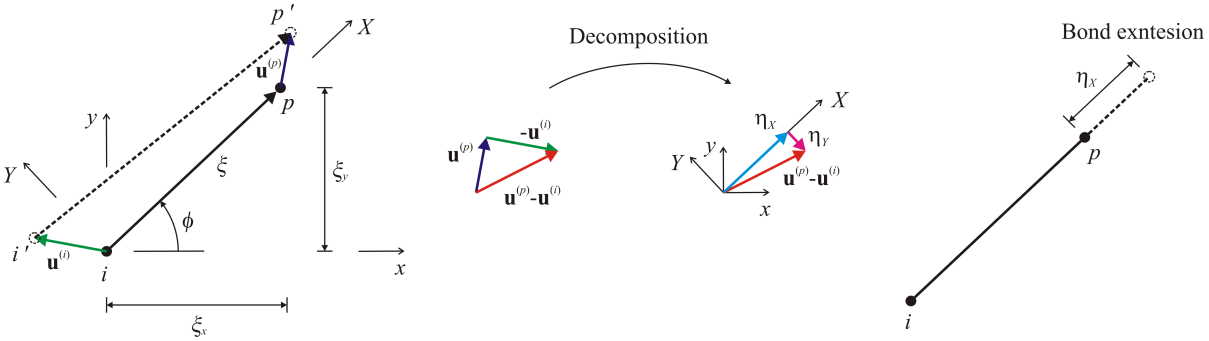


**Figure A.4.** Relative displacement between material points $i$ and $p$.

As shown in Figure A.4, the relative displacement, $(\bar{u}_X^{(p)} - \bar{u}_X^{(i)})$, can be obtained in terms of the components of the displacement vectors $\bar{\boldsymbol{u}}^{(i)^T} = \{\bar{u}_x^{(i)}, \bar{u}_y^{(i)}\}^T$ and $\bar{\boldsymbol{u}}^{(p)^T} = \{\bar{u}_x^{(p)}, \bar{u}_y^{(p)}\}^T$ of the material points $i$ and $p$, respectively. Coordinate transformation from an $(x, y)$ coordinate system to an $(X, Y)$ coordinate system leads to their explicit expressions as

$$\begin{Bmatrix} \bar{u}_X^{(p)} - \bar{u}_X^{(i)} \\ \bar{u}_Y^{(p)} - \bar{u}_Y^{(i)} \end{Bmatrix} = \begin{bmatrix} \cos(\phi) & \sin(\phi) \\ -\sin(\phi) & \cos(\phi) \end{bmatrix} \begin{Bmatrix} \bar{u}_x^{(p)} - \bar{u}_x^{(i)} \\ \bar{u}_y^{(p)} - \bar{u}_y^{(i)} \end{Bmatrix}. \tag{A.6}$$

Based on Figure A.5, the relative displacements of the material points $i$ and $p$ in the horizontal and vertical directions, $(\bar{u}_x^{(p)} - \bar{u}_x^{(i)})$ and $(\bar{u}_y^{(p)} - \bar{u}_y^{(i)})$, respectively, can also be obtained from

$$\bar{u}_x^{(p)} - \bar{u}_x^{(i)} = \bar{\epsilon}_{xx}\xi_x + \frac{\bar{\gamma}_{xy}}{2}\xi_y \tag{A.7a}$$

$$\bar{u}_y^{(p)} - \bar{u}_y^{(i)} = \frac{\bar{\gamma}_{xy}}{2}\xi_x + \bar{\epsilon}_{yy}\xi_y, \tag{A.7b}$$

where $\xi_x = \xi\cos(\phi)$ and $\xi_y = \xi\sin(\phi)$ are the components of the initial relative position vector, $\boldsymbol{\xi}$.

After invoking the mechanical strain components from (A.3) into (A.7a) and (A.7b) results in

$$\bar{u}_x^{(p)} - \bar{u}_x^{(i)} = \zeta\xi\left(\cos\phi - \frac{\mu_{xy}}{2}\sin\phi\right) - \xi\Delta T\left(\alpha_x\cos\phi + \frac{\alpha_{xy}}{2}\sin\phi\right), \tag{A.8a}$$

$$\bar{u}_y^{(p)} - \bar{u}_y^{(i)} = -\zeta\xi\left(\nu_{xy}\sin\phi + \frac{\mu_{xy}}{2}\cos\phi\right) - \xi\Delta T\left(\alpha_y\sin\phi + \frac{\alpha_{xy}}{2}\cos\phi\right). \tag{A.8b}$$

Using the coordinate transformation given in (A.6) along with (A.8), the mechanical stretch, $\bar{s}$, can be obtained in the form

$$\bar{s} = \zeta\left(\cos^2\phi - \mu_{xy}\sin\phi\cos\phi - \nu_{xy}\sin^2\phi\right) - \left(\alpha_x\cos^2\phi + \alpha_y\sin^2\phi + \alpha_{xy}\sin\phi\cos\phi\right)\Delta T. \tag{A.9}$$

Comparing this expression with (A.4) reveals that the expression in parentheses corresponds to the thermal expansion coefficient of the PD bond, $\alpha\phi$, defined as

$$\alpha\phi = \alpha_x\cos^2\phi + \alpha_y\sin^2\phi + \alpha_{xy}\sin\phi\cos\phi. \tag{A.10}$$

In the absence of thermal loading, that is, $\Delta T = 0^\circ$ in (A.9), the mechanical stretch reduces to

$$\bar{s} = s = \zeta\left(\cos^2\phi - \mu_{xy}\sin\phi\cos\phi - \nu_{xy}\sin^2\phi\right), \tag{A.11}$$

which represents the total stretch due to uniaxial tension. By using (7) in conjunction with (19), the strain energy density based on PD theory at a material point in a composite lamina can be evaluated as

$$\begin{aligned} U_{\mathrm{PD}} = {} & \frac{1}{2}\left(\frac{1}{2}\int_H c(\phi)\cos^4(\phi)\xi(\phi)\,dH - 2\nu_{xy}\int_H c(\phi)\sin^2(\phi)\cos^2(\phi)\xi(\phi)\,dH\right)\zeta^2 \\ & + \frac{1}{2}\left(-2\mu_{xy}\int_H c(\phi)\sin(\phi)\cos^3(\phi)\xi(\phi)\,dH + 2\nu_{xy}\mu_{xy}\int_H c(\phi)\sin^3(\phi)\cos(\phi)\xi(\phi)\,dH\right)\zeta^2 \\ & + \frac{1}{2}\left(\nu_{xy}^2\int_H c(\phi)\sin^4(\phi)\xi(\phi)\,dH + \mu_{xy}^2\int_H c(\phi)\sin^2(\phi)\cos^2(\phi)\xi(\phi)\,dH\right)\zeta^2. \end{aligned} \tag{A.12}$$

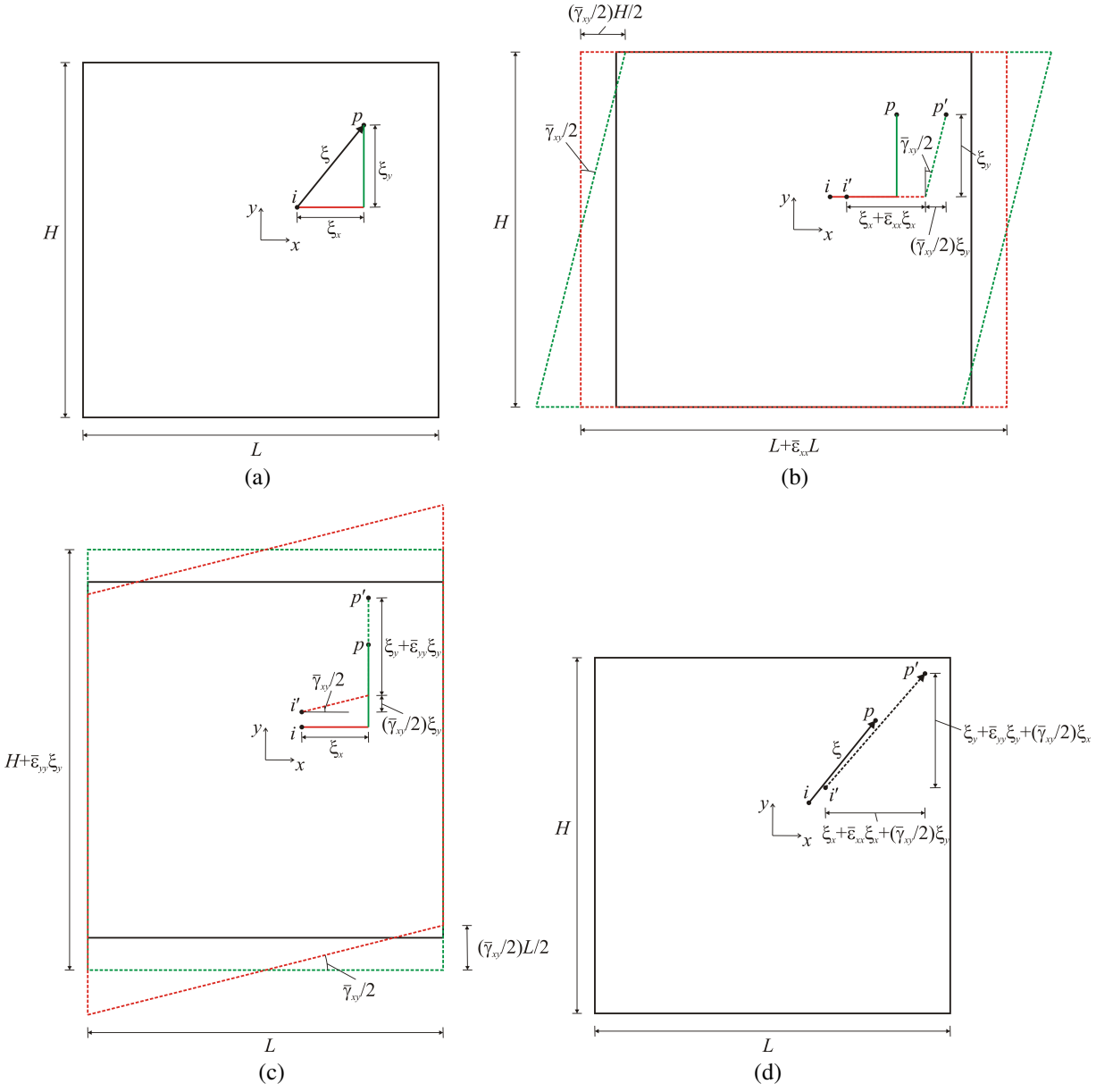


**Figure A.5.** Relative positions of points $i$ and $p$: (a) undeformed state, (b) extension and simple shear in the $x$-direction, (c) extension and simple shear in the $y$-direction, and (d) extensions in $x$- and $y$-directions and pure shear.

Using (14) in conjunction with (16), the strain energy density of a material point based on classical continuum mechanics can be written as

$$U_E = \tfrac{1}{2}(\overline{Q}_{11} - 2\nu_{xy}\overline{Q}_{12} - 2\mu_{xy}\overline{Q}_{16} + 2\nu_{xy}\mu_{xy}\overline{Q}_{26} + \nu_{xy}^2\overline{Q}_{22} + \mu_{xy}^2\overline{Q}_{66})\zeta^2, \tag{A.13}$$

in which

$$\overline{Q}_{11} = Q_{11}\cos^4(\theta) + Q_{22}\sin^4(\theta) + 2(Q_{12} + 2Q_{66})\sin^2(\theta)\cos^2(\theta), \tag{A.14a}$$

$$\overline{Q}_{12} = (Q_{11} + Q_{22} - 4Q_{66})\sin^2(\theta)\cos^2(\theta) + Q_{12}\big(\cos^4(\theta) + \sin^4(\theta)\big), \tag{A.14b}$$

$$\overline{Q}_{16} = (Q_{11} - Q_{12} - 2Q_{66})\cos^3(\theta)\sin(\theta) - (Q_{22} - Q_{12} - 2Q_{66})\sin^3(\theta)\cos(\theta), \tag{A.14c}$$

$$\overline{Q}_{22} = Q_{11}\sin^4(\theta) + Q_{22}\cos^4(\theta) + 2(Q_{12} + 2Q_{66})\sin^2(\theta)\cos^2(\theta), \tag{A.14d}$$

$$\overline{Q}_{26} = (Q_{11} - Q_{12} - 2Q_{66})\cos(\theta)\sin^3(\theta) - (Q_{22} - Q_{12} - 2Q_{66})\cos^3(\theta)\sin(\theta), \tag{A.14e}$$

$$\overline{Q}_{66} = (Q_{11} + Q_{22} - 2Q_{12} - 2Q_{66})\sin^2(\theta)\cos^2(\theta) + Q_{66}\big(\sin^4(\theta) + \cos^4(\theta)\big), \tag{A.14f}$$

with

$$Q_{11} = \frac{E_1}{1 - \nu_{21}\nu_{12}}, \qquad Q_{12} = \frac{\nu_{12}E_2}{1 - \nu_{21}\nu_{12}}, \qquad Q_{22} = \frac{E_2}{1 - \nu_{21}\nu_{12}}, \qquad Q_{66} = G_{12}, \tag{A.15a}$$

provided that

$$1 - \nu_{12}\nu_{21} > 0 \tag{A.15b}$$

and subject to

$$\frac{\nu_{12}}{E_1} = \frac{\nu_{21}}{E_2}. \tag{A.15c}$$

Equating the coefficients of like terms in the strain energy density expressions from classical continuum theory, (A.13) and PD theory, (A.12), leads to

$$\overline{Q}_{11} = \frac{1}{2}\int_H c(\phi)\cos^4(\phi)\xi(\phi)\,dH, \tag{A.16a}$$

$$\overline{Q}_{12} = \frac{1}{2}\int_H c(\phi)\sin^2(\phi)\cos^2(\phi)\xi(\phi)\,dH, \tag{A.16b}$$

$$\overline{Q}_{16} = \frac{1}{2}\int_H c(\phi)\sin(\phi)\cos^3(\phi)\xi(\phi)\,dH, \tag{A.16c}$$

$$\overline{Q}_{22} = \frac{1}{2}\int_H c(\phi)\sin^4(\phi)\xi(\phi)\,dH, \tag{A.16d}$$

$$\overline{Q}_{26} = \frac{1}{2}\int_H c(\phi)\sin^3(\phi)\cos(\phi)\xi(\phi)\,dH, \tag{A.16e}$$

$$\overline{Q}_{66} = \frac{1}{2}\int_H c(\phi)\sin^2(\phi)\cos^2(\phi)\xi(\phi)\,dH. \tag{A.16f}$$

Using the approximation given in (20), (A.16) can be rewritten in the form

$$\overline{Q}_{11} = \frac{1}{2}\sum_{q=1}^{Q} c_f \cos^4(\theta)\xi_{qi} V_q + \frac{t}{2}\int_0^{2\pi}\int_0^{\delta} c_m\big(\cos^4(\phi)\xi\big)\xi\, d\xi d\phi, \tag{A.17a}$$

$$\overline{Q}_{12} = \frac{1}{2}\sum_{q=1}^{Q} c_f \sin^2(\theta)\cos^2(\theta)\xi_{qi} V_q + \frac{t}{2}\int_0^{2\pi}\int_0^{\delta} c_m\big(\sin^2(\phi)\cos^2(\phi)\xi\big)\xi\, d\xi d\phi, \tag{A.17b}$$

$$\overline{Q}_{16} = \frac{1}{2}\sum_{q=1}^{Q} c_f \sin(\theta)\cos^3(\theta)\xi_{qi} V_q + \frac{t}{2}\int_0^{2\pi}\int_0^{\delta} c_m\big(\sin(\phi)\cos^3(\phi)\xi\big)\xi\, d\xi d\phi, \tag{A.17c}$$

$$\overline{Q}_{22} = \frac{1}{2}\sum_{q=1}^{Q} c_f \sin^4(\theta)\xi_{qi} V_q + \frac{t}{2}\int_0^{2\pi}\int_0^{\delta} c_m\big(\sin^4(\phi)\xi\big)\xi\, d\xi d\phi, \tag{A.17d}$$

$$\overline{Q}_{26} = \frac{1}{2}\sum_{q=1}^{Q} c_f \sin^3(\theta)\cos(\theta)\xi_{qi} V_q + \frac{t}{2}\int_0^{2\pi}\int_0^{\delta} c_m\big(\sin^3(\phi)\cos(\phi)\xi\big)\xi\, d\xi d\phi, \tag{A.17e}$$

$$\overline{Q}_{66} = \frac{1}{2}\sum_{q=1}^{Q} c_f \sin^2(\theta)\cos^2(\theta)\xi_{qi} V_q + \frac{t}{2}\int_0^{2\pi}\int_0^{\delta} c_m\big(\sin^2(\phi)\cos^2(\phi)\xi\big)\xi\, d\xi d\phi. \tag{A.17f}$$

Performing the integrations in (A.17) results in the relations between the engineering constants and the PD material constants, $c_f$ and $c_m$, as

$$\overline{Q}_{11} = \big(\beta\cos^4(\theta)\big)c_f + \frac{\pi t\delta^3}{8}c_m, \tag{A.18a}$$

$$\overline{Q}_{12} = \big(\beta\sin^2(\theta)\cos^2(\theta)\big)c_f + \frac{\pi t\delta^3}{24}c_m, \tag{A.18b}$$

$$\overline{Q}_{16} = \big(\beta\sin(\theta)\cos^3(\theta)\big)c_f, \tag{A.18c}$$

$$\overline{Q}_{22} = \big(\beta\sin^4(\theta)\big)c_f + \frac{\pi t\delta^3}{8}c_m, \tag{A.18d}$$

$$\overline{Q}_{26} = \big(\beta\sin^3(\theta)\cos(\theta)\big)c_f, \tag{A.18e}$$

$$\overline{Q}_{66} = \big(\beta\sin^2(\theta)\cos^2(\theta)\big)c_f + \frac{\pi t\delta^3}{24}c_m, \tag{A.18f}$$

where

$$\beta = \frac{1}{2}\sum_{q=1}^{Q}\xi_{qi} V_q. \tag{A.19}$$

Examination of these equations show that the right-hand sides of (A.18b) and (A.18f) are the same, requiring that

$$\overline{Q}_{12} = \overline{Q}_{66}. \tag{A.20}$$

Substituting from (A.14b) and (A.14f) into (A.20) leads to

$$Q_{12} = Q_{66}. \tag{A.21}$$

Examination of (A.18c) and (A.18e) reveals that

$$\beta c_f = \frac{\overline{Q}_{16}}{\sin(\theta)\cos^3(\theta)} = \frac{\overline{Q}_{26}}{\sin^3(\theta)\cos(\theta)}. \tag{A.22}$$

Invoking the requirement given by (A.21) into (A.14c) and (A.14e) renders this equation as

$$(Q_{11} - 3Q_{12}) - (Q_{22} - 3Q_{12})\frac{\sin^2(\theta)}{\cos^2(\theta)} = (Q_{11} - 3Q_{12}) - (Q_{22} - 3Q_{12})\frac{\cos^2(\theta)}{\sin^2(\theta)}. \tag{A.23}$$

For this equation to be valid for all fiber orientation, it is required that

$$Q_{22} = 3Q_{12}. \tag{A.24}$$

After invoking the requirements given by (A.21) and (A.24) into (A.14a) and (A.14d), subtracting (A.18d) from (A.18a) results in

$$c_f = \frac{Q_{11} - Q_{22}}{\beta}. \tag{A.25}$$

Similarly, invoking the requirements given by (A.21) and (A.24) into (A.14a) and substituting from (A.25) into (A.18a) leads to

$$c_m = \frac{24Q_{12}}{\pi t \delta^3}. \tag{A.26}$$

The expressions for the bond constants, $c_f$ and $c_m$, given by (A.25) and (A.26), as well as the relations given (A.21) and (A.24), can be rewritten in terms of the engineering constants as

$$c_f = \frac{2E_1(E_1 - E_2)}{(E_1 - \frac{1}{9}E_2)\left(\sum_{q=1}^{Q} \xi_{qi} V_q\right)}, \quad c_m = \frac{8E_1E_2}{(E_1 - \frac{1}{9}E_2)\pi t \delta^3}, \quad G_{12} = \frac{\nu_{12}E_2}{1 - \nu_{21}\nu_{12}}, \quad \nu_{12} = \frac{1}{3}. \tag{A.27}$$

## Appendix B: Surface correction factors for a composite lamina

The surface correction factors for fiber and matrix bonds are determined by computing the strain energy density at two distinct material points under uniaxial strain conditions in the $x$-, and $y$-directions, that is, $\epsilon_{xx} \neq 0, \epsilon_{yy} = \gamma_{xy} = 0$ and $\epsilon_{yy} \neq 0, \epsilon_{xx} = \gamma_{xy} = 0$. The first material point located near an external surface has a truncated horizon, as shown in Figure B.1. The second material point is located far away from an external boundary and is completely embedded in a single lamina, as shown in Figure B.2.

The strain energy density of a material point at $\boldsymbol{x}$ is decomposed as

$$W = W_{(f)} + W_{(m)}, \tag{B.1}$$

where $W_{(f)}(x)$ and $W_{(m)}(x)$ represent the contribution of fiber bonds and matrix bonds, respectively.

First, uniaxial strain loading is applied in the $x$-direction, and the resulting displacement field can be expressed at material point $\boldsymbol{x}$ as

$$\boldsymbol{u}^T(\boldsymbol{x}) = \left\{ \frac{\partial u_x^*}{\partial x} x \;\; 0 \right\}, \tag{B.2}$$

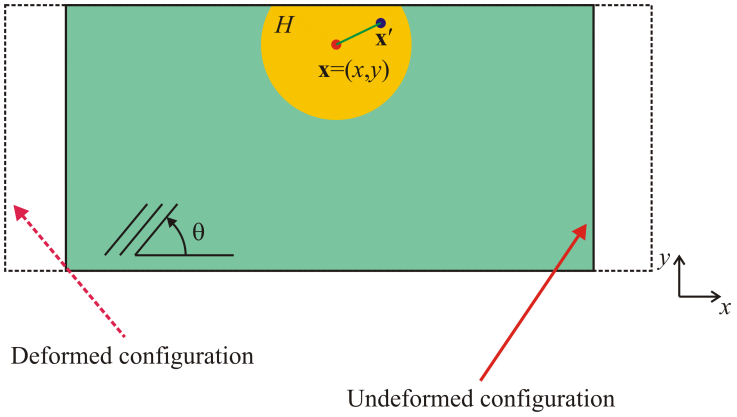


**Figure B.1.** Material point $\boldsymbol{x}$ with a truncated horizon in a lamina.

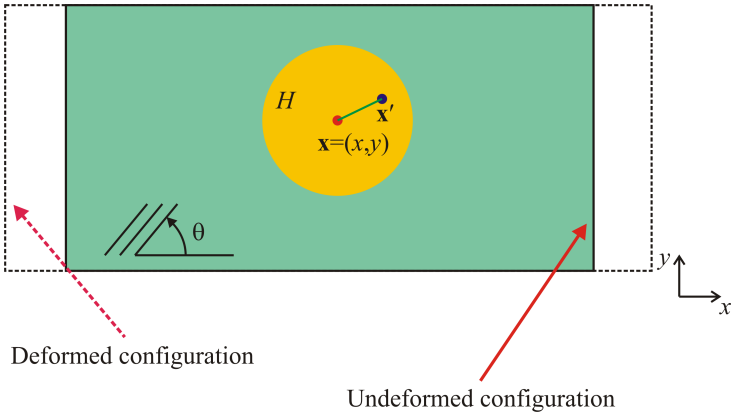


**Figure B.2.** Material point $\boldsymbol{x}$ far away from external surfaces of a lamina.

in which $\partial u_x^*/\partial x$ is the applied constant displacement gradient. The strain energy density, $W_x(\boldsymbol{x})$, due to this applied displacement gradient is expressed as

$$W_x(\boldsymbol{x}) = \int_H w(\boldsymbol{u}' - \boldsymbol{u}, \boldsymbol{x}' - \boldsymbol{x})\, dH, \tag{B.3}$$

where $H$ represents the horizon of the material point at $\boldsymbol{x}$ and $w$ represents the strain energy density of the PD bond between material points at $\boldsymbol{x}$ and $\boldsymbol{x}'$. The strain energy density, $W_y(\boldsymbol{x})$, of the material point at $\boldsymbol{x}$ can also be computed due to uniaxial strain in the $y$-direction. The subscripts $x$and $y$ denote uniaxial strain loading condition in $x$- and $y$-directions, respectively.

In accordance with (B.1), the strain energy density at material point $\boldsymbol{x}$ due to the applied uniaxial strain loading in $x$- and $y$-directions can be decomposed as

$$W_x = W_{(f)x} + W_{(m)x}, \qquad W_y = W_{(f)y} + W_{(m)y}. \tag{B.4}$$

With this decomposition, the strain energy density vectors, $\boldsymbol{W}_{(f)}(\boldsymbol{x})$ and $\boldsymbol{W}_{(m)}(\boldsymbol{x})$, can be formed as

$$\boldsymbol{W}_{(f)}^{T}(\boldsymbol{x}) = \left\{ W_{(f)x} \;\; W_{(f)y} \right\}, \qquad \boldsymbol{W}_{(m)}^{T}(\boldsymbol{x}) = \left\{ W_{(m)x} \;\; W_{(m)y} \right\}, \tag{B.5}$$

where $\boldsymbol{W}_{(f)}(\boldsymbol{x})$ and $\boldsymbol{W}_{(m)}(\boldsymbol{x})$ represent the contribution of fiber bonds and matrix bonds to the strain energy density of the material point at $\boldsymbol{x}$, respectively.

For both fiber and matrix bonds, the correction factors corresponding to the two loading directions can be defined as the ratio of the strain energy density of the material point embedded far away from an external surface in a lamina, $W_{(\beta)\alpha}^{(\infty)}$, to that of a material point near an external surface with a truncated horizon, $W_{(\beta)\alpha}$, with $\alpha = x, y$ and $\beta = f, m$. For a material point whose horizon is completely embedded in a single lamina, the strain energy densities for the uniaxial strain loading condition in the $x$- and $y$-directions can be computed using classical continuum mechanics as

$$W_{x}^{(\infty)} = \tfrac{1}{2}\,\overline{Q}_{11}\zeta^{2}, \qquad W_{y}^{(\infty)} = \tfrac{1}{2}\,\overline{Q}_{22}\zeta^{2}, \tag{B.6}$$

where $\overline{Q}_{11}$ and $\overline{Q}_{22}$ are the coefficients of the transformed reduced stiffness matrix $\overline{\boldsymbol{Q}}$ [Kaw 2006]. The strain energy densities given by (B.6) can be decomposed into two parts which are associated with the deformations of fiber and matrix materials, that is, $W_{(\beta)\alpha}^{(\infty)}$, with $\alpha = x, y$ and $\beta = f, m$, as

$$W_{x}^{(\infty)} = W_{(f)x}^{(\infty)} + W_{(m)x}^{(\infty)}, \qquad W_{y}^{(\infty)} = W_{(f)y}^{(\infty)} + W_{(m)y}^{(\infty)}. \tag{B.7}$$

However, the explicit form of this decomposition is not known because each lamina is treated as homogeneous and orthotropic within the realm of classical continuum mechanics. Therefore, this decomposition is assumed similar in form to that of between $c_f$ and $c_m$ as given by (A.18a) and (A.18d), respectively. This assumption leads to the following decomposition of strain energies given by (B.6) in the form

$$W_{x}^{(\infty)} = \overline{W}_{(f)}^{(\infty)}\cos^{4}(\theta) + \overline{W}_{(m)}^{(\infty)} \qquad W_{y}^{(\infty)} = \overline{W}_{(f)}^{(\infty)}\sin^{4}(\theta) + \overline{W}_{(m)}^{(\infty)}, \tag{B.8}$$

where $\overline{W}_{(f)}^{(\infty)}$ and $\overline{W}_{(m)}^{(\infty)}$, representing the contribution of fiber and matrix materials, respectively, are to be determined. Substituting for the strain energy density expressions given by (B.8) in (B.6) permits the determination of $\overline{W}_{(f)}^{(\infty)}$ and $\overline{W}_{(m)}^{(\infty)}$ in terms of the material constants $\overline{Q}_{11}$ and $\overline{Q}_{22}$ as

$$\overline{W}_{(f)}^{(\infty)} = \frac{1}{2}\left\{ \frac{(\overline{Q}_{11} - \overline{Q}_{22})}{\cos^{4}(\theta) - \sin^{4}(\theta)} \right\}\zeta^{2}, \qquad \overline{W}_{(m)}^{(\infty)} = \frac{1}{2}\left\{ \frac{\left(\overline{Q}_{22}\cos^{4}(\theta) - \overline{Q}_{11}\sin^{4}(\theta)\right)}{\cos^{4}(\theta) - \sin^{4}(\theta)} \right\}\zeta^{2}. \tag{B.9}$$

The final form of the terms, $W_{(\beta)\alpha}^{(\infty)}$, with $\alpha = x, y$ and $\beta = f, m$, in (B.7) can be written as

$$W_{(f)x}^{(\infty)} = \frac{1}{2}\left\{ \frac{(\overline{Q}_{11} - \overline{Q}_{22})\cos^{4}(\theta)}{\cos^{4}(\theta) - \sin^{4}(\theta)} \right\}\zeta^{2}, \tag{B.10a}$$

$$W_{(m)x}^{(\infty)} = \frac{1}{2}\left\{ \frac{\left(\overline{Q}_{22}\cos^{4}(\theta) - \overline{Q}_{11}\sin^{4}(\theta)\right)}{\cos^{4}(\theta) - \sin^{4}(\theta)} \right\}\zeta^{2}, \tag{B.10b}$$

$$W_{(f)y}^{(\infty)} = \frac{1}{2}\left\{ \frac{(\overline{Q}_{11} - \overline{Q}_{22})\sin^{4}(\theta)}{\cos^{4}(\theta) - \sin^{4}(\theta)} \right\}\zeta^{2}, \tag{B.10c}$$

$$W_{(m)y}^{(\infty)} = \frac{1}{2}\left\{ \frac{\left(\overline{Q}_{22}\cos^{4}(\theta) - \overline{Q}_{11}\sin^{4}(\theta)\right)}{\cos^{4}(\theta) - \sin^{4}(\theta)} \right\}\zeta^{2}. \tag{B.10d}$$

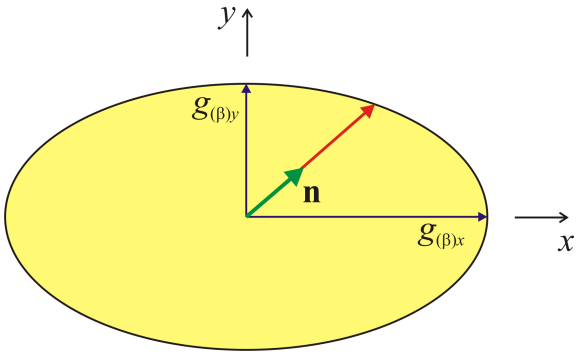


**Figure B.3.** Construction of an ellipse for surface correction factors.

With these values, a vector of correction factors for fiber and matrix bonds at material point $\boldsymbol{x}$ can be formed as

$$\boldsymbol{g}_{(\beta)}(\boldsymbol{x}) = \{g_{(\beta)x}, g_{(\beta)y}\}^T = \{W^{(\infty)}_{(\beta)x}/W_{(\beta)x}, W^{\infty}_{(\beta)y}/W_{(\beta)y}\}^T, \qquad \text{with } \beta = f, m. \tag{B.11}$$

These correction factors are only based on loading in the $x$- and $y$-directions. However, they can be used as the principal values of an ellipse in order to approximate the surface correction factor in an arbitrary direction of unit vector, $\boldsymbol{n}$ (Figure B.3).

In the case of a surface correction factor for a PD bond between material points $\boldsymbol{x}_{(i)}$ and $\boldsymbol{x}_{(j)}$ under general loading conditions, shown in Figure B.4a, the correction factors in the direction of the relative position vector, $\boldsymbol{n} = \boldsymbol{\xi}/|\boldsymbol{\xi}| = \{n_x, n_y\}^T$, in the undeformed configuration between these two material points, can be obtained in a similar manner.

A vector of correction factors at material points, $\boldsymbol{x}_{(i)}$ and $\boldsymbol{x}_{(j)}$ can be formed as

$$\boldsymbol{g}_{(\beta)(i)}(\boldsymbol{x}_{(i)}) = \{g_{(\beta)x(i)}, g_{(\beta)y(i)}\}^T = \{W^{(\infty)}_{(\beta)x}/W_{(\beta)x(i)}, W^{(\infty)}_{(\beta)y}/W_{(\beta)y(i)}\}^T, \tag{B.12}$$

$$\boldsymbol{g}_{(\beta)(j)}(\boldsymbol{x}_{(j)}) = \{g_{(\beta)x(j)}, g_{(\beta)y(j)}\}^T = \{W^{(\infty)}_{(\beta)x}/W_{(\beta)x(j)}, W^{(\infty)}_{(\beta)y}/W_{(\beta)y(j)}\}^T. \tag{B.13}$$

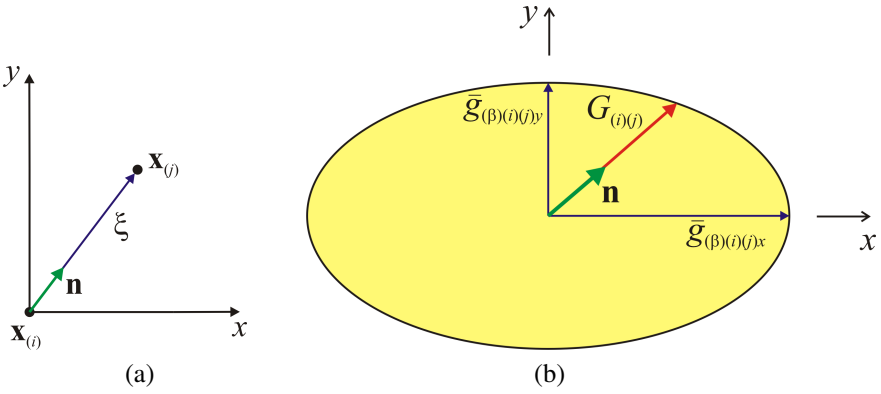


**Figure B.4.** (a) PD bond between material points at $x_{(i)}$ and $x_{(j)}$ (left) and (b) the ellipse for the surface correction factor.

These correction factors are, in general, different at material points $\boldsymbol{x}_{(i)}$ and $\boldsymbol{x}_{(j)}$. Therefore, the correction factor for a PD bond between material points $\boldsymbol{x}_{(i)}$ and $\boldsymbol{x}_{(j)}$ can be obtained by their mean values as

$$\bar{\boldsymbol{g}}_{(\beta)(i)(j)} = \{\bar{g}_{(\beta)(i)(j)x}, \bar{g}_{(\beta)(i)(j)y}\}^T = (\boldsymbol{g}_{(\beta)(i)} + \boldsymbol{g}_{(\beta)(j)})/2, \tag{B.14}$$

which can be used as the principal values of an ellipse, as shown in Figure B.4. The intersection of the ellipse and a relative position vector of material points $\boldsymbol{x}_{(i)}$ and $\boldsymbol{x}_{(j)}$, $\boldsymbol{n}$, provides the correction factors as

$$G_{(\beta)(i)(j)} = \left([n_x/\bar{g}_{(\beta)(i)(j)x}]^2 + [n_y/\bar{g}_{(\beta)(i)(j)y}]^2\right)^{-\frac{1}{2}}. \tag{B.15}$$

After considering the surface effects, the discrete form of the equations of motion given in (13) is corrected as

$$\rho(\boldsymbol{x}_{(i)})\ddot{\boldsymbol{u}}(\boldsymbol{x}_{(i)}, t) = \sum_{j=1}^{M} \begin{pmatrix} a_{(i)(j)} G_{(f)(i)(j)} \boldsymbol{f}\left(\boldsymbol{u}(\boldsymbol{x}_{(j)}, t) - \boldsymbol{u}(\boldsymbol{x}_{(i)}, t), \boldsymbol{x}_{(j)} - \boldsymbol{x}_{(i)}\right) + \\ b_{(i)(j)} G_{(m)(i)(j)} \boldsymbol{f}\left(\boldsymbol{u}(\boldsymbol{x}_{(j)}, t) - \boldsymbol{u}(\boldsymbol{x}_{(i)}, t), \boldsymbol{x}_{(j)} - \boldsymbol{x}_{(i)}\right) \end{pmatrix} V_{(j)} + \boldsymbol{b}(\boldsymbol{x}_{(i)}, t). \tag{B.16}$$

where the coefficients $a_{(i)(j)}$ and $b_{(i)(j)}$ take a value of either 1 or 0 if the interaction between material points $\boldsymbol{x}_{(i)}$ and $\boldsymbol{x}_{(j)}$ is a fiber bond or a matrix bond, respectively.

Based on numerical experimentation with varying values of displacement gradients, there is no significant effect on the surface corrections. Thus, the displacement gradient $\partial u_x^*/\partial x$ is assigned a value of 0.001.

## Appendix C: PD interlayer and shear bond constants of a laminate

The interlayer bond constant, $c_{in}$, and the shear bond constant, $c_{is}$, shown in Figure C.1, can be expressed in terms of engineering constants based on the transverse normal and shear deformation response of the isotropic matrix material by equating the total strain energy density of interlayer and shear bonds

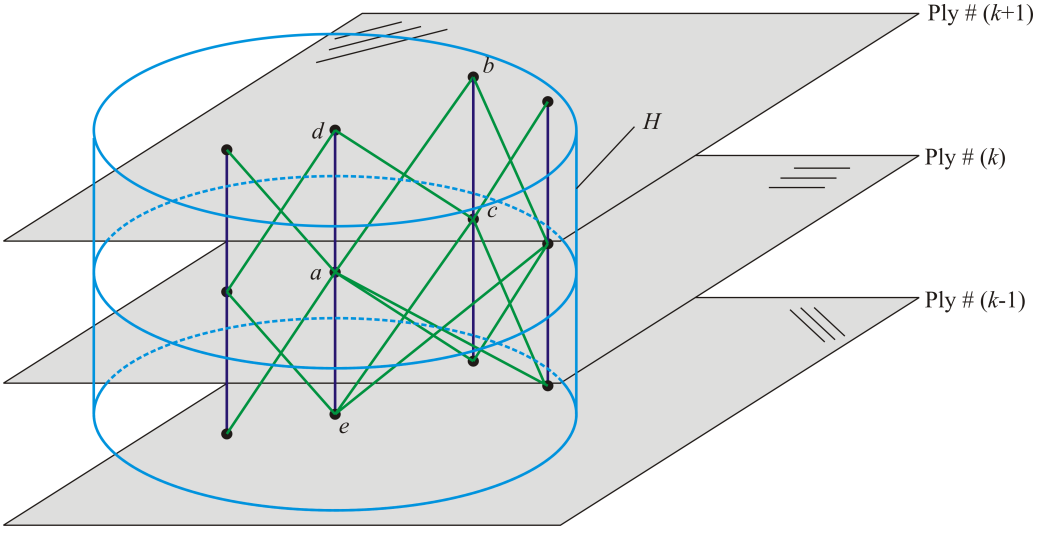


**Figure C.1.** Interlayer and shear bonds between neighboring plies (only some of the interactions are depicted explicitly for clarity).

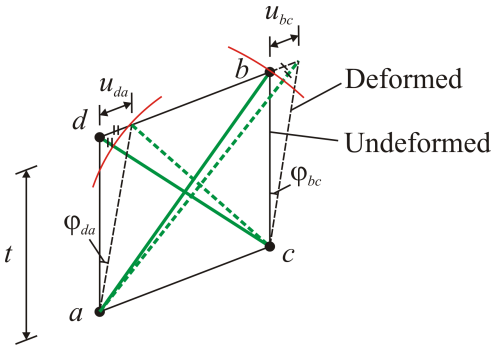


**Figure C.2.** Shear bonds between material points $b$ and $a$, and between material points $d$ and $c$, in both undeformed and deformed configurations.

calculated from PD theory and classical continuum mechanics. The strain energy density of the interlayer bonds associated with the material point $a$ can be computed by summing the strain energy density of the two interlayer bonds between material points $d$ and $e$ and the material point $a$ (Figure C.1). It can be readily obtained by multiplying the micropotential given in (8a) with the material volume.

Furthermore, the strain energy density of shear bonds can be obtained by using $(28)_2$ in conjunction with (7). Thus, the total strain energy density due to the interlayer and shear bonds can be computed as

$$U_{\mathrm{PD}} = \frac{1}{2}\sum_{j=d,e}\frac{c_{in}s_{ja}^2\xi_{ja}}{2}V_j + \frac{1}{2}\int_H \frac{c_{is}\varphi^2}{2}\,dH. \tag{C.1}$$

The expression for the shear angle in (C.1) is obtained by determining the average shear angle inside the quadrilateral formed by material points $a$, $b$, $c$, and $d$, as shown in Figure C.2. Averaging is achieved by computing the shear angles along the lines between material points $a$ and $d$, and $b$ and $c$, which are defined as $\varphi_{da}$ and $\varphi_{bc}$, respectively.

These shear angles are obtained from the ratio of the displacements $u_{da}$ and $u_{bc}$ of material points $d$ and $b$ with respect to $a$ and $c$, respectively, to the ply thickness, $t$, as

$$\varphi_{da} = \frac{u_{da}}{t}, \qquad \varphi_{bc} = \frac{u_{bc}}{t}. \tag{C.2}$$

The relative displacements $u_{da}$ and $u_{bc}$ are approximated as the change in length of the bonds between material points $d$ and $c$, and $b$ and $a$, respectively,

$$u_{da} = -\big(|\boldsymbol{\xi}_{dc} + \boldsymbol{\eta}_{dc}| - |\boldsymbol{\xi}_{dc}|\big), \tag{C.3a}$$

$$u_{bc} = |\boldsymbol{\xi}_{ba} + \boldsymbol{\eta}_{ba}| - |\boldsymbol{\xi}_{ba}|. \tag{C.3b}$$

Note that the minus sign in (C.3a) arises due to the contraction of the shear bond between material points $d$ and $c$, whereas the bond between material points $b$ and $a$ extends. The average value of the shear strains $\varphi_{da}$ and $\varphi_{bc}$ results in

$$\varphi = \frac{\varphi_{da} + \varphi_{bc}}{2} = \frac{(|\boldsymbol{\xi}_{ba} + \boldsymbol{\eta}_{ba}| - |\boldsymbol{\xi}_{ba}|) - (|\boldsymbol{\xi}_{dc} + \boldsymbol{\eta}_{dc}| - |\boldsymbol{\xi}_{dc}|)}{2t}, \tag{C.4}$$

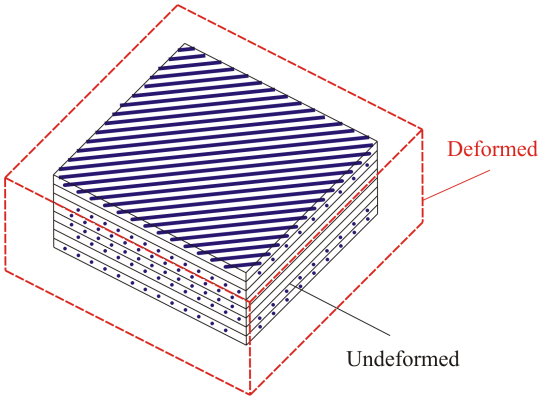


**Figure C.3.** A composite laminate subjected to isotropic expansion loading.

where $\boldsymbol{\xi}_{ba}$ and $\boldsymbol{\xi}_{dc}$ correspond to the bond vectors between material points $b$ and $a$, and between material points $d$ and $c$, respectively. Similarly, the vectors $\boldsymbol{\eta}_{ba}$ and $\boldsymbol{\eta}_{dc}$ are the relative displacement vectors between material points $b$ and $a$, and between material points $d$ and $c$, respectively.

In order to obtain the interlayer bond constant, the laminate is subjected to an isotropic expansion loading of $s = \zeta$, as shown in Figure C.3.

For a material point, $a$, located in the $k$-th ply of the laminate (Figure C.4), the contributions of the interlayer and shear bonds to the strain energy density of the material point due to isotropic expansion loading can be calculated using (C.1)

$$U_{\mathrm{PD}} = \frac{1}{2} \sum_{j=d,e} \frac{c_{in} s_{ja}^2 \xi_{ja}}{2} V_j. \tag{C.5}$$

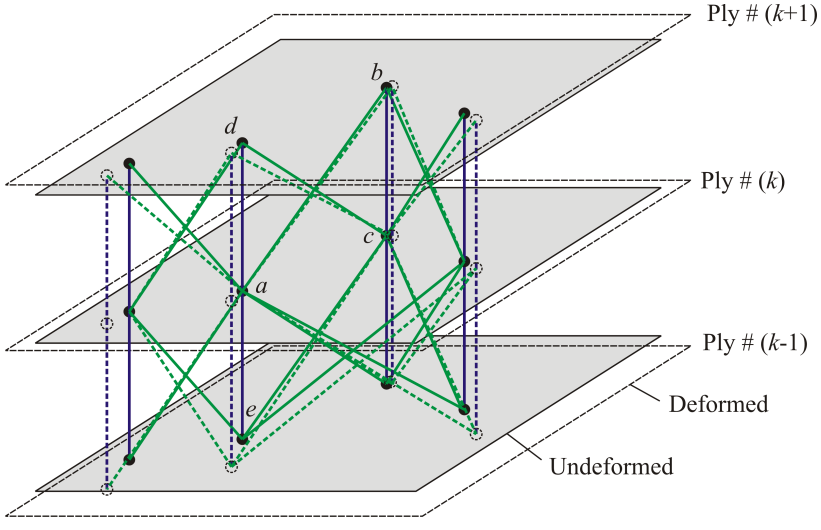


**Figure C.4.** Deformation of interlayer and shear bonds between neighboring plies (only some of the interactions are depicted explicitly for clarity).

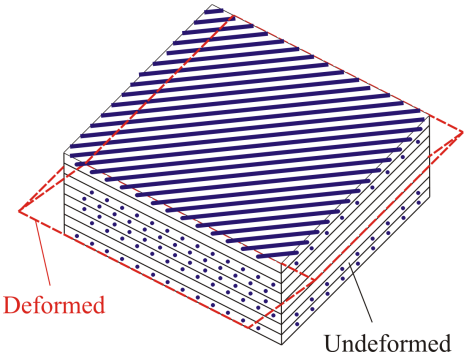


**Figure C.5.** A composite laminate subjected to simple shear loading.

Note that the shear strain, $\varphi$, defined in (C.2) has a zero value for this loading condition because the relative displacements $u_{da}$ and $u_{bc}$ given in (C.3a) and (C.3b) are equal in magnitude with opposite signs. Therefore, shear bonds do not have any contribution to the strain energy density for this loading condition. Both of the bond lengths $\xi_{da}$ and $\xi_{ea}$ are equivalent to the ply thickness, $t$. Therefore, for this loading condition, (C.5) can be evaluated as

$$U_{\mathrm{PD}} = \frac{c_{in}\zeta^2 t\overline{V}}{2}, \tag{C.6}$$

where $\overline{V}$ is equal to the volume of material points $d$ and $e$, that is, $\overline{V} = V_d = V_e$.

The corresponding strain energy density of the material point for the same loading condition can be calculated using classical continuum mechanics as

$$U_E = \tfrac{1}{2} E_m \zeta^2, \tag{C.7}$$

with $E_m$ representing the elastic modulus of the matrix material. Equating strain energy densities from (C.6) and (C.7) results in the relation between the interlayer bond constant, $c_{in}$, as

$$c_{in} = \frac{E_m}{t\overline{V}}. \tag{C.8}$$

The shear bond constant, $c_{is}$, can be evaluated similarly. In this case, the laminate is subjected to a simple shear loading of $\gamma = \zeta$, as shown in Figure C.5. For this loading condition, the interlayer bonds do not extend (Figure C.6). Therefore, their stretch values are zero. Hence, the interlayer bonds do not contribute to the strain energy density of the laminate.

As shown in Figure C.7, the original and deformed lengths of the shear bond between material points $b$ and $a$ can be expressed as

$$|\boldsymbol{\xi}_{ba}| = \sqrt{\ell^2 + t^2}, \tag{C.9a}$$

$$|\boldsymbol{\xi}_{ba} + \boldsymbol{\eta}_{ba}| = \sqrt{\bar{\ell}^2 + t^2}, \tag{C.9b}$$

where $t$ is the ply thickness.

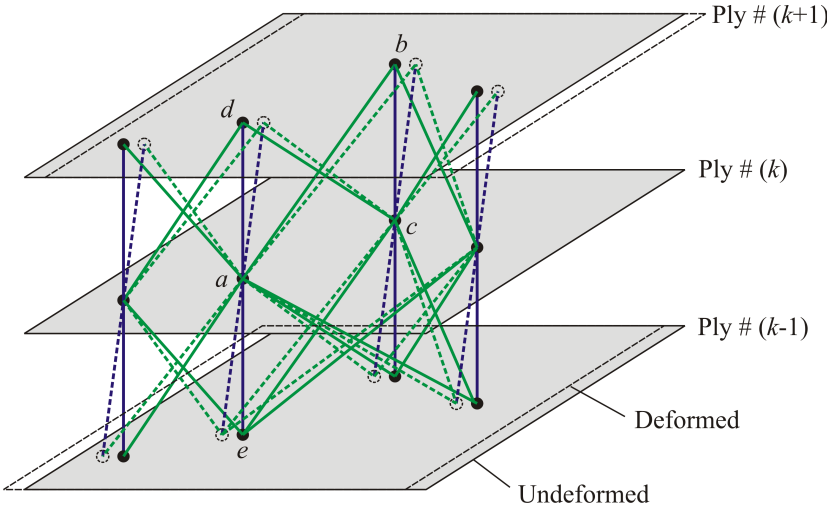


**Figure C.6.** Deformation of interlayer and shear bonds between neighboring plies (only some of the interactions are depicted explicitly for clarity).

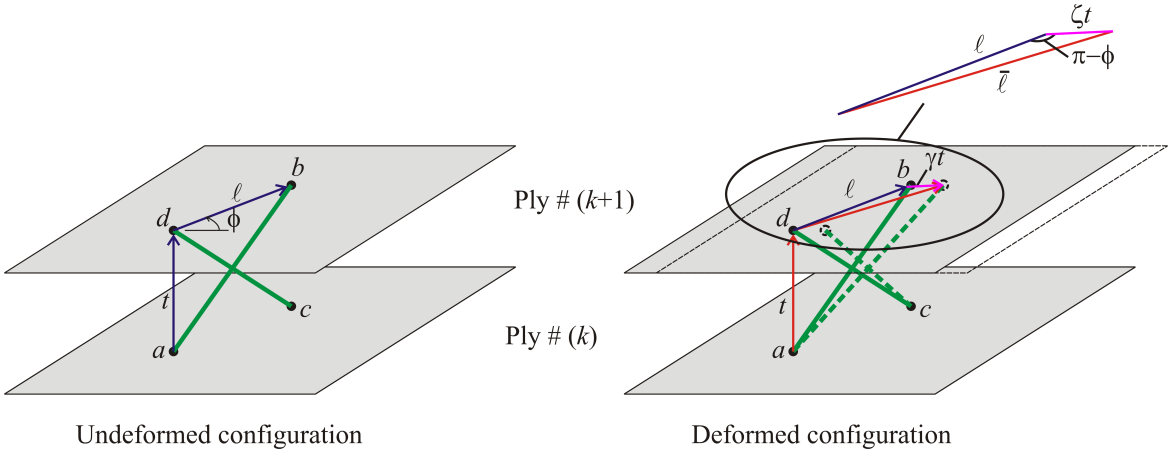


**Figure C.7.** Shear bonds between material points $b$ and $a$, and between material points $d$ and $c$, in both undeformed and deformed configurations.

For the triangle depicted in Figure C.7, by utilizing the law of cosines, the length of the radial component of the deformed bond vector, $\bar{\ell}$, can be written in terms of the length of the radial component of the original bond vector, $\ell$, and magnitude of displacement vector, $\zeta t$, as

$$\bar{\ell}^2 = \ell^2 + (\zeta t)^2 - 2\ell\zeta t \cos(\pi - \theta). \tag{C.10}$$

After substituting (C.10) in (C.9b), the deformed bond length can be rewritten as

$$|\boldsymbol{\xi}_{ba} + \boldsymbol{\eta}_{ba}| = \sqrt{\ell^2 + t^2 + 2\ell\zeta t \cos(\theta)}. \tag{C.11}$$

In deriving (C.11), the $(\zeta t)^2$ term is neglected with respect to $t^2$ because $\zeta$ is much less than unity. The square root term on the right-hand side of (C.11) can be further simplified by using the square root approximation

$$\sqrt{N^2+d} = N + \frac{d}{2N}, \tag{C.12}$$

where $d \ll N$. Therefore, the deformed bond length expression given in (C.11) can be rewritten as

$$|\boldsymbol{\xi}_{ba} + \boldsymbol{\eta}_{ba}| = \sqrt{\ell^2+t^2} + \frac{\ell\zeta t\cos(\theta)}{\sqrt{\ell^2+t^2}}. \tag{C.13}$$

The original and deformed bond lengths between material points $d$ and $c$ can be computed similarly as

$$|\boldsymbol{\xi}_{dc}| = \sqrt{\ell^2+t^2}, \tag{C.14a}$$

$$|\boldsymbol{\xi}_{dc} + \boldsymbol{\eta}_{dc}| = \sqrt{\ell^2+t^2} - \frac{\ell\zeta t\cos(\theta)}{\sqrt{\ell^2+t^2}}. \tag{C.14b}$$

Therefore, the shear angle for this loading condition can be computed using (C.4) as

$$\varphi = \frac{\ell\zeta\cos(\theta)}{\sqrt{\ell^2+t^2}}. \tag{C.15}$$

After substituting the shear angle expression given in (C.15) to the strain energy density expression given in (C.1), performing the integration results in

$$U_{\mathrm{PD}} = \left\{\frac{\pi c_s t}{4}\left(\delta^2 + t^2\ln\frac{t^2}{t^2+\delta^2}\right)\right\}\zeta^2. \tag{C.16}$$

The corresponding strain energy density based on classical continuum mechanics can be computed as

$$U_{\mathrm{CCM}} = \tfrac{1}{2}G_m\zeta^2. \tag{C.17}$$

After equating the strain energy densities calculated from PD theory and classical continuum mechanics, that is, (C.16) and (C.17), leads to the explicit form of the shear bond constant in terms of the shear modulus of the matrix material, $G_m$,

$$c_{i\mathrm{S}} = \frac{2G_m}{\pi t}\,\frac{1}{\left(\delta^2 + t^2\ln\left(\frac{t^2}{\delta^2+t^2}\right)\right)}. \tag{C.18}$$

## Appendix D: Critical stretch values for bond constants

The critical stretch value for fiber and matrix bonds can be obtained by performing various experiments as explained in [Oterkus et al. 2012]. In this study, for simplicity, the matrix bond constant is evaluated by using the critical stretch expression given by (12) for an isotropic matrix material, that is, epoxy. The derivation of this critical stretch expression is given by [Silling and Askari 2005]. The elastic, bulk, and shear moduli of the epoxy material are specified as $E_m = 3.792\,\mathrm{GPa}$, $\kappa_m = 3.792\,\mathrm{GPa}$, and $G_m = 1.422\,\mathrm{GPa}$, respectively. It has a critical energy release rate of $G_{\mathrm{IC}} = 2.37\times10^{-3}$ MPa-m. Therefore,

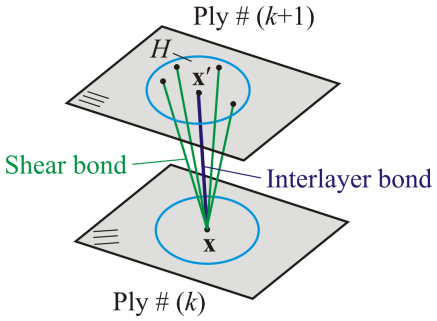


**Figure D.8.** Interlayer and shear bonds between material point $\boldsymbol{x}$ and other material points located at the $(k+1)$-th ply.

the critical stretch expression of the matrix bond for a horizon value of $\delta = 1.92 \times 10^{-3}$ m can be computed as

$$s_{\text{mt}} = \sqrt{\frac{5G_{\text{IC}}}{9\kappa_m \delta}} = 0.0135. \tag{D.1}$$

The critical stretch for the interlayer bond, $s_{i\text{n}}$, can be computed by equating the energy required to break an interlayer bond between material point $\boldsymbol{x}$ located at the $k$-th ply and material point $\boldsymbol{x}'$ located at the $(k+1)$-th ply, shown in Figure D.8, to the mode-I critical energy release rate of the material $G_{\text{IC}}$ as

$$t\left(\frac{c_{i\text{n}} s_{i\text{n}}^2 t}{2}\right)\overline{V} = G_{\text{IC}}, \tag{D.2}$$

where $t$ and $\overline{V}$ represent the thickness of the ply and the volume of the material point, $\boldsymbol{x}'$, respectively.

Using the relation given by (D.2) in conjunction with the bond constant expression given by $(27)_1$ results in the critical stretch expression for the interlayer bond as

$$s_{i\text{n}} = \sqrt{\frac{2G_{\text{IC}}}{t E_m}}. \tag{D.3}$$

This critical stretch value for epoxy material with a ply thickness of $t = 1.651 \times 10^{-4}$ m is computed as $s_{i\text{n}} = 0.087$.

As opposed to interlayer bonds, multiple shear bonds exist between the material point $\boldsymbol{x}$ and other material points in the $(k+1)$-th ply, as shown in Figure D.8. The failure of these shear bonds corresponds to a mode-II type of failure. Therefore, the energy required to break all of these shear bonds can be equated to the mode-II critical energy release rate of the material, $G_{\text{IIC}}$, as

$$t\int_H \frac{c_{i\text{s}}\varphi_c^2}{2}\, dH = G_{\text{IIC}}, \tag{D.4}$$

where $\varphi_c$ is the critical shear angle. This equation is rewritten, after splitting the domain of integration, as

$$t\left(t\frac{c_{i\text{s}}\varphi_c^2}{2}\int_0^{\delta} \ell\, d\ell \int_0^{2\pi} d\phi\right) = G_{\text{II}}. \tag{D.5}$$

Performing the integrations results in the critical shear angle expression:

$$\varphi_c = \sqrt{\frac{G_{\mathrm{IIC}}}{tG_m}}. \tag{D.6}$$

As explained in [Araki et al. 2005], the value of the mode-II critical energy release rate of the material, $G_{\mathrm{IIC}}$, is dependent on the postcuring temperature of epoxy. Therefore, it is assumed that $G_{\mathrm{IIC}}$ is equal to $\frac{3}{4}G_{\mathrm{IC}}$, which results in the critical shear angle, $\varphi_c$, being equal to the critical stretch, $s_{i\mathrm{n}}$, that is, $\varphi_c = s_{i\mathrm{n}} = 0.087$.

## References


[Araki et al. 2005] W. Araki, K. Nemoto, T. Adachi, and A. Yamaji, "Fracture toughness for mixed mode I/II epoxy resin", *Acta Mater.* **53**:3 (2005), 869–875.

[Askari et al. 2006] E. Askari, J. Xu, and S. Silling, "Peridynamic analysis of damage and failure in composites", in *44th AIAA/ASME/ASCE/AHS/ASC Aerospace Sciences Meeting and Exhibit* (Reno, NV, 2006), AIAA, Reston, VA, 2006. Paper #2006-88.

[Bogert et al. 2006] P. B. Bogert, A. Satyanarayana, and P. B. Chuncu, "Comparison of damage path predictions for composite laminates by explicit and standard finite element analysis tools", in *47th AIAA/ASME/ASCE/AHS/ASC Structures, Structural Dynamics, and Materials Conference* (Newport, RI, 2006), AIAA, Reston, VA, 2006. Paper #2006-1750.

[Colavito et al. 2007a] K. W. Colavito, B. Kilic, E. Celik, E. Madenci, E. Askari, and S. Silling, "Effect of nanoparticles on stiffness and impact strength of composites", in *48th AIAA/ASME/ASCE/AHS/ASC Structures, Structural Dynamics, and Materials Conference* (Honolulu, 2007), AIAA, Reston, VA, 2007. Paper #2007-2021.

[Colavito et al. 2007b] K. W. Colavito, B. Kilic, E. Celik, E. Madenci, E. Askari, and S. Silling, "Effect of void content on stiffness and strength of composites by peridynamic analysis and static indentation test", in *48th AIAA/ASME/ASCE/AHS/ASC Structures, Structural Dynamics, and Materials Conference* (Honolulu, 2007), AIAA, Reston, VA, 2007. Paper #2007-2251.

[Gerstle et al. 2005] W. Gerstle, N. Sau, and A. Silling, "Peridynamic modeling of plain and reinforced concrete structures", pp. 54–68 in *18th International Conference on Structural Mechanics in Reactor Technology* (Beijing, 2005), SMiRT **18**, IASMiRT, Raleigh, NC, 2005. Paper #B01-2.

[Green et al. 2007] B. G. Green, M. R. Wisnom, and S. R. Hallet, "An experimental investigation into the tensile strength scaling of notched composites", *Compos. A Appl. Sci. Manuf.* **38**:3 (2007), 867–878.

[Hallett and Wisnom 2006] S. R. Hallett and M. R. Wisnom, "Experimental investigation of progressive damage and the effect of layup in notched tensile tests", *J. Compos. Mater.* **40**:2 (2006), 119–141.

[Kaw 2006] A. K. Kaw, *Mechanics of composite materials*, 2nd ed., CRC Press, Boca Raton, FL, 2006.

[Kilic 2008] B. Kilic, *Peridynamic theory for progressive failure prediction in homogeneous and heterogeneous materials*, Ph.D. thesis, Department of Aerospace and Mechanical Engineering, University of Arizona, Tucson, AZ, 2008.

[Kilic et al. 2009] B. Kilic, A. Agwai, and E. Madenci, "Peridynamic theory for progressive damage prediction in centre-cracked composite laminates", *Compos. Struct.* **90**:2 (2009), 141–151.

[Macek and Silling 2007] R. W. Macek and S. A. Silling, "Peridynamics via finite element analysis", *Finite Elem. Anal. Des.* **43**:15 (2007), 1169–1178.

[Oterkus and Madenci 2012] E. Oterkus and E. Madenci, "Peridynamics based on the principle of virtual work", in *53th AIAA/ASME/ASCE/AHS/ASC Structures, Structural Dynamics, and Materials Conference* (Honolulu, 2012), AIAA, Reston, VA, 2012.

[Oterkus et al. 2010] E. Oterkus, A. Barut, and E. Madenci, "Damage growth prediction from loaded composite fastener holes by using peridynamic theory", in *51st AIAA/ASME/ASCE/AHS/ASC Structures, Structural Dynamics, and Materials Conference* (Orlando, FL, 2010), AIAA, Reston, VA, 2010. Paper #2010-3026.

[Oterkus et al. 2012] E. Oterkus, E. Madenci, O. Weckner, S. Silling, P. Bogert, and A. Tessler, "Combined finite element and peridynamic analyses for predicting failure in a stiffened composite curved panel with a central slot", *Compos. Struct.* **94** (2012), 839–850.

[Satyanarayana et al. 2007] A. Satyanarayana, P. B. Bogert, and P. B. Chuncu, "The effect of delamination on damage path and failure load prediction for notched composite laminates", in *48th AIAA/ASME/ASCE/AHS/ASC Structures, Structural Dynamics, and Materials Conference* (Honolulu, 2007), AIAA, Reston, VA, 2007. Paper #2007-1993.

[Silling 2000] S. A. Silling, "Reformulation of elasticity theory for discontinuities and long-range forces", *J. Mech. Phys. Solids* **48**:1 (2000), 175–209.

[Silling and Askari 2005] S. A. Silling and E. Askari, "A meshfree method based on the peridynamic model of solid mechanics", *Comput. Struct.* **83**:17–18 (2005), 1526–1535.

[Silling et al. 2007] S. A. Silling, M. Epton, O. Weckner, J. Xu, and E. Askari, "Peridynamic states and constitutive modeling", *J. Elasticity* **88**:2 (2007), 151–184.

[Wu 1968] E. M. Wu, "Fracture mechanics of anisotropic plates", pp. 20–43 in *Composite Materials Workshop* (St. Louis, MO, 1967), edited by S. W. Tsai et al., Progress in Materials Science **1**, Technomic, Stamford, CT, 1968.

[Xu et al. 2007] J. Xu, A. Askari, O. Weckner, H. Razi, and S. Silling, "Damage and failure analysis of composite laminates under biaxial loads", in *48th AIAA/ASME/ASCE/AHS/ASC Structures, Structural Dynamics, and Materials Conference* (Honolulu, 2007), AIAA, Reston, VA, 2007. Paper #2007-2315.

[Xu et al. 2008] J. Xu, A. Askari, O. Weckner, and S. Silling, "Peridynamic analysis of impact damage in composite laminates", *J. Aerosp. Eng.* (*ASCE*) **21**:3 (2008), 187–194.

Received 2 Dec 2010. Revised 13 Aug 2011. Accepted 4 Sep 2011.

ERKAN OTERKUS: erkan.oterkus@strath.ac.uk
*Department of Naval Architecture and Marine Engineering, University of Strathclyde, Henry Dyer Building, 100 Montrose street, Glasgow G4 0LZ, United Kingdom*

ERDOGAN MADENCI: madenci@email.arizona.edu
*Department of Aerospace and Mechanical Engineering, The University of Arizona, Tucson, AZ 85721-0119, United States*

JOURNAL OF MECHANICS OF MATERIALS AND STRUCTURES
Vol. 7, No. 1, 2012

msp

# POSTBUCKLING AND DELAMINATION GROWTH FOR DELAMINATED PIEZOELECTRIC ELASTOPLASTIC LAMINATED BEAMS UNDER HYGROTHERMAL CONDITIONS

YING-LI LI, YI-MING FU AND HONG-LIANG DAI

The postbuckling and delamination growth for delaminated piezoelectric elastoplastic laminated beams under hygrothermal conditions are investigated. By considering hygrothermal environments, transverse shear deformation, geometrical nonlinearity and piezoelectric effect, the incremental nonlinear equilibrium equations of the piezoelectric elastoplastic laminated beams with delamination are obtained. The finite difference method and iterative method are adopted to solve the equations. Based on these, the delamination growth for the piezoelectric elastoplastic laminated beams is studied using J-integral theory. In the numerical examples, the effects of hygrothermal environments, transverse shear deformation, geometrical nonlinearity and piezoelectricity on the postbuckling behavior and delamination growth for the delaminated piezoelectric elastoplastic laminated beams are discussed in detail.

## 1. Introduction

Piezoelectric laminated structures have great application potential in mechanical, aerospace, nuclear, reactor, and civil engineering, and in many modern industries due to their excellent properties. The challenge is that, during the manufacturing and service process, damage can arise that weakens the mechanical properties and reduce significantly the service life of the structure. Delamination is the main form of damage in laminated structures, and its growth has a detrimental influence on the behavior of the structure. The concentration of load-induced stress along the delamination front an cause delamination growth and ultimately lead to structural failure. At the same time, as structures can still bear loads after exceeding their yield limits, it is uneconomical to restrict structural design to the elastic regime. To make the best of the material, investigation should be extended to the mechanical properties in plastic stage.

Temperature and humidity variations cause hygrothermal stress, which also influences the performance of the piezoelectric composites. Consequently, it is important to analyze the postbuckling and delamination growth of delaminated piezoelectric elastoplastic beams by considering the effects of the hygrothermal conditions, transverse shear deformation, geometric nonlinearity, and the piezoelectric effect.

We mention some relevant studies. Davidson et al. [2000] analyzed energy release rates and stress intensity factors for delaminated composite laminates. Applying the finite element method, Nilsson et al. [2001] researched delamination buckling and growth in a slender composite panel. Park and Sankar [2002] and Wang and Qiao [2004] computed energy release rates of delaminated plates with the first-order shear deformable theory. A boundary layer theory of shell buckling was extended to the case of shear deformable laminated cylindrical panels under hygrothermal environments and a singular perturbation technique was employed to determine the buckling loads and postbuckling equilibrium paths in [Shen

*Keywords:* hygrothermal conditions, piezoelectric effect, postbuckling, delamination growth, J-integral.

2002; Shen 2001]. Tafreshi [2006] used the virtual crack closure technique to find the distribution of the local strain energy release rate along the delamination front. Münch and Ousset [2002] developed a numerical method to simulate delamination growth in layered composite structures within the framework of fracture mechanics in large displacement.

Much research has been conducted in elastoplastic mechanics. But most existing elastoplastic models are based on Hill's yield criterion, which suppose the material yield is independent of the spherical stress tensor. Actually, under the acting of the spherical stress tensor, the structures will be distorted due to the different elastic constants in each principal direction. According to the von Mises distortion energy yield criteria, the materials will get into the plastic stage if the distortion energy reaches a certain value, and the materials have apparent Bauschinger effect under the action of the stresses. Hence, Hill's hypothesis is inconsistent with the practical situation. Against the flaw mentioned above, Yuan and Zheng [1990] established a new yield criterion that relate to the spherical stress tensor, and obtained the associated plastic flow law for the elastoplastic material. Pi and Bradford [2003] investigated elastic and elasto-plastic flexural–torsional buckling and postbuckling behavior of arches that are subjected to a central concentrated load by using the rational finite element model.

In order to analysis the growth of the delamination, we have to get a clue of the stress field along the delamination front. Rice [1968] proposed the $J$ integral theory in 1968 and used an integral to describe the intensity of the stress and strain field in the vicinity of the crack tip of elastoplastic structure. Yang et al. [2002] studied the theory of $J$ integral near crack tip in the plate of linear-elastic orthotropic composite material by using a complex function method. Simha et al. [2008] discussed the crack driving force in elastic–plastic materials, with particular emphasis on incremental plasticity, by using the configurational forces approach and standard constitutive models for finite strain. Based on the law of conservation of energy, the generalized piezoelectric $J$ integral was defined in [Pak and Herrmann 1986; Pak 1990; Zuo and Sih 2000], including piezoelectric effects and was proved to be unaffected by the choice of a contour. However, up to now, the analysis of delaminated piezoelectric elastoplastic laminated beams is still open.

This paper aims to study the postbuckling behavior and energy release rate of the delaminated piezoelectric elastoplastic laminated beams and investigate the effects of hygrothermal conditions, transverse shear deformation, geometric nonlinearity and piezoelectricity on their behavior. The incremental theory of elastoplastic is employed to derive the governing equations. The numerical solutions are obtained by using the finite difference method and the iteration method. Numerical simulations demonstrate the effects of the hygrothermal conditions, yield stress, piezoelectricity, slenderness ratio, delamination size, and delamination length on postbuckling behavior and energy release rate.

## 2. Elastoplastic constitutive models of mixed hardening orthotropic materials

In the case of the elastoplastic deformation, we make these assumptions:

(1) Spherical stress tensors produce plastic deformations, and plastic strains are compressible.

(2) Uniform dilatation produced by active stresses will not influence the plastic deformation.

(3) The yield surface moves and expands along with plastic deformation.

(4) The dimensionless yield criterion of orthotropic material is isomorphic with the von Mises criterion of isotropic material.

Based on there assumptions, Tian et al. [2009] defined the dimensionless yield function as

$$f = \frac{K^2}{2}\big[(\tilde{\sigma}_{11}^{'} - \tilde{\sigma}_{22}^{'})^2 + (\tilde{\sigma}_{22}^{'} - \tilde{\sigma}_{33}^{'})^2 + (\tilde{\sigma}_{33}^{'} - \tilde{\sigma}_{11}^{'})^2 + 2(\tilde{\sigma}_{44}^{'2} + \tilde{\sigma}_{55}^{'2} + \tilde{\sigma}_{66}^{'2})\big], \tag{1}$$

where

$$\tilde{\sigma}_{ij}^{'} = \frac{\sigma_{ij} - b_{ij}}{\Sigma_{ij}} \quad \text{(no sum over } i, j), \tag{2}$$

The constant $K$, with dimensions of stress, can be determined by experiments in the simple stress state; $\sigma_{ij}$ and $\Sigma_{ij}$ are the stress tensor and yield stress tensor components, respectively, along each direction of orthotropic materials; $b_{ij}$ is the back stress tensor, which represents the transition of the center of the yield surface, and reflects the kinematics hardening.

By defining the effective active stress as

$$\tilde{\sigma} = \frac{K}{\sqrt{2}}\sqrt{(\tilde{\sigma}_{11}^{'} - \tilde{\sigma}_{22}^{'})^2 + (\tilde{\sigma}_{22}^{'} - \tilde{\sigma}_{33}^{'})^2 + (\tilde{\sigma}_{33}^{'} - \tilde{\sigma}_{11}^{'})^2 + 2(\tilde{\sigma}_{44}^{'2} + \tilde{\sigma}_{55}^{'2} + \tilde{\sigma}_{66}^{'2})}, \tag{3}$$

the mixed hardening yield function can be given as

$$F_p = f(\tilde{\sigma}_{ij}^{'}) - [\tilde{\sigma}(\bar{\varepsilon}^p)]^2, \tag{4}$$

where $\tilde{\sigma}$ is the effective stress defined in (3), which is the function of effective plastic strain $\bar{\varepsilon}^p$, and can be acquired by the simple extension experimental curves.

Assuming a non-associated flow rule, the plastic part of the strain tensor increment $d\varepsilon_{ij}^p$ is proportional to the gradient of the stress function $F_p$, commonly named plastic potential function

$$d\varepsilon_{ij}^p = \lambda_p \frac{\partial F_p}{\partial \sigma_{ij}} = \lambda_p \frac{\partial f}{\partial \sigma_{ij}}, \tag{5}$$

where $\lambda_p$ is a non-negative scalar called plastic multiplier or consistency parameter.

Substituting (1) and (2) into (4), the following formulas can be obtained

$$\begin{aligned}
d\varepsilon_{11}^p &= \lambda_p \frac{K^2}{\Sigma_{11}}(2\tilde{\sigma}_{11}^{'} - \tilde{\sigma}_{22}^{'} - \tilde{\sigma}_{33}^{'}), \quad d\varepsilon_{44}^p = 2\lambda_p \frac{K^2}{\Sigma_{44}}\tilde{\sigma}_{44}^{'}, \\
d\varepsilon_{22}^p &= \lambda_p \frac{K^2}{\Sigma_{22}}(2\tilde{\sigma}_{22}^{'} - \tilde{\sigma}_{33}^{'} - \tilde{\sigma}_{11}^{'}), \quad d\varepsilon_{55}^p = 2\lambda_p \frac{K^2}{\Sigma_{55}}\tilde{\sigma}_{55}^{'}, \\
d\varepsilon_{33}^p &= \lambda_p \frac{K^2}{\Sigma_{33}}(2\tilde{\sigma}_{33}^{'} - \tilde{\sigma}_{11}^{'} - \tilde{\sigma}_{22}^{'}), \quad d\varepsilon_{66}^p = 2\lambda_p \frac{K^2}{\Sigma_{66}}\tilde{\sigma}_{66}^{'}.
\end{aligned} \tag{6}$$

Substituting (6) into (3), we have

$$\begin{aligned}
\tilde{\sigma} = \frac{1}{3\sqrt{2}K\lambda_p}\big((\Sigma_{11}d\varepsilon_{11}^p - \Sigma_{22}d\varepsilon_{22}^p)^2 + (\Sigma_{22}d\varepsilon_{22}^p - \Sigma_{33}d\varepsilon_{33}^p)^2 + (\Sigma_{33}d\varepsilon_{33}^p - \Sigma_{11}d\varepsilon_{11}^p)^2 \\
+ \tfrac{9}{2}[(\Sigma_{44}d\varepsilon_{44}^p)^2 + (\Sigma_{55}d\varepsilon_{55}^p)^2 + (\Sigma_{66}d\varepsilon_{66}^p)^2]\big)^{\frac{1}{2}}.
\end{aligned} \tag{7}$$

Define the effective plastic strain increment as

$$d\bar{\varepsilon}^p = \frac{\sqrt{2}}{3K}\big((\Sigma_{11}d\varepsilon_{11}^p - \Sigma_{22}d\varepsilon_{22}^p)^2 + (\Sigma_{22}d\varepsilon_{22}^p - \Sigma_{33}d\varepsilon_{33}^p)^2 + (\Sigma_{33}d\varepsilon_{33}^p - \Sigma_{11}d\varepsilon_{11}^p)^2 + \tfrac{9}{2}[(\Sigma_{44}d\varepsilon_{44}^p)^2 + (\Sigma_{55}d\varepsilon_{55}^p)^2 + (\Sigma_{66}d\varepsilon_{66}^p)^2]\big)^{\frac{1}{2}}. \quad (8)$$

According to (7) and (8), we obtain

$$d\bar{\varepsilon}^p = 2\tilde{\sigma}\lambda_p. \quad (9)$$

The plastic strain can be decomposed as

$$d\varepsilon_{ij}^p = d\varepsilon_{ij}^{p(\mathrm{I})} + d\varepsilon_{ij}^{p(\mathrm{II})}, \quad (10)$$

where $d\varepsilon_{ij}^{p(\mathrm{I})}$, the incremental plastic strain of isotropic hardening, and $d\varepsilon_{ij}^{p(\mathrm{II})}$, the incremental plastic strain of kinematics hardening, are defined by

$$d\varepsilon_{ij}^{p(\mathrm{I})} = a d\varepsilon_{ij}^p, \quad d\varepsilon_{ij}^{p(\mathrm{II})} = (1-a)\, d\varepsilon_{ij}^p. \quad (11)$$

Here $a$ is the mixed hardening parameter within span $(-1, 1)$; the value $a = 1$ denotes pure isotropic hardening, and $a = 0$ denotes pure kinematic hardening. When $a$ is negative, the yield surface shrinks. Other values denote mixed hardening. The incremental back stress tensor can be defined as a linear function of incremental plastic strain tensor of kinematics hardening:

$$db_{ij} = c d\varepsilon_{ij}^{p(\mathrm{II})}, \quad (12)$$

where $c$ is the ratio constant. According to (5) and (11), the back stress increment can be expressed as

$$db_{ij} = c(1-a)\lambda_p \frac{\partial f}{\partial \sigma_{ij}}. \quad (13)$$

The total strain increment is decomposed into elastic and plastic strain increments:

$$d\varepsilon_{ij} = d\varepsilon_{ij}^e + d\varepsilon_{ij}^p. \quad (14)$$

The elastic constitutive equation is

$$d\sigma_{ij} = C_{ijkl}^e d\varepsilon_{kl}^e; \quad (15)$$

using (14) and (15), one gets

$$d\sigma_{ij} = C_{ijkl}^e \left( d\varepsilon_{kl} - \lambda_p \frac{\partial f}{\partial \sigma_{kl}} \right). \quad (16)$$

According to the consistency condition, and letting $H' = d\tilde{\sigma}/d\bar{\varepsilon}^p$, from (4), we have

$$\frac{\partial f}{\partial \tilde{\sigma}_{ij}'} d\tilde{\sigma}_{ij}' - 2\tilde{\sigma} H' d\bar{\varepsilon}^p = 0. \quad (17)$$

Substituting (5), (9), (13) and (16) into this, we obtain

$$\lambda_p = \frac{X_{ij} d\varepsilon_{ij}}{S}, \quad (18)$$

where

$$X_{ij} = \frac{1}{\Sigma_{kl}} \frac{\partial f}{\partial \tilde{\sigma}'_{kl}} C^e_{klij},$$
$$S = \frac{1}{\Sigma_{ij}} \frac{\partial f}{\partial \tilde{\sigma}'_{ij}} C^e_{ijkl} \frac{1}{\Sigma_{kl}} \frac{\partial f}{\partial \tilde{\sigma}'_{kl}} + \frac{1}{\Sigma_{ij}} \frac{\partial f}{\partial \tilde{\sigma}'_{ij}} c(1-\alpha) \frac{1}{\Sigma_{ij}} \frac{\partial f}{\partial \tilde{\sigma}'_{ij}} + 4\tilde{\sigma}^2 H'. \tag{19}$$

Substituting (18) into (16), the incremental elastoplastic constitutive equation can be written as

$$d\sigma_{ij} = (C^e_{ijkl} - C^p_{ijkl})\, d\varepsilon_{kl}, \tag{20}$$

where $C^p_{ijkl} = X_{ij} X_{kl}/S$. Therefore, the incremental elastoplastic constitutive equation of orthotropic materials is

$$d\sigma_{ij} = (C^e_{ijkl} - \chi C^p_{ijkl})\, d\varepsilon_{kl}. \tag{21}$$

If $F_p = 0$ and $\dfrac{\partial f}{\partial \sigma_{ij}} d\sigma_{ij} > 0$, then $\chi = 1$. If $F_p < 0$ or $\dfrac{\partial f}{\partial \sigma_{ij}} d\sigma_{ij} \le 0$, then $\chi = 0$.

## 3. Fundamental equations of delaminated piezoelectric laminated beams under hygrothermal conditions

Consider a delaminated piezoelectric laminated beam under an axial load $P$ depicted in Figure 1. The delaminated piezoelectric laminated beam is composed of a fiber-reinforced laminated beam and the upper and lower piezoelectric layers. Take the piezoelectric layers as elastic layers and the fiber-reinforced laminates to be elastoplastic. The global coordinate system $oxz$ is shown in Figure 1 and the reference

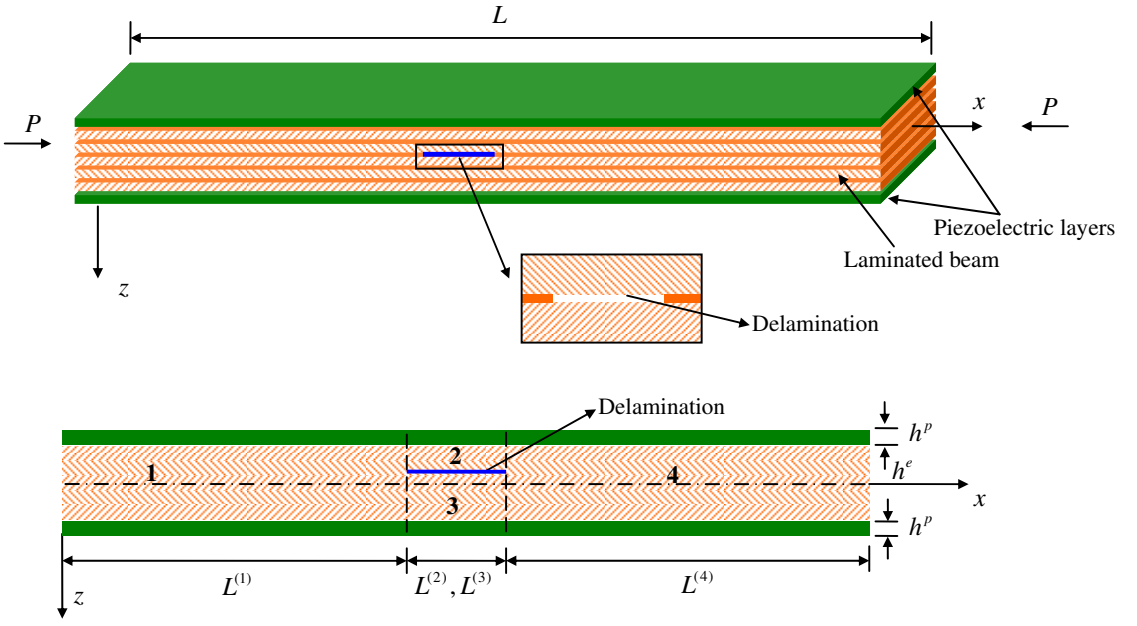


**Figure 1.** Geometric configuration (top) and transverse geometry (bottom) of piezoelectric laminated beam.

plane $z = 0$ is located at the midsurface of the undeformed laminated beams. The beam with throughout width delamination has length $L$, thickness $h^e$ and delaminated length $L^{(2)}$. $L^{(1)}$ is the distance from the left end of the delamination to that of the beam. In order to investigate the delamination growth, the delaminated laminated beam is divided into four regions which are respectively denoted as $\Omega^{(i)e}$ $(i = 1, 2, 3, 4)$. Here the indices 2 and 3 represent the delaminated segments, while 1 and 4 represent the intact segments. The length of each region is defined as $L^{(i)}$, and the coordinate $x$ for each region is measured from the left end. The thickness of regions 2 and 3 are $h^{(2)e}$ and $h^{(3)e}$ respectively, and obviously $h^{(2)e} + h^{(3)e} = h^e$. The piezoelectric layers with thickness $h^p$ are perfectly bonded on the upper and lower surfaces of the laminated beam. The corresponding piezoelectric layers bonded on the regions $\Omega^{(i)e}$ are denoted by $\Omega^{(i)p}$. Then the whole piezoelectric laminated beam is divided into four regions denoted by $\Omega^{(i)}$, and $\Omega^{(i)} = \Omega^{(i)e} + \Omega^{(i)p}$. The coordinate system of every region $ox^{(i)}z^{(i)}$ is located at the midsurface of the related region. The thickness of the whole piezoelectric laminated beams is $h = h^e + 2h^p$.

Supposing $\bar{u}^{(i)}$, $\bar{w}^{(i)}$ denote the displacements of an arbitrary point in region $\Omega^{(i)}$ throughout the $x$, $z$ direction, respectively, and $\phi^{(i)}$ denotes the angle the section rotate along the neutral axis, then the displacement components are given by

$$\begin{aligned} \bar{u}^{(i)}(x, z) &= u^{(i)}(x) + z\phi^{(i)}(x), \\ \bar{w}^{(i)}(x, z) &= w^{(i)}(x) + \tilde{w}^{(i)}(x), \end{aligned} \tag{22}$$

where $u^{(i)}$, $w^{(i)}$ are displacement components of the points on the midsurface. $\tilde{w}^{(i)}$ denotes the initial deflection and $x$, $z$ is the coordinate of corresponding region.

If that $\bar{\varepsilon}_x^{(i)}$, $\bar{\varepsilon}_{xz}^{(i)}$ are the strains of an arbitrary point in region $\Omega^{(i)}$, the nonlinear strain-displacement relations can be written as

$$\bar{\varepsilon}_x^{(i)} = \varepsilon_x^{(i)} + z\kappa_x^{(i)}, \quad \bar{\varepsilon}_{zx}^{(i)} = \varepsilon_{zx}^{(i)}, \tag{23}$$

where $\varepsilon_x^{(i)}$, $\varepsilon_{xz}^{(i)}$ are the strains of the corresponding points on the midsurface, and $\kappa_x^{(i)}$ is the curvature, and

$$\varepsilon_x^{(i)} = u_{,x}^{(i)} + \tfrac{1}{2}w_{,x}^{(i)2} + w_{,x}^{(i)}\tilde{w}_{,x}^{(i)}, \quad \varepsilon_{zx}^{(i)} = w_{,x}^{(i)} + \phi^{(i)}, \quad \kappa_x^{(i)} = \phi_{,x}^{(i)} \tag{24}$$

where the comma denotes the derivative with respect to the coordinate.

When the load acting on the beam varies, the displacement and strains of an arbitrary point of the beam would alter accordingly. Then, the strain increments of the midsurface are

$$d\varepsilon_x^{(i)} = du_{,x}^{(i)} + \tfrac{1}{2}dw_{,x}^{(i)2} + (w_{,x}^{(i)} + \tilde{w}_{,x}^{(i)})\, dw_{,x}^{(i)}, \quad d\varepsilon_{zx}^{(i)} = dw_{,x}^{(i)} + d\phi^{(i)}, \quad d\kappa_x^{(i)} = d\phi_{,x}^{(i)}. \tag{25}$$

The incremental elastoplastic stress-strain relations of a single layer for the fiber-reinforced laminated beam in the local coordinate can be obtained as

$$\begin{Bmatrix} d\sigma_x^{(i)k} \\ d\tau_{zx}^{(i)k} \end{Bmatrix} = \begin{pmatrix} C_{11}^e - \chi C_{11}^p & C_{15}^e - \chi C_{15}^p \\ C_{15}^e - \chi C_{15}^p & C_{55}^e - \chi C_{55}^p \end{pmatrix} \begin{Bmatrix} d\bar{\varepsilon}_x^{(i)k} \\ d\bar{\varepsilon}_{zx}^{(i)k} \end{Bmatrix}. \tag{26}$$

Under hygrothermal conditions, the incremental elastoplastic stress-strain relations of the $k$th layer for the fiber-reinforced laminated beam are

$$\begin{Bmatrix} d\sigma_x^{(i)k} \\ d\tau_{zx}^{(i)k} \end{Bmatrix} = \begin{pmatrix} Q_{11}^k & Q_{15}^k \\ Q_{15}^k & Q_{55}^k \end{pmatrix} \begin{Bmatrix} d\bar{\varepsilon}_x^{(i)k} - \vartheta_x^k dT - \gamma_x^k dc \\ d\bar{\varepsilon}_{zx}^{(i)k} \end{Bmatrix}, \tag{27}$$

where $\vartheta_x^k = \vartheta_{11}\cos^2\theta_k + \vartheta_{22}\sin^2\theta_k$, and $\gamma_x^k = \gamma_{11}\cos^2\theta_k + \gamma_{22}\sin^2\theta_k$. $d\sigma_x^{(i)k}$, $d\tau_{zx}^{(i)k}$ denote the normal stress and shear stress increments of any points in the laminated beam, respectively, and $Q_{ij}^k$ denotes the stiffness factor of the fiber-reinforced materials in the global coordinate. Denote $\theta_k$ as the playing angle of the $k$th layer, $\vartheta_{11}$, $\vartheta_{22}$ as the thermal expansion coefficients in the longitudinal and lateral direction of the orthotropic material, and $\gamma_{11}$, $\gamma_{22}$ as the humidity expansion coefficients. $dT$ is the variation of the temperature and $dc$ is the wet variation, which is defined as the ratio of the incremental mass $dM$ after moisture absorption to the dry mass $M$.

According to the (25) and (27), the incremental membrane stress resultants $dN^{(i)L}$, the shear stress resultants $dQ^{(i)L}$ and stress couples $dM^{(i)L}$ of the fiber-reinforced laminated beam can be written as

$$\begin{bmatrix} dN^{(i)L} \\ dQ^{(i)L} \\ dM^{(i)L} \end{bmatrix} = \begin{pmatrix} A_1^{(i)L} & A_2^{(i)L} & B_1^{(i)L} \\ A_2^{(i)L} & A_3^{(i)L} & B_2^{(i)L} \\ B_1^{(i)L} & B_2^{(i)L} & D_1^{(i)L} \end{pmatrix} \begin{Bmatrix} d\varepsilon_x^{(i)} \\ d\varepsilon_{zx}^{(i)} \\ d\kappa_x^{(i)} \end{Bmatrix} - \begin{Bmatrix} dN_T^{(i)} \\ dQ_T^{(i)} \\ dM_T^{(i)} \end{Bmatrix}, \tag{28}$$

where

$$\begin{aligned}
dN_T^{(i)} &= \int_{\Omega^{(i)e}} Q_{11}^k(\vartheta_x^k dT + \gamma_x^k dc)\, dz, & A_1^{(i)e} &= \int_{\Omega^{(i)e}} Q_{11}^k dz, & B_1^{(i)L} &= \int_{\Omega^{(i)e}} Q_{11}^k z\, dz, \\
dQ_T^{(i)} &= \int_{\Omega^{(i)e}} \eta Q_{15}^k(\vartheta_x^k dT + \gamma_x^k dc)\, dz, & A_2^{(i)L} &= \int_{\Omega^{(i)e}} Q_{15}^k dz, & B_2^{(i)L} &= \int_{\Omega^{(i)e}} Q_{15}^k z\, dz, \\
dM_T^{(i)} &= \int_{\Omega^{(i)e}} Q_{11}^k(\vartheta_x^k dT + \gamma_x^k dc) z\, dz, & A_3^{(i)L} &= \int_{\Omega^{(i)e}} \eta Q_{55}^k dz, & D_1^{(i)L} &= \int_{\Omega^{(i)e}} Q_{11}^k z^2 dz,
\end{aligned}$$

where the last term of (28) is the stress resultants and couples resulting from the hygrothermal conditions. $\eta$ denotes the shear stress modified coefficient, which is assumed as $\eta = 5/6$. As only cross-ply beams are considered in this paper, $Q_{15}^k = 0$ and $A_2^{(i)e} = B_2^{(i)e} = 0$.

The elastic constitutive relations of orthotropic piezoelectric layers can be described as

$$\begin{Bmatrix} \sigma_x^{(i)p} \\ \tau_{zx}^{(i)p} \end{Bmatrix} = \begin{pmatrix} Q_{11}^p & 0 \\ 0 & Q_{55}^p \end{pmatrix} \begin{Bmatrix} \bar{\varepsilon}_x^{(i)} \\ \bar{\varepsilon}_{xz}^{(i)} \end{Bmatrix} - \begin{pmatrix} 0 & e_{31} \\ 0 & 0 \end{pmatrix} \begin{Bmatrix} E_x^{(i)} \\ E_z^{(i)} \end{Bmatrix} - \begin{Bmatrix} \varsigma \\ 0 \end{Bmatrix} \Delta T, \tag{29}$$

$$\boldsymbol{D}^{(i)} = \begin{Bmatrix} D_x^{(i)} \\ D_z^{(i)} \end{Bmatrix} = \begin{pmatrix} 0 & 0 \\ e_{31} & 0 \end{pmatrix} \begin{Bmatrix} \bar{\varepsilon}_x^{(i)} \\ \bar{\varepsilon}_{xz}^{(i)} \end{Bmatrix} + \begin{pmatrix} t_{11} & 0 \\ 0 & t_{33} \end{pmatrix} \begin{Bmatrix} E_x^{(i)} \\ E_z^{(i)} \end{Bmatrix} = \boldsymbol{e} \cdot \begin{Bmatrix} \bar{\varepsilon}_x^{(i)} \\ \bar{\varepsilon}_{xz}^{(i)} \end{Bmatrix} + \boldsymbol{t} \cdot \boldsymbol{E}^{(i)}, \tag{30}$$

where $\sigma_x^{(i)p}$ and $\tau_{xz}^{(i)p}$ are the stress components of the piezoelectric layer, $\varsigma$ is the heat stress coefficient, $D_x^{(i)}$ and $D_z^{(i)}$ are the electric displacement components, $E_x^{(i)}$ and $E_z^{(i)}$ are the electric-field intensity components, $Q_{ij}^p$ is the elastic constant, $e_{ij}$ is the piezoelectric stress constant, and $t_{ij}$ are dielectric constants.

It is assumed that only the electric field component $E_z^{(i)}$ throughout the thickness direction is applied on the piezoelectric layers. Denoting $V_T^{(i)}$, $V_B^{(i)}$ and $E_T^{(i)}$, $E_B^{(i)}$ as the electric voltages and the electric-field intensity on the upper and down surface, respectively, then the following relations are obtained

$$E_T^{(i)} = V_T^{(i)}/h^p, \quad E_B^{(i)} = V_B^{(i)}/h^p. \tag{31}$$

According to (29) and (23), the membrane stress resultants $N^{(i)p}$, shear stress resultants $Q^{(i)p}$ and stress couples $M^{(i)p}$ of the piezoelectric layers can be written as

$$\begin{bmatrix} N^{(i)p} \\ Q^{(i)p} \\ M^{(i)p} \end{bmatrix} = \begin{pmatrix} A_1^{(i)p} & A_2^{(i)p} & B_1^{(i)p} \\ A_2^{(i)p} & A_3^{(i)p} & B_2^{(i)p} \\ B_1^{(i)p} & B_2^{(i)p} & D_1^{(i)p} \end{pmatrix} \begin{Bmatrix} \varepsilon_x^{(i)} \\ \varepsilon_{zx}^{(i)} \\ \kappa_x^{(i)} \end{Bmatrix} - \begin{Bmatrix} N_a^{(i)p} \\ 0 \\ M_a^{(i)p} \end{Bmatrix} - \begin{Bmatrix} N_e^{(i)p} \\ 0 \\ M_e^{(i)p} \end{Bmatrix}, \tag{32}$$

where the last term is the change of stress resultants and stress couples after applying voltages on piezoelectric layer, and

$$\begin{aligned} N_a^{(i)p} &= \int_{\Omega^{(i)p}} \varsigma \Delta T \, dz, & A_1^{(i)p} &= \int_{\Omega^{(i)p}} Q_{11}^p dz, & B_1^{(i)p} &= \int_{\Omega^{(i)p}} Q_{11}^p z \, dz, \\ M_a^{(i)p} &= \int_{\Omega^{(i)p}} \varsigma \Delta T z \, dz, & A_2^{(i)p} &= 0, & B_2^{(i)p} &= 0, \\ N_e^{(i)p} &= \int_{\Omega^{(i)p}} \boldsymbol{e} \cdot \boldsymbol{E}^{(i)} dz, & A_3^{(i)p} &= \int_{\Omega^{(i)p}} Q_{55}^p dz, & D_1^{(i)p} &= \int_{\Omega^{(i)p}} z^2 Q_{11}^p dz, \\ M_e^{(i)p} &= \int_{\Omega^{(i)p}} \boldsymbol{e} \cdot \boldsymbol{E}^{(i)} z \, dz. \end{aligned} \tag{33}$$

From (27) and (32), the membrane stress resultants $N^{(i)}$, shear stress resultants $Q^{(i)}$ and stress couples $M^{(i)}$ of piezoelectric laminated beam can be written as

$$\begin{aligned} \begin{bmatrix} N^{(i)} \\ Q^{(i)} \\ M^{(i)} \end{bmatrix} &= \begin{bmatrix} N^{(i)e} \\ Q^{(i)e} \\ M^{(i)e} \end{bmatrix} + \begin{bmatrix} N^{(i)p} \\ Q^{(i)p} \\ M^{(i)p} \end{bmatrix} \\ &= \begin{pmatrix} A_1^{(i)} & A_2^{(i)} & B_1^{(i)} \\ A_2^{(i)} & A_3^{(i)} & B_2^{(i)} \\ B_1^{(i)} & B_2^{(i)} & D_1^{(i)} \end{pmatrix} \begin{Bmatrix} \varepsilon_x^{(i)} \\ \varepsilon_{zx}^{(i)} \\ \kappa_x^{(i)} \end{Bmatrix} - \begin{Bmatrix} N_b^{(i)} \\ Q_b^{(i)} \\ M_b^{(i)} \end{Bmatrix} \\ &= \begin{pmatrix} A_1^{(i)e} + A_1^{(i)p} & A_2^{(i)e} + A_2^{(i)p} & B_1^{(i)e} + B_1^{(i)p} \\ A_2^{(i)e} + A_2^{(i)p} & A_3^{(i)e} + A_3^{(i)p} & B_2^{(i)e} + B_2^{(i)p} \\ B_1^{(i)e} + B_1^{(i)p} & B_2^{(i)e} + B_2^{(i)p} & D_1^{(i)e} + D_1^{(i)p} \end{pmatrix} \begin{Bmatrix} \varepsilon_x^{(i)} \\ \varepsilon_{zx}^{(i)} \\ \kappa_x^{(i)} \end{Bmatrix} - \begin{Bmatrix} N_T^{(i)} + N_a^{(i)p} + N_e^{(i)p} \\ Q_T^{(i)} \\ M_T^{(i)} + M_a^{(i)p} + M_e^{(i)p} \end{Bmatrix}, \end{aligned} \tag{34}$$

where

$$N_b^{(i)} = N_T^{(i)} + N_a^{(i)p} + N_e^{(i)p}, \quad Q_b^{(i)} = Q_T^{(i)}, \quad M_b^{(i)} = M_T^{(i)} + M_a^{(i)p} + M_e^{(i)p}. \tag{35}$$

According to the classical nonlinear theory of laminated plates, and in view of the effect of the shear stress resultants on the membrane stress resultants, the nonlinear equilibrium equations of the laminated beams with initial deflection are acquired as

$$N^{(i)}_{,x} - (Q^{(i)}\phi^{(i)})_{,x} = 0, \quad Q^{(i)}_{,x} + [N^{(i)}(w^{(i)}_{,x} + \tilde{w}^{(i)}_{,x})]_{,x} = 0, \quad Q^{(i)} - M^{(i)}_{,x} = 0. \tag{36}$$

When the axial load acting on the piezoelectric laminated beam increases by a small quantity $dP$, the incremental nonlinear equilibrium equations can be obtained as

$$\begin{aligned}
&dN^{(i)}_{,x} - Q^{(i)}_{,x}d\phi^{(i)} - dQ^{(i)}_{,x}\phi^{(i)} - dQ^{(i)}_{,x}d\phi^{(i)} - Q^{(i)}d\phi^{(i)}_{,x} - dQ^{(i)}\phi^{(i)}_{,x} - dQ^{(i)}d\phi^{(i)}_{,x} = 0,\\
&dQ^{(i)}_{,x} + dN^{(i)}_{,x}(w^{(i)}_{,x} + \tilde{w}^{(i)}_{,x}) + N^{(i)}_{,x}dw^{(i)}_{,x} + dN^{(i)}_{,x}dw^{(i)}_{,x} + dN^{(i)}(w^{(i)}_{,xx} + \tilde{w}^{(i)}_{,xx}) + N^{(i)}dw^{(i)}_{,xx} + dN^{(i)}dw^{(i)}_{,xx} = 0,\\
&dQ^{(i)} - dM^{(i)}_{,x} = 0.
\end{aligned} \tag{37}$$

By introducing the dimensionless parameters

$$\begin{aligned}
&\xi^{(i)} = \frac{x^{(i)}}{L^{(i)}}, \quad W^{(i)} = \frac{w^{(i)}}{h}, \quad U^{(i)} = \frac{u^{(i)}}{L}, \qquad \varphi = \phi,\\
&\alpha_i = \frac{h^{(i)}}{h}, \qquad \beta_i = \frac{L^{(i)}}{L}, \qquad \lambda_i = \frac{L^{(i)}}{h}, \qquad H = \frac{L}{h},\\
&\bar{A}^{(i)}_1 = \frac{A^{(i)}_1}{Kh}, \quad \bar{A}^{(i)}_3 = \frac{A^{(i)}_3}{Kh}, \quad \bar{B}^{(i)}_1 = \frac{B^{(i)}_1}{Kh^2}, \quad \bar{D}^{(i)}_1 = \frac{D^{(i)}_1}{Kh^3},\\
&\bar{N}^{(i)}_b = \frac{N^{(i)}_b}{Kh}, \quad \bar{M}^{(i)}_b = \frac{M^{(i)}_b}{Kh^2}, \qquad \bar{P} = \frac{P}{Kh}, \quad \tilde{W}^{(i)} = \frac{\tilde{w}^{(i)}}{h}
\end{aligned}$$

and substituting them, together with (27) and (34), into (37), we obtain the dimensionless nonlinear equilibrium equations of the delaminated piezoelectric laminated beam with initial deflection under the action of the axial load $P$. They read as follows, where $i = 1, 2, 3, 4$:

$$\begin{aligned}
&\bar{A}^{(i)}_1\left[\frac{1}{\beta_i}dU^{(i)}_{,\xi\xi} + \frac{1}{\lambda_i^2}(W^{(i)}_{,\xi} + \tilde{W}^{(i)}_{,\xi})\,dW^{(i)}_{,\xi\xi} + \frac{1}{\lambda_i^2}(W^{(i)}_{,\xi\xi} + \tilde{W}^{(i)}_{,\xi\xi})\,dW^{(i)}_{,\xi} + \frac{1}{\lambda_i^2}dW^{(i)}_{,\xi\xi}dW^{(i)}_{,\xi}\right]\\
&\quad + \frac{\bar{B}^{(i)}_1}{\lambda_i}d\varphi^{(i)}_{,\xi\xi} - \bar{A}^{(i)}_3\varphi^{(i)}_{,\xi}\left(\frac{1}{\lambda_i}dW^{(i)}_{,\xi} + d\varphi^{(i)}\right) - \bar{A}^{(i)}_3\varphi^{(i)}\left(\frac{1}{\lambda_i}dW^{(i)}_{,\xi\xi} + d\varphi^{(i)}_{,\xi}\right)\\
&\quad - \bar{A}^{(i)}_3 d\varphi^{(i)}_{,\xi}\left(\frac{1}{\lambda_i}dW^{(i)}_{,\xi} + d\varphi^{(i)}\right) - \bar{A}^{(i)}_3 d\varphi^{(i)}\left(\frac{1}{\lambda_i}dW^{(i)}_{,\xi\xi} + d\varphi^{(i)}_{,\xi}\right) - \bar{Q}^{(i)}d\varphi^{(i)}_{,\xi} - \bar{Q}^{(i)}_{,\xi}d\varphi^{(i)} = 0,
\end{aligned}$$

$$\begin{aligned}
&\bar{A}^{(i)}_3\left(\frac{1}{\lambda_i}dW^{(i)}_{,\xi} + d\varphi^{(i)}\right) - \left[\bar{B}^{(i)}_1\left[\frac{1}{\lambda_i\beta_i}dU^{(i)}_{,\xi\xi} + \frac{1}{\lambda_i^3}(W^{(i)}_{,\xi} + \tilde{W}^{(i)}_{,\xi})\,dW^{(i)}_{,\xi\xi}\right.\right.\\
&\qquad \left.\left. + \frac{1}{\lambda_i^3}(W^{(i)}_{,\xi\xi} + \tilde{W}^{(i)}_{,\xi\xi})dW^{(i)}_{,\xi} + \frac{1}{\lambda_i^3}dW^{(i)}_{,\xi\xi}dW^{(i)}_{,\xi}\right] + \frac{\bar{D}^{(i)}_1}{\lambda_i^2}d\varphi^{(i)}_{,\xi\xi}\right] = 0,
\end{aligned} \tag{38}$$

$$\bar{A}_3^{(i)}\left(\frac{1}{\lambda_i}dW_{,\xi\xi}^{(i)}+d\varphi_{,\xi}^{(i)}\right)+\frac{1}{\lambda_i}\bar{N}^{(i)}dW_{,\xi\xi}^{(i)}+\frac{1}{\lambda_i}\bar{N}_{,\xi}^{(i)}dW_{,\xi}^{(i)}$$
$$+\frac{1}{\lambda_i}\left(W_{,\xi\xi}^{(i)}+\tilde{W}_{,\xi\xi}^{(i)}+dW_{,\xi\xi}^{(i)}\right)\left\{\bar{A}_1^{(i)}\left[\frac{1}{\beta_i}dU_{,\xi}^{(i)}+\frac{1}{\lambda_i^2}(W_{,\xi}^{(i)}+\tilde{W}_{,\xi}^{(i)})\,dW_{,\xi}^{(i)}+\frac{1}{2\lambda_i^2}dW_{,\xi}^{(i)2}\right]+\frac{\bar{B}_1^{(i)}}{\lambda_i}d\varphi_{,\xi}^{(i)}\right\}$$
$$+\frac{1}{\lambda_i}\left(W_{,\xi}^{(i)}+\tilde{W}_{,\xi}^{(i)}+dW_{,\xi}^{(i)}\right)\left\{\bar{A}_1^{(i)}\left[\frac{1}{\beta_i}dU_{,\xi\xi}^{(i)}+\frac{1}{\lambda_i^2}(W_{,\xi}^{(i)}+\tilde{W}_{,\xi}^{(i)})\,dW_{,\xi}^{(i)}\right.\right.$$
$$\left.\left.+\frac{1}{\lambda_i^2}(W_{,\xi\xi}^{(i)}+\tilde{W}_{,\xi\xi}^{(i)})\,dW_{,\xi}^{(i)}+\frac{1}{\lambda_i^2}dW_{,\xi\xi}^{(i)}dW_{,\xi}^{(i)}\right]+\frac{\bar{B}_1^{(i)}}{\lambda_i}d\varphi_{,\xi\xi}^{(i)}\right\}$$
$$=0. \quad (39)$$

Now we consider the dimensionless boundary conditions, continuity conditions of displacements and equilibrium conditions of moments and forces of delaminated piezoelectric laminated beams.

Assuming that the both ends of piezoelectric laminated beams are clamped with in-plane movable, the dimensionless boundary conditions are

$$\begin{aligned} &dW^{(1)}(0)=0, \quad d\bar{N}^{(1)}(0)=-d\bar{P}, \quad d\varphi^{(1)}(0)=0,\\ &dW^{(4)}(1)=0, \quad d\bar{N}^{(4)}(1)=-d\bar{P}, \quad d\varphi^{(4)}(1)=0. \end{aligned} \quad (40)$$

The dimensionless continuity conditions of displacements are

$$\begin{aligned} &dU^{(2)}(0)=dU^{(1)}(1)-\frac{1-\alpha_2}{2H}d\varphi^{(1)}(1), \quad dU^{(3)}(0)=dU^{(1)}(1)+\frac{1-\alpha_3}{2H}d\varphi^{(1)}(1),\\ &dW^{(1)}(1)=dW^{(2)}(0)=dW^{(3)}(0), \qquad d\varphi^{(1)}(1)=d\varphi^{(2)}(0)=d\varphi^{(3)}(0),\\ &dU^{(2)}(1)=dU^{(4)}(0)-\frac{1-\alpha_2}{2H}d\varphi^{(4)}(0), \quad dU^{(3)}(1)=dU^{(4)}(0)+\frac{1-\alpha_3}{2H}d\varphi^{(4)}(0),\\ &dW^{(4)}(0)=dW^{(2)}(1)=dW^{(3)}(1), \qquad d\varphi^{(4)}(0)=d\varphi^{(2)}(1)=d\varphi^{(3)}(1). \end{aligned} \quad (41)$$

The dimensionless equilibrium conditions of moments and forces are

$$\begin{aligned} &d\bar{N}^{(1)}(1)=d\bar{N}^{(2)}(0)+d\bar{N}^{(3)}(0), \quad d\bar{Q}^{(1)}(1)=d\bar{Q}^{(2)}(0)+d\bar{Q}^{(3)}(0),\\ &d\bar{M}^{(1)}(1)=d\bar{M}^{(2)}(0)+d\bar{M}^{(3)}(0)-\frac{1-\alpha_2}{2}d\bar{N}^{(2)}(0)+\frac{1-\alpha_3}{2}d\bar{N}^{(3)}(0),\\ &d\bar{N}_4(0)=d\bar{N}^{(2)}(1)+d\bar{N}^{(3)}(1), \qquad d\bar{Q}_4(0)=d\bar{Q}^{(2)}(1)+d\bar{Q}^{(3)}(1),\\ &d\bar{M}_4(0)=d\bar{M}^{(2)}(1)+d\bar{M}^{(3)}(1)-\frac{1-\alpha_2}{2}d\bar{N}^{(2)}(1)+\frac{1-\alpha_3}{2}d\bar{N}^{(3)}(1). \end{aligned} \quad (42)$$

## 4. Analysis of energy release rate along delamination front

In order to analyze the fatigue growth of the delamination, the stress field near the delamination front must be known. In fact, it is quite a tough task to analyze the stress of the delamination front due to its singularity. However, the energy release rate, which indicates intensity of stress fields near delamination

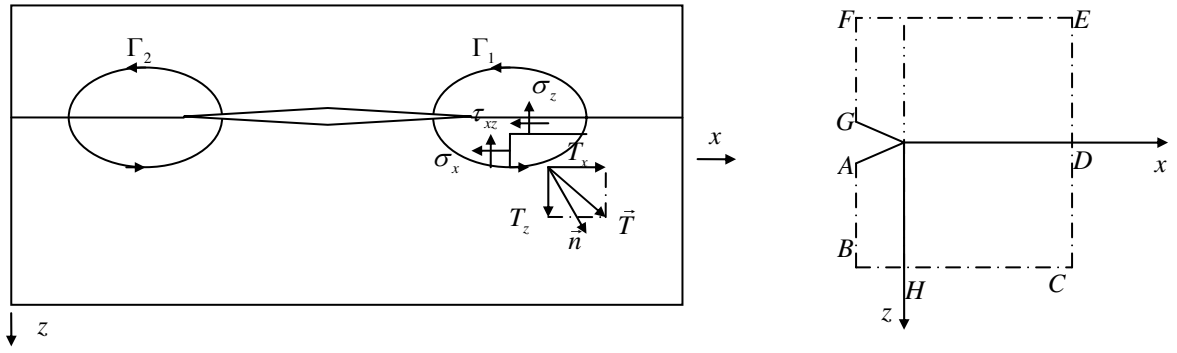


**Figure 2.** Left: the path of the $J$ integral along the delamination front. Right: a rectangular path of the $J$ integral along the delamination front.

front, can be determined. As a result, most researches of delamination growth were carried out by investigating the energy release rate. Rice [1968] proposed the $J$ integral to describe the intensity of the stress and strain field in the vicinity of the crack tip for the elastoplastic structure. The $J$ integral denotes the energy released when the crack tip propagates at a unit distance in the direction along the crack surface, that is, the energy release rate of an elastoplastic crack. In the case of linear elastic, the $J$ integral is equal to the energy release rate $G$.

Rice [1968] defined the $J$ integral of a two-dimensional crack as

$$J = \int_{\Gamma} \left( U dz - T_i \frac{\partial u_i}{\partial x} ds \right), \tag{43}$$

where $U = \int_0^{\varepsilon_{ij}} \sigma_{ij} d\varepsilon_{ij}$ is the strain energy density, $T_i = \sigma_{ij} n_j$ is the stress tensor along the length element $ds$, $u_i$ is the displacement vector, $\vec{n}$ is the unit external normal vector, and $\Gamma$ is an arbitrary contour surrounding the crack tip as shown in Figure 2, left. The counter-clockwise is supposed as the positive direction of the arc $s$.

Based on the law of conservation of energy, the generalized piezoelectric $J$ integral was defined in [Pak and Herrmann 1986; Pak 1990; Zuo and Sih 2000], including piezoelectric effects and was proved to be independent of the choice of a contour:

$$J = \int_{\Gamma} (H n_k - T_i u_{i,k} + D_j n_j E_k) \, d\Gamma, \tag{44}$$

where $H = U - E_j D_j$.

Offsetting the global coordinate system $oxz$ to the right end of the delamination and taking the integral path surrounding the right end of the delamination as a rectangle as shown in Figure 2, right, then yields (see [Li et al. 2011])

$$J_1 = J_{AB} + J_{BC} + J_{CD} + J_{DE} + J_{EF} + J_{FG}. \tag{45}$$

Noting that along the path $AB$, $CE$ and $FG$, $dx = 0$ and for the path $BC$ and $EF$, $dz = 0$.

## 5. Solution methodology

It is impossible to seek an analytic solution satisfying (38)–(39) and all the conditions (40)–(42). We therefore employ the finite difference method to discretize the coordinate variable. The considered domain of each region is $0 \le \xi_1, \xi_2, \xi_3, \xi_4 \le 1$ and each region is divided into $M$ sections. All derivative terms relative to the space coordinate variable are replaced by difference scheme for the nonlinear equilibrium equations (38)–(39) and solution-determining conditions (40)–(42). The difference schemes of all derivative terms in these equations as $dU^{(i)}_{,\xi}$, $dU^{(i)}_{,\xi\xi}$, $dW^{(i)}_{,\xi}$, $dW^{(i)}_{,\xi\xi}$, $d\varphi^{(i)}_{,\xi}$, $d\varphi^{(i)}_{,\xi\xi}$ can be easily obtained. Given that $C^p_{ij}$ in (26) relates to the current stresses and strains, the value of $A^{(i)}_1$, $A^{(i)}_3$, $B^{(i)}_1$, $D^{(i)}_1$ can not be obtained by direction integration along the thickness of the beam. Therefore, we discrete $C^p_{ij}$ along the thickness of the beam, and divide the thickness into $n$ uniform parts. Then by setting $z_k = -h/2 + kh/n$, the values of $A^{(i)}_1$, $A^{(i)}_3$, $B^{(i)}_1$, $D^{(i)}_1$ can be obtained by using the compound trapezoid formula. The compound trapezoid formula is also utilized to work out the $J$ integral value, where the partial derivations of the displacements are approximated by difference schemes.

Then the nonlinear terms of governing equations and corresponding conditions are linearized and can be written as

$$(X \cdot Y)_j = (X)_j (Y)_{j_p}, \tag{46}$$

in which $(Y)_{J_p}$ is the value of the former iterative step. For the primary iteration, secondary extrapolation method is introduced to obtain the value of $(Y)_{J_p}$, that is

$$(Y)_{j_p} = A(Y)_{j-1} + B(Y)_{j-2} + C(Y)_{j-3}. \tag{47}$$

As for different iterations, the coefficients $A$, $B$ and $C$ are given by

$$\begin{aligned} &j=1: && A=1, && B=0, && C=0,\\ &j=2: && A=2, && B=-1, && C=0,\\ &j\ge 3: && A=3, && B=-3, && C=1. \end{aligned} \tag{48}$$

The cubic nonlinear terms are treated by the same method as the quadratic nonlinearity.

## 6. Numerical results and discussion

To ensure the accuracy and effectiveness of the present approaches, buckling of the isotropic elastic delaminated beams is analyzed. Neglecting the initial deflection, hygrothermal effects, piezoelectric effects and nonlinearity, (38)–(39) degenerates to

$$\begin{aligned} &\frac{\bar{A}^{(i)}_1}{\beta_i} dU^{(i)}_{,\xi\xi} + \frac{\bar{B}^{(i)}_1}{\lambda_i} d\varphi^{(i)}_{,\xi\xi} = 0,\\ &\frac{\bar{A}^{(i)}_3}{\lambda_i} dW^{(i)}_{,\xi\xi} + \bar{A}^{(i)}_3 d\varphi^{(i)}_{,\xi} - \frac{\alpha_i \bar{P}_{cr} \bar{A}^{(i)}_1}{\lambda_i} dW^{(i)}_{,\xi\xi} = 0,\\ &\frac{\bar{A}^{(i)}_3}{\lambda_i} dW^{(i)}_{,\xi} + \bar{A}^{(i)}_3 d\varphi^{(i)} - \frac{\bar{B}^{(i)}_1}{\beta_i \lambda_i} dU^{(i)}_{,\xi\xi} - \frac{\bar{D}^{(i)}_1}{\lambda_i^2} d\varphi^{(i)}_{,\xi\xi} = 0 \quad (i = 1, 2, 3, 4), \end{aligned} \tag{49}$$

| | Geometric parameters | | | | |
|---|---|---|---|---|---|
| | $\beta_2 = 0.2$ | $\beta_2 = 0.3$ | $\beta_2 = 0.5$ | $\beta_2 = 0.6$ | $\beta_2 = 0.8$ |
| [Li and Zhou 2000] | 0.63758 | 0.61012 | 0.43127 | 0.33275 | 0.12437 |
| present | 0.64312 | 0.62135 | 0.44805 | 0.34107 | 0.13841 |

**Table 1.** Values of $\bar{P}_{cr}$ for different delaminated lengths: current method compared with [Li and Zhou 2000].

where $\bar{P}_{cr}$ is the critical load of the isotropic delaminated beam. By (49), in conjunction with the conditions (40)–(42), the critical buckling load can be obtained.

Table 1 shows the critical loads of delaminated isotropic beams obtained with the present approach and compares them with those in [Li and Zhou 2000], the material parameters and geometric parameters being the same. The close agreement observed lends credibility to the present method.

The constant $K$ in (1) can be determined by a simple tension test, and then $\Sigma_{11}(= K)$ can be determined. In the following numerical examples, set $\tilde{\sigma}(\bar{\varepsilon}^p) = \Sigma_{11} + \Sigma_{11}(\bar{\varepsilon}^p)^{0.51}$, $a = 0.6$ and $c = 2K/3$.

Let the dimensionless initial deflections be

$$\tilde{W}^{(i)} = \frac{\tilde{W}_0}{\beta_i} \sin \xi\pi, \tag{50}$$

where $\tilde{W}_0$ is the amplitude of the initial deflection of the beam without delamination.

If there is no specific explanation, in the following numerical examples we select PZT-5A as the piezoelectric layers and the corresponding material parameters are $E_L = E_T = 61\,\text{GPa}$, $G_{LT} = 22.6\,\text{GPa}$, $G_{LZ} = G_{TZ} = 21.1\,\text{GPa}$, $\upsilon_{LT} = 0.35$, $e_{31} = 7.209\,\text{C/m}^2$, $V_T = V_B$. The material parameters of the laminated beam are adopted as $E_L = 181.0\,\text{GPa}$, $E_T = 10.3\,\text{GPa}$, $G_{LT} = G_{LZ} = 7.17\,\text{GPa}$, $G_{TZ} = 3.87\,\text{GPa}$, $\upsilon_{LT} = 0.28$, $\Sigma_{11} = 500\,\text{MPa}$, $\Sigma_{55} = 200\,\text{MPa}$, $\vartheta_{11} = 6.1 \times 10^{-6}\,\text{K}^{-1}$, $\vartheta_{22} = 30.3 \times 10^{-6}\,\text{K}^{-1}$, $\gamma_{11} = 0$, $\gamma_{22} = 0.6 \times 10^{-6}$. For the sake of simplification, in present study, both ambient temperature and moisture are assumed to have a uniform distribution and leave out the hygrothermal effects of the piezoelectric layers. The material properties are assumed to be independent of temperature and moisture. The slenderness ratio of the beams is $H = 10$ and all layers have same thickness. The stacking sequences of the fiber-reinforced beam are $[0°/90°/0°]_{10}$. To simplify, only the postbuckling and delamination growth of piezoelectric elastoplastic laminated beams with symmetrical delamination are investigated in the numerical examples.

***Analysis of postbuckling for delaminated piezoelectric elastoplastic laminated beams under hygrothermal conditions.*** In the calculation examples, the influences of the yield stress, delamination sizes and depths, hygrothermal conditions and piezoelectric effects on the postbuckling of delaminated piezoelectric elastoplastic laminated beams are discussed respectively. When analyze the postbuckling problem, we set $\tilde{W}_0 = 0.1$. In the following figures, $\bar{P}/\bar{P}^*_{cr}$ is the ratio of the dimensionless axial load to the dimensionless critical load of the beam without delamination, and $W_0^{(3)}$ is the maximum dimensionless deflection of region 3.

Figure 3, left, shows the comparison of postbuckling behavior between delaminated piezoelectric elastic and elastoplastic laminated beams, when $\alpha_2 = 0.4$, $\beta_2 = 0.5$ and $V = \Delta T = \Delta c = 0$. It can be

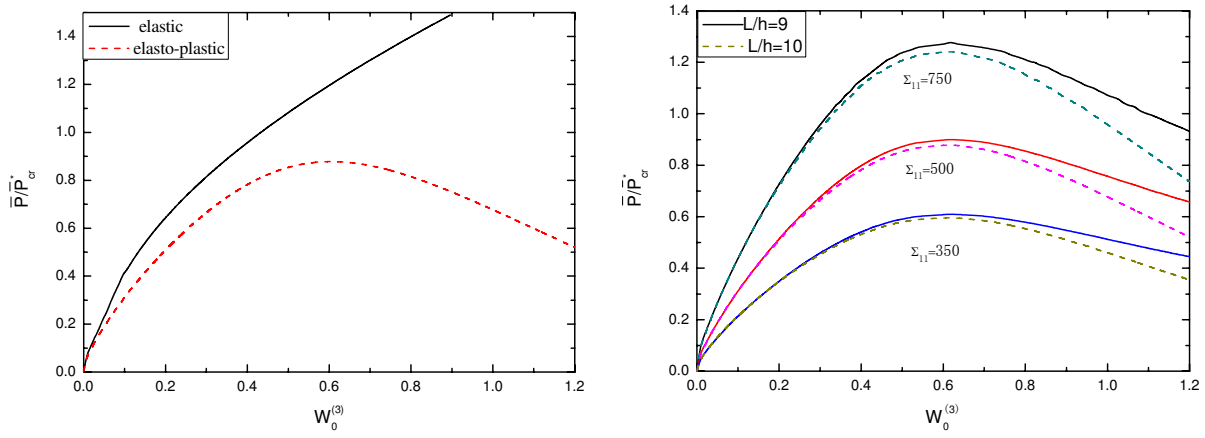


**Figure 3.** Left: comparison of postbuckling behavior between delaminated elastic and elastoplastic laminated beams. Right: Effect of yield stress on postbuckling behavior of delaminated piezoelectric elastoplastic laminated beams.

seen that the postbuckling curve of delaminated elastoplastic beams is quite different from the elastic beams. There exists a maximum in the elastoplastic postbuckling curve, which means that when the axial load surpasses the load carrying capacity, the deflection of the beams would increase rapidly.

For delaminated piezoelectric elastoplastic laminated beams with different slenderness ratio and yield stress, the variable curves of dimensionless load with the largest deflection of region 3 are presented in Figure 3, right, with $\alpha_2 = 0.4$, $\beta_2 = 0.5$ and $V = \Delta T = \Delta c = 0$. It is illustrated that the larger the slenderness ratio is, the more easily the delaminated piezoelectric elastoplastic laminated beams would yield, and the lower the load carrying capacity is. Note that when the yield stress of the fiber-reinforced material is less, the load carrying capacity of the delaminated piezoelectric elastoplastic beams is reduced.

Setting $\beta_2 = 0.5$ and $V = 0$, the effects of hygrothermal condition and delamination depths on the postbuckling curves of the delaminated piezoelectric elastoplastic laminated beams are depicted in Figure 4, left. As $\Delta T$ is much larger than $\Delta c$ in practice, we take $\Delta T = 0 \sim 100^\circ$ C and $\Delta c = 0\% \sim 1\%$. Since magnitude of $\vartheta_x^k$, $\gamma_x^k$ are of the same order and the variation of humidity $\Delta c$ is quite limited, so the humidity has little impact on the postbuckling curve and temperature is the main influencing factor. From the figure we can see that, with the same load, the increase of temperature decreases the load carrying capacity. That is because the increase of temperature is equivalent to an axial pressure, which reduces the stiffness of the beam. Under the same load, the beam with hygrothermal effects would yield a larger deflection than the beam in the thermostatic environments. In addition, the deeper the delamination is, the smaller the load carrying capacity is.

Under the action of the three types of electric load, the effects of delamination sizes on the postbuckling curves of the delaminated piezoelectric elastoplastic laminated beams with $\alpha_2 = 0.4$ are shown in Figure 4, right. The dimensionless control voltages are taken as $V = e_{31} V_T / Kh = 0.1, 0$ and $-0.1$, respectively, and the hygrothermal effects are not considered, namely, $\Delta T = \Delta c = 0$. It is indicated that, with the same geometric parameters and external load, acting a positive voltage on the beams is equivalent to an axial load, which leads to a larger deflection of the beams. It is just the opposite for the negative voltage. On the other hand, the larger the delamination size is, the lower the load carrying capacity is.

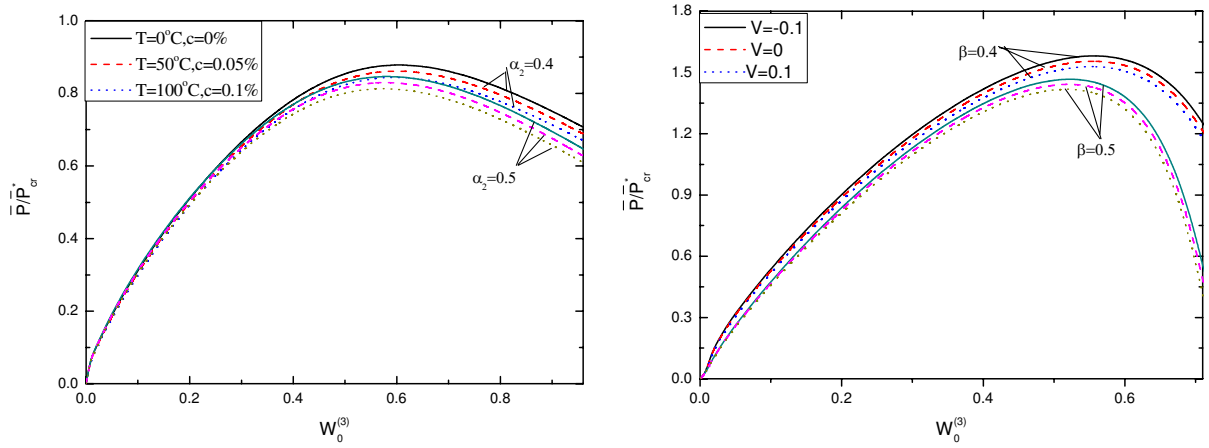


**Figure 4.** Left: effect of hygrothermal conditions on postbuckling behavior of delaminated piezoelectric elastoplastic laminated beams. Right: effect of control voltage on postbuckling behavior of delaminated piezoelectric elastoplastic laminated beams.

***Analysis of delamination growth for delaminated piezoelectric elastoplastic laminated beams under hygrothermal conditions.*** In the following calculation examples, the influences of the yield stress, delamination sizes and depths, hygrothermal conditions and piezoelectric effects on the energy release rate of delaminated piezoelectric elastoplastic laminated beams without initial deflections are discussed respectively. In the following figures, $\bar{J}(= J_1/Kh)$ is the dimensionless value of $J$ integral along the right delamination front.

Figure 5, left, presents the variation curves of energy release rate for delaminated piezoelectric elastoplastic laminated beams with different slenderness ratio and yield stress, when $\alpha_2 = 0.4$, $\beta_2 = 0.5$ and $V = \Delta T = \Delta c = 0$. It can be observed that the larger the slenderness ratio is, the larger the value of

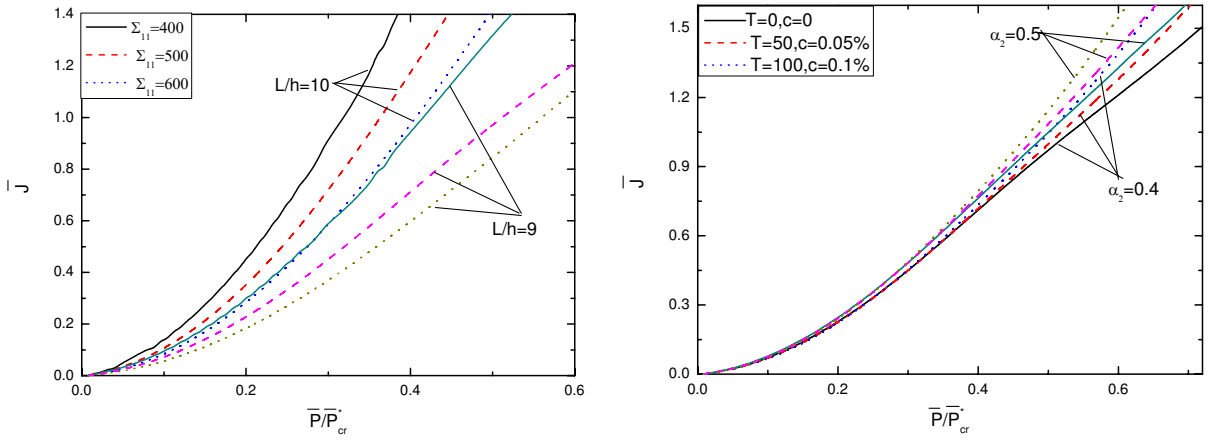


**Figure 5.** Left: effect of yield stress on energy release rate of delaminated piezoelectric elastoplastic laminated beams. Right: Effect of hygrothermal conditions on energy release rate of delaminated piezoelectric elastoplastic laminated beams.

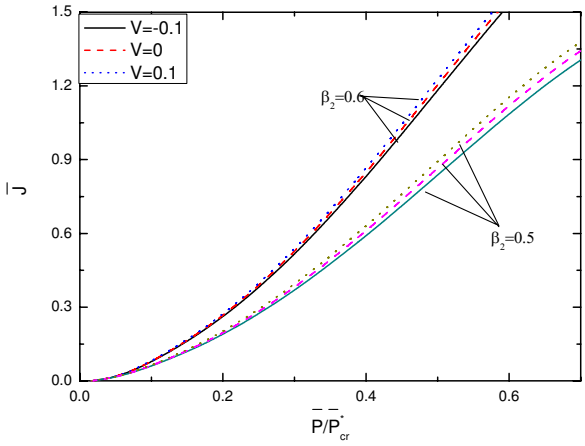


**Figure 6.** Effect of control voltage on energy release rate of delaminated piezoelectric elastoplastic laminated beams.

$J$ integral, that is, the energy release rate, along the right delamination front is, which results in the delamination growth easier to occur. Moreover, when the yield stress of the fiber-reinforced material is larger, the $J$ integral value along the right delamination front rises more quickly.

Setting $\beta_2 = 0.5$ and $V = 0$, the effects of hygrothermal condition and delamination depths on the energy release rate curves of the delaminated piezoelectric elastoplastic laminated beams are shown in Figure 5, right. It can be noticed that, with the same load, the increase of temperature make the energy release rate rise and the delamination propagate more easily. In addition, the deeper the delamination is, the larger the energy release rate is.

Subjected to three types of electric load, the effects of delamination sizes on the energy release rate of the delaminated piezoelectric elastoplastic laminated beams with $\alpha_2 = 0.4$ and $\Delta T = \Delta c = 0$ are presented in Figure 6. It is shown that, with the same geometric parameters and external load, applying a positive voltage leads to the energy release rate larger. However, the negative voltage is good for the stability of the delaminated beam. On the other hand, the larger the delamination size is, the larger the energy release is and the delamination growth is easier to occur.

## 7. Conclusions

The postbuckling and delamination growth for delaminated piezoelectric elastoplastic laminated beams under hygrothermal conditions are investigated in this paper. The numerical solutions are presented by using the finite difference method and the iteration method. The main conclusions can be drawn as follows. Under the same axial load, the postbuckling behavior of a delaminated elastic-plastic laminated beam is quite different with that of the delaminated elastic laminated beam and there is a load carrying capacity for the delaminated elastic-plastic laminated beam. With smaller yield stress, larger slenderness ratio, deeper and larger delamination, the load carrying capacity of the delaminated piezoelectric elastoplastic beam is lower. The effects of temperature increasing and positive voltage are equivalent to the axial pressures, which lead to the larger deformation of the beam and have a detrimental effect on the stability of the delaminated beams. The larger yield stress of the fiber-reinforce material makes

the energy release rate rise more quickly. When the slenderness ratio of the delaminated piezoelectric elastoplastic laminated beam, the external axial load, the increase of the temperature and the positive voltage are larger, and the delamination is deeper or larger, the energy release rates are larger and the delamination growth is easier to occur.

## Acknowledgements

This project is supported by the National Natural Science Foundation of China (No. 11072076).

## References

[Davidson et al. 2000] B. D. Davidson, S. J. Gharibian, and L. J. Yu, "Evaluation of energy release rate-based approaches for predicting delamination growth in laminated composites", *Int. J. Fract.* **105**:4 (2000), 343–365.

[Li and Zhou 2000] D. Li and J. Zhou, "Buckling analysis of delaminated beam for the higher-order shear deformation theory", *Acta Mech. Solida Sin.* **2000**:3 (2000), 225–233.

[Li et al. 2011] Y. L. Li, Y. M. Fu, and Y. Q. Mao, "Analysis of delamination fatigue growth for delaminated piezoelectric elasto-plastic laminated beams under hygrothermal conditions", *Compos. Struct.* **93**:2 (2011), 889–901.

[Münch and Ousset 2002] A. Münch and Y. Ousset, "Numerical simulation of delamination growth in curved interfaces", *Comput. Methods Appl. Mech. Eng.* **191**:19-20 (2002), 2073–2095.

[Nilsson et al. 2001] K.-F. Nilsson, L. E. Asp, J. E. Alpman, and L. Nystedt, "Delamination buckling and growth for delaminations at different depths in a slender composite panel", *Int. J. Solids Struct.* **38**:17 (2001), 3039–3071.

[Pak 1990] Y. E. Pak, "Crack extension force in a piezoelectric material", *J. Appl. Mech.* (*ASME*) **57**:3 (1990), 647–653.

[Pak and Herrmann 1986] Y. E. Pak and G. Herrmann, "Conservation laws and the material momentum tensor for the elastic dielectric", *Int. J. Eng. Sci.* **24**:8 (1986), 1365–1374.

[Park and Sankar 2002] O. Park and B. V. Sankar, "Crack-tip force method for computing energy release rate in delaminated plates", *Compos. Struct.* **55**:4 (2002), 429–434.

[Pi and Bradford 2003] Y.-L. Pi and M. A. Bradford, "Elasto-plastic buckling and postbuckling of arches subjected to a central load", *Comput. Struct.* **81**:18–19 (2003), 1811–1825.

[Rice 1968] J. R. Rice, "A path independent integral and the approximate analysis of concentration by notches and cracks", *J. Appl. Mech.* (*ASME*) **35**:2 (1968), 397–386.

[Shen 2001] H.-S. Shen, "Postbuckling of shear deformable laminated plates with piezoelectric actuators under complex loading conditions", *Int. J. Solids Struct.* **38**:44–45 (2001), 7703–7721.

[Shen 2002] H.-S. Shen, "Hygrothermal effects on the postbuckling of axially loaded shear deformable laminated cylindrical panels", *Compos. Struct.* **56**:1 (2002), 73–85.

[Simha et al. 2008] N. K. Simha, F. D. Fischer, G. X. Shan, C. R. Chen, and O. Kolednik, "$J$-integral and crack driving force in elastic-plastic materials", *J. Mech. Phys. Solids* **56**:9 (2008), 2876–2895.

[Tafreshi 2006] A. Tafreshi, "Delamination buckling and postbuckling in composite cylindrical shells under combined axial compression and external pressure", *Compos. Struct.* **72**:4 (2006), 401–418.

[Tian et al. 2009] Y. P. Tian, Y. M. Fu, and Y. Wang, "Nonlinear dynamic response of piezoelectric elasto-plastic laminated plates with damage", *Compos. Struct.* **88**:2 (2009), 169–178.

[Wang and Qiao 2004] J. Wang and P. Qiao, "On the energy release rate and mode mix of delaminated shear deformable composite plates", *Int. J. Solids Struct.* **41**:9–10 (2004), 2757–2779.

[Yang et al. 2002] W. Yang, S. Zhang, and Y. Ma, "Theoretical research of crack tip $J$-integral for orthotropic composite plate", *J. Taiyuan Heavy Mach. Inst.* **2002**:3 (2002), 226–232.

[Yuan and Zheng 1990] Z.-P. Yuan and Y. Zheng, "A study on yield and flow of orthotropic materials", *Appl. Math. Mech.* **11**:3 (1990), 247–253.

[Zuo and Sih 2000] J. Z. Zuo and G. C. Sih, "Energy density theory formulation and interpretation of cracking behavior for piezoelectric ceramics", *Theor. Appl. Fract. Mech.* **34**:1 (2000), 17–33.

Received 24 Dec 2010. Revised 10 Apr 2011. Accepted 11 Apr 2011.

YING-LI LI: liyingli298@yahoo.com
*State Key Lab of Advanced Design and Manufacturing for Vehicle Body, College of Mechanical and Vehicle Engineering, Hunan University, Changsha, 410082, China*

YI-MING FU: fym_2581@hnu.cn
*College of Mechanical and Vehicle Engineering, Hunan University, Changsha, 410082, China*

HONG-LIANG DAI: hldai520@sina.com
*College of Mechanical and Vehicle Engineering, Hunan University, Changsha, 410082, China*

JOURNAL OF MECHANICS OF MATERIALS AND STRUCTURES
Vol. 7, No. 1, 2012

msp

# EQUIVALENT INHOMOGENEITY METHOD FOR EVALUATING THE EFFECTIVE CONDUCTIVITIES OF ISOTROPIC PARTICULATE COMPOSITES

SOFIA G. MOGILEVSKAYA, VOLODYMYR I. KUSHCH,
OLESYA KOROTEEVA AND STEVEN L. CROUCH

The problem of calculating the effective conductivity of isotropic composite materials with periodic or random arrangements of spherical particles is revisited by using the equivalent inhomogeneity method. The approach can be viewed as an extension of classical Maxwell's methodology. It is based on the idea that the effective conductivity of the composite material can be deduced from the effect of the cluster embedded in an infinite space on the far-fields. The key point of the approach is to precisely account for the interactions between all the particles in the cluster that represent the composite material in question. It is done by using a complete, multipole-type analytical solution for the problem of an infinite isotropic matrix containing a finite cluster of isotropic spherical particles, regarded as the finite cluster model of particulate composite. The effective conductivity of the composite is evaluated by applying the "singular-to-singular" re-expansion formulae and comparing the far-field asymptotic behavior with the equivalent inhomogeneity solution. The model allows one to adequately capture the influence of the micro-structure of composite material on its overall properties.

Numerical realization of the method is simple and straightforward. Comparison of the numerical results obtained by the proposed approach with those available in literature (both for periodic and random arrangements) demonstrate its accuracy and numerical efficiency.

## 1. Introduction

The problem of evaluating the effective conductivities (thermal, electrical, etc.) of particulate composites with spherical particles is well studied, especially for the case of periodic arrangements of particles. In the latter case, following the direction outlined by Lord Rayleigh [Rayleigh 1892], and the techniques developed in the series of follow up papers [Runge 1925; de Vries 1952; Meredith and Tobias 1960; Zuzovsky and Brenner 1977; McPhedran and McKenzie 1978; McKenzie et al. 1978; O'Brien 1979; Sangani and Acrivos 1983], the complete, multipole-type analytical solutions are obtained for three cubic arrays of identical spheres. The basis concept of the method is to directly account for triple periodicity by enforcing periodic conditions on the boundary of a unit cell and to use local expansions for the fields (e.g., temperature) in terms of solid spherical harmonics. Zuzovsky and Brenner [1977] and Sangani and Acrivos [1983] also used a special representation for the temperature as a spatially periodic function.

The conduction through a random suspension of spheres is also relatively well studied. Jeffrey [1973] used the method suggested in [Batchelor 1972; Batchelor and Green 1972], which accounts only for a pair-wise interaction between the particles and employs an information about the particles distribution in the form of simple probability density functions. In [Sangani and Yao 1988; Bonnecaze and Brady 1990;

*Keywords:* particulate composites, effective conductivity, equivalent inhomogeneity, multipole expansion.

1991; Zinchenko 1994], the problem of a random dispersion was treated as a triple-periodic problem with random arrangement of the particles in a cubic unit cell. Sangani and Yao [1988] employed a method of multiple expansion developed in [Zuzovsky and Brenner 1977; Sangani and Acrivos 1983], while Bonnecaze and Brady [1990; 1991] used a "Stokesian dynamics"-like approach. Zinchenko [1994] used the boundary integral equation method with the triply periodic Green function and the approximations of the boundary temperature by a series of surface spherical harmonics. In the latter paper an efficient iterative algorithm is constructed to obtain the solution for suspensions with arbitrary conductivity ratio. A different approach was suggested by Kim and Torquato [1990; 1991], who developed a generalized Brownian motion simulation technique.

There is also an extensive literature related to effective medium theories and variational bounds (see [Milton 2002; Torquato 2002] for reviews). In [Batchelor and O'Brien 1977; Suen et al. 1979; Zinchenko 1998] asymptotic relations are suggested for obtaining the effective conductivities of materials with closely packed highly conducting particles. The latest developments include the extension of Rayleigh's method to include the effects of interfacial resistance [Lu and Lin 1996; Cheng and Torquato 1997] and coating. (For the latter problem mostly approximate methods are available; see, e.g., [Lu and Lin 1996; Hashin 2001; Sevostianov and Kachanov 2007].) Moosavi et al. [2003], extended the method of [Zuzovsky and Brenner 1977] to predict the effective thermal properties of a periodic array of multi-coated spheres.

Although those developments have been influenced by the pioneering work of Maxwell [1892], his original methodology was based on a somewhat different concept. Maxwell, who studied electrical conductivity of materials, suggested that a cluster of spherical particles affects the fields at large distances from the cluster in the same way as an equivalent sphere whose conductivity is equal to the effective one. Maxwell did not account for the interactions between the particles, and therefore, he concluded that the method would only be valid for materials with low volume fractions $c$ of particles. In other words, Maxwell's solution was that of order $c$. Hasselman and Johnson [1987] extended Maxwell's methodology on the case of the composites with interfacial thermal barrier resistance. In [Lu and Lin 1996; Lu 1998] this was used it to estimate the effective conductivities of aligned spheroids dispersions with perfect and imperfect interfaces. Maxwell's methodology was recently extended to multi-phase composites in [McCartney and Kelly 2008; McCartney 2010]. All these papers employed the original Maxwell's methodology that does not account for the interactions between the particles.

In [Mogilevskaya et al. 2010], the Maxwell's concept of the finite cluster was generalized to evaluate the effective transverse properties of linearly elastic, multi-phase unidirectional composites. The key point of the approach was to precisely account for the interactions between all the fibers in the cluster that represents the composite material in question. The same approach was adopted in [Pyatigorets and Mogilevskaya 2011] to evaluate the effective transverse mechanical properties of transversely isotropic viscoelastic composites and in [Koroteeva et al. 2010] to solve the problem of evaluating the effective thermal conductivity of isotropic porous materials. It was demonstrated that the approach allows to adequately capture the influence of the micro-structure of composite material on its overall properties.

In the present paper the approach based on Maxwell's concept of the finite cluster is employed to evaluate the effective thermal conductivity of isotropic suspensions with highly conducting particles that are either in perfect contact with the matrix or possess an interface resistance. The cluster is embedded into an infinite matrix subjected to the prescribed temperature gradient at infinity. The interactions

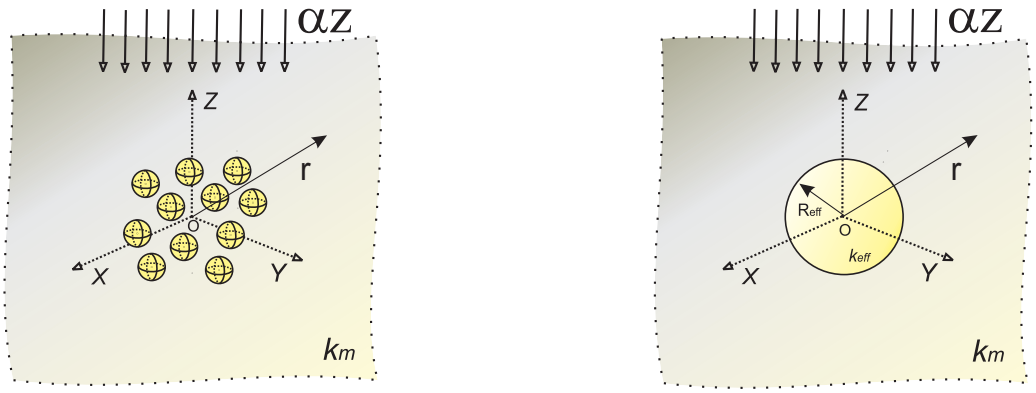


**Figure 1.** Left: a cluster of spherical particles. Right: an equivalent inhomogeneity.

among all the particles in the cluster are precisely accounted for by using a complete, multipole-type analytical solution for the problem. The effective conductivity of the composite is evaluated by applying the singular-to-singular re-expansion formulae and comparing the far-field asymptotic behavior with the equivalent inhomogeneity solution. The results obtained by the proposed approach are compared with those available in literature both for periodic and random arrangements of particles.

## 2. The finite cluster model

Consider the two problems shown in Figure 1. The left-hand side of the figure contains a cluster of $N$ non-overlapping spherical particles arranged in an isotropic pattern representative of the composite material. The cluster is embedded in an infinite matrix with the conductivity $k_m$, and the temperature gradient $T = \alpha z$ is applied at infinity. The particles may have different radii and conductivities, but here, for simplicity, we assume that the particles have the same radii $a_p = 1$ and conductivities $k_p$.

The particles are either in perfect contact with the matrix or possess an interface resistance. The interface conditions, in the local spherical coordinate system $(O_p, r_p, \theta_p, \varphi_p)$ of the $p$-th particle ($p = 1, \ldots, N$), are as follows ($r_p = a_p$):

(a) perfect thermal contact:
$$T_p = T_m; \quad k_p \frac{\partial T_p}{\partial r_p} = k_m \frac{\partial T_m}{\partial r_p} \tag{1}$$

(b) interface resistance:
$$\frac{T_p - T_m}{\widetilde{R}} = -k_p \frac{\partial T_p}{\partial r_p}; \quad k_p \frac{\partial T_p}{\partial r_p} = k_m \frac{\partial T_m}{\partial r_p} \tag{2}$$

where $T_p$, $T_m$ are the temperatures in the $p$-th particle and matrix, respectively, and $\widetilde{R}$ can be defined through the limiting process described in [Torquato and Rintoul 1995].

Figure 1, right, contains only one (equivalent) inhomogeneity/particle of radius $R_{\text{eff}}$ and center $O$, which coincides with the origin of global coordinate system $(O, r, \theta, \varphi)$ used in both problems. The inhomogeneity is in perfect contact with the matrix and its conductivity coincides with the effective conductivity $k_{\text{eff}}$ of the composite material. The choice of the radius of the equivalent inhomogeneity

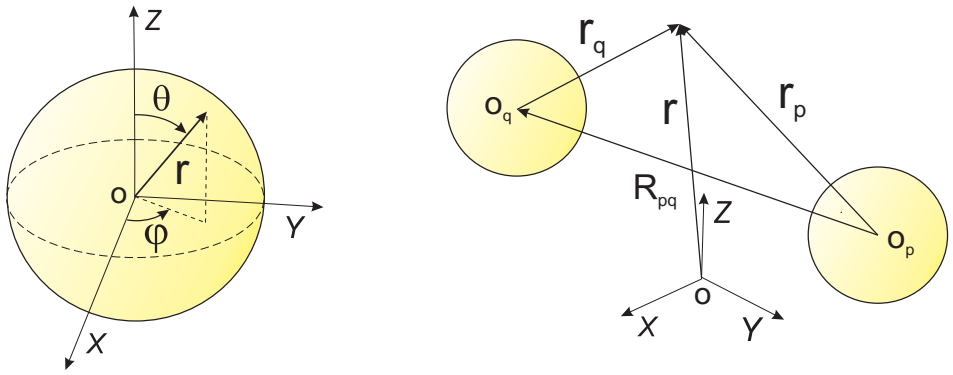


**Figure 2.** Coordinate systems: local (left) and global (right).

$R_{\text{eff}}$ is natural and follows from the definition of the volume fraction $c$:

$$R_{\text{eff}} = (N/c)^{1/3} \tag{3}$$

Because only isotropic materials are considered in this work, the choice of point $O$ is also natural. For the periodic composites it is located at the center of a unit cell; for random composites it is located at the center of the cube, in which the random arrangement of the particles is generated.

The basic idea of the method is that the temperatures at large distances ($r \gg R_{\text{eff}}$) are the same for the cluster and for the equivalent inhomogeneity. In [Koroteeva et al. 2010] these temperatures are compared using discrete set of points at finite distances away from the cluster. In the present paper the assumption that the temperatures have the same asymptotic behavior is employed, in this case the choice of the center $O$ of the cluster is not even important.

## 3. Solutions for the two problems

Both problems are governed by Laplace's equation $\Delta T = 0$. The exact expression for the temperature in the matrix for the equivalent inhomogeneity problem in the local spherical coordinate system $(O, r, \theta, \varphi)$ (see Figure 2, left) has the form

$$T_m^*(\boldsymbol{r}) = T_{\text{far}}(\boldsymbol{r}) + B_{10}^* Y_1^0(\boldsymbol{r}) \tag{4}$$

where $\boldsymbol{r}$ is a radius vector, $T_{\text{far}}(\boldsymbol{r}) = \alpha r \cos\theta$, $Y_1^0(\boldsymbol{r})$ is a solid spherical harmonic (see the Appendix), and $B_{10}^*$ is given by

$$B_{10}^* = -\alpha R_{\text{eff}}^3 \frac{k_{\text{eff}} - k_m}{k_{\text{eff}} + 2k_m} \tag{5}$$

The problem of a finite cluster can be solved using a complete, multipole-type semi-analytical solution. The main steps of the solution can be described as follows. Using the superposition principle, the temperature field inside the matrix $T = T^{(0)}$ can be represented in the form

$$T^{(0)}(\boldsymbol{r}) = T_{\text{far}}(\boldsymbol{r}) + \sum_{q=1}^{N} T_{\text{dist}}^{(q)}(\boldsymbol{r}_q) \tag{6}$$

where $T_{\text{far}} = \alpha r \cos\theta$, while $T^{(q)}_{\text{dist}}(\boldsymbol{r}_q)$ is the disturbance of the field caused by the $q$-th particle, and the meaning of $\boldsymbol{r}_q$ is clear from Figure 2, right.

The temperature $T^{(q)}_{\text{dist}}(\boldsymbol{r}_q)$ is represented in the form

$$T^{(q)}_{\text{dist}}(\boldsymbol{r}_q) = \sum_{t=1}^{\infty}\sum_{s=-t}^{t} A^{(q)}_{ts} Y^s_t(\boldsymbol{r}_q), \tag{7}$$

where the $A^{(q)}_{ts}$ are unknown complex coefficients.

Applying the re-expansion formula (S2R decomposition, see (28) in the Appendix), the temperature $T^{(0)}(\boldsymbol{r})$ can be expressed in terms of the spherical coordinate system associated with the $p$-th particle as follows

$$T^{(0)}(\boldsymbol{r}_p) = \alpha[z^{(p)}_c + r_p y^0_1(\boldsymbol{r}_p)] + \sum_{t=1}^{\infty}\sum_{s=-t}^{t} A^{(p)}_{ts} Y^s_t(\boldsymbol{r}_p) + \sum_{t=0}^{\infty}\sum_{s=-t}^{t} a^{(p)}_{ts} y^s_t(\boldsymbol{r}_p), \tag{8}$$

where $z^{(p)}_c$ is the $z$-th coordinate of the center of the $p$-th particle.

$$a^{(p)}_{ts} = (-1)^{t+s} \sum_{\substack{q=1\\ q\neq p}}^{N}\sum_{k=1}^{\infty}\sum_{l=-k}^{k} A^{(q)}_{kl} Y^{l-s}_{k+t}(\boldsymbol{R}_{qp}), \tag{9}$$

where $\boldsymbol{R}_{\mathbf{pq}} = \boldsymbol{r}_p - \boldsymbol{r}_q$ (Figure 2, right).

The temperature inside the $p$-th particle is represented by the series

$$T^{(p)}(\boldsymbol{r}_p) = \sum_{t=0}^{\infty}\sum_{s=-t}^{t} D^{(p)}_{ts} y^s_t(\boldsymbol{r}_p), \tag{10}$$

where $D^{(p)}_{ts}$ are unknown complex coefficients.

The fluxes $k_p \partial T_p / \partial r_p$, $k_m \partial T_m / \partial r_p$ can be represented by the series similar to those given by Eqs. (8)-(10) by using differentiation rules (25)-(27) in the Appendix and the properties of spherical harmonics. Substituting the series expressions into the boundary conditions (1) (case of perfect thermal contact) or (2) (case of interface resistance) and using some algebra, an infinite set of linear equations can be obtained:

$$\lambda_p \frac{(t-s)!\,(t+s)!}{(a_p)^{2t+1}} A^{(p)}_{ts} + (-1)^{t+s} \sum_{\substack{q=1\\ q\neq p}}^{N}\sum_{k=1}^{\infty}\sum_{l=-k}^{k} A^{(q)}_{kl} Y^{l-s}_{k+t}(R_{qp}) = -\alpha\delta_{t1}\delta_{s0}. \tag{11}$$

Here $t = 1, 2, \ldots,\ |s| \le t,\ p = 1, \ldots, N$, and

$$\lambda_p = \frac{\omega_p + (1+1/t)(1+t\gamma)}{\omega_p - 1 - t\gamma}, \tag{12}$$

where $\omega_p = k_p/k_m$, and $\gamma$ equals 0 for the case of a perfect thermal contact and $\widetilde{R}k_p/a_p$ for the case of interface resistance. The number of unknowns in (11) can be reduced by taking into account the equation

$$A^{(q)}_{k,-l} = (-1)^l \overline{A^{(q)}_{kl}},$$

which follows directly from (23) in the Appendix and the fact that the temperature is a real-valued quantity. The resulting system can be truncated by adopting the maximum value of $t = t_{\max}$ and solved in terms of the unknown coefficients $A_{ts}^{(p)}$.

## 4. Evaluation of the effective conductivity of the material

The temperature $T_{\text{dist}}(\boldsymbol{r})$ in expression (7) can also be re-expanded in a series of spherical harmonics in terms of the spherical coordinate system associated with some sphere with the center $O$ and radius $\|\boldsymbol{r}\|$:

$$T_{\text{dist}}(\boldsymbol{r}) = \sum_{q=1}^{N} T_{\text{dist}}^{(q)}(\boldsymbol{r}_q) = \sum_{t=1}^{\infty} \sum_{s=-t}^{t} B_{ts} Y_t^s(\boldsymbol{r}) \tag{13}$$

Assuming that $\|\boldsymbol{r}\| \geq R_{\text{eff}}$ and using the re-expansion formula (30) from the Appendix, we obtain

$$B_{10} = \sum_{q=1}^{N} A_{10}^{(q)} \tag{14}$$

Using Equations (4)–(6) and (13)–(14) and assuming that the far-field asymptotic behavior of $T^{(0)}$ in (6) is the same as that of $T_m^*(\boldsymbol{r})$ in (4), the coefficient $B_{10}$ can be equated with the coefficient $B_{10}^*$:

$$B_{10} = B_{10}^* \tag{15}$$

The effective conductivity $k_{\text{eff}}$ can then be found from (5). We obtain

$$k_{\text{eff}} = k_m \frac{1 - 2A_{10}^*}{1 + A_{10}^*}, \tag{16}$$

where we have set

$$A_{10}^* = \frac{c}{\alpha} \langle A_{10}^{(p)} \rangle, \tag{17}$$

with

$$\langle A_{10}^{(p)} \rangle = \frac{1}{N} \sum_{p=1}^{N} A_{10}^{(p)} \tag{18}$$

The analytical approach to find $k_{\text{eff}}$ allows one to note several interesting facts. It can be seen from expressions (16)–(18) that the effective conductivity $k_{\text{eff}}$ is independent of the choice of the center $O$ of the cluster. In addition, it is independent on the value of the temperature gradient at infinity, as the coefficients $A_{10}^{(p)}$ are directly proportional to the value of $\alpha$ (it follows from Eq. (11)). Expressions (16)-(18) involve only the average of the first coefficients from series (7) but, in our model, even those coefficients contain the information about the particles interactions as they are obtained from a complete, multipole-type semi-analytical solution and they are expressed via all the coefficients $A_{ts}^{(q)} (q = 1, \ldots, N,\ q \neq p)$ of Eq. (11). In case of non-interacting particles, the coefficients $A_{10}^{(p)}$ are the same for all particles (see Eqs. (11)-(12) with $a_p = 1$). They can be written as

$$A_{10}^{(p)} = -\alpha \frac{k_p - k_m(1+\gamma)}{k_p + 2k_m(1+\gamma)}$$

When the interface conditions are those of perfect thermal contact ($\gamma = 0$), Eq. (16) reduces to classical Maxwell's estimate for the effective conductivity

$$k_{\text{eff}} = k_m \frac{k_p(1+2c) + 2k_m(1-c)}{k_p(1-c) + k_m(2+c)} \tag{19}$$

while for $\gamma \neq 0$ (interface resistance), it reduces to the following expression obtained by in [Hasselman and Johnson 1987]

$$k_{\text{eff}} = k_m \frac{2c[k_p - k_m(1+\gamma)] + k_p + 2k_m(1+\gamma)}{c[k_m(1+\gamma) - k_p] + k_p + 2k_m(1+\gamma)} \tag{20}$$

It is interesting to note that estimate (19) coincides with those by Mori–Tanaka method [Markov 2000, Eq. 5.46] and the Hashin–Shtrikman formula [1962] for coated sphere assemblage [Milton 2002, Eq. 7.7]. Additionally, Equation (20) has the same form as the estimate by the generalized self-consistent model [Lee et al. 2006, Eq. 28].

## 5. The results

It was demonstrated in [Koroteeva et al. 2010] that the approach based on the equivalent inhomogeneity method allows to adequately capture the influence of the micro-structure of porous material on its overall properties. Here we employed it to evaluate the effective thermal conductivity of isotropic suspensions with conducting particles that are either in perfect contact with the matrix or possess an interface resistance. The maximum number of spherical harmonics used in the numerical simulations reported below was $t_{\max} = 15$ for periodic arrays and $t_{\max} = 11$ for random arrays.

***Periodic composites, perfect thermal contact.*** Consider three cubic arrays of identical particles: the simple cubic array (SC), the body-centered cubic array (BCC), and the face-centered array (FCC) (see Figure 3), and assume that $\alpha = k_p/k_m = 10$.

Table 1 compares our results with those of [Sangani and Acrivos 1983; Cheng and Torquato 1997]. Sangani and Acrivos's results are obtained by using their expression (31), which is of order $O(c^9)$. The coefficients involved in the expression are given by [Sangani and Acrivos 1983, Table 1]. Cheng and Torquato's results [1997] are also of order $O(c^9)$. They are obtained by using expression (3.1) in their paper with the coefficients presented in their Table 1. We have also compared our results with those

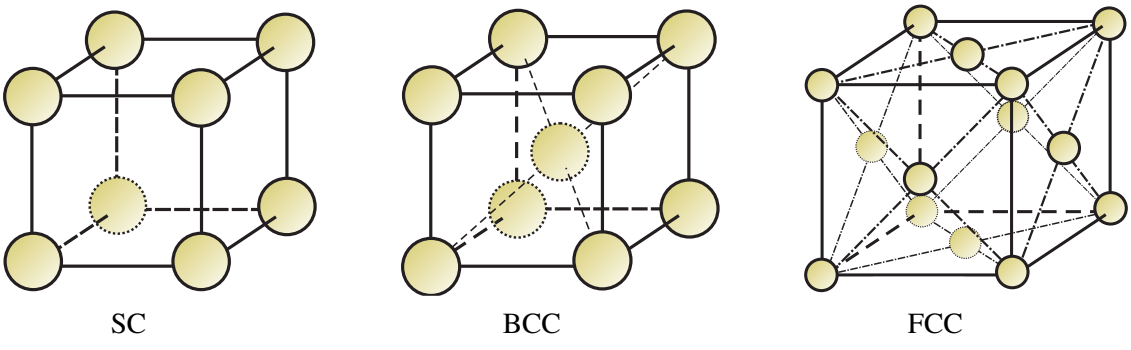


**Figure 3.** The three cubic arrays: simple (SC), body-centered (BCC), and face-centered (FCC).

| $c =$ | 0.1 | 0.2 | 0.3 | 0.4 | 0.45 | 0.5 | 0.6 | 0.65 | 0.7 |
|---|---|---|---|---|---|---|---|---|---|
| | | | | $k_{\text{eff}}/k_m$ for simple cubic array | | | | | |
| Finite cluster model ($N = 8$) | 1.24 | 1.53 | 1.89 | 2.35 | 2.65 | 3.04 | | | |
| Finite cluster model ($N = 27$) | 1.24 | 1.53 | 1.89 | 2.37 | 2.69 | 3.13 | | | |
| Repetitive unit cell | 1.24 | 1.53 | 1.89 | 2.36 | 2.69 | 3.14 | | | |
| [Sangani and Acrivos 1983] | 1.24 | 1.53 | 1.89 | 2.36 | 2.68 | 3.09 | | | |
| [Cheng and Torquato 1997] | 1.24 | 1.53 | 1.89 | 2.36 | 2.66 | 3.05 | | | |
| Maxwell, (19) | 1.24 | 1.53 | 1.87 | 2.29 | 2.53 | 2.80 | | | |
| Differential scheme | 1.26 | 1.59 | 2.03 | 2.59 | 2.92 | 3.30 | | | |
| [Hashin and Shtrikman 1962] | 1.65 | 2.34 | 3.08 | 3.86 | 4.28 | 4.71 | | | |
| | | | | $k_{\text{eff}}/k_m$ for BCC array | | | | | |
| Finite cluster model ($N = 9$) | 1.24 | 1.53 | 1.88 | 2.32 | | 2.89 | 3.69 | 4.26 | |
| Finite cluster model ($N = 35$) | 1.24 | 1.53 | 1.88 | 2.33 | | 2.92 | 3.79 | 4.44 | |
| Repetitive unit cell | 1.24 | 1.53 | 1.87 | 2.30 | | 2.84 | 3.62 | 4.19 | |
| [Sangani and Acrivos 1983] | 1.24 | 1.53 | 1.87 | 2.30 | | 2.84 | 3.60 | 4.12 | |
| [Cheng and Torquato 1997] | 1.24 | 1.53 | 1.87 | 2.30 | | 2.84 | 3.58 | 4.06 | |
| Maxwell, (19) | 1.24 | 1.53 | 1.87 | 2.29 | | 2.80 | 3.45 | 3.85 | |
| Differential scheme | 1.26 | 1.59 | 2.03 | 2.59 | | 3.30 | 4.19 | 4.72 | |
| [Hashin and Shtrikman 1962] | 1.65 | 2.34 | 3.08 | 3.86 | | 4.71 | 5.61 | 6.09 | |
| | | | | $k_{\text{eff}}/k_m$ for FCC array | | | | | |
| Finite cluster model ($N = 14$) | 1.24 | 1.53 | 1.88 | 2.32 | | 2.90 | 3.71 | | 5.05 |
| Finite cluster model ($N = 63$) | 1.24 | 1.53 | 1.88 | 2.32 | | 2.90 | 3.73 | | 5.13 |
| Repetitive unit cell | 1.24 | 1.53 | 1.87 | 2.29 | | 2.83 | 3.56 | | 4.69 |
| [Sangani and Acrivos 1983] | 1.24 | 1.53 | 1.87 | 2.29 | | 2.82 | 3.50 | | 4.45 |
| [Cheng and Torquato 1997] | 1.24 | 1.53 | 1.87 | 2.29 | | 2.83 | 3.55 | | 4.60 |
| Maxwell, (19) | 1.24 | 1.53 | 1.87 | 2.29 | | 2.80 | 3.45 | | 4.32 |
| Differential scheme | 1.26 | 1.59 | 2.03 | 2.59 | | 3.30 | 4.19 | | 5.29 |
| [Hashin and Shtrikman 1962] | 1.65 | 2.34 | 3.08 | 3.86 | | 4.71 | 5.61 | | 6.58 |

**Table 1.** Normalized effective conductivity $k_{\text{eff}}/k_m$ for the simple (top), body-centered (middle) and face-centered (bottom) cubic arrays.

obtained by direct solution of a triple-periodic problem that employs the concept a repetitive unit cell (RUC) (the "direct substitution method", according to the terminology of Sangani and Acrivos). The latter solution also involves a series of spherical harmonics to approximate the temperature on every sphere in the unit cell, and the value of $t_{\max}$ was set to be $t_{\max} = 25$. For the case of a simple cubic array, the RUC results are in perfect agreement with the Brownian motion simulation data in [Kim and Torquato 1991, Table II]. We also include estimates by the differential scheme [Markov 2000, Eq. 10.42] and the classical results of Maxwell given in (19). The latter estimate coincides with those by Mori–Tanaka method, the

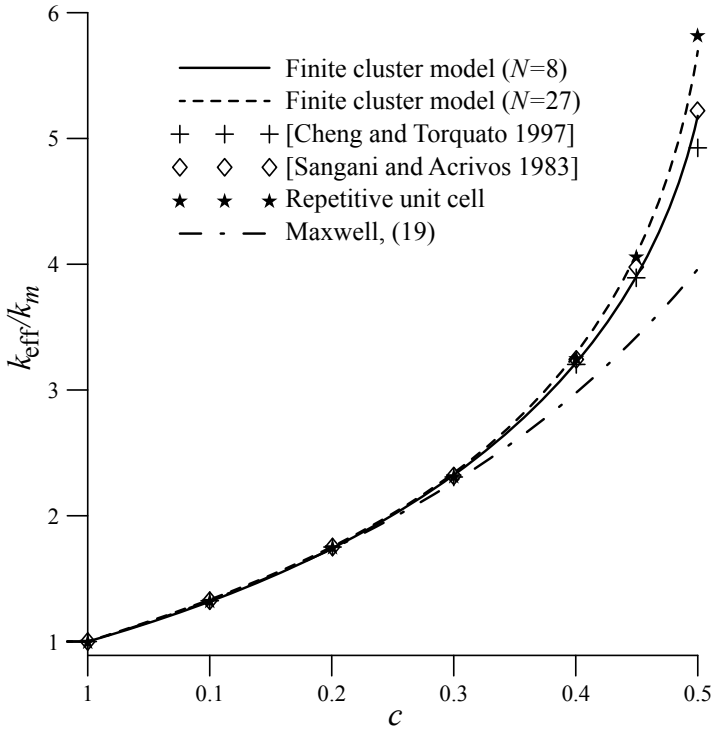


**Figure 4.** Normalized effective conductivity versus volume fraction for the simple cubic case; $k_p/k_m = 1000$.

Hashin–Shtrikman formula for coated sphere assemblage and with the lower bounds of [Hashin and Shtrikman 1962]. Hashin and Shtrikman's upper bounds are included in the tables (last line).

The results for the SC and BCC lattices (top and middle in Table 1) are in good agreement with the those obtained by using a RUC concept and with the results of [Sangani and Acrivos 1983; Cheng and Torquato 1997] (especially for the SC case). However for the FCC lattice, the results agree well only for volume fractions $c < 0.6$. Classical Maxwell estimate underpredicts the values of $k_{\text{eff}}$, while the estimate by the differential scheme overpredicts those values.

A similar trend can be observed on Figures 4 and 5, where the results for the periodic arrays are presented for more severe case, $\alpha = k_p/k_m = 1000$. One can also notice that for the case of very high volume fractions, there is a significant scatter in the previously available results. As in the previous case, the results for the SC lattice are in excellent agreement with the RUC results.

***Random composites: perfect thermal contact.*** We apply our approach to isotropic materials with random arrangement of highly conducting particles ($k_p/k_m = 1000$). To generate the cluster with a random distribution of particles, the method of molecular dynamics of growing particles is used [Sangani and Yao 1988]. To have representative data set, the simulation was executed 30 times with $N = 40$ particles generated in every run. In the case of near-touching spheres, the minimal gap between particles 0.02 was allowed. Our results are compared with those from [Kim and Torquato 1991; Bonnecaze and Brady 1990], who gave the estimated for the case of $\alpha = \infty$.

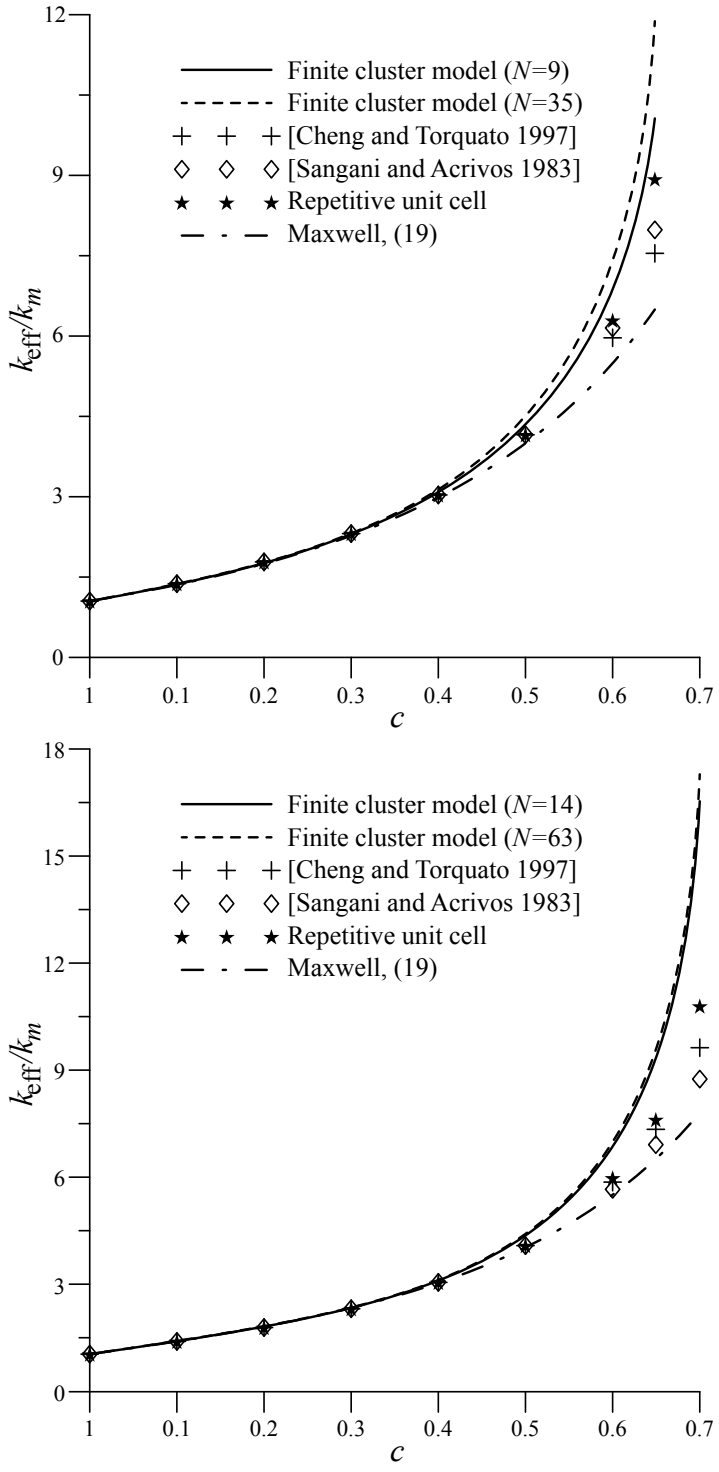


**Figure 5.** Normalized effective conductivity versus volume fraction for the BCC (top) and FCC (bottom) cases; $k_p/k_m = 1000$.

| | | $k_{\text{eff}}/k_m$ | | | | | |
|---|---|---|---|---|---|---|---|
| | $c=$ | 0.1 | 0.2 | 0.3 | 0.4 | 0.5 | 0.6 |
| FCM | $(N=40)$ | 1.34 | 1.80 | 2.44 | 3.40 | 4.76 | 7.84 |
| [Kim and Torquato 1991] | $(\alpha=\infty)$ | 1.34 | 1.83 | 2.48 | 3.42 | 4.78 | 8.32 |
| [Bonnecaze and Brady 1990] | $(\alpha=\infty)$ | 1.35 | 1.82 | 2.53 | 3.59 | 4.97 | 8.85 |
| Maxwell | $(\alpha=1000)$ | 1.33 | 1.75 | 2.28 | 2.99 | 3.98 | 5.47 |

**Table 2.** Normalized effective conductivity (random array).

The results presented in Table 2 show that, as expected, our estimates are slightly below those obtained by Kim and Torquato as well as Bonnecaze and Brady for the superconducting spheres ($\alpha=\infty$). It can also be seen that the classical Maxwell estimate underpredicts the value of the effective conductivity for larger volume fractions.

***Random composites: interface resistance.*** In this case the materials with random distribution of particles which possess interfacial resistance are considered. We obtained the results for a cluster of $N=20$ particles with conductivities $\alpha=k_p/k_m=1000$, and then compare them to the experimental data of Araujo and Rosenberg [1976], who measured the effective thermal conductivity of random dispersions of metallic spheres in an epoxy matrix. The same data were used by Torquato and Rintoul [1995] to compare their bounds. In Araujo and Rosenberg's experiment, the resistance at the boundaries of particles appears at low temperatures (less than 20 K) due to an acoustic mismatch. As one can see from Figure 6, the estimates of our approach agree well with the experimental results. Comparing with the

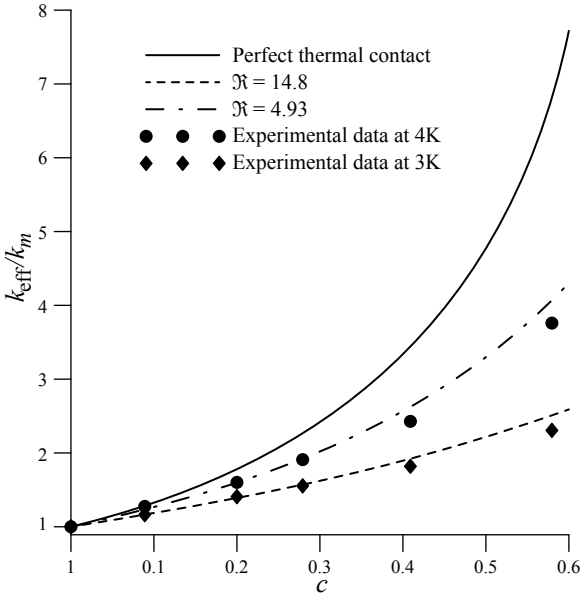


**Figure 6.** Normalized effective conductivity versus volume fraction: comparison with experimental data ($k_p/k_m=1000,\ \mathfrak{R}=a_p/\widetilde{R}$).

results for the perfectly bonded particles, one can see a noticeable drop in the effective conductivity due to interfacial resistance.

## 6. Discussion and summary

In this paper, the approach based on the concept of the equivalent inhomogeneity is employed to evaluate the effective thermal conductivities of isotropic suspensions with highly conducting particles that are either in perfect contact with the matrix or possess an interface resistance. The approach can be viewed as an extension of the classical Maxwell's methodology, but, with the interactions between the particles in the cluster precisely accounted for. The approach has been tested on a number of benchmark solutions for suspensions with highly conducting particles. The numerical results indicate that, in the latter case, the classical Maxwell methodology accurately predict the effective thermal conductivity only for relatively low volume fractions. In the case of high volume fractions, the interactions between the particles must be taken into account to obtain better estimates. The approach is especially attractive for study the materials with random statistically homogeneous micro-structure, as it does not require the concept of a repetitive unit cell, which itself violates the notion of randomness. The analytical solution of the cluster problem is also simpler than the solution of the corresponding triple-periodic problem. In the present paper, the representative clusters for random composites were generated inside the cube, but they could also be generated inside the sphere (the influence of the shape and the size of the cluster will be the topic of future research). The method could be useful for estimation of the overall properties of the material based on the small samples (obtained by e.g., scanning electron micrograph, X-ray micro-tomography, etc). The approach can be extended on the case of macroscopically anisotropic materials containing isotropic particles, if the concept of an equivalent anisotropic inhomogeneity is adopted.

## Appendix: solid harmonics

We adopt the following representation of the solid spherical harmonics (see [Kushch 1985]):

$$y_t^s(\boldsymbol{r}) = \frac{r^t}{(t+s)!}\chi_t^s(\theta,\varphi) \text{ and } Y_t^s(\boldsymbol{r}) = \frac{(t-s)!}{r^{t+1}}\chi_t^s(\theta,\varphi) \tag{21}$$

where $y_t^s(\boldsymbol{r})$ and $Y_t^s(\boldsymbol{r})$ are the regular and singular solid spherical harmonics, respectively, and $\boldsymbol{r} = (x, y, z)$ is the radius vector. Here,

$$\chi_t^s(\theta,\varphi) = P_t^s(\cos\theta)\exp(\mathrm{i}s\varphi) \tag{22}$$

are the surface spherical harmonics, $t \geq 0$, $|s| \leq t$, $\mathrm{i} = \sqrt{-1}$, and $P_t^s(\cos\theta)$ are the associated Legendre polynomials [Hobson 1955].

The normalization adopted in (21) is convenient in many aspects.

$$y_t^{-s}(\boldsymbol{r}) = (-1)^s\overline{y_t^s(\boldsymbol{r})}, \quad Y_t^{-s}(\boldsymbol{r}) = (-1)^s\overline{Y_t^s(\boldsymbol{r})} \tag{23}$$

For $t = 1$ we get

$$y_1^0(\boldsymbol{r}) = z, \quad y_1^1(\boldsymbol{r}) = \frac{1}{2}(x+\mathrm{i}y), \quad y_1^1(\boldsymbol{r}) = -\frac{1}{2}(x-\mathrm{i}y). \tag{24}$$

and the following differentiation rule can be used:

$$D_1 y_t^s = y_{t-1}^{s-1}, \quad D_2 y_t^s = -y_{t-1}^{s+1}, \quad D_3 y_t^s = y_{t-1}^s; \tag{25}$$
$$D_1 Y_t^s = Y_{t+1}^{s-1}, \quad D_2 Y_t^s = -Y_{t+1}^{s+1}, \quad D_3 Y_t^s = Y_{t+1}^s;$$

where $D_i$ are the differential operators

$$D_1 = \left(\frac{\partial}{\partial x} - \mathrm{i}\frac{\partial}{\partial y}\right), \quad D_2 = \overline{D_1} = \left(\frac{\partial}{\partial x} + \mathrm{i}\frac{\partial}{\partial y}\right), \quad D_3 = \frac{\partial}{\partial z}. \tag{26}$$

Operators $D_2$ and $D_3$ also satisfy

$$(D_2)^s (D_3)^{t-s} \left(\frac{1}{r}\right) = (-1)^t Y_t^s(\boldsymbol{r}) \tag{27}$$

The solid spherical harmonics can be re-expanded in terms of spherical coordinates of a particular local coordinate system using the re-expansion formulae. Let $\boldsymbol{r}_p = \boldsymbol{R}_{pq} + \boldsymbol{r}_q$ (Figure 2, left). In our notations, the re-expansions take the simplest possible form:
singular to regular (S2R):

$$Y_t^s(\boldsymbol{r}_p) = \sum_{k=0}^{\infty} \sum_{l=-k}^{k} (-1)^{k+l} Y_{t+k}^{s-l}(\boldsymbol{R}_{pq}) y_k^l(\boldsymbol{r}_q), \quad \|\boldsymbol{r}_q\| < \|\boldsymbol{R}_{pq}\|; \tag{28}$$

regular to regular (R2R):

$$y_t^s(\boldsymbol{r}_p) = \sum_{k=0}^{t} \sum_{l=-k}^{k} y_{t-k}^{s-l}(\boldsymbol{R}_{pq}) y_k^l(\boldsymbol{r}_q); \tag{29}$$

singular to singular (S2S):

$$Y_t^s(\boldsymbol{r}_p) = \sum_{k=t}^{\infty} \sum_{l=-k}^{k} (-1)^{t+k+s+l} y_{k-t}^{s-l}(\boldsymbol{R}_{pq}) Y_k^l(\boldsymbol{r}_q), \quad \|\boldsymbol{r}_q\| > \|\boldsymbol{R}_{pq}\|. \tag{30}$$

## References


[Araujo and Rosenberg 1976] F. F. T. Araujo and H. M. Rosenberg, "The thermal conductivity of epoxy-resin/metal-powder composite materials from 1.7 to 300K", *J. Phys. D Appl. Phys.* **9**:4 (1976), 665–675.

[Batchelor 1972] G. K. Batchelor, "Sedimentation in a dilute dispersion of spheres", *J. Fluid Mech.* **52**:2 (1972), 245–268.

[Batchelor and Green 1972] G. K. Batchelor and J. T. Green, "The determination of the bulk stress in a suspension of spherical particles to order $c^2$", *J. Fluid Mech.* **56**:3 (1972), 401–427.

[Batchelor and O'Brien 1977] G. K. Batchelor and R. W. O'Brien, "Thermal or electrical conduction through a granular material", *Proc. R. Soc. Lond. A* **355**:1682 (1977), 313–333.

[Bonnecaze and Brady 1990] R. T. Bonnecaze and J. F. Brady, "A method for determining the effective conductivity of dispersions of particles", *Proc. R. Soc. Lond. A* **430**:1879 (1990), 285–313.

[Bonnecaze and Brady 1991] R. T. Bonnecaze and J. F. Brady, "The effective conductivity of random suspensions of spherical particles", *Proc. R. Soc. Lond. A* **432**:1886 (1991), 445–465.

[Cheng and Torquato 1997] H. Cheng and S. Torquato, "Effective conductivity of periodic arrays of spheres with interfacial resistance", *Proc. R. Soc. Lond. A* **453**:1956 (1997), 145–161.

[Hashin 2001] Z. Hashin, "Thin interphase/imperfect interface in conduction", *J. Appl. Phys.* **89**:4 (2001), 2261–2267.

[Hashin and Shtrikman 1962] Z. Hashin and S. Shtrikman, "A variational approach to the theory of the effective magnetic permeability of multiphase materials", *J. Appl. Phys.* **33**:10 (1962), 3125–3131.

[Hasselman and Johnson 1987] D. P. H. Hasselman and L. F. Johnson, "Effective thermal conductivity of composites with interfacial thermal barrier resistance", *J. Compos. Mater.* **21**:6 (1987), 508–515.

[Hobson 1955] E. W. Hobson, *The theory of spherical and ellipsoidal harmonics*, Chelsea, New York, 1955.

[Jeffrey 1973] D. J. Jeffrey, "Conduction through a random suspension of spheres", *Proc. R. Soc. Lond. A* **335**:1602 (1973), 355–367.

[Kim and Torquato 1990] I. C. Kim and S. Torquato, "Determination of the effective conductivity of heterogeneous media by Brownian motion simulation", *J. Appl. Phys.* **68**:8 (1990), 3892–3903.

[Kim and Torquato 1991] I. C. Kim and S. Torquato, "Effective conductivity of suspensions of hard spheres by Brownian motion simulation", *J. Appl. Phys.* **69**:4 (1991), 2280–2289.

[Koroteeva et al. 2010] O. Koroteeva, S. Mogilevskaya, S. Crouch, and E. Gordeliy, "A computational technique for evaluating the effective thermal conductivity of isotropic porous materials", *Eng. Anal. Bound. Elem.* **34**:9 (2010), 793–801.

[Kushch 1985] V. I. Kushch, Напряженное состояние и физико-механические характеристики упругихзернистых композитных материалов регулярной структуры, Ph.D. thesis, Institute of Mechanics, Kiev, 1985.

[Lee et al. 2006] Y.-M. Lee, R.-B. Yang, and S.-S. Gau, "A generalized self-consistent method for calculation of effective thermal conductivity of composites with interfacial contact conductance", *Int. Commun. Heat Mass* **33**:2 (2006), 142–150.

[Lu 1998] S.-Y. Lu, "Effective conductivities of aligned spheroid dispersions estimated by an equivalent inclusion model", *J. Appl. Phys.* **84**:5 (1998), 2647–2655.

[Lu and Lin 1996] S.-Y. Lu and H.-C. Lin, "Effective conductivity of composites containing aligned spheroidal inclusions of finite conductivity", *J. Appl. Phys.* **79**:9 (1996), 6761–6769.

[Markov 2000] K. Z. Markov, "Elementary micromechanics of heterogeneous media", pp. 1–162 in *Heterogeneous media: micromechanics modeling methods and simulations*, edited by K. Z. Markov and L. Preziosi, Birkhäuser, Boston, 2000.

[Maxwell 1892] J. C. Maxwell, *A treatise on electricity and magnetism*, vol. 1, 3rd ed., Clarendon, Oxford, 1892.

[McCartney 2010] L. N. McCartney, "Maxwell's far-field methodology predicting elastic properties of multiphase composites reinforced with aligned transversely isotropic spheroids", *Philos. Mag. Lett.* **90**:31–32 (2010), 4175–4207.

[McCartney and Kelly 2008] L. N. McCartney and A. Kelly, "Maxwell's far-field methodology applied to the prediction of properties of multi-phase isotropic particulate composites", *Proc. R. Soc. Lond. A* **464**:2090 (2008), 423–446.

[McKenzie et al. 1978] D. R. McKenzie, R. C. McPhedran, and G. H. Derrick, "The conductivity of lattices of spheres, II: The body centred and face centred cubic lattices", *Proc. R. Soc. Lond. A* **362**:1709 (1978), 211–232.

[McPhedran and McKenzie 1978] R. C. McPhedran and D. R. McKenzie, "The conductivity of lattices of spheres, I: The simple cubic lattice", *Proc. R. Soc. Lond. A* **359**:1696 (1978), 45–63.

[Meredith and Tobias 1960] R. E. Meredith and C. W. Tobias, "Resistance to potential flow through a cubical array of spheres", *J. Appl. Phys.* **31**:7 (1960), 1270–1273.

[Milton 2002] G. W. Milton, *The theory of composites*, Cambridge Monographs on Applied and Computational Mathematics **6**, Cambridge University Press, Cambridge, 2002.

[Mogilevskaya et al. 2010] S. G. Mogilevskaya, S. L. Crouch, H. K. Stolarski, and A. Benusiglio, "Equivalent inhomogeneity method for evaluating the effective elastic properties of unidirectional multi-phase composites with surface/interface effects", *Int. J. Solids Struct.* **47**:3-4 (2010), 407–418.

[Moosavi et al. 2003] A. Moosavi, P. Sarkomaa, and W. Polashenski, Jr., "The effective conductivity of composite materials with cubic arrays of multi-coated spheres", *Appl. Phys. A Mater. Sci. Process.* **77**:3–4 (2003), 441–448.

[O'Brien 1979] R. W. O'Brien, "A method for the calculation of the effective transport properties of suspensions of interacting particles", *J. Fluid Mech.* **91**:1 (1979), 17–39.

[Pyatigorets and Mogilevskaya 2011] A. V. Pyatigorets and S. G. Mogilevskaya, "Evaluation of effective transverse mechanical properties of isotropic viscoelastic composite materials", *J. Compos. Mater.* **45**:25 (2011), 2641–2658.

[Rayleigh 1892] L. Rayleigh, "On the influence of obstacles arranged in rectangular order upon the properties of a medium", *Philos. Mag.* **34**:211 (1892), 481–502.

[Runge 1925] I. Runge, "Zur elektrischen Leitfähigkeit metallischer Aggregate", *Z. Tech. Phys.* **6**:91 (1925), 61–68.

[Sangani and Acrivos 1983] A. S. Sangani and A. Acrivos, "The effective conductivity of a periodic array of spheres", *Proc. R. Soc. Lond. A* **386**:1791 (1983), 263–275.

[Sangani and Yao 1988] A. S. Sangani and C. Yao, "Bulk thermal conductivity of composites with spherical inclusions", *J. Appl. Phys.* **63**:5 (1988), 1334–1341.

[Sevostianov and Kachanov 2007] I. Sevostianov and M. Kachanov, "Effect of interphase layers on the overall elastic and conductive properties of matrix composites: applications to nanosize inclusion", *Int. J. Solids Struct.* **44**:3-4 (2007), 1304–1315.

[Suen et al. 1979] W. M. Suen, S. P. Wong, and K. Young, "The lattice model of heat conduction in a composite material", *J. Phys. D Appl. Phys.* **12**:8 (1979), 1325–1338.

[Torquato 2002] S. Torquato, *Random heterogeneous materials: microstructure and macroscopic properties*, Interdisciplinary Applied Mathematics **16**, Springer, New York, 2002.

[Torquato and Rintoul 1995] S. Torquato and M. D. Rintoul, "Effect of the interface on the properties of composite media", *Phys. Rev. Lett.* **75**:22 (1995), 4067–4070.

[de Vries 1952] D. A. de Vries, "Het warmtegeleidingsvermogen van grond", *Meded. Landbouwhogesch. Wagening.* **52**:1 (1952), 1–73. Translated as "The thermal conductivity of soil" in *Library Communication* **759**, Building Research Station, Watford.

[Zinchenko 1994] A. Z. Zinchenko, "An efficient algorithm for calculating multiparticle thermal interaction in a concentrated dispersion of spheres", *J. Comput. Phys.* **111**:1 (1994), 120–135.

[Zinchenko 1998] A. Z. Zinchenko, "Effective conductivity of loaded granular materials by numerical simulation", *Phil. Trans. R. Soc. A* **356**:1749 (1998), 2953–2998.

[Zuzovsky and Brenner 1977] M. Zuzovsky and H. Brenner, "Effective conductivities of composite materials composed of cubic arrangements of spherical particles embedded in an isotropic matrix", *Z. Angew. Math. Phys.* **28**:6 (1977), 979–992.

Received 26 Jan 2011. Revised 30 Mar 2011. Accepted 9 May 2011.

SOFIA G. MOGILEVSKAYA: mogil003@umn.edu
*Department of Civil Engineering, University of Minnesota, 500 Pillsbury Drive SE, Minneapolis MN 55455, United States*
http://www.ce.umn.edu/people/faculty/mogilevs/

VOLODYMYR I. KUSHCH: vkushch@bigmir.net
*Inst for Superhard Materials, Ukrainian Academy of Sciences, 2, Avtozavodskaya Str, Kiev, 04074, Ukraine*

OLESYA KOROTEEVA: olesya.koroteeva@gmail.com
*Department of Civil Engineering, University of Minnesota, 500 Pillsbury Drive SE, Minneapolis 55455, United States*

STEVEN L. CROUCH: crouch@umn.edu
*Department of Civil Engineering, University of Minnesota, 500 Pillsbury Drive SE, Minneapolis 55455, United States*
http://www.ce.umn.edu/directory/faculty/crouch

## SUBMISSION GUIDELINES

### ORIGINALITY

Authors may submit manuscripts in PDF format online at the Submissions page. Submission of a manuscript acknowledges that the manuscript is original and has neither previously, nor simultaneously, in whole or in part, been submitted elsewhere. Information regarding the preparation of manuscripts is provided below. Correspondence by email is requested for convenience and speed. For further information, write to one of the Chief Editors:


| | |
|---|---|
| Davide Bigoni | bigoni@ing.unitn.it |
| Iwona Jasiuk | ijasiuk@me.concordia.ca |
| Yasuhide Shindo | shindo@material.tohoku.ac.jp |


### LANGUAGE

Manuscripts must be in English. A brief abstract of about 150 words or less must be included. The abstract should be self-contained and not make any reference to the bibliography. Also required are keywords and subject classification for the article, and, for each author, postal address, affiliation (if appropriate), and email address if available. A home-page URL is optional.

### FORMAT

Authors can use their preferred manuscript-preparation software, including for example Microsoft Word or any variant of TEX. The journal itself is produced in LATEX, so accepted articles prepared using other software will be converted to LATEX at production time. Authors wishing to prepare their document in LATEX can follow the example file at www.jomms.net (but the use of other class files is acceptable). At submission time only a PDF file is required. After acceptance, authors must submit all source material (see especially Figures below).

### REFERENCES

Bibliographical references should be complete, including article titles and page ranges. All references in the bibliography should be cited in the text. The use of BibTEX is preferred but not required. Tags will be converted to the house format (see a current issue for examples); however, for submission you may use the format of your choice. Links will be provided to all literature with known web locations; authors can supply their own links in addition to those provided by the editorial process.

### FIGURES

Figures must be of publication quality. After acceptance, you will need to submit the original source files in vector format for all diagrams and graphs in your manuscript: vector EPS or vector PDF files are the most useful. (EPS stands for Encapsulated PostScript.)

Most drawing and graphing packages—Mathematica, Adobe Illustrator, Corel Draw, MATLAB, etc.—allow the user to save files in one of these formats. Make sure that what you're saving is vector graphics and not a bitmap. If you need help, please write to graphics@msp.org with as many details as you can about how your graphics were generated.

Please also include the original data for any plots. This is particularly important if you are unable to save Excel-generated plots in vector format. Saving them as bitmaps is not useful; please send the Excel (.xls) spreadsheets instead. Bundle your figure files into a single archive (using zip, tar, rar or other format of your choice) and upload on the link you been given at acceptance time.

Each figure should be captioned and numbered so that it can float. Small figures occupying no more than three lines of vertical space can be kept in the text ("the curve looks like this:"). It is acceptable to submit a manuscript with all figures at the end, if their placement is specified in the text by means of comments such as "Place Figure 1 here". The same considerations apply to tables.

### WHITE SPACE

Forced line breaks or page breaks should not be inserted in the document. There is no point in your trying to optimize line and page breaks in the original manuscript. The manuscript will be reformatted to use the journal's preferred fonts and layout.

### PROOFS

Page proofs will be made available to authors (or to the designated corresponding author) at a Web site in PDF format. Failure to acknowledge the receipt of proofs or to return corrections within the requested deadline may cause publication to be postponed.

Journal of Mechanics of Materials and Structures

Volume 7, No. 1 January 2012



1559-3959(2012)7:1;1-D